Dissertation

submitted to the

Combined Faculties of Mathematics, Engineering and Natural Sciences

of Heidelberg University, Germany

for the degree of

Doctor of Natural Sciences

Put forward by

Judith Besuglow

born in Bergisch Gladbach, Germany

Oral examination: 02.12.2024

Towards the Clinical Application of Helium Ions at the Heidelberg Ion-Beam Therapy Center

– Physical and Clinical Aspects

Referees:

Prof. Dr. Dr. Jürgen Debus

Prof. Dr. Hans-Christian Schulz-Coulon

„Ich wollte nie erwachsen sein.“ (‘Nessaja’, Peter Maffay and Rolf Zuchowski)

„‚Du bist so STARK* ich könnte das ja nicht.‘
*Aus der Serie: Dinge, die junge Menschen mit Krebs nicht mehr hören können“
(Deutsche Stiftung für junge Erwachsene mit Krebs, Treffpunkt Köln)

Abstract - Kurzfassung

Towards the Clinical Application of Helium Ions at the Heidelberg Ion-Beam Therapy Center

Long before the invention of current standard modalities such as intensity-modulated radiotherapy, helium ions were already incorporated clinically in the 1980s at the Lawrence Berkeley National Lab. At the onset of this research, although helium ion beams are available for pre-clinical experiments at the Heidelberg Ion-Beam Therapy Center (HIT), a clinically validated Treatment Planning System (TPS) with a refined dose calculation model was still warranted for a safe clinical application. This doctoral thesis reports and outlines a comprehensive database of beam properties created to this end. This database includes the geometric dose distribution for each of the available 255 initial beam energies at HIT, as well as measurements of depth and lateral dose profiles measured and recreations thereof via a Monte Carlo beam model. Moreover, the thereby prepared beam model allowed for the investigation on the influence of the dose received by a patient in the presence of any variations. These efforts significantly contributed to the successful commissioning of the first commercial TPS for helium ion beams, enabling the first patient treatment. Finally, to correctly assess the biological damage induced by this new radiation modality, a retrospective analysis of a past clinical trial was carried out, evaluating models of relative biological effectiveness for protons and carbon ions regarding their predictive capability for the tumor control of prostate cancer.

Zur klinischen Anwendung von Heliumionen am Heidelberger Ionenstrahltherapiezentrum

Lange vor Erfindung heutiger Standardmodalitäten wie der intensitätsmodulierten Strahlentherapie wurden Heliumionen bereits in den 1980er Jahren am Lawrence Berkeley National Lab klinisch eingesetzt. Zu Beginn dieser Forschungsarbeit standen Helium-Ionenstrahlen zwar für präklinische Experimente am Heidelberger Ionenstrahl-Therapiezentrum (HIT) zur Verfügung, doch war eine sichere klinische Anwendung noch nicht gewährleistet, da kein klinisch validiertes Behandlungsplanungssystem (TPS) mit einem detaillierten Dosisberechnungsmodell vorhanden war. In dieser Dissertation wird eine umfassende Datenbank mit Strahleigenschaften vorgestellt, welche zu diesem Zweck erstellt wurde. Sie enthält die geometrische Dosisverteilung für jede der 255 am HIT verfügbaren Strahlenergien, sowie Messungen von Tiefendosiskurven und lateralen Dosisprofilen, welche mit Hilfe eines Monte-Carlo-Strahlmodells rekonstruiert wurden. Darüber hinaus ermöglichte das so erstellte Strahlmodell die Untersuchung des Einflusses von Variationen der Strahleigenschaften auf die Dosis im Patienten. Diese Bemühungen trugen wesentlich zur erfolgreichen Inbetriebnahme des ersten kommerziellen TPS für Helium-Ionenstrahlen bei, wodurch erste Patientenbehandlungen möglich wurden. Für die korrekte Einschätzung der biologischen Schäden, welche durch diese neue Bestrahlungsmodalität induziert werden, wurde schließlich eine retrospektive Analyse einer früheren klinischen Studie durchgeführt. Dabei wurden Modelle der relativen biologischen Wirksamkeit (RBE) für Protonen und Kohlenstoffionen hinsichtlich ihrer Vorhersagefähigkeit für die Tumorkontrolle bei Prostatakrebs bewertet.

Contents

List of Figures

List of Tables

List of Abbreviations

EPR	entrance-to-peak ratio 9, 37, 38, 98, 139
FWHM	full width at half maximum 4, 27, 37, 98, 135, 136, 137
LET_d	dose-averaged linear energy transfer xi, 7, 15, 23, 30, 31, 41, 100, 104, 109, 149
TPR	tail-to-peak ratio 37, 139
EQD_2	equivalent dose to 2 Gy fractionation 14, 18, 25
ADT	androgen deprivation therapy 42, 107
BAMS	beam application and monitoring system 26, 30, 32, 98, 110
BED	biologically effective dose xi, 14, 25, 43, 105, 107, 110
BEV	beam's eye view 26
BME	Boltzmann Master equation 9, 97, 145
BP	Bragg peak 4, 8, 9, 17, 26, 32, 33, 35, 97, 98, 103
bRFS	biological relapse-free survival 19, 21, 42, 43, 105, 107
CSDA	continuous slowing down approximation 9
CT	computed tomography 23, 24
CTCAE	common terminology criteria for adverse effects 21
CTV	clinical target volume xi, 24, 43, 148
DICOM	Digital Imaging and Communications in Medicine 23, 24, 31
DNA	desoxyribonucleic acid 13, 15
DVH	dose-volume-histogram xi, 18, 19, 31, 42, 43, 101, 147, 149
EUD	equivalent uniform dose 18, 21
FLUKA	Fluktuierende Kaskade 9, 29, 30, 36, 37, 38, 39, 41, 65, 66, 97, 98, 99, 100, 101, 135, 137, 143, 145
FRoG	Fast Recalculation on GPU 29, 30, 31, 38, 41, 43, 66, 98, 100, 101
Fx	irradiation fraction 14, 104, 105
GTV	gross target volume 24

HIT	Heidelberg Ion Beam Therapy Center 3, 4, 5, 8, 9, 10, 16, 17, 25, 27, 29, 30, 31, 37, 40, 41, 42, 97, 98, 100, 103, 104, 106, 110
HU	Hounsfield unit 23
IC	ionization chamber 10, 11, 12, 32, 33, 34, 35, 65
IDD	laterally integrated depth dose distribution 4, 11, 31, 32, 37, 38, 65, 97, 98, 135, 136, 139
IPI	Ion Prostate Irradiation xi, 42, 43, 100, 101, 104, 107, 109, 110, 147, 149
ITV	internal target volume 24
LEM	Local Effect Model 16, 17, 42
LEM-IV	Local Effect Model, version 4 16, 17
LEM-I	Local Effect Model, version 1 16, 41, 104, 106
LET	linear energy transfer 7, 8, 12, 15, 17, 106, 110
LIBC	accelerator library containing nominal beam energies, beamwidths and intensity settings 27, 38, 136, 137
LKB	Lyman-Kutcher-Burman 21, 43, 109
LQ	linear-quadratic 13, 14, 15, 16, 20, 41, 43, 147
MC	Monte Carlo 5, 9, 23, 29, 30, 31, 36, 37, 97, 100, 110, 137
MEFI	medical combinations of energy, focus and intensity 27
MKM	Microdosimetric Kinetic Model 16, 17
mMKM	modified Microdosimetric Kinetic Model xi, xiii, 16, 17, 31, 41, 42, 66, 101, 104, 105, 106, 107, 147, 149
MonteRay	a fast Monte Carlo Dose Engine for Protons, Helium Ions and Carbon Ions 30
MWPC	multi-wire proportional chamber 26, 27
noRiFi	no ripple filter in the beamline 38, 135, 136, 137
NTCP	normal tissue complication probability 21, 43, 105, 109
OAR	organ at risk 24, 43, 101, 104, 105, 110, 147
OS	overall survival 19
PFS	progression-free survival 19, 20
PMMA	polymethylmethacrylate 9, 10, 12, 26, 33, 39
POI	point of interest 24
PROM	patient reported outcome measure 20, 105
PRV	planning risk volume 24
PSA	prostate specific antigen 19
PTV	planning target volume 24
QA	quality assurance 27

QUANTEC	Quantitative Analysis of Normal Tissue Effects in the Clinic 21, 24, 43
RaShi	range shifter 26
RBE	relative biological effectiveness xi, xiii, 13, 15, 16, 17, 19, 22, 23, 25, 31, 41, 42, 43, 66, 100, 101, 104, 105, 106, 107, 109, 110, 147, 149
RiFi3mm	3mm thick ripple filter 26, 135, 136, 137, 140
ROI	region of interest 24
RQMD	relativistic quantum molecular dynamics model 9, 97, 145
RTOG	Radiation Therapy Oncology Group, USA 21, 105
SIB	simultaneously integrated boost 24
SOBP	spread-out Bragg peak 4, 10, 12, 17, 27, 36, 39, 98, 109, 110, 137, 138, 143
SOMA/LENT	subjective objective management analytic / late effect of normal tissues 21
SPR	stopping power ratio 24
TCP	tumor control probability 20, 21, 42, 43, 101, 105, 107, 110, 147
TPS	treatment planning system 4, 5, 17, 18, 23, 24, 25, 27, 29, 30, 31, 32, 33, 36, 40, 97, 98, 100, 103, 109, 110, 135, 136, 138
VSAD	virtual source axis distance 26, 30, 98
WEPL	water equivalent path-length 39

List of Symbols

$(\alpha/\beta)_{\mathrm{x}}$	alphabeta-ratio of photon reference radiation xi, 14, 17, 25, 43, 101, 104, 105, 106, 110, 147, 148, 149
α_{x}	alpha of photon reference radiation 14, 16, 17, 25, 41, 147
β_{x}	beta of photon reference radiation 14, 16, 17, 25, 41, 101, 147
D	absorbed (energy) dose xi, 7, 8, 16, 23, 41, 149
DFO	distal fall-off, $\lvert R_{20d} - R_{80d} \rvert$ 37, 139
D_{peak}	highest dose of a Bragg peak 37
E	effective dose 8
E#	energy index 27, 136
ϵ	energy imparted 7
e	Euler's number 43
H	equivalent dose 8
m_e	electron mass (0.511 MeV) 9
w_{peak}	peak size, $\lvert R_{80d} - R_{80p} \rvert$ 9, 26, 37, 139
Φ	fluence 7, 23, 39
R_d	radius of a domain 17, 147
R_{first}	first data point in a Bragg peak 37
ρ	density 7, 23
R_{last}	last data point in a Bragg peak 37
R_n	radius of a nucleus 17, 147
R_{peak}	position of maximum dose in a Bragg peak 35, 37
R_{tail}	$R_{\mathrm{tail}} = R_{90} + 10\,\mathrm{mm}$ 33, 37, 139
R_x	distal position of x% dose level 37
$R_{xx,p}$	proximal position of x% dose level 37
S_{col}	collision stopping power 9
SF	survival fraction 13, 14, 20, 21
z	specific energy 7, 17
z^*_{1d}	dose-mean averaged saturation-corrected specific energy of an event 17, 30, 31, 41, 101, 147

Part I

Comprehensive Introduction

1 Motivation

The clinical adaptation of helium ions for radiotherapy has been long planned. This doctoral thesis in medical physics covers the physical and clinical steps towards the first patient treatment with raster-scanned helium ions.

1.1 Why Helium Ions?

Why should we add another technique of radiotherapy to the quiver of cancer treatments? And why should it be helium ions, one might ask.

Technically, helium ions have been an option long before the invention of modern standard modalities, such as intensity modulated radiotherapy (IMRT). In the 1980s, the irradiation with helium ions was even used as the reference irradiation [1] for the treatment of uveal melanoma [2] and even pancreatic tumors [3]. Back then, helium ions were accelerated by the Bevatron at Berkeley [4] and then passively scattered to form irradiation fields and depths that matched the tumor dimensions [5]. With the shut-down of medical research at Bevatron, accelerated helium ions were no longer available for use of reference experiments.

However, helium ions became available for research again, when a third ion source was added to the clinical facility Heidelberg Ion Beam Therapy Center (HIT) in 2012 [6]. At HIT, pencil beams of protons, helium, carbon and oxygen ions are accelerated by a synchrotron and then raster-scanned to cover target volumes with high doses of ionizing irradiation [7]. Protons and carbon ions are currently used successfully for cancer treatment in several centers all over the world. Helium ions are expected to combine their favorable properties, by allowing slimmer pencil beams than protons and depositing less dose in the fragment tail than carbon ions. Hence, the question is rather: Why not? Before a "Let's do it again!", the physical, biological and clinical properties of helium ions have to be characterized more precisely than previous experimental works did. The details of this endeavor are explained in the following chapters.

1.2 Aim of the Thesis

The primary aim of the presented research is to facilitate the treatment of cancer patients with helium ion beams. This begins with the rigorous characterization of the physical properties of helium ion beams. First attempts at such characterizations were made by Lyman and Howard at the 184" synchro-cyclotron at the Lawrence Berkeley National Laboratory in 1977 [8]. They had installed a beam monitoring system and systematically measured the depth dose curves and beam

sizes with a parallel-plate ionization chamber. Splitting the collecting electrode into concentric rings allowed a relatively crude estimate, by today's standards, of the beam size as full width at half maximum (FWHM) of the lateral distribution. The passively scattered beam of the synchro-cyclotron allowed a field diameter up to 30 cm with a large penumbra (90% to 10%) of 3 mm to 8 mm.

General characterization of the ion beams at HIT have been published for protons and carbon ions [9, 10] shortly after its commissioning. Tessonnier et al. also measured width and depth for ten of the 255 available energies of the helium ion beam. More specifically, they investigated laterally integrated depth dose distribution (IDD) and charge collection efficiency for 10 energies [11], and the lateral beam width in water for 3 energy levels [12].

The planned treatment of patients requires a thorough characterization of all available beam configurations for precise dose calculation. In preparation for this thesis, a complete set of base data for a clinical treatment planning system (TPS) is created. This set includes IDDs and the evolution of lateral dose distributions along the depth of a Bragg peak (BP) in air and water. Absolute dosimetry is necessary to scale the relative depth and lateral distributions appropriately. During the acquisition of base data, the following research questions arise:

1. How much smaller is the lateral scattering of helium ions compared to protons?

2. Would a more complex lateral beam profile as input to the simulations, improve agreement with measurements?

3. How much influence does the fluctuation of beam width have on a treatment plan?

German radiation protection laws require the commissioning of the resulting clinical TPS before the first treatment of a patient. Commissioning compares the TPS's predictions to measurements of complex dose distributions consisting of several BPs, such as larger fields or spread-out Bragg peaks (SOBPs). These measurements are used to validate the predictions of any beam model created from the collected base data. If successful, commissioning answers:

4. Which dose computation algorithm adequately predicts the physical properties of helium ion beams of HIT?

Finally, considerations about helium ions' biological and clinical properties are required for broader applications in clinical trials. Within the presented work, these considerations focus on the example of prostate cancer:

5. Which biological model can explain treatment outcome of prostate cancer after proton and carbon ion treatment?

6. How could this treatment outcome benefit from helium ions compared to other ions?

1.3 Outline

As this work is put forward as a cumulative thesis, the author's peer-reviewed publications (part II) are preceded by a comprehensive introduction (part I) and followed by a coherent overall discussion (part III).

In the introduction, Chapter 2 explains the physical (section 2.1), biological (section 2.2) and clinical (section 2.4) fundamentals of radiotherapy, followed by the technical aspects of treatment planning (section 2.5) and acceleration of ions for radiotherapy at HIT (section 2.6). Chapter 3 contains a more thorough methodology than the journal publications (Chapters 4 to 6) allowed. Section 3.1 describes the different methods of creating beam models and their requirements. The measurement setups for base data acquisition are detailed in section 3.2. Section 3.3 describes how the physical base data for an analytic dose engine is extracted from a Monte Carlo (MC) beam model. The methods of commissioning a TPS are already covered by the second publication [13], therefore its methodology is not repeated. Creation of biological dose models is described in section 3.5. Section 3.6 describes the methodology necessary to apply all previous models for the evaluation of prostate cancer treatments.

Part II contains the peer-reviewed publications on

- the investigation of the lateral dose distributions of helium ions in Chapter 4, published in January 2022 [14];
- the commissioning process of the clinical TPS and the first patient treatment in Chapter 5, published in July 2023 [13];
- and the re-investigation of a clinical trial on prostate cancer in Chapter 6, published in August 2024 [15].

Part III discusses the impact of the publications fabricating this thesis in the context of past and future ion therapy. Unpublished results of base data creation and the prostate-cancer re-investigation are presented as part of the appendix for reference.

2 Fundamentals

In this chapter, we will cover the fundamental aspects of radiotherapy from radiation physics and radiobiology to clinical consideration, treatment planning and ion beam acceleration.

2.1 Physics of Particle Therapy

As the physical characteristics of particle beams, specifically helium ion beams, constitute a major part of the base data creation for treatment planning, the underlying physics behind radiotherapy with ion beams will be described in the following sections.

2.1.1 Physical Quantities in Question

The physical quantities used to describe the properties of ionizing radiation traversing materials are:

Fluence Φ is a measure for the number of particles that traverse a unit area at a given time point.

Linear energy transfer (LET) is the energy loss of an ionizing particle per unit length of its trajectory. In practice, the LET_d of a particle fluence is measured or provided.

Specific energy z is the total energy imparted $\epsilon = \sum_{i \in V} \epsilon_i$ within a volume V of mass m divided by the mass of the volume. As ϵ and z are statistical variables, most often the mean specific energy is considered:

$$\langle z \rangle = \int_0^\infty z \cdot f(z) \mathrm{d}z = \frac{\bar{\epsilon}}{m}. \tag{2.1}$$

Absorbed Dose D is always defined in conjunction with the absorbing material, e.g. water, air or tissue. The dose is then the mean energy imparted in an infinitesimal volume $\mathrm{d}V$ of mass $\mathrm{d}m$ following the limit of mean specific energy. Absorbed or *physical* dose is measured in units of "Gray".

$$D = \frac{\mathrm{d}\bar{\epsilon}}{\mathrm{d}m} = \frac{1}{\rho} \cdot \frac{\mathrm{d}\bar{\epsilon}}{\mathrm{d}V} = \lim_{m \to 0} \langle z \rangle \quad \text{unit "Gray"} \left(1\,\mathrm{Gy} = 1\,\mathrm{J\,kg^{-1}}\right) \tag{2.2}$$

Equivalent dose H is measured in "Sievert" and not to be confused with absorbed dose, as it includes a weighting factor accounting for the quality Q of the radiation.

$$H = D \cdot Q(L) \quad \text{unit "Sievert"}(1\,\text{Sv} = 1\,\text{J}\,\text{kg}^{-1}), \tag{2.3}$$

where L is a measure comparable to the LET.

Effective dose E adds additional weighting factors for the biological radiosensitivity of a tissue w_T or organ and the spectrum of radiation qualities w_Q. With the sum of weights over all tissues T and radiation types R, E yields

$$E = \sum_T w_T \cdot \sum_R w_{Q,R} D_{T,R}. \tag{2.4}$$

H and E are used for radiation protection purposes. The concept of weighting absorbed dose with biological sensitivity and radiation quality is mirrored in radiotherapy with the concept of biologically effective and equivalent doses to quantify the difference in biological effects between absorbed doses imparted by different types of radiation. Further details follow in section 2.2.

2.1.2 Interaction of Charged Particles with Matter

Charged particles interact differently with matter than the photons of conventional radiotherapy. Particle therapy includes the irradiation with hadrons, such as protons, neutrons or pions, but also the nuclei of atoms, which have been stripped off their electrons. This thesis focuses on the ions of hydrogen (protons), helium, carbon and oxygen, which are accelerated at the HIT. Due to the high energies achieved by acceleration (velocities of about $0.7\,c$), the ions become directly ionizing radiation.

Elastic scattering on the Coulomb field of atomic electrons of the absorbing material results in energy loss and continuous slowing down of these relativistic ions. The slower they are, the more energy they loose with each interaction. Bragg and Kleeman [16] discovered that charged particles actually stop completely and deposit a high proportion of their energy shortly before reaching their finite range. Therefor, the characteristic depth dose distribution of ions is known as a *Bragg peak (BP)*. Wilson investigated the ionization curve of protons further and saw the BP's high potential for cancer treatment [17]. The depth of the BP depends on the incident energy E and mass of the ions, allowing for precise positioning of the peak into a tumor. Instead of considering each individual Coulomb interaction, most theories gather *multiple Coulomb scattering* into one formula. Molière's theory of multiple scattering [18–20] is probably the most prominent. For simplified calculation of the range, Highland's approximation is often used

[21, 22]. The rate of energy loss per unit of path length due to Coulomb interactions is called electron collision *stopping power* S_{col} and generally follows the Bethe formula [23], here a simplified version:

$$\frac{S_{\text{col}}}{\rho} = k \cdot \frac{Z}{A} \cdot \frac{z^2}{\beta^2} \cdot L(\beta) \quad \text{with } L(\beta) = \frac{1}{2} \ln\left(\frac{2m_e c^2 \beta^2}{(1-\beta^2)I^2}\right) - \beta^2. \tag{2.5}$$

It depends on the *mean excitation energy* I and reduced electron density Z/A of the absorbing material (in the case of ion therapy mostly water with $I_{H_2O} = 76.8, \rho_{H_2O} = 0.998\,\text{g}\,\text{cm}^{-3}$); as well as the charge z and velocity β of the incident ion. The proportionality factor is $k = 4\pi {r_e}^2 m_e c^2 u^{-1} \approx 0.307\,\text{MeV}\,\text{cm}^2\,\text{g}^{-1}$. The stopping number per electron $L(\beta)$ can contain several corrections[23, 24]. An extended tabulation of the stopping powers of helium ions can be found in Ziegler et al. [25, 26] or Report 90 of the ICRU [27]. With the continuous slowing down approximation (CSDA)[28], the range of a particle with initial kinetic energy E_0 can be estimated by the integral over the inverse stopping power:

$$R(E) = \int_0^{E_0} \frac{\mathrm{d}E}{S(E)}. \tag{2.6}$$

As most beams do not remain mono-energetic when traversing material, the BP is smeared out and widened. Thus, w_{peak} increases and entrance-to-peak ratio (EPR) decreases. The process causing this smearing is called *range straggling* and was described for protons by Paganetti et al. [29]. The position of the distal 80 % level of the peak, $R_{80\%}$, is mostly independent of the beam's initial energy or momentum distribution.

Interactions of the incident ion beam with nuclei of the absorbing material produce secondary particles. Their subsequent transport through the absorber creates a dose tail behind the BP's maximum. Not many cross-sections of nuclear interactions in the therapeutically used energy range are published. One example are the measurements of Brissaud and Tatischeff for 166 MeV [30, 31]. Marafini et al. [32] measured the secondary flux and energy spectra of the HIT's helium beam on polymethylmethacrylate (PMMA) for energies 102 MeV u^{-1}, 125 MeV u^{-1} and 145 MeV u^{-1}. Double differential cross-sections were measured by Kurosawa et al. [33–36]. More entries in the EXFOR database [37, 38] are awaited, as requested in Norbury et al. [39]. During the research for this thesis, Luoni et al. [40] gathered a more recent collection of total nuclear reaction cross-sections. Theories to describe the nuclear interactions are the relativistic quantum molecular dynamics model (RQMD) by Sorge et al. [41] or the Boltzmann Master equation (BME) [42, 43].

Detailed cross-section measurements aid in the correct implementation of beam models into MC codes such as Fluktuierende Kaskade (FLUKA), which are the gold standard for dose calculation (section 3.1). For a more thorough description of the interaction of charged particles with matter, the reader is referred to chapters 2 and 6 of Podgoršak's book "Radiation Physics for Medical Physicists" ([44]).

2.1.3 Acceleration of Ion Beams

The desired incident beam energies (several hundreds of MeV u^{-1}) are achieved by either a *cyclotron* or a *synchrotron*. A cyclotron's dimensions determine the maximum energy to which an ion is accelerated between switching magnetic fields. If a lower energy is desired, the beam requires "degrading" by a *range modulator*. Typically made of PMMA or brass, the range modulator produces an energy spectrum, that creates a SOBP with the depth required for patient treatment and reduces the maximum energy to reach the deepest tumor position. In contrast to a synchrotron's interrupted spills, the cyclotron can produce a continuous ion intensity. A synchrotron can be tuned to several beam energies. A bunch of ions is accelerated further with each turn in the synchrotron. The more turns this bunch takes before extraction, the higher is its final energy. Downstream elements still influence the energy distribution, but have little influence on the mean energy of the beam. Each accelerated bunch of ions is called a *spill*.

A more detailed description of the beam line at HIT follows in section 2.6.

2.1.4 Dosimetry of Particle Beams

To measure the physical properties of particle beams, several types of detectors can be used. Guidelines, on how to perform dosimetry, are the TRS 398 [45] and TRS 438 [46] reports of the International Atomic Energy Agency (IAEA), as well as DIN 6800 [47–49]. Reviews from Karger et al. [50] and Schardt et al. [51] describe the development of quality assurance dosimetry in ion beams.

All detectors used in this thesis are some form of an *ionization chamber (IC)*, which consists of an anode and a cathode separated by an ionizable material, most often some gas. So, an IC is basically a capacitor with an attached electrometer circuit. Whenever ionizing radiation travels through the filling material, ion-pairs are created. The resulting positive ions and dissociated electrons travel to the electrodes with opposing polarity and produce a measurable current proportional to the created charge.

Conversion of the raw detector readout M to dose in water D_w requires some correction factors for the detector response. The response depends on detector saturation, intrinsic energy-dependence, detector dimensions and material, environmental factors and quality of measured ionizing radiation Q. These factors are defined by the DIN 6800 standard [47, 48].

If the detector is calibrated under reference conditions and then used in similar conditions, the calibration factor $N_{D,w;Q_0}$ contains all detector intrinsic corrections. And only the deviations from reference conditions need to be taken into account:

$$D = N_{D,w;Q_0} \cdot M \cdot \prod_i k_i. \tag{2.7}$$

The factors k_i account for deviations in air density, humidity, temperature, polarity of chamber's voltage potential, detector positioning and beam quality $k_{Q;Q_0}$.

Additional rules apply in certain circumstances of highly ionizing irradiation or light ion irradiation. These are defined by DIN 6800-2 in its newest version [48] and DIN 6801-1 [52].

Depending on the task, differently shaped ICs are used:

Parallel Plate Ionization Chambers are used to measure the laterally integrated dose of a beam. In the PEAKFINDER® (PTW, Freiburg, Germany), two such parallel chambers (TM34070 Bragg-Peak) are combined with an adjustable column of water. The relative dose between these two chambers is used to determine the IDD, see section 3.2.1.

Point doses are measured with small thimble shaped ICs, such as a Farmer chamber or PinPoint® chamber (TM31015, PTW, Freiburg). The anode is shaped like a cylinder or thimble with a central cathode wire. The relatively small active volume of a thimble chamber allows dosimetry in small fields, when positioned correctly [53–56]. Palmans et al. agreed that the reference point of a thimble chamber is at three quarters of the cavities radius, when irradiated from the side. Figure 2.1 sketches the shape of a PinPoint® chamber.

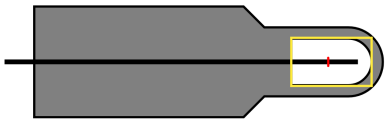

Figure 2.1: *Sketch of a PinPoint® chamber* (TM31015, PTW-Freiburg) with a sensitive volume of 0.03 cm^3 and a diameter of 2.9 mm.

For absolute dosimetry, such as a monitor calibration, reference conditions are very important. Typically slightly bigger thimble shaped Farmer chambers are used [57]. They are irradiated with large homogeneous fields to reduce positioning uncertainties.

Geometrical accuracy of the dose measurements can be assured by the usage of detector arrays, as relative positioning uncertainty between the individual chambers is reduced. The OCTAVIUS® 1000 SRS P (SN: 000308, PTW-Freiburg, Freiburg, Germany), a prototype 2D IC array detector, consists of 977 small air filled ICs on a Cartesian grid. It is used to measure lateral dose distributions of single pencil beams in the first two publications of this thesis (Chapters 4 and 5), but could also measure a complex intensity modulated treatment field [58]. An array of 24-pinpoint chambers (MP3, PTW, Freiburg) is routinely used for patient specific quality assurance, as it allows the simultaneous measurement of three depths inside a water tank [59, 60], compare Figure 2.2. In the commis-

sioning process, both detector types are used for the measurement of SOBPs and in phantom models.

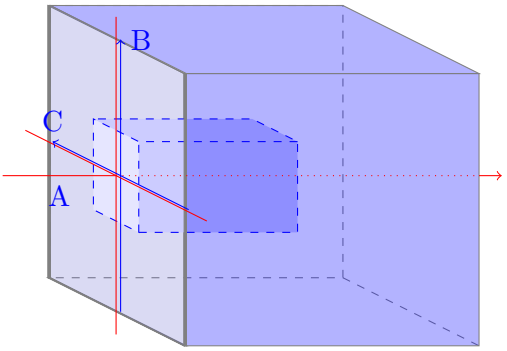

(a) The tank is positioned with the entrance window at the treatment rooms isocenter (indicated by red lasers). The origin of the tank's coordinate system (A: along the beam axis, B: horizontal and C: vertical) is set 5 mm away from the inside of the water tank's entrance window.

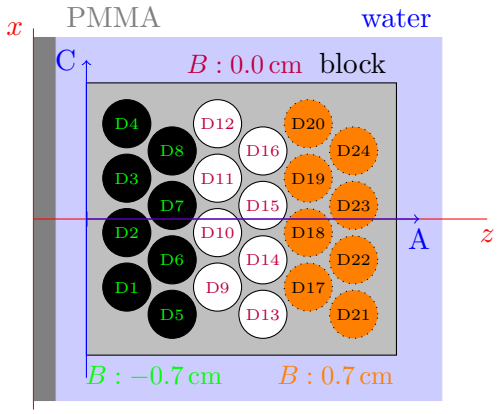

(b) Each chamber position is indicated relative to the block and tank coordinates. The first two rows (in black) are dropped 0.7 cm below the center, and the last two rows (in orange) are 0.7 cm above the central rows (in white).

Figure 2.2: *Ionization Chambers for Absolute Dosimetry inside a watertank.* The MP3 water phantom (PTW-Freiburg, Germany) is equipped with 24 PinPoint® ionization chambers (TM31015, PTW-Freiburg) in a motorized PMMA block.

Additionally, radiochromic or radio-graphic films yield fine-grained geometric information. For quality assurance, they have been used for decades [49, 61–63], although the LET dependence of film discoloration has made their use in ion beams complicated [64–67]. For portal imaging or homogeneity measurements, they are still routinely used, however.

Scintillators emit photons in the visible spectrum, when ionizing radiation passes through. They have been tested as replacement for films as position detectors [68–71].

In very small field or at ultra high dose rates, ICs are not reliable anymore. For these cases diamond detectors are tested [72–75].

For a review of recent developments in ion beam dosimetry the reader is referred to Vedelago et al. [76].

2.2 Radiobiology of Cells

The purpose of radiotherapy is to 'kill' tumor cells by applying sufficient dose. Mostly, the cells won't die directly (apoptosis), but their desoxyribonucleic acid (DNA) is damaged irreparably, so that they loose their ability to proliferate and thus the tumor stops growing. *In vitro* studies yield important information on the dose required to inhibit cell proliferation. The survival of a cell *in vitro* is defined by its ability to form colonies. Hence, the cells' response to radiation exposure can be measured in terms of the survival fraction (SF), the number of colonies formed in an irradiated sample divided by the number of colonies in a control sample.

The dependence of this SF on the total dose D applied to a cell culture can be fitted by a linear-quadratic model as depicted in Figure 2.3.

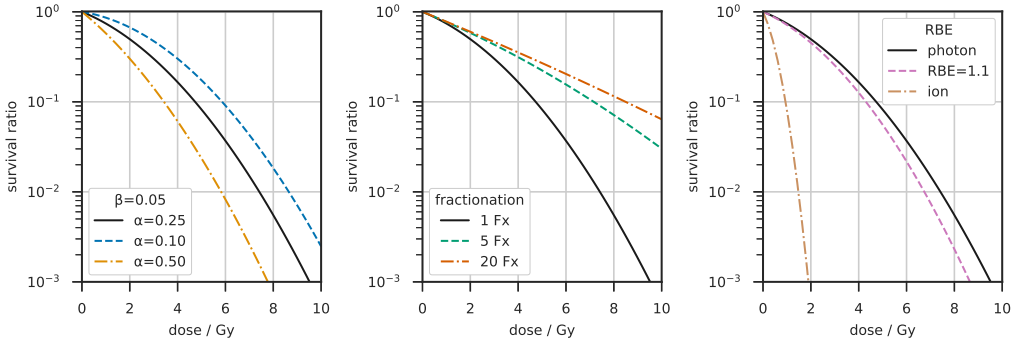

Figure 2.3: *The linear-quadratic (LQ) model of cell survival.* Left panel: Survival for cell lines with high, medium and low radio-sensitivity is differentiable by the parameters α and β. Center panel: The effect of fractionation. Right panel: Comparing the SF of the same cell line for different types of radiotherapy allows for the calculation of RBE.

2.2.1 The linear-quadratic Model of Cell Survival

The basic formulation of the linear-quadratic (LQ) model combines the initial linear response for low doses $D \ll \alpha/\beta$ with a more quadratic term beyond the "shoulder" in semi-logarithmic plots with the total applied dose D, the n fractions and the dose d per fraction:

$$-\ln SF = -\ln N/N_0 = \alpha D + \beta d D. \tag{2.8}$$

The curves in the left panel of Figure 2.3 follow this basic formulation.

Cells might not all have the same radio-sensitivity so the overall survival in a heterogeneous tissue could be described by the product of several SF_i with:

$$-\ln(SF_i) = \alpha_i D + \beta_i d D. \tag{2.9}$$

2.2.2 Fractionation Effect

When the treatment dose is split into several deliveries, so called irradiation fractions (Fxs), the total dose necessary for the same effect is increased. This phenomenon becomes understandable, if thinking of it as the superposition of the LQ-model's 'shoulder' as depicted in Figure 2.3b). In between two fractions, the cells have some time to recover. Thus with the next fraction, the remaining cells' SF follows the low-dose part of the LQ-model again. This effect is depicted in the center panel of Figure 2.3.

With time for recovery, adjacent or unaffected cells can repopulate the irradiated area and raise the culture's total number of cells. If an incompletely repaired cell receives a second dose, its ability to form colonies might be further reduced. Both scenarios can be accounted for by adding additional terms to Equation (2.8). Other corrections, e.g. for oxygenation of the cell culture or cell cycle at irradiation time, are possible and several mechanistic or phenomenological descriptions of the underlying processes have been published [77].

For higher fraction doses above the threshold D_t, dose and $-\ln SF$ might have a more linear relationship again, which is accounted for in Equation (2.10) of the linear-quadratic-linear model:

$$-\ln SF = \begin{cases} \alpha_\mathrm{x} D + \beta_\mathrm{x} D^2, & \text{for } D < D_t \\ \alpha_\mathrm{x} D_t + \beta_\mathrm{x} {D_t}^2 + s_\mathrm{max}(D - D_t), & \text{for } D \geq D_t, \end{cases} \tag{2.10}$$

with $s_\mathrm{max} = \alpha_\mathrm{x} + 2\beta_\mathrm{x} D_t$ being the maximal slope.

For fraction doses of about 1 Gy to 6 Gy, the basic LQ-model as defined by Equation (2.8) on the preceding page can be used to derive the biologically effective dose (BED) for a given effect. BED is defined so that n fractions of dose d yield the same survival effect as to the total dose D applied in infinitesimal fraction doses d':

$$\begin{aligned} -\ln SF/\alpha &= -\ln SF'/\alpha \\ \iff D\left(1 + \frac{\beta}{\alpha} d\right) &= D'\left(1 + \frac{\beta}{\alpha} d'\right) \\ \iff D' &= D\left(\frac{(\alpha/\beta)_\mathrm{x} + d}{(\alpha/\beta)_\mathrm{x} + d'}\right) \end{aligned} \tag{2.11}$$

$$BED = \frac{-\ln SF}{\alpha_x} = \lim_{d' \to 0} D' = nd\left(1 + \frac{d}{(\alpha/\beta)_\mathrm{x}}\right) \tag{2.12}$$

Two fractionation schemes with the same BED equivalently affect a tissue that has radio-sensitivity parameters α_x and β_x. Often, the so called 'normofractionated' scheme with $d = 2\,\mathrm{Gy}$ is used for comparison of doses. Then, Equation (2.11) transforms to the definition of equivalent dose to 2 Gy fractionation (EQD_2):

$$EQD_2 = nd\left(\frac{(\alpha/\beta)_\mathrm{x} + d}{(\alpha/\beta)_\mathrm{x} + 2\,\mathrm{Gy}}\right) = BED/\left(1 + \frac{2\,\mathrm{Gy}}{(\alpha/\beta)_\mathrm{x}}\right) \tag{2.13}$$

for a fractionation scheme with n fractions of dose d.

2.3 RBE models - How to compare the effects of different radiation entities

Section 2.1 already touched on the quality of radiation in terms of LET or ion type. The difference in ionizing potential, microscopic structure of dose distribution and physical processes, that create the energy deposition also results in different biological responses to the same absorbed dose.

With the relative biological effectiveness (RBE), a quantitative comparison of different radiation qualities is possible via the doses required to yield the same effect (iso-effect), e.g. 10 % survival after two months. It is defined as:

$$RBE = \left.\frac{\text{dose(investigated radiation)}}{\text{dose(reference radiation)}}\right|_{\text{iso-effect}}. \tag{2.14}$$

In the right panel of Figure 2.3, the relevant doses for calculating the RBE are indicated for cell cultures with a single cell type. In cell experiments, RBE can be measured for very specific situations, as Bronk et al. did [78]. However, involved cell types, radio-sensitivity under reference conditions, locally absorbed dose d, the LET_d and thus fluence of different beam particles and any other correction factors applicable in the LQ-model all intertwine, when whole organs or even patients are involved. For these complex cases, carefully adjusted RBE models allow the comparison of dose-distributions from inherently different modalities with regard to their biological effects.

Once an RBE prediction model is sufficiently validated by *in vitro* and *in vivo* data, it can be used to calculate the *RBE-weighted dose distribution* of an ion irradiation according to:

$$D_{RBE} = RBE(\alpha, \beta, \text{ion}, d, \text{LET}_d, \text{celltype}, ...) \cdot D \tag{2.15}$$

in analogy to the effective dose E (Equation (2.3) on page 8). Throughout this thesis, RBE-weighted doses are indicated by either GyRBE or subscripted with the applied RBE-model to differentiate between weighted and unweighted doses.

There are two categories into which RBE models may be separated: phenomenological or mechanistic. Phenomenological approaches simply describe experimental data with mathematical expressions following the linear-quadratic model. A comparison of phenomenological models applicable for proton therapy has been published [79]. Noteworthy examples of such phenomenological models are the *data-driven phenomenological model (DDM)* [80–82] and the *McNamara model* for protons [83]. An intermediate approach might be the *repair-misrepair-fixation model (RMF)* [84–86] which describes the induction and processing of double-strand breaks in a cell's DNA with a set of coupled non-linear ordinary differential equations. The second category of RBE models tries to derive the

mathematical expression with mechanistic considerations. Many mechanistic models were inspired by the historic formulation of the *Theory of dual radiation action* which Kellerer and Rossi [87, 88] envisioned. For a detailed comparison of mechanism-inspired models, we refer the reader to the reviews of Stewart et al. and Bellinzona et al. [89, 90]. The models relevant for helium ions are *Local Effect Model (LEM)* [82, 91–94], *Microdosimetric Kinetic Model (MKM)* and it's specification *mMKM* [82, 95–98]. As derived in [82], an LQ-based RBE can be described by:

$$RBE\left(\left(\frac{\alpha}{\beta}\right)_x, D, \mathrm{RBE}_\alpha, R_\beta\right) = -\frac{1}{2D}\left(\frac{\alpha}{\beta}\right)_x + \frac{1}{D}\sqrt{\frac{1}{4}\left(\frac{\alpha}{\beta}\right)_x + \mathrm{RBE}_\alpha\left(\frac{\alpha}{\beta}\right)_x D + R_\beta D^2}. \tag{2.16}$$

The specification of RBE_α and R_β varies between models.

In Chapter 6 (the third publication), this author evaluates which of the RBE models might become a better predictor of treatment results in the case of prostate cancer. Hence, a brief description of the two models applied in this thesis follows.

2.3.1 LEM: Local Effect Models

The *Local Effect Model (LEM)* was developed at the Helmholtz Centre for Heavy-Ion Research (GSI, Darmstadt, Germany) for experimental treatment with carbon ions in the mid 1990s [99–101]. Its original version Local Effect Model, version 1 (LEM-I) is still applied in European clinics and HIT to this day [89, 102]. Four updates have been proposed since. In 2007, version II [103] was introduced, quickly followed by version III in 2008 [104]. Local Effect Model, version 4 (LEM-IV) [91] has been used as comparative means in clinical trials after its publication in 2010, but not for initial planning of any treatments. In 2021, a fifth version was suggested [105]. LEM's premise is local parity. That means, inside microscopic sub-volumes, chosen small enough to have a locally homogeneous dose distributions, ions have the same effect as photons [103]. Inside these subvolumes, survival follows the linear-quadratic-linear model defined in Equation (2.10) on page 14. LEM's free parameters are the ratio of α_x and β_x and the threshold dose D_t. Up to the threshold, we can describe the RBE with

$$RBE_{\alpha,LEM} = \frac{1 - \exp\left(-\alpha_z d_1\right)}{\alpha_z d_1} \tag{2.17}$$

$$\text{and } R_{\beta,LEM} = \left(\frac{\alpha}{\alpha_z}\right)^2 \left(\frac{\beta_z}{\beta_\mathrm{x}}\right), \tag{2.18}$$

where α_z and β_z are microscopic parameters and d_1 the dose deposited by a single particle traversal of that sub-volume, compare with the supplementary material of [106].

The five versions differ in their approach of breaking down the macroscopic heterogeneous dose distribution to these microscopic sub-volumes. Originally, LEM was exclusively intended to compare the effects of carbon ions to photon references. Implementations into TPSs, focused mostly on the parameter settings for chondrosarcoma and other tumors of the brain. However, in a pragmatic adaptation of TRiP98 for helium ions, Krämer et al. [92] compared the dose and LEM-IV-based RBE predictions to the survival distributions of Chinese hamster ovary cells in a helium ion SOBP. So LEM-IV has been tested for helium ions, which to our knowledge has not been shown for earlier versions. While the research for this thesis was conducted, Mein et al. [82] found an underestimation of LEM-IV-based RBE in the lower LET region of a single energy BP, which became less noticeable in SOBP scenarios. Similar effects were seen for carbon ions [106].

2.3.2 MKM: Microdosimetric-kinetic Models

The *Microdosimetric Kinetic Model (MKM)* is used for treatment planning in Japan [107]. It has been envisioned by Hawkins [108–110] based on the ideas of dual radiation action proposed by Kellerer and Rossi [88]. Originally, MKM used neutrons as reference radiation and human salivary gland cells as reference cell line. Since then, several extensions, modifications and adaptations have been proposed, the latest being [111]. Bellinzona et al. gave a comprehensive overview of these extensions in [90]. The main premise of all MKM versions is, that in the basic formulation of a linear-quadratic model Equations (2.8) and (2.16) on page 13 and on the facing page, $\beta = \beta_{\mathrm{x}}$ is a cell line specific constant and $\alpha = \alpha(\alpha_{\mathrm{x}}, z)$ a function of the specific energy of a single event $\overline{z}_1$ (compare Equation (2.1) on page 7) by the mixed radiation field traversing a microscopic domain with radius R_d inside any cell. Hence,

$$RBE_{\alpha,mMKM} = 1 + \left((\alpha/\beta)_{\mathrm{x}}{}^{-1}\overline{z_1}\right) \tag{2.19}$$

$$\text{and } R_{\beta,mMKM} = 1, \tag{2.20}$$

where z_1 is a function of ion, $x, y, z, R_d, R_n, \ldots$.

Among the modifications, Kase et al. [112] introduced a saturation correction $z_{sat}(R_d, R_n)$ to the parameterization, substituting $\overline{z}_1$ with z^*_{1d} which includes the overkill effect observed for high-LET radiation. Inaniwa et al. [113] extended Kase's description to a mixed radiation field, thereby creating the *modified Microdosimetric Kinetic Model (mMKM)*, which was adapted for the ion beams of HIT [82, 96, 97, 106]. Inaniwa's approach of 2010 computes the probability density $f(z)$ via the Kieffer-Chatterjee parameterization of radial dose distributions surrounding the particle tracks [114], which could theoretically be measured as well, with tissue-equivalent proportional counters.

The assumption, that stochastic cell nucleus specific energies $z_{\mathrm{n}} = D$ are constant, induces a disagreement in β-coefficients as measured β increases with very

high LET. To resolve this, Sato and Furusawa introduced the *stochastic and double-stochastic microdosimetric-kinetic models (SMK and DSMK)* [115], which include the stochastic nature of specific energies in domain z_d and nucleus z_n. In 2018, Inaniwa and Kanematsu introduced another adaptation [116], which replaces a dose-averaged nucleus specific energy per event $\overline{z}_{n,D}$ instead of the full distribution of z_n. This latter adaptation is called *modified SMK*.

2.4 Clinical Radiobiology

When radiation is not applied to cells in a Petri-dish (*in vitro*), but for actual patient treatments, beam geometries, tissue dependencies, and thus dose distributions become a lot more complex. Also measuring dose inside of a patient for verification is almost impossible, as it would require implanting a dosimeter inside a patient. These and more quirks of clinical radiobiology are explained in this section.

2.4.1 How to quantify and compare dose in a patient?

Since routine and frequent dosimetry inside a patient is rarely possible and would only yield point doses, dose distributions inside of a patient are predicted by so called TPSs. More on these in section 2.5.

For evaluation of doses in certain organs, DVHs are calculated. They gather the partial volumes v_i of an organ receiving a dose d_i into a cumulative histogram, such as in Figure 2.4. DVH of many patients or several treatment plans can be compared for coverage, maximum doses and other constraints on tolerable doses, which might be empirically derived via dose escalation trials or survival trials after nuclear accidents and warfare.

Constructions, such as the equivalent uniform dose (EUD), can then be used to compare heterogeneous doses of patient treatments with the mostly homogeneous doses of cell experiments. Nimierko et al. stated: “For any dose distribution, the corresponding Equivalent Uniform Dose (EUD) is the dose in Gy, which, when distributed uniformly across the target volume, causes the survival of the same number of clonogens.” ([117]) Thus, EUD is defined as

$$EUD = \sum v_i (EQD_{2_i})^{\frac{1}{n}}. \tag{2.21}$$

If an organ is not irradiated in its entirety, it might have a higher dose tolerance. The tissue-specific parameter n in the EUD formulation accounts for this *volume effect*. The radio-sensitivity of the irradiated organ is already accounted for in the EQD_2. For comparisons of actual dose distributions and effects beyond averaged doses or prescription doses, the documentation of treatment plans, imaging and if possible dose distribution and positioning is key.

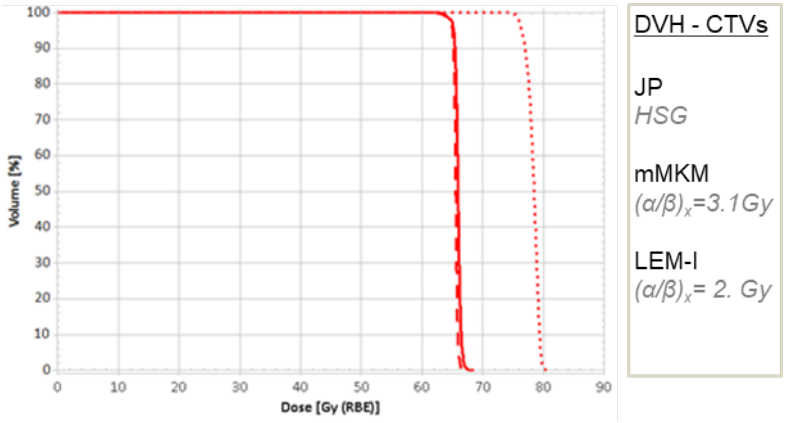

Figure 2.4: Dose-volume-histogram of a carbon ion treatment plan for prostate cancer. The vertical axis is classically normalized by organ volume. Horizontal axis can be shown in absolute or relative dose. Depending on the treatment modality, dose is provided as absorbed (physical) dose or the RBE-weighted 'biodose'. Objectives for treatment planning are often defined as points or limits on the DVH, such as the dose D_50 to 50 % of a volume. Modified from [15].

2.4.2 How to define survival in patients?

Counting clonogenic assays in a patient to measure survival fractions is impossible for obvious reasons (e.g., missing control, dose uncertainty). So for patients, other measures of effectiveness have to be implemented.

Such a measure could be the number of patients still alive at a specified time after receiving a given treatment. This is called the *overall survival (OS)*. A trial might distinguish between tumor related deaths or deaths from other causes to separate likely causality and timely correlation. As cancer is (for the most part) well treatable, measuring tumor specific survival takes a long time. And it's unlikely that a patient would remain untreated if a first-line curative treatment fails. Hence, OS is rarely a good measure to compare the effectiveness of treatment regimen. *Tumor progression*, however, can be measured by tumor growth on diagnostic imaging, local recurrence or detection of metastasis (distal recurrence). Hence, Progression-free survival (PFS) is the measure of choice, especially when overall survival is very high. For some tumors, blood markers are early indicators of tumor progression. One such example is the prostate specific antigen (PSA) for prostate cancer. A raise in PSA concentration of more than $2\,\mathrm{ng\,mL^{-1}}$ above the lowest measure after irradiation therapy (nadir+2) counts as *biochemical progression* after the Phoenix-definition [118]. Its absence is called biological relapse-free survival (bRFS).

Another measure might be the number of patients experiencing *adverse effects* or even toxicities in tissues surrounding the previous tumor. These are considered *normal tissue complications*.

With improving treatment options, prolonging the progression-free period is often more relevant than the mere question of death or survival. The time-dependent effect of cancer treatment is measured in so called *Kaplan-Meier plots* [119]. These contain information of all surviving or unaffected patients, and mark the time point at which any patient of the investigated cohort experiences an adverse event, dies or is lost to follow-up for other reasons. Wilson et al. [120] stated and quantified the importance of transparent differentiation between these reasons for no longer including a patients' participation in a trials Kaplan-Meier plot.

While the Kaplan-Meier-plot typically notes clinician reported results such as tumor progression or change in treatment course obtained at follow-up appointments in a clinic, there are other options of reporting the effects of radiation. *Patient reported outcome measures (PROMs)* might be obtained by handing approved questionnaires to the patients, which are to be filled out at specified times after or even during treatment. Especially when considering 'mild' adverse effects, that might not warrant clinical intervention, but compromise the patients' quality of life severely enough to infer with their willingness to continue treatment, PROMs become valuable [121–126]. Questionnaires, such as the EPIC [127, 128] also enable the calculation of so-called *Quality of Life-adjusted years* of survival.

2.4.2.1 Probability of Tumor Control

For dose-dependencies of tumor control or PFS and the occurrence of adverse effects, sigmoidal shapes are most often used. Models of *tumor control probability (TCP)* are motivated by statistical descriptions of the assumption that a tumor is controlled if and only if all tumor cells are controlled. So the mathematical descriptions are based off of LQ survival fractions and should consider dose inhomogeneities, partial volumes and ability of tissue to repopulate. The most common formulations are either based on Poisson statistics of hitting and killing individual tumor cells with a given dose, or fitted via logistic regression to phenomenological data.

Logistic TCP is defined as

$$TCP = \frac{1}{(1 + N_0 SF)}. \tag{2.22}$$

Insertion of any LQ for SF typically results in the free parameters TD_{50} and γ_{50} representing the total dose and slope at which tumor control equals 50 %. The logistic model is applied by Marteinsdottir and Paganetti [129].

Poisson TCP describes the probability as

$$TCP = \exp\left(-N_0 SF\right), \tag{2.23}$$

where N_0 parametrizes the total number of cells in the tumor before treatment. One specific formulation [130, 131] expresses the Poisson tumor control probability (TCP) in terms of the dose TD_{50} required to achieve 50 % control probability and the steepest slope γ_{50}. In the third publication comprising this thesis (Chapter 6 and section 3.6), I use the latter formulation by Warkentin et al. [131] to predict rate of bRFS after prostate irradiation.

2.4.2.2 Probability of Adverse Effects

While the dose-dependency of *normal tissue complication probability (NTCP)* generally follows the same sigmoidal shape as TCP and could be described with Equation (2.22) on the facing page, its quantification is more complex. On one hand, the healthy tissue surrounding the tumor typically receives quite heterogeneous dose distributions. On the other hand, there are different types and time points of complications. Differentiation of toxicity into fast (acute) and late reactions can be helpful. An example of acute toxicity is skin erydema, whereas late reactions have a more statistical nature of occurrence and include infertility or bone loss. Tentatively, quantitative categories of adverse effects have been gathered in the common terminology criteria for adverse effects (CTCAE) [132]. The most recent version (CTCAE 6.0) is expected to be published in fall of 2024 by the cancer treatment evaluation group of NIH Cancer, USA. Other collections of criteria have been collected by the Radiation Therapy Oncology Group, USA (RTOG), USA and European Organization for Research and Treatment of Cancer (EORTC) [133] or in the subjective objective management analytic / late effect of normal tissues (SOMA/LENT) [134] categories.

The Lyman-Kutcher-Burman model [135–138] accounts for partial irradiation of organs. Lyman-Kutcher-Burman (LKB) takes advantage of the Gaussian Error Integral's sigmoidal shape, while encompassing the position TD_{50}, slope m and radio-sensitivity in the argument t:

$$NTCP = \frac{1}{\sqrt{2\pi}} \int_{-\infty}^{t} \exp\left(-x^2/2\right) \mathrm{d}x, \quad \text{with } t = \frac{1}{m}\left(\frac{EUD}{TD_{50}} - 1\right). \tag{2.24}$$

The parameter n from the definition of EUD in Equation (2.21) on page 18 accounts for sensitivity to partial volume irradiation, which in its own account is a measure of the organs functional sub-units.

Several dose and volume constraints for various organs have been motivated by the LKB model. Following the empirical publications of Emami et al. [139], the Quantitative Analysis of Normal Tissue Effects in the Clinic (QUANTEC) initiative [140, 141], systematically defined constraints for several organs in 2010

[142–146]. Improvements for acquiring data backing up these models were already suggested then [147, 148]. For hypo-fractionated treatment the HyTEC initiative suggested parameterization. And most recently, the PENTEC initiative published dose constraints for pediatric treatments [149].

2.4.3 RBE in Clinical Trials

Clinical trials are typically designed to answer a given research question with statistical certainty. If reanalyzing a trial's data, for a different question, the results might not always have as much significance. The buzz-words for a statistician would be the 'power' (number of patients in each cohort) of a study, and whether it's a randomized control or multi-arm trial. The clinical RBE can be derived from dose-escalation trials, that have equivalent cohorts of patients for a reference modality and a new treatment method. The differences in dose distributions complicate the direct comparison of photon reference plans and ion beam therapy plans.

2.5 Requirements for a Treatment Planning System

In the previous section, measures for complications and tumor control have been introduced. Balancing these to objectives for the benefit of the patients is the imperative of treatment planning. Adequate calculation of dose and prediction of its effects necessitate the consideration of all previously mentioned physical and biological principles in the TPS. Hence, a TPS includes all of the following components: databases of the radiation properties, a model representation of the treated patient, volume definitions, a plan optimizer and for ions a model of radiobiological effectiveness.

2.5.1 Databases

The databases can either include a full model of the treatment machine or at least a library of possible beam configurations and the quantitative properties of the beam before it would enter a patient. The beam configuration includes all position and angle combinations of the patient table and treatment machine, that are possible without a collision of robots, the patient and other machines in the treatment room. Speed limits for rotation of robots and switching between energies or scan spot positions are also included. Most importantly a list of all primary beam energies and widths, which are the initial characteristics of the ion beam itself, is required. For each of the energy and width configurations, the geometric distribution of the physical quantities *absorbed dose* D, *dose-averaged linear energy transfer (*LET_d*)*, and in case of ion beams energy and *fluence* Φ *of primary and secondary particles* and the *RBE-weighted dose* D_{RBE} in a reference material are obtained. Usually, these quantities are measured for a selection of configurations and then interpolated by sophisticated MC or analytic models. Further details of the beam model and database creation are be described later in sections 3.1 and 3.3.

2.5.2 Patient Model

A model of the patient is usually created from their computed tomography (CT). The CT image represents the patient geometrically accurate. Image data is saved in the standardized Digital Imaging and Communications in Medicine (DICOM) format [150], including meta data about the patient, acquisition time and imaging machine. Extensions of this standard for radiotherapy also store the dose distribution (RTDose), beam configuration (RTPlan) and definable structures (RTStruct) overlaid onto the image data. CTs values are stored in Hounsfield unit (HU), which correspond to the photon absorption coefficient μ. Tables from Schneider et al. [151, 152] convert these HUs into electron density ρ_e or physical density ρ of the imaged material. This conversion allows the estimation of particle range in the patient, which is seldom the same as in the reference material of the database. Especially if air, bone or implants are present, the electron density

is not sufficient to calculate the range of ions in the material. Then, imaging with a dual energy CT provides additional information from which voxelized stopping power ratios (SPRs) can be extracted [153, 154]. So the TPS needs to be able to read and display DICOM data and convert it to a voxelized model of the patient.

2.5.3 Volumes

Volumes region of interest (ROI) and points of interest (POIs) inside the CT image are mostly contoured by physicians and saved to the *RTStruct*. These volumes define the outlines of organs and tissues or other materials. The *External* describes the outline of the whole patient in contrast to surrounding air. It can be used for collision avoidance and checking available angles and couch positions. The *target volumes* define the area which are supposed to receive a significant amount of dose. The *gross target volume (GTV)* surrounds the microscopically visible or clinically palpable tumor mass. If the tumor mass moves and a time-tracked 4D-CT is acquired, the *internal target volume (ITV)* includes all observed positions of the target. The *clinical target volume (CTV)* includes possible microscopic lesions and involved lymph-nodes. Additional margins accounting for positioning uncertainties expand a CTV to the *planning target volume (PTV)*. Organs in the vicinity of the target, so called *organs at risk (OARs)*, should be spared as much as possible. Therefor, they are also delineated. Sometimes, they are also expanded with a planning risk volume (PRV), comparable to the planning target volume (PTV). Especially hollow organs or those not fully included in the imaged volume (e.g., the spine, bowels) benefit from such a PRV.

2.5.4 Optimization

The primary aim of optimizing a treatment plan is delivering the prescribed dose to the target, while meeting constraints on the OARs. First, the clinician defines *prescription* dose, fractionation and possibly a boost volume, that can receive higher dose simultaneously with each fraction (simultaneously integrated boost (SIB)) or as additional fractions (consecutive). Whether irradiation will be delivered daily or every other day, has influence on the overall treatment time and the total biologically effective dose. The prescription dose can be defined for CTV or the PTV as the minimum dose, mean dose or a iso-dose covering the specified percentage of the target. It will be the objective in the optimization. Secondly, *constraints* are specified as a distance to fall-off; mean or maximum dose $D_{x\%}$ to a certain percentage x of the OAR's volume; or as a maximum volume $V_{y\mathrm{Gy}}$ receiving a given dose y. These constraints can enter the optimization as objectives or hard constraints. Guideline initiatives, such as QUANTEC [140], HyTEC [155] or PENTEC [156] provide comprehensive orientation for reasonable constraints. Lastly, the *scan path* needs to be optimized to reduce treatment time. The line between two consecutive spots shouldn't cross any OARs. And the spills of the accelerator should be most fully used. Too few ions per spot will circumvent

the accelerators ability to measure its fluence. Once the optimization is finished, all the above information are saved as *RTPlan*.

2.5.5 RBE-weighted Dose for Treatment Planning

For ion therapy, the plan optimization is often performed on the RBE-weighted dose (compare section 2.3). Thus, the TPS has to allow the assignment of $(\alpha/\beta)_x$, α_x and β_x to volumes in RTStruct. A module of the TPS for biologically weighted dose calculation requires the input of biological databases. Aforementioned constraints are typically extracted from experience with conventional photon radiation and defined in absorbed dose D. Thus, they may require translation to the ion dependent radiobiology. Spatial and temporal fractionation changes the tolerance doses of many tissues as well. BED and EQD_2 calculation assists the comparison of differently fractionated treatment plans inside the TPS.

The international guidelines, on how to prescribe and report treatment doses for light ions including helium are reported in Report 93 of the ICRU [157].

2.6 The Ion Beam of the Heidelberg Ion Beam Therapy Center

The Heidelberg Ion Beam Therapy Center (HIT) has been envisioned at the "Gesellschaft für Schwerionenforschung" (GSI, Darmstadt) in the late 1990s [158]. It was built on the campus of the Heidelberg University Hospital and commissioned for use as depicted in Figure 2.5 [159, 160]. In contrast to many proton

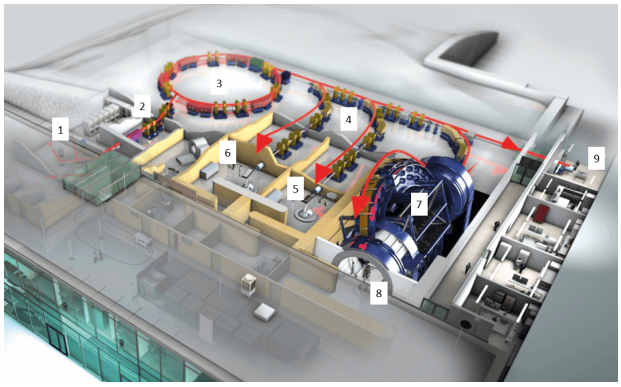

Figure 2.5: *Layout of HIT.* Numbers mark the components of the beam line: (1) sources, (2) linear accelerator, (3) synchrotron, (4) high energy beam transport, (5) and (6) horizontal treatment rooms, (7) gantry, (8) gantry treatment room, (9) experimental cave. The image is modified from [159].

therapy centres, HIT utilizes active beam scanning [7]. This means, the ion beam

scans over a targets area. But in contrast to an old-fashioned tube television, several layers in depth (iso-energy layers) are covered by adjusting the beams energy. This section describes its layout and the resulting beam properties.

2.6.1 Beam Production

Helium molecules are pumped into an *electron-cyclotron resonance ion source* [6, 161–163] were the molecules are split into atoms and stripped off their electrons. The ions are then transported along the *low energy beam transport* line into a *linear accelerator*. Before entering the *synchrotron* [160], the ions have an energy of about 7 MeV u^{-1}. Upon slow knockout extraction with the so-called *scraper* [164, 165], the ions have reached their final energy. For helium ions this is 50 MeV u^{-1} to 220 MeV u^{-1}. Along the *high energy beam transport*, the bunch or *spill* of ions are transported and deflected towards the treatment rooms. Upstream of each treatment room, *focusing magnets* and *scanning magnets* adjust the lateral beam width and the scan position (spot). A feedback loop between these magnets and the *beam application and monitoring system (BAMS)* [166], consisting of two multi-wire proportional chambers (MWPCs) and three ionization chambers (ICs), ensures that the beam has the correct selected energy, position and width when leaving the vacuum of the beam line in each *treatment room*. This end of the beam line is referred to as *nozzle*. There are two treatment rooms, where the beam arrives horizontally, and a gantry, that deflects the beam and can rotates 360° around the third treatment room [160]. When entering the treatment rooms, the beam is almost non-divergent with a virtual source axis distance (VSAD) of about 7 m in the horizontal rooms and 43 m in the gantry. All rooms are equipped with a *laser marked iso-center*, which is 1 m away from the nozzle in the horizontal rooms, and 80 cm in the gantry room. The marked iso-center defines the reference point (and plane in beam's eye view (BEV)) for patient positioning. Robots move the patient couch (table) and imaging devices into specified positions relative to this iso-center. Table positions are mostly adjusted, so that the room's iso center is aligned to the middle of the target.

2.6.2 Beam Shaping Devices

To adapt the pristine BPs leaving the nozzle, several devices in the treatment room are used. The *range shifter (RaShi)*, a 2 cm thick PMMA-plate reduces the BP's range by about 2 cm. It is moved inside the space between patient and nozzle and broadens the beam laterally. For shallow positions, this allows the use of higher energies and thus less scattering.

A *3mm thick ripple filter (RiFi3mm)* [167] widens the peak size w_{peak} of any pristine BP by about 3 mm, reducing the number of necessary energy slices for homogeneous filling of a target volume. The distance from patient surface to the nozzle (*air gap*) has an influence on the lateral scattering and can thus also be used to modify the beam shape, as shown in the fist publication (Chapter 4).

2.6.3 Beam Characteristics

Although, continuous energies and widths would be technically possible, discrete steps are defined in the accelerator library containing nominal beam energies, beamwidths and intensity settings (LIBC). The LIBC serves as reference table for any tuning on the beam line or accelerator settings. For each ion type, 255 discrete initial kinetic energies E# are indexed. For helium ions, these range from 50.57 MeV u^{-1} to 220.51 MeV u^{-1} ensuring penetration depths of about 2 cm to 30 cm. Focus is specified in 4 clinically used and 2 research beam widths. The focus index specifies the FWHM at the isocentre. Filling of the synchrotron and extraction duration define the particle rate, which is indexed in 10 steps of beam intensity (ions/s).

Clinical Energy Steps

Clinically, an additional table for beam settings is used that defines the allowed medical combinations of energy, focus and intensity (MEFI). The width corresponding to each energy is chosen, so that the spacing of the scan spot grid can be consistent for all energies used in a typical treatment plan. The followed rule of thumb says, that the spot spacing should be smaller than a third of the nominal FWHM [168]. For helium ions, the MEFI-table "F6mm" requires a jump from focus index 1 to 2 for energies higher than 166.80 MeV u^{-1} (E169), ensuring that the FWHM of all energies is greater or equal to 6 mm. For protons, focus index 1 allows a FWHM $\geq$ 8 mm for all energies. Two MEFI tables are specified for carbon ions, "F10mm" and "F6mm". The new clinical TPS, RayStation®, applies a hexagonal grid, so the standard distance between two spots is about 2.41 mm.

To cover the target volume of a treatment plan with a prescribed dose, several iso-energy layers and raster-scan positions are combined into a so called SOBP.

2.6.4 Quality Assurance of the Beam

To assure constant quality of the beam delivery, daily, weekly and monthly measurements are routinely taken by the medical physicists at HIT. A third MWPC is positioned in the iso-center of the treatment room to measure beam width and position of a selected set of energies every morning. The monitor calibration is checked as well, alternating between ions on a daily basis. This assures, that the dose delivered by a fixed number of primaries remains the same. The setups for this absolute and relative dosimetry, were mimicked in the measurements performed for base data creation (see section 3.2). In addition to the routine of quality assurance (QA), every clinical treatment plan is delivered into a water tank with 24-Pinpoint chambers (PTW, Freiburg) and compared to forward calculated dose distributions. Only, if the predicted and measured dose for each chamber match within 5 %, is the plan approved for patient treatment. Further details of this water tank are described in the methods, section 3.2.5.

3 Methods in the Scope of this Thesis

This chapter explains the methods used for this thesis, where the peer-reviewed publications lacked detail. The creation of helium ion beam models in the analytical dose engine Fast Recalculation on GPU (FRoG) and the MC code FLUKA is not included in the publications of this thesis. Hence it is described here. A focus is on the acquisition of the physical database inputs that were also used to create the helium ion base data of the commercial TPS RayStation®. The second publication in Chapter 5 only briefly mentions the base data. The adaptation of radiobiological models resulting in the third publication (Chapter 6) are also presented.

3.1 Beam Modelling Methods

The inputs required by a beam model depend on the general type of its dose calculation algorithm. Either a MC code or some analytical algorithm are typically used. This section briefly explains both types to motivate the acquisition of base data. It also provides a description of the specific dose calculation tools used for patient treatment and pre-clinical research at HIT.

3.1.1 Monte Carlo for Dose Calculation

In general, MC codes calculate a distribution or the track of particles by randomly drawing from statistical distributions of interaction cross-sections. Once a sufficient number of primary particles are calculated, the MC simulation can yield a detailed geometrical distribution of dose, energy or any other requested information on the effect of these particles in the matter they traversed. Usually, the input includes a definition of the initial beam properties, as well as a geometric representation of beam line and detectors including their materials. Heterogeneous materials and the magnetic fields can be implemented, as well.

3.1.1.1 FLUKA

FLUKA [169, 170] was created as a general purpose MC simulation package. That implies, it is capable to simulate almost everything related to high energy experimental physics and engineering[1]. It has been applied to predict detector responses at the Large Hadron Collider at CERN or the impact of extraterrestrial radiation on astronauts in the ISS. The efforts of many contributors allowed

[1] www.fluka.org

the built of a MC treatment planning tool on top of the general FLUKA code [171–174], even coupling biological dose calculation [175]. The geometry of HIT's BAMS and beam modifiers were implemented into FLUKA by Parodi, Tessonnier et al. [166, 176, 177]. This implementation takes the initial beam profile in vacuum at the VSAD, the initial beam energy and the momentum distribution as input. Section 3.3 and Chapter 4 describes, how these input parameters are adjusted to reproduce measured dose profiles of the helium ion beam (section 3.2). Introducing various *scoring* geometries, these FLUKA simulations are used to extract distributions of dose to water, dose to medium, energy and particle fluence. A special user routine, usrsuw, allows the weighting of fluence with specified factors. This later option is used to score dose-weighted biological parameters, z^*_{1d} or LET_d, required as input to the biological databases of RayStation®and FRoG in section 3.5.

Higher level user routines of FLUKA were used to investigate its implementation of nuclear reaction cross-sections (appendix appendix B).

3.1.1.2 MonteRay

A fast Monte Carlo Dose Engine for Protons, Helium Ions and Carbon Ions (MonteRay) was developed during the research phase of this thesis by Lysakovski et al. [178]. It is a slightly simplified but fast MC tool. Interactions of electrons [179], protons [180], helium ions [181] and carbon ions [182] in electromagnetic fields are accounted for. The nuclear reactions of these primaries with the twelve most common elements for radiotherapy were extracted from FLUKA by the author of this thesis with a dedicated user routine [180, 181]. For a detailed description of MonteRay, the reader is referred to above publications, especially the dissertation of Peter Lysakovski [178].

3.1.1.3 RayStation Protons

The commercial TPS RayStation® contains a simplified MC model for protons. Only primary protons and light secondary ions up to 4He ions are transported, though. And no model for heavier ions exists, yet. Janson et al. [183] provide a detailed description of RayStation®'s dose models for protons.

3.1.2 Analytical Dose Models

Analytical dose models parameterize the dose distributions with analytical functions. Most are only capable to predict dose to water or water-equivalent materials with adjusted density. The analytic model separates the dose distribution into several components, one for the depth dose and one or more for the lateral distribution. Collapsed-cone algorithms or raytracing are used to project the lateral component onto the depth dose. Material heterogeneity is more specifically considered by pencil beam splitting, compare [184]. Analytical dose models take

either measurements under reference conditions or detailed MC simulations of the dose distributions as input.

3.1.2.1 FRoG

FRoG [58, 185, 186] was developed as an in-house research dose engine. As one of the developers stated in his PhD Thesis "FRoG is a multi-purpose sandbox environment written in python and C++ to perform rapid and accurate computations using a PB model [187] with triple Gaussian lateral evolution parametrization [188–190] and GPU-optimized Siddon raytracing [191] for physical dose, LETd, RBE and effective dose." ([184, p. 18]) Hence, FRoG requires a depth dependent parametrization of the triple Gaussian fit to the lateral dose distribution in water as input for each available beam energy. Additionally, depth distributions of dose and LET_d are required. The calculation of effective dose or RBE-weighted dose requires dose-weighted distributions of α_d, β_d and $z^*_{1d\mathrm{mix}}$. FRoG's implementation of mMKM prediction for helium ions was published in Kopp et al. [97]. For the third publication within this cumulative thesis (Chapter 6), several bio databases were created. Section 3.5 describes the creation of these biodatabases in more detail. The output of FRoG is saved in the DICOM format RTDose. Thus, voxelized representations of absorbed dose, LET_d, α_d, β_d and $z^*_{1d\mathrm{mix}}$ can be obtained. In addition to these distributions, FRoG can calculate DVHs, when RTstructs are defined. For the third publication, this feature was scripted to also extract characteristic point from these DVHs for 91 patients.

3.1.2.2 Syngo PT

Syngo PT (Siemens AG) was the original clinical TPS at HIT. It was CE-labeled for the planning of proton and carbon ion irradiation. This TPS was discontinued in favor of RayStation®.

3.1.2.3 RayStation

In 2018, RayStation® (RaySearch Laboratories, Stockholm, Sweden) was installed at HIT [192]. The analytic pencil beam algorithm already supported the calculation of proton and carbon ion doses. Thus, the RayStation® treatment plan for carbon ions was delivered to a patient in summer 2019 [193]. In the following year, a helium beam model was developed for RayStation® and implemented at HIT [194]. The creation of this beam model and its validation is the subject of this thesis. Section 3.3 and Chapter 4 describe the creation of reference databases for RayStation®'s helium beam model. The validation of this model in Chapter 5 has been published [13]. The database input required for the helium beam is listed in Table 1 of Chapter 5. It consists of IDDs, lateral dose distributions in air, particle fluence spectra and absolute dosimetry.

The following sections describe the acquisition of base data trough measurement and simulation.

3.2 Measurement of Beam Characteristics

As described in section 2.5, the physical characteristics of the helium ion beam are required as input to the TPS. IDDs and lateral dose distributions, as well as absolute dose at a reference positioned were measured. This section describes the setups in detail.

3.2.1 Depth Dose Distributions

The 'Kiel'-PEAKFINDER® (SN: 2874290001, TM34070 PTW-Freiburg, Germany) was the detector of choice for IDD measurement (compare section 2.1.4). Its two parallel plate ICs have an active radius 4.08 cm (TM34070, PTW-Freiburg). The reference chamber collects the dose at the entrance and a monitor chamber moves through a column of water, measuring along the full range of any BP. Figure 3.1 sketches the PEAKFINDER®'s setup with respect to beam line and treatment room.

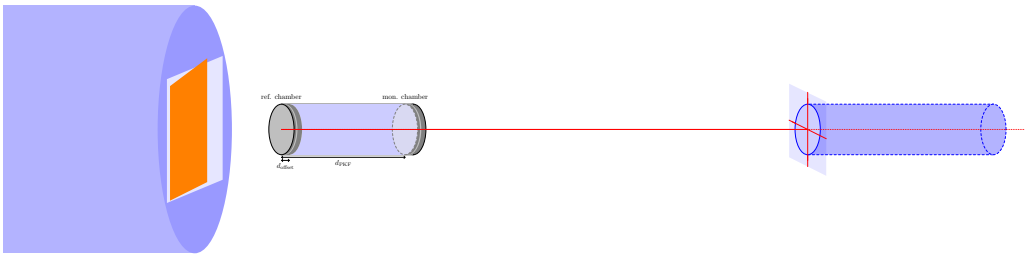

Figure 3.1: Sketch of PEAKFINDER® and cylindric scoring region of FLUKA simulation relative to the treatment rooms isocenter.

A trigger system connected PEAKFINDER® and BAMS to assure constant beam intensity at each data point. In average three data points were measured per spill, with smaller gaps around the estimated BP maximum. The ratio of both ICs' readout in dependence of the monitor chambers depth yields the relative depth dose distribution, laterally integrated over their active radius. Because the reference chamber is always at the same depth along each BP, the standard deviation of its readout is a good estimate on the measurement uncertainty. Correction factors for charge collection efficiency had been measured previously by Tessonnier et al. [166] and were internally applied to the PEAKFINDER®'s dose readout. The position readout d_{PKF} is internally shifted by $d_{\mathrm{offset}} = 15.30\,\mathrm{mm}$ to match the total water-equivalent thickness from vacuum exit of the beam line to the entrance of the PEAKFINDER®'s reference chamber.

In the horizontal treatment room H2, the IDDs for 28 of the 255 available energy levels were measured in three data sets. Table A.1 on page 136 provides an overview of the configurations applied for each of these sets. An example of a measured IDD is presented in Figure 7.1b). Table 1 of Chapter 5 lists the 24

energy levels, which RaySearch Laboratories used to create the analytic pencil beam model of the commercial TPS.

3.2.2 Lateral Distribution in Air

A detector array, like the OCTAVIUS® 1000 SRS P (SN: 000308, PTW-Freiburg, Germany) allows the fast measurement of two dimensional dose distributions. Its PMMA casing holds 977 ICs with an effective depth of measurement of 5 mm behind its surface. Figure 3.2a sketches the geometric arrangement of these ICs. The positioning of the OCTAVIUS® 1000 SRS P in the treatment rooms and the evaluation of these measurements is described thoroughly in the first publication (Figure 1 and Sections 2.2-2.4 of Chapter 4). In addition to the published data (set 4), additional sets were measured in the gantry (compare Figure A.2) and with preliminary accelerator settings. An overview of all measured settings is provided in Table A.2 on page 137.

3.2.3 Lateral Distribution in Water

A custom built PMMA sleeve allows the positioning of the OCTAVIUS® 1000 SRS P inside of a water tank. Its dimensions are depicted in Figure 3.2b on the next page. With this motorized setup, the author measured the lateral dose distribution in water for 13 energy levels of the helium ion beam. The minimum water-equivalent thickness at the closest possible position of measurement was estimated to (44.6 ± 0.3) mm by adding up the thicknesses the setup components as marked in Figure 3.2b. This estimate was compared to the measured shift in BP position of a 200.28 MeV u^{-1} carbon ion beam[2].

Per measured beam energy, the detector was positioned at five depths, roughly equivalent to the proximal 50 % and 80 % and distal 50 % and 80 % dose levels and R_{tail}. Apart from energy indices 1 and 6, the same energies and beam intensities as for the lateral dose distributions in air were used. These two lower beam energies correspond to ranges below the minimal achievable detector position.

3.2.4 Field Size Dependence and Absolute Dosimetry

At least one reference point per energy requires absolute dosimetry to which the previously described relative dose measurements can be scaled. The required correction factors and setups are standardized [48, 52, 76, 195]. Here, a quadratic field of variable edge length was irradiated by a scanned grid of mono-energetic helium ion beams. At the center of this field, a thimble shaped IC is positioned along the beam axis. The irradiation plan contains 5×10^6 particles for each scanned spot to allow calibration of the relative measurements and beam models. The repetition of this measurement with different field sizes between $(2 \times 2)\,\text{cm}^2$ and $(20 \times 20)\,\text{cm}^2$ serves a double purpose: reference dosimetry and validation

[2] personal communication with Stephan Brons, Oct 25th, 2019

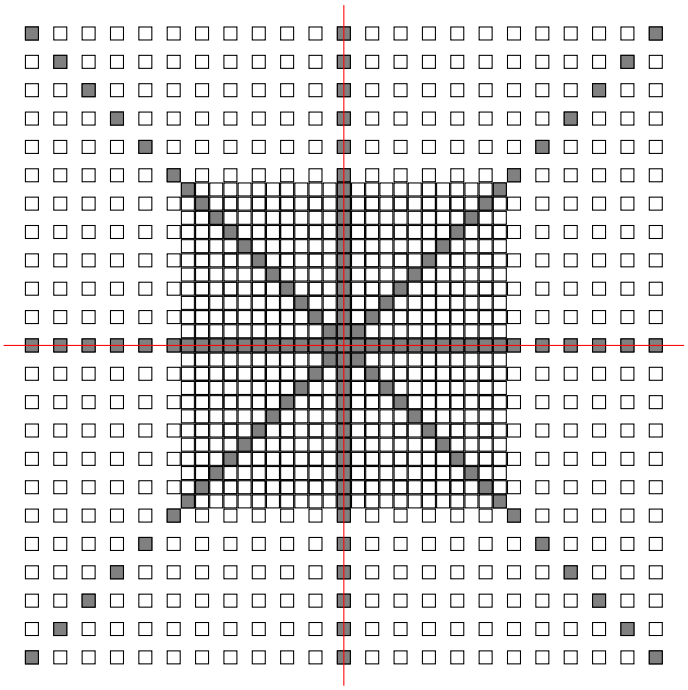

(a) The 977 air-filled ICs have a sensitive volume of $(2.3 \times 2.3 \times 0.5)\,\mathrm{mm}^3$. In the inner area the chambers are spaced on a 2.5 mm grid, whereas the center-to-center distance in the outer area is 5 mm. Each square in this sketch represents one ICs. Readout of the ICs indicated by gray squares is used for the lateral profiles.

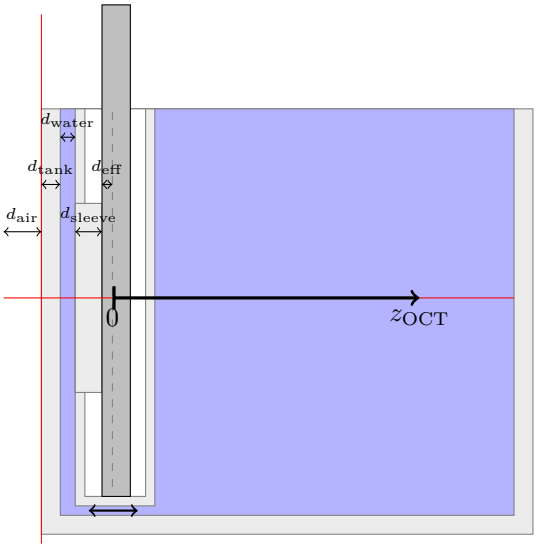

(b) Setup inside the watertank. Red lines indicate the position of the water tank relative to the laser-marked isocentre. The closest achievable position of the detector to the entrance window of the water tank is the sum of all indicated depths: $d_{\mathrm{air}} = 3.05\,\mathrm{mm}_{\mathrm{H_2O}}$, $d_{\mathrm{tank}} = 11.65\,\mathrm{mm}_{\mathrm{H_2O}}$, $d_{\mathrm{water}} = 7.9\,\mathrm{mm}_{\mathrm{H_2O}}$, $d_{\mathrm{sleeve}} = 16.48\,\mathrm{mm}_{\mathrm{H_2O}}$, $d_{\mathrm{eff}} = 5.5\,\mathrm{mm}_{\mathrm{H_2O}}$.

Figure 3.2: The OCTAVIUS® 1000 SRS P detector.

of lateral beam transport model. Chapter 5 only considers the $(8 \times 8)\,\mathrm{cm}^2$ field, and refers to the evaluation process as *monitor calibration.*

As reference for the "entrance" dose, a PinPoint® chamber (TM31015-0013, $N_{D,w} = 1.196 \times 10^9\,\mathrm{Gy\,C^{-1}}$, PTW, Freiburg) is placed in a dedicated solid water (RW3) plate at a water-equivalent depths of 3.9 mm. The electrometer UNIDOS is set to *'Electrical, Medium Range, intensity I9'* and triggered to yield separate readout for each iso-energy layer defined in the irradiation plan. The air density and air temperature correction factor $k_{p,T}$ is determined on each measurement shift.

As reference in depth, the same irradiation plan was irradiated onto the MP3 water phantom equipped with a block of 24 PinPoint® ICs. Figure 2.1 sketches the PinPoint® chambers and their positions inside the block. Their correction factor $k_{p,T}$ was determined with the water temperature. The chamber block was positioned so that the water-equivalent depth of chamber D2 (TM31015-0444, $N_{dW} = 1.203 \times 10^9\,\mathrm{Gy\,C^{-1}}$, PTW, Freiburg) corresponded to three quarters of the BP position R_{peak} for each investigated energy. For correlation of the detector positions, the reader is referred to Figure 2.2 on page 12 and Table 3.1. The

Table 3.1: *Measurement positions in the MP3 water tank, at which absolute dose was measured in dependence on the field size.* The 24-pinpoint blocks coordinates in B and C were 7.0 mm and 3.0 mm respectively, so that chamber D2 (compare Figure 2.2) was positioned in the center of the field.

iE	A/mm	WEPL/mm	$0.75R_{\mathrm{peak}}$/mm	R_{peak}/mm
1.00	−4.4	15.3	13.2	17.6
22.00	−1.9	17.8	17.0	22.6
33.00	18.3	38.0	37.2	49.6
67.00	43.9	63.6	62.8	83.7
107.00	73.9	93.6	92.8	123.8
120.00	83.9	103.3	102.5	136.7
152.00	107.7	127.4	126.6	168.8
198.00	144.5	164.2	163.4	217.8
226.00	176.0	195.7	194.9	259.9
255.00	208.6	228.3	227.6	302.4

electrometer connected to chamber D2 had the same settings as for entrance dose measurements.

3.2.5 Multidimensional Distributions

Part of the commissioning process was the measurement of SOBPs of various sizes and depths. The measured dose profiles and point doses were compared by the dose distribution calculated with the implemented beam model. As preliminary validation of the MC model implemented in FLUKA (section 3.1), SOBPs were optimized with PRECISE [196] and measured in the water tank (MP3, SN 951, PTW-Freiburg). The calculation and optimization is extensively described in Kopp et al. [97]. A list of measured configurations and exemplary results for two SOBPs are provided in the appendix A.3 and Figure A.4. Mein et al. [58] published the dosimetric validation of SOBPs with an anthropomorphic phantom and a preliminary beam model for helium ions. The setup for commissioning of the clinical TPS RayStation® is published in the second peer-reviewed article comprising this thesis (Chapter 5). There, a setup comparable to Mein et al.'s was also employed.

3.3 Creation of a Database for the treatment planning system

With reference data measured, MC simulations with FLUKA fill in the gaps for those beam configurations that cannot be measured.

Table 1 of the second publication (Chapter 5) lists the inputs required for RayStation®. To create these inputs, we updated a previous implementation of HIT's beam line to a more recent version of the MC code FLUKA [11, 12, 166]. The developers of FLUKA had updated the transport code for helium ions with recent measurements of helium ion interaction cross-sections [36, 197, 198]. Thus, the energy-dependent input parameters to the FLUKA simulation, namely Gaussian beam width (FWHM) and Gaussian momentum spread ($\Delta p/p$), had to be determined anew. Tested against the measured dose distribution of single-energy beams of section 3.2, the full MC simulations with FLUKA would then yield the database of depth and lateral dose distributions. The secondary particle spectra extracted from FLUKA were published by Kopp et al. [97].

This section describes how the setting and input parameters for the database simulations were found.

3.3.1 Depth Dose Distributions for each energy step

The main task was to find reasonable estimates of the momentum spread $\Delta p/p$, so that the FLUKA simulations adequately reproduce the shape and characteristics of the measured IDDs of section 3.2.1. Hence, a cylindrical scoring region at the treatment rooms isocentre was defined. Water was assigned as material assuming an ionization potential of $I_{H_2O} = 76.8\,\text{mm}$ and a density of $\rho_{H_2O} = 0.998\,\text{g}\,\text{cm}^{-3}$. The scoring was extended to a lengths of 60 cm with a bin width of $dz = 0.05\,\text{mm}$. For comparison to the measurements, the scoring radius was $r_{\text{max}} = 4.08\,\text{cm}$. All simulations were performed with the developers version fluka2019.2.dev of FLUKA.

In order to match the simulated and measured IDDs, several positions were extracted from the data sets for each IDD: the first and last data point (R_{first} and R_{last}), the position of the maximum R_{peak}, distal ranges (R_x) at 90 %, 80 %, 50 % and 20 % of the dose maximum, the R_{tail} $R_{\text{tail}} = R_{90} + 10\,\text{mm}$ and the proximal position of the 50 %, 80 % and 90 % dose levels $R_{xx,p}$. From these, several properties were derived: the DFO (DFO $= R_{20} - R_{80}$), the w_{peak} ($|R_{80d} - R80p|$), the peak center (center of 80% dose level), the D_{peak}, the EPR, and the tail-to-peak ratio (TPR). This extraction was performed for each IDD individually. For comparison of the peak shape, the measured dose was then normalized by *ratio of areas under the curve* from the first measured point to the tail position for measured and simulated peak. For a more precise matching, the shift and scaling factor of the measured curve were then optimized by least-square optimization to fit the simulated curve. The resulting curves were analyzed again for the above mentioned properties, and the residual differences plotted for each curve. This

process was repeated in 10 iterations with different momentum spreads as input parameter to the simulation until the residual plots were satisfactory.

For the final base data simulation, the radius was enlarged to $r_{\max} = 14\,\text{cm}$. An overall offset was defined for all energies, so that $z = 0$ is at the vacuum window instead of the iso-center. To retrieve this offset, the difference of range R_{80} was averaged over all energies, resulting in $R_{80} = 2.993\,\text{mm}$.

In contrast to matching over the area (total deposited dose), RaySearch requested scaling at the *entrance dose at* 2 cm *depth*. At this depth, the measurement and also simulation are still affected by interactions on the detector surfaces.

Even in the final iteration of momentum spread testing, the EPRs were not fully matching. This issue could have been potentially resolved if the momentum spread were described by more complex distribution than a Gaussian. With the settings for a double Gaussian lateral beam profile in vacuum, the IDD simulations were repeated in PEAKFINDER®configuration with fluka2020.3.dev. Figure 7.1 on page 99 shows the impact of this double Gaussian on lateral and depth dose curves for one energy. A comparison of all IDDs' characteristics is shown in Figure A.1 on page 139.

Evidently, RaySearch used the measured IDDs to create their own beam model.

3.3.2 Entrance Dose: Lateral Profiles at 5 Positions in Air

The input for lateral Gaussian beam width was optimized to reproduce the reference width of LIBC at the isocentre of the treatment rooms, when no beam modifier is placed into the air gap (no ripple filter in the beamline (noRiFi)). Measurement of these distribution is described in detail by section 3.2.2 and a detailed analysis of variations in initial beam width was published as [14] (Chapter 4).

3.3.3 Lateral Evolution in Material

In addition to the lateral distribution in air, the lateral dose distribution $D(r, z)$ in water was extracted from a FLUKA simulation. Therefor, a 32 cm long water tank with cylindrical coordinates ($r = 14\,\text{cm}$, $\Delta z = 0.1\,\text{mm}$, $\Delta r = 0.5\,\text{mm}$) was defined as scoring region. Just as for the distributions in air, the initial Gaussian beam width was chosen to reproduce the LIBC settings. Additionally an initial double Gaussian beam shape was tested. These results are presented in section 4.2 and figure 6 of the first peer-reviewed publication (Chapter 4).

For the FRoG input, these simulations were fitted with a triple Gaussian lateral parametrization, see section 3.5.

3.3.4 Absolute Dosimetry to Determine the Scale of Depth Dose Distributions

Absolute dosimetry was performed with homogeneous quadratic fields of various edge lengths, as described in section 3.2.4. The same spot pattern is simulated in FLUKA with a $(30 \times 30 \times 30)\,\mathrm{cm}^3$ water cube positioned with the side closest to the nozzle at the isocentre. The material deviation of the MP3 phantoms PMMA entrance window is neglected for these simulations. The scoring region is a 1 mm thick slice $(2 \times 2)\,\mathrm{cm}^2$ surrounding the water equivalent path-length (WEPL) depths of the chamber in the measurements. The depth corresponding to the measurement positions are indicated in Table 3.1 on page 35.

For evaluation, the measured and calculated doses are plotted against the edge length of the corresponding field and normalized at a field size of $(10 \times 10)\,\mathrm{cm}^2$. This field size corresponds to the reference conditions for absolute dosimetry as defined in the codes of practice TRS-398 and TRS-483 [46, 199]. The uncertainty for simulated dose was calculated as standard deviation among all summed voxels.

A comparison of measured and simulated SOBPs, including the improved match caused by the added second Gaussian in the initial lateral beam profile is also shown there in appendix A.3.

3.3.5 Particle Spectra

The fluence Φ of all possible secondary and primary particles over depth in material and their energies at given depths were extracted from FLUKA simulations as described by [97]. RaySearch Laboratories used these to create their physical dose model for helium ions.

3.4 Commissioning of the Clinical treatment planning system

The clinical TPS RayStation® must to be commissioned at HIT, before any patient treatments may be planned. The measurements for commissioning were predominantly performed by Thomas Tessonnier and the clinical medical physicists to follow the fourth-eye principle: not the same person should verify a system, as has created it. The whole process is described in 5, the second publication comprising this thesis.

3.5 Creation of a (Bio)Database for FRoG

For calculation of effective doses, or RBE-weighted doses, databases of biological parameters are required, see sections 2.2 and 2.5.

For mMKM, this database contains tabulated energies and the corresponding z^*_{1d} of all primary and secondary particles, convoluted with the fluence spectra. This convolution yields a depth-dependent $\overline{z^*_{1d,mix}}$. Linear quadratic parameters are derived according to $\alpha_{mmkm} = \alpha_x + z^*_{1d\mathrm{mix}}\beta_x$ and $\beta_{mmkm} = \beta_x$. The calculation of z^*_{1d} follows the description in [96]. For LEM-I, the energy and corresponding α_{LEM} and β_{LEM} are convoluted with the spectra. The required parameters have to be obtained from the PT RBE Generator software by Siemens which is available at HIT.

RayStation® allows the input of z^*_{1d} tables locally. Hence, this author created said tables for β_x from $0.01\,\mathrm{Gy}^{-2}$ to $0.07\,\mathrm{Gy}^{-2}$ in increments of $0.01\,\mathrm{Gy}^{-2}$, as well as for $\beta_\mathrm{x} = 0.025\,\mathrm{Gy}^{-2}$. The α_x can be specified independently to for calculation of the mMKM based RBE. For the retrospective analysis of prostate cancer trials section 3.6, additional tables with the parameters of Table C.1 on page 147 were created.

The in-house GPU-based robust recalculation tool FRoG [97, 185] requires tabulation of depth-dependent dose D, LET_d, α_{rbe} and β_{rbe}. These can be obtained from the FLUKA beam model, by weighting the particle fluence with z^*_{1d}, thereby obtaining the dose-weighted average $\overline{z^*_{1d,mix}}$ as a function of depth for all available beam energies and beam particles. In the same FLUKA run we obtained physical dose and LET_d distribution. The lateral dose distribution in water was simulated for 19 energies and fitted it with a triple Gaussian (TG) function for each increment in depth. Then, the TG-parameters were interpolated for all energies as a function of depth. Full FRoG databases, were created for $\mathrm{LEM\text{-}I}_{3.1}$ and for mMKM with the prostate-specific parameters in table C.1 The code for creating these tables, had previously been created by Mein et al., but had to be executed for each assumed combination of photon LQ parameters (α_x and β_x).

3.6 Retrospective Analysis of tumor control probability and normal tissue complication probability

The plausible radiosensitivity parameters of prostate tumors has been a controversial debate for over 20 years. As most RBE models are based on on them, the appropriate choice of sensitivity parameters does have a large influence on them. For the third publication comprising this chapter (Chapter 6) we recalculated the effective doses received by 91 prostate patients at HIT. As both arms of the IPI trial (randomized groups receiving either proton or carbon ion irradiation) were presumably treated under the same conditions, they offer a unique opportunity to investigate the clinical RBE of carbon ions in prostate tissue. Figure 3.3 depicts the evaluation plan this investigation.

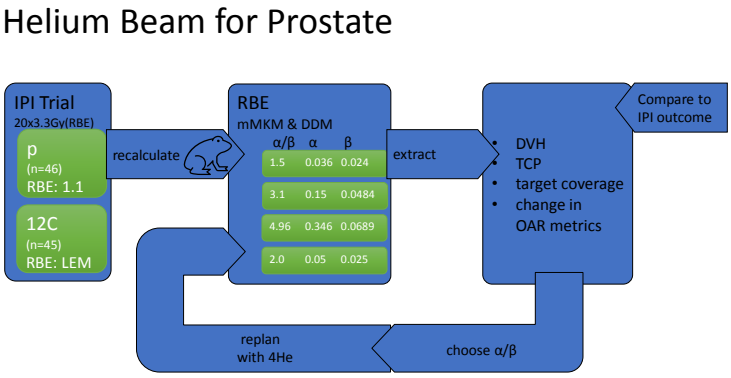

Figure 3.3: Analysis strategy of the IPI trial

As starting point, we chose the parameter sets, that Marteinsdottir et al. [129] used for their analysis of the McNamara [83] and repair-misrepair-fixation (RMF) [84–86] models for the RBE of protons, as well as the standard setting for late reacting tissue, currently applied at HIT. We used mMKM and LEM for this recalculation of treatment doses. From the calculation, DVHs of absorbed and effective dose are extracted. One example of these is depicted in Figure 2.4 on page 19.

In parallel to the RBE-weighted dose recalculations, we tried do find a TCP function and parametrization, that would accurately predict the outcome of the IPI trial, as published by Eichkorn et al. [200]. Therefor, we searched the literature for data on 5-year bRFS that clearly separated the outcome based on the received dose, risk-stratification and usage of androgen deprivation therapy (ADT). These data from photon irradiations should ideally have a fractionation scheme in a similar range as the 66 $\mathrm{Gy_{RBE}}$ of IPI. The data selection of Miralbell

et al. [201]. It contains the trial results of [202–206]. The data collection of Royce et al. [207] focused on ultra-hypofractionated treatments.

A Poisson TCP curve (compare Equation (2.23)) was fitted to the bRFS and corresponding BED. The equation [130, 131]

$$TCP\,(BED) = \left(\tfrac{1}{2}\right)^{\exp\left(e\gamma\left[1-\left(\frac{BED}{\mathrm{TBED}_{50}}\right)\right]\right)}, \tag{3.1}$$

where γ is the maximum slope and $TCP\,(\mathrm{TBED}_{50}) = 50\,\%$. BED of the IPI patients was calculated from the RBE-weighted $D_{95\%}$ of the CTV. The parameters $(\alpha/\beta)_x$ for BED calculation were the same as for the RBE model. This was repeated for each set of LQ-parameter combination. The combination which predicted the outcome of IPI the best, is presented in the third peer-reviewed publication, comprising this thesis (Chapter 6 and appendix D).

3.6.1 Doses to Organ at risk

For a preliminary analysis of the adverse effects, DVHs of the OARs surrounding the prostate were extracted from the recalculations in FRoG, see appendix Figure C.2. The NTCP of Equation (2.24) was calculated for each patient for bladder and rectum. Parameters of the LKB-model were taken from the literature [131, 141, 208–213]. Then, predicted probabilities were compared to the incidence rates of acute toxicity reported in table observed results in table 2 of Habl et al. [214]. Further analysis may include the tolerance doses of Emami et al. [139] or the QUANTEC reports [141, 142].

However direct comparison of adverse effects is complicated by the differences in time of occurrence, the grading definition, fractionation and reported doses.

Part II

Peer Reviewed Publications

As per regulations of the Department of Physics and Astronomy of Heidelberg University, this work is in the form of a *cumulative thesis*. It comprises three peer-reviewed articles published in internationally acclaimed scientific journals, presented individually in chronological order of their publication date. Besides the publications themselves, a detailed description of the author's contribution to each of the publications is included together with the list of authors, the publication status, journal references, the DOI and copyright claims. The author of this thesis is the sole first author of the first (Chapter 4) and third publication (Chapter 6). The second publication (Chapter 5) was written by Thomas Tessonnier with significant contributions by the author of this thesis. None of the publications have been used for a cumulative thesis before. During the time these studies were conducted, the author of this thesis contributed to further scientific publications, which were not directly related to this thesis or ineligible for inclusion. These additional contributions are listed in Chapter 9 on page 111.

4 First Publication: The Evolution of Lateral Dose Distributions of Helium Ion Beams in Air: From Measurement and Modeling to Their Impact on Treatment Planning

Authors: **Judith Besuglow**, Thomas Tessonnier, Benedikt Kopp, Stewart Mein and Andrea Mairani
Publication status: Received: 18 October 2021; Accepted: 24 November 2021; Published: 07 January 2022
Journal reference: Frontiers in Physics, 07 January 2022, Sec. Radiation Detectors and Imaging, Volume 9-2021, 797354.
DOI: 10.3389/fphy.2021.797354

Authors' contributions: **JB** was the principal author. TT gave substantial scientific advice and created the patient treatment plans. AM contributed to the conception and design of the study and pre-optimized the initial beam widths for helium. SM pre-optimized the initial beam widths for carbon. BK pre-optimized the lateral profiles for the proton beam. **JB** performed the analysis and most measurements, simulated the last version of the helium base data, recalculated the proton and carbon profiles, and wrote the manuscript. All authors contributed to manuscript revision, read, and approved the submitted version.

frontiers in Physics

ORIGINAL RESEARCH
published: 07 January 2022
doi: 10.3389/fphy.2021.797354

The Evolution of Lateral Dose Distributions of Helium Ion Beams in Air: From Measurement and Modeling to Their Impact on Treatment Planning

Judith Besuglow[1,2,3,4], *Thomas Tessonnier*[5], *Benedikt Kopp*[1,2,3], *Stewart Mein*[1,2,3] *and Andrea Mairani*[1,5,6]*

[1]Clinical Cooperation Unit Translational Radiation Oncology, German Cancer Consortium (DKTK) Core-Center Heidelberg, National Center for Tumor Diseases (NCT), Heidelberg University Hospital (UKHD) and German Cancer Research Center (DKFZ), Heidelberg, Germany, [2]Division of Molecular and Translational Radiation Oncology, Heidelberg Faculty of Medicine (MFHD) and Heidelberg University Hospital (UKHD), Heidelberg Ion-Beam Therapy Center (HIT), Heidelberg, Germany, [3]Heidelberg Faculty of Medicine (MFHD), Heidelberg Institute of Radiation Oncology (HIRO), National Center for Radiation Oncology (NCRO), Heidelberg University Hospital (UKHD), Heidelberg Ion-Beam Therapy Center (HIT), and German Cancer Research Center (DKFZ), Heidelberg, Germany, [4]Department of Physics and Astronomy, Heidelberg University, Heidelberg, Germany, [5]Heidelberg Ion-Beam Therapy Center (HIT), Department of Radiation Oncology, Heidelberg University Hospital (UKHD), Heidelberg, Germany, [6]National Centre of Oncological Hadrontherapy (CNAO), Medical Physics, Pavia, Italy

OPEN ACCESS

Edited by:
Miguel Antonio Cortés-Giraldo, Sevilla University, Spain

Reviewed by:
Alejandro Bertolet, Massachusetts General Hospital and Harvard Medical School, United States
Mauro Valente, CCT CONICET Córdoba, Argentina

***Correspondence:**
Andrea Mairani
andrea.mairani@med.uni-heidelberg.de

Specialty section:
This article was submitted to Radiation Detectors and Imaging, a section of the journal Frontiers in Physics

Received: *18 October 2021*
Accepted: *24 November 2021*
Published: *07 January 2022*

Citation:
Besuglow J, Tessonnier T, Kopp B, Mein S and Mairani A (2022) The Evolution of Lateral Dose Distributions of Helium Ion Beams in Air: From Measurement and Modeling to Their Impact on Treatment Planning. Front. Phys. 9:797354. doi: 10.3389/fphy.2021.797354

To start clinical trials with the first clinical treatment planning system supporting raster-scanned helium ion therapy, a comprehensive database of beam characteristics and parameters was required for treatment room-specific beam physics modeling at the Heidelberg Ion-Beam Therapy Center (HIT). At six different positions in the air gap along the beam axis, lateral beam profiles were systematically measured for 14 initial beam energies covering the full range of available energies at HIT. The 2D-array of liquid-filled ionization chambers OCTAVIUS from PTW was irradiated by a pencil beam focused at the central axis. With a full geometric representation of HIT's monitoring chambers and beamline elements in FLUKA, our Monte Carlo beam model matches the measured lateral beam profiles. A second set of measurements with the detector placed in a water tank was used to validate the adjustments of the initial beam parameters assumed in the FLUKA simulation. With a deviation between simulated and measured profiles below ±0.8 mm for all investigated beam energies, the simulated profiles build part of the database for the first clinical treatment planning system for helium ions. The evolution of beamwidth was also compared to similar simulations of the clinically available proton and carbon beam. This allows a choice of treatment modality based on quantitative estimates of the physical beam properties. Finally, we investigated the influence of beamwidth variation on patient treatment plans in order to estimate the relevance and necessary precision limits for lateral beam width models.

Keywords: particle therapy, Monte Carlo simulation, Helium, treatment planning system, ion beam, lateral profiles, dosimetry

1 INTRODUCTION

Lyman and Howard measured the first helium Bragg peaks to use in radiotherapy in the 1970s [1]. Between 1975 and 1992, over 2000 patients received helium ion radiotherapy at the Lawrence Berkeley National Laboratory (LBNL) [2–6]. However, the treatment with helium ions was discontinued in the early 1990s, when the Bevatron and 184-inch-synchrocyclotron were dismantled.

At the Heidelberg Ion-Beam Therapy Center (HIT), protons, helium, carbon, and oxygen ions are accelerated and delivered with active beam scanning [7] for radiotherapeutic and research purposes since 2009. To this day, only protons and carbon ions are in regular clinical use. However, with the work presented in this study the first clinical application of helium ion beams was possible this year.

The treatment planning system (TPS) previously used (syngo® PT Treatment, Siemens AG, Erlangen, Germany) had only been commissioned for carbon ion and proton treatment. Therefore, we supported the beam physics modeling within the first commercial TPS (RayStation, RaySearch Laboratories, Stockholm, Sweden [8]) supporting helium ion irradiation through the creation of a database comprising beam-specific parameters and characteristics based on measurements or simulations.

A general attempt at gathering facility-specific helium beam properties at HIT had been made by Tessonnier et al. [9–12] by establishing a Monte Carlo (MC) framework for recalculating irradiation plans with FLUKA [13, 14]. However, the agreement between measurement and simulations showed limitations for fields with high initial beam energies [10], calling for a more precise estimation of secondary particle production in medium. Since then, new charge- and mass-changing cross-sections in the energy region between 70–220 MeV/u have been determined experimentally [15] and updated in FLUKA. At HIT, attempts of measuring the secondary particles produced by helium ions have been made [16]. Additional characterization of the double differential nuclear reaction cross-section for helium in the therapeutically relevant energy range could further improve dose estimation in beam entrance and fragmentation tail [17]. The implementation of this newly available data calls for revalidation of the beam properties in our MC framework.

Helium ions exhibit physical and biological properties that are moderate between protons and carbon ions. In contrast, carbon ions feature a very sharp lateral penumbra, a sharp peak in the depth dose distribution, and a high linear energy transfer (LET) compared to helium ions and protons. However, their produced secondary particles result in a more significant fragmentation tail. Proton Bragg peaks, on the other hand, exhibit a smaller peak-to-plateau ratio than helium ions. Both, carbon ions and protons, have distinct strengths and weaknesses in the context of clinical practice, as nicely summarized in review papers [18, 19]. Thus, helium ions can bridge the gap in achievable dose conformality and LET between proton and carbon ion beams.

Similar to the HIT carbon ion commissioning [20–23], the set of data gathered for beam physics modeling in the RayStation TPS included laterally integrated depth dose curves (iDDDs), calibration of absolute dose per particle, and particle spectra [24]. However, while the collection of depth dose curves and absolute calibrations of helium ion dose was updated with respect to previous publications, lateral profiles in the air gap between the last beamline element and phantom had never been thoroughly investigated for raster-scanned helium ion beams.

Schardt et al. reported in [25] how beamline materials and the airgap affect the beam widths of proton and carbon ions. On the one hand, carbon ions are relatively heavy, and the beam broadening in air is primarily independent of the initial beam energy. The broadening of proton beams, on the other hand, is much more considerable than for carbon of any energy, and it depends heavily on the initial beam energy. The same multiple scattering processes apply to helium ions. While the resulting broadening of beamwidth could be estimated analytically via the Highland approximation [26, 27], this approach would neglect large angle scattering and the dose contribution of secondary hadron production in the beamline. Analytical calculations of beam broadening by multiple scattering via Molière-theory [28–30] would be quite time-intensive and would still neglect the beam shape specific to the HIT beamline. Moreover, no knowledge of the actual beam shape in air could be gained. Würl et al. [31] showed for protons that the beam shape in air impacts the dose distribution in the patient as well.

Therefore, precise knowledge of the profiles in the air between the vacuum exit and the patient should improve the prediction of the beam shape at the surface entrance point of a phantom or patient. As the lateral dose distribution in this airgap has not been investigated for actively scanned helium beams before, this work quantifies the evolution of the beamwidth and its impact on treatment planning.

Measured beam profiles in air provide the starting beam parameters in vacuum for our MC physical beam model. The MC model then provides particle spectra and lateral dose distributions as base data to the clinical TPS in addition to measured iDDDs. The TPS then parameterizes the beam profile at the surface entrance point of the patient and propagates the dose based on analytical dose models. Apart from clinical use of the TPS, the MC beam model with all validated beam parameters can support further experimental studies at HIT.

This work reports on the creation of the database of lateral dose profiles specific to the HIT beamline for the first commercial TPS for helium ions. The lateral profiles of single-spot pencil beams are measured in the air gap between the last element of the beamline and patient, as well as inside a water tank. As not all profiles of the 255 available beam energies can be measured, an MC beam model is created, and a database of the lateral beam profiles is simulated in FLUKA.

Furthermore, the beam profiles of helium are compared to those of carbon and proton beams. Lastly, the impact of deviations in the beam profile on dose distributions in patients is studied, and possible applications of the gained knowledge are discussed.

2 MATERIALS AND METHOD

2.1 Helium Ions at Heidelberg Ion Beam Therapy-Center

The HIT is a synchrotron-based particle therapy center with two horizontal treatment rooms and a gantry. Three ion sources

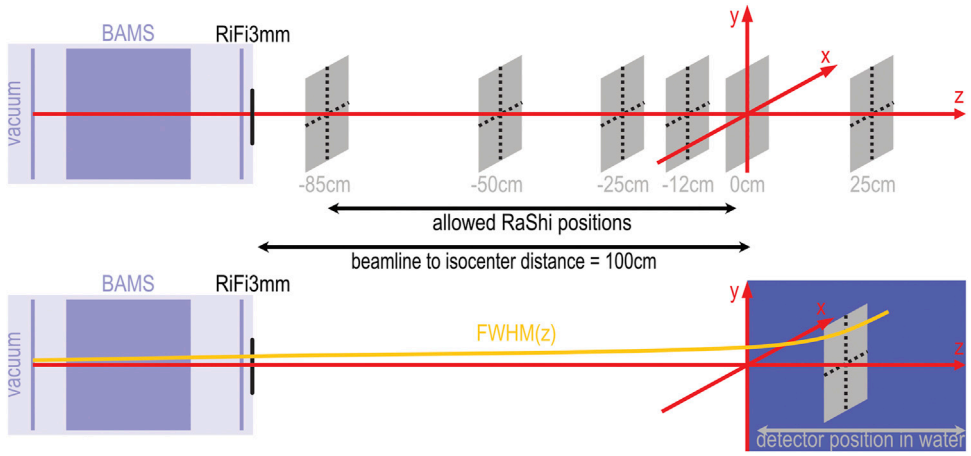

FIGURE 1 | Experimental setup schematic for measurements and simulation. The upper half shows the beamline with monitor system (BAMS) and ripple filter (RiFi3mm) and the positions at which measurements were performed with the OCTAVIUS phantom in air. The lower half of the sketch shows the position of the water tank relative to the isocenter marked by the red coordinate system. A yellow curve sketches the assumed evolution of the beamwidth. The beamline to isocenter distance is 100 cm in the horizontal treatment rooms. At the gantry, this distance is reduced to 80 cm. The allowed positions for the range shifter (RaShi) are continuous between −85 and −2 cm for the horizontal treatment room and between −38.5 and −2 cm for the gantry.

enable the acceleration of protons (1H), helium (4He), carbon (12C), and oxygen (16O) ions. Since 2009, patients have been treated daily with proton and carbon ion beams. The synchrotron accelerates helium ions to 255 discrete energies between 50.57 MeV/u and 220.51 MeV/u, corresponding to ranges of approximately 2.1 and 30.8 cm in water without any beam modifiers. Bunches of primary ions are extracted from the synchrotron by the so-called beam scraper using slow knockout extraction [32, 33] and sent to the individual treatment rooms. Scanning magnets bend the beam across the treated volume, which results in a virtual source-axis-distance of approximately 7 m in the horizontal rooms and about 43 m in the gantry.

Before entering each patient treatment room, the beam passes through a monitoring system (BAMS) consisting of three ionization chambers and two multi-wire proportional chambers, as described by Tessonnier et al. [9]. Behind the BAMS chambers, additional beam modifiers can be inserted into the beamline at positions indicated in **Figure 1**. A 3 mm ripple filter (RiFi3mm) [34] spreads out the individual Bragg peaks to about 2–3 mm and reduces the range by the same length. The insertion of the ripple filter allows a tumor volume to be irradiated faster, as homogeneity in depths can be achieved using only every third available beam energy. A PMMA range shifter of approximately 2 cm water equivalent thickness allows the irradiation of very superficial tumors. It can be placed anywhere between the beamline exit and the room's isocenter.

Each irradiation requires a control file including desired beam energies, beam positions, discrete nominal beamwidths and particle intensity chosen from the accelerator library (LIBC). This so-called irradiation plan also includes the gantry angle and detector or patient table position.

While the beam position (spot) can theoretically be any continuous position in the x,y-plane at the room's isocenter, in practice at HIT, spots are placed on a cartesian or hexagonal grid with fixed spacing to compensate for variations in beamwidth caused by the synchrotron and beamline. The nominal beamwidth is defined as the full width at half maximum (FWHM) in the treatment room's isocenter without any beam modifiers placed in the room. The methodology of creating the accelerator library has been described before [12]. The LIBC contains four discrete nominal beamwidths for each beam energy. Within each discrete configuration, the total beamwidth decreases with increasing beam energy. For treatment planning, a relatively stable spot size over the whole energy range is desired to achieve a homogeneous dose with a fixed spot spacing. Following the results of Parodi et al. [20], beamwidths at least three times larger than the spot spacing still assure homogeneity of the treatment fields. This assumption was made during the first trials for raster scanning ion beams [7, 35]. Thus, for a proposed spot spacing of approximately 2 mm, the beamwidth must be at least 6 mm to achieve a robust homogeneity against beamwidth variation. As the smallest available nominal beamwidth is smaller than this threshold for energies larger than 167 MeV/u, the second nominal beamwidth setting is used for higher energies.

2.2 Measurements with Octavius Phantom

To measure the lateral profiles in air, we positioned a 2D-ionization chamber array (OCTAVIUS 1000 SRS, SN000308, PTW Freiburg) perpendicular to the central beam axis at six positions along the beam axis. Relative to the treatment room's isocenter, the reference point of the detector was positioned at −85, −50, −25, −12, 0 and 12 cm, where "-" denotes any upstream positions. In **Figure 1**, the measurement positions relative to the isocenter are depicted by grey squares.

The OCTAVIUS 1000 SRS consists of 977 liquid-filled ionization chambers with a sensitive volume of 3 mm^3 in a cartesian grid of

2.5 mm spacing in a central area of $(5.5 \times 5.5)\,cm^2$. At the outer edges the ionization chambers are spaced twice as far apart.

With a dynamic measurement range from 0.2 to 36 Gy/min, the OCTAVIUS chamber array allowed a 0.1 mGy resolution in absolute dose measurement, with a relative uncertainty of ±0.5% local dose, according to the manufacturer.

For each measurement position and tabulated beamwidth, we obtained the lateral dose distributions for 14 initial beam energies distributed over the entire available energy range by irradiating the detector with approximately 10^9 helium ions on the central beam axis. The particle intensity was adjusted for each energy to ensure dose deposition rates within the measurement range.

At the isocenter, we irradiated the same spots without the ripple filter inserted into the beam, allowing for comparison to the accelerator specifications.

Following the same protocol, we measured lateral dose distributions in the gantry at a 90° rotation angle.

2.3 Monte Carlo Simulation

Our simulation of the lateral profiles was based on the MC code FLUKA [13, 14] with the implementation of BAMS and RiFi3mm reported in previous works [9, 10, 21]. All physical interactions were simulated in FLUKA with the HADROTHERAPY defaults. We assumed that delta electrons are not transported by switching off delta ray production. Additionally, we reduced the step size for charged hadrons and muons to 0.02 of the kinetic energy. The evaporation model for heavy fragments and coalescence mechanism was activated as well. All simulations ran with the physics models of the currently available FLUKA version.

The beam was assumed to be non-divergent before leaving the vacuum window of the beamline. For each discrete beam setting of the accelerator, the simulation required three beam parameters: initial beam energy in vacuum, initial Gaussian momentum dispersion, and the Gaussian width of the beam's initial lateral fluence profile. The initial beam energy was assumed to be identical to the nominal beam energy. Following previous works [9], we manually modified the initial momentum spread until simulated depth dose curves matched the commissioning measurements in shape and peak width. With the ripple filter removed from the simulated beamline, we iteratively optimized the initial Gaussian fluence profile to reproduce the nominal beamwidth at the isocenter. Some fine-tuning of the initial parameters regarding those used in previous works [11] was necessary for the updated FLUKA version (2021.1).

Once we found the optimal initial beamwidth, the profiles at all six detector positions were simulated with the ripple filter in place as follows: The simulated geometry included a detailed representation of BAMS and additional beam modifiers. For the profiles in air, a thin disk of water ($r = 14\,cm$, $\Delta z = 1\,mm$), at the detector position relative to the beamline, represented the detector. Within this disk, we scored the dose profile D(r) in cylindrical coordinates summing over the azimuthal angle in increments of $\Delta r = 0.5\,mm$. For each setting, the dose distribution was averaged over 10^8 primary helium ions initiated in the simulation.

2.4 Evaluation and Comparison of Profiles

From the 2D dose array of the OCTAVIUS, we extracted the central x- and y-profiles and diagonal profiles. These four profiles were fitted with a Gaussian to determine the beam center and normalization. If necessary, a shift and normalization to the maximal dose were applied to overcome lateral positioning uncertainties.

Previous simulations for protons and carbon ions assumed the lateral beamwidth $FWHM_{tot}(z)$ could be parametrized by the depth-dependent spread due to scattering and the inherent beamwidth in vacuum $FWHM_{vac}$ [22, 21, 10]. Whereas the depth-dependent width can be further split into the constant contribution of the beam modifiers (BAMS and RiFi3mm) and the contribution of the air gap:

$$FWHM_{tot}(z)^2 = FWHM_{vac}^2 + \left(FWHM_{BAMS}^2 + FWHM_{RiFi3mm}^2 + FWHM_{air}(z)^2\right).$$

At the isocenter ($z = 0$), the total beamwidth without ripple filter should per definition be identical to the nominal beam width $FWHM_{nom}$. Since the measurable beam width is subject to daily variations, a scaling factor s_{daily} is introduced for the measurements. Although the contribution of air gap and beam modifiers should be constant, we assumed that the factor equally applies to both sides of the equation. This factor scales the measured profile to the nominal $FWHM_{nom}$ of the accelerator library that the simulation was set up to reproduce.

$$\begin{aligned} s_{daily} &= \frac{FWHM_{nom}}{FWHM_{OCTAVIUS,\,noRiFi}(z=0)} \\ &\Rightarrow FWHM_{OCTAVIUS,RiFi3mm}(z)^2 \cdot s_{daily}^2 \\ &= s_{daily}^2 \cdot \left[FWHM_{vac,daily}^2 + \left(FWHM_{BAMS}^2 \right.\right. \\ &\quad \left.\left. + FWHM_{RiFi3mm}^2 + FWHM_{air}(z)^2\right)\right] \\ &\cong FWHM_{tot}(z)^2 \\ &= FWHM_{FLUKA,\,RiFi3mm}(z)^2 \end{aligned}$$

The shape of measurable horizontal profiles is influenced by the slow knockout-extraction from the synchrotron [32]. Thus, only the beam width from the vertical y-profiles measured without ripple filter at the isocenter was considered in calculating the scaling factor.

After scaling the profiles measured with ripple filter by s_{daily}, the beamwidth of scaled, measured profiles should thus be reproduced by the simulated profiles. The simulated and scaled, measured profiles were plotted directly against each other to determine whether the beam shape was sufficiently reproduced. The absolute beam widths (FWHM) were extracted by calculating the width at half of the maximum dose. We reported the average of the four extracted profiles for measured beam widths to even out deviations from axial symmetry. The extracted widths were then analyzed and compared in dependency on the position along the beam axis and initial energy.

2.5 Impact of Beam Width Variation on Patient Treatment

We investigated the effect of the beamwidth at the surface entry point on a treatment plan optimized with RayStation 10 A. A clinical-like treatment plan for helium therapy was generated using multi-field optimization on a patient data set representative for meningioma treatment. For simplicity, we chose beam angles of 0° and 270° and placed the isocenter in the center of the treatment volume. The biological dose optimization was based on the modified

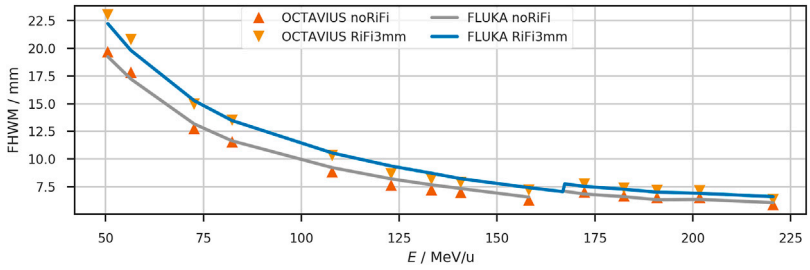

FIGURE 2 | The lateral beam width (FWHM) at the isocenter of the horizontal treatment room. Comparison between measurement (triangles) and simulation (solid lines) with and without ripple filter. For clinical application, the ripple filter is inserted into the beamline. The measurements were scaled to reproduce the nominal accelerator settings when the ripple filter is not used. Between the measured energies, the beam width is interpolated linearly. At nominal beam energy of 167 MeV/u, the beam width jumps to the next higher tabulated focus to fulfill the >6 mm requirement. The measured FWHM has a standard deviation of approximately 0.2 mm at the isocenter.

TABLE 1 | Lateral Widths (FWHM) of the lateral dose profile of a helium beam at the isocenter (z = 0 cm) without ripple filter as extracted from the simulated profiles in FLUKA and scaled profiles measured with the OCTAVIUS detector. Range (R80) and initial beam energy (E) of the unmodified beam and nominal width are also provided in addition to the absolute and relative deviation (ΔFWHM) between measured and simulated profiles.

E in MeV/u		50.57	56.44	72.65	82.33	107.93	122.93	133.21	140.71	158.08	172.28	182.43	190.85	201.71	220.51
R80 in cm		2.14	2.65	4.25	5.36	8.78	11.09	12.79	14.10	17.31	20.12	22.23	24.04	26.45	30.82
FWHM in mm	nominal	18.6	16.7	12.8	11.3	8.9	7.9	7.4	7.1	6.3	6.8	6.6	6.4	6.3	6.1
	OCTAVIUS	19.7	17.8	12.7	11.6	8.8	7.6	7.2	7.0	6.3	7.0	6.7	6.5	6.5	5.9
	FLUKA	19.3	17.2	13.2	11.6	9.2	8.2	7.7	7.3	6.6	6.8	6.6	6.3	6.3	6.0
ΔFWHM in mm		−0.5	−0.6	0.4	0.1	0.4	0.6	0.5	0.4	0.3	−0.2	−0.1	−0.2	−0.2	0.2
ΔFWHM in %		−2.3	−3.4	3.3	0.6	4.5	7.3	6.2	5.3	4.1	−2.8	−1.3	−3.4	−2.8	2.8

microdosimetric-kinetic model (mMKM) with an α/β-ratio of 2 Gy [24].

Then, we varied the beamwidth of the individual pencil beams in air close to the patient entrance point by approximately ∓10% for the same plan to investigate the impact on the irradiated field and organs at risk. The dose distributions produced with varied beam width were forward calculated in the TPS.

From the recalculated plans, we extracted lateral profiles of biological and physical dose in the entrance channel of each beam and diagonally through the clinical target volume (CTV). The profiles extracted from the patient plan were compared and analyzed for differences in the penumbra (lateral distance between 20% and 80% of maximum dose) among the three scenarios. Additionally, we analyzed the dose-volume histograms (DVH) of the target volume (CTV around meningioma) and three neighboring organs at risk (OAR), namely the left parotid gland, right optical nerve and the brain stem.

3 RESULTS

3.1 Beam Profiles

The beamwidth at FWHM at the isocenter is reproduced by the simulations as shown in **Figure 2** and **Table 1**. The nominal accelerator beamwidth is reproduced within 4% when the ripple filter is removed from the beamline. The beam widening by the ripple filter is also reproduced in the simulations, as the dark blue line in **Figure 2** shows. The scaled measurements agree well with the beamwidth extracted from simulated profiles for the beam with the ripple filter in place. The standard deviation of the scaled measured FWHM extracted from the four measured lateral profiles (horizontal, vertical and diagonal) is approximately 0.2 mm or 2% for each position and energy.

Figure 3 shows the shape of lateral profiles at all measured positions for the helium beam with an initial energy of 107.93 MeV/u (158.08 MeV/u). This energy corresponds to a range of approximately 8.8 cm (17.3 cm) in water after passing the beamline and ripple filter. Triangles depict the measured profile. The simulated profiles are scaled to their maximum and shown as a blue line. While the nominal beamwidth without ripple filter is 8.9 mm (6.3 mm) at the isocenter, the measurement yields an average width of 8.8 mm (6.3 mm). The simulation produces a width of 9.2 mm (6.5 mm). With the ripple filter, the average measured beam width is 10.3 mm (7.2 mm) after scaling, and the simulated profile has a beamwidth of 10.5 mm (7.4 mm) at the isocenter. So, the ripple filter broadens the beam of this specific energy by approximately 1.4 mm (0.9 mm). For other investigated beam energies, the extracted profiles with ripple filter are provided in **Table 2**.

3.2 Effect of Beam Width Variation on Patient Treatment

In **Figure 4**, we show the effects of beamwidth variation on the dose distribution produced by a patient treatment plan. In the top panel (A), a selected slice of the patient CT with overlaid dose

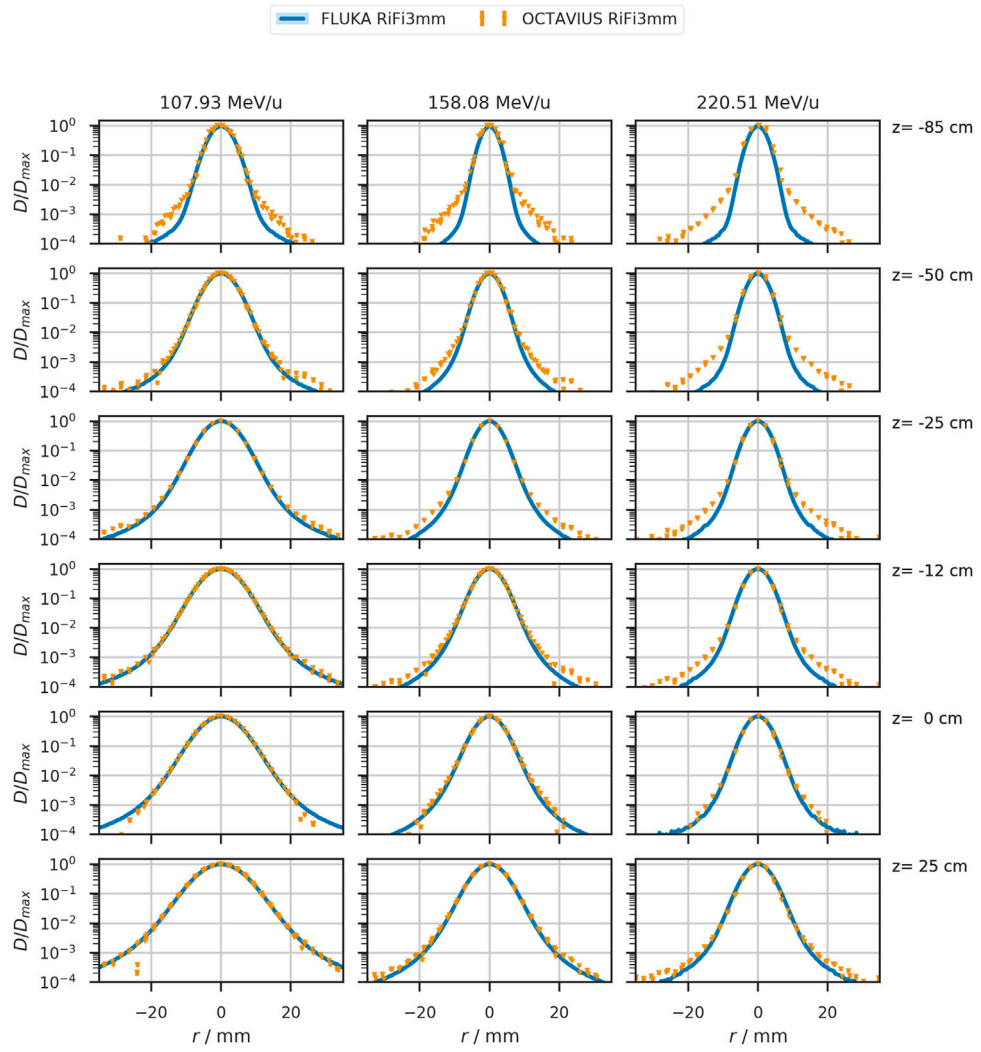

FIGURE 3 | Lateral beam profiles in air of the 107.93 MeV/u, 158.08MeV/u, and 220.51 MeV/u helium beam as simulated in FLUKA (solid blue line) and measured (orange triangles). The detector position relative to the treatment room's isocenter is indicated on the right of each row. Measured data contains datapoints from the four prominent profiles with an estimated uncertainty of at least 0.5% or 1 mGy for the local dose deposition. This uncertainty corresponds to four orders of magnitude lower than the local dose maximum in each profile.

distribution is depicted for the original case, reduced and increased beam width from left to right. Dose profiles were extracted at the entrance of each of the two treatment fields, indicated by the purple (superior field) and orange (left field) line in panel (A). These dose profiles show a variation in the penumbra (distance between 20% and 80% of local dose maximum) between $15.3^{-1.0}_{+0.9}$ mm in the lateral field impinging from the left and $11.2^{-0.8}_{+0.7}$ mm for the field superiorly impinging as plotted in panel (B). The profile extracted diagonally through the target volume is indicated as a green line; the contributions of the individual fields are plotted separately in the bottom graph of panel (B). The differences in dose distribution are non-significant, with only slight deviations even in the dose-volume-histogram (panel (C)) of **Figure 4C**. The dose received by >98% of the clinical target volume varies by + 0.8% and −1.2%. And the $D_{50\%}$ varies by +0.8% and −0.9%. Organs at risk in lateral proximity to tumor and beam path are the brainstem, left parotid gland, and the right optic nerve. The highest dose received by <2% of the brainstem is $(51.18^{+0.66}_{-0.69})$Gy (RBE), while less than 2% of the left parotid gland (delineated in bright orange) receive a high dose of $(39.52^{+0.06}_{-0.24})$Gy (RBE). In the right optic nerve, $D_{2\%}$ is $(26.04^{+0.34}_{-0.15})$Gy (RBE).

4. DISCUSSION

4.1 Beamwidth in Air

The measured lateral profiles without ripple filter showed deviations from the nominal beam width (i.e., FWHM) at the isocenter of about 5%, which agrees with the standard deviation of the four averaged profiles.

TABLE 2 | Lateral beamwidth (FWHM) of the helium beam with ripple filter (RiFi3mm) at measured positions z in the airgap behind the last beamline component. Dose profiles were either measured with the OCTAVIUS phantom and scaled by the daily deviation of the unmodified beam from nominal beam width or simulated with FLUKA as the dose to water in a thin slice at the corresponding position in the treatment room. The standard deviation of measured lateral beamwidth for each position is approximately 0.2 mm for each position and energy. The profiles corresponding to the initial beam energies E, highlighted in italics, are plotted in **Figure 3**.

E in MeV/u	Dataset	FWHM in mm with RiFi3mm at position z relative to the isocenter					
		–85 cm	–50 cm	–25 cm	–12 cm	0 cm	25 cm
50.57	OCTAVIUS	12.07	15.43	19.10	21.09	23.01	27.24
	FLUKA	12.60	15.79	18.85	20.66	22.24	26.25
56.44	OCTAVIUS	10.52	13.63	17.10	19.03	20.79	24.74
	FLUKA	11.35	14.20	16.92	18.50	19.83	23.31
72.65	OCTAVIUS	5.62	8.83	11.90	13.43	14.94	18.10
	FLUKA	8.45	10.79	12.89	14.08	15.27	17.92
82.33	OCTAVIUS	5.59	8.33	10.86	12.25	13.51	16.27
	FLUKA	7.48	9.55	11.32	12.44	13.47	15.77
107.93	*OCTAVIUS*	*6.17*	*7.17*	*8.58*	*9.39*	*10.32*	*12.18*
	FLUKA	*6.00*	*7.63*	*9.00*	*9.77*	*10.54*	*12.28*
122.93	OCTAVIUS	5.82	6.46	7.45	8.04	8.67	10.23
	FLUKA	5.31	6.81	7.98	8.68	9.36	10.83
133.21	OCTAVIUS	5.54	6.07	7.04	7.60	8.17	9.61
	FLUKA	5.03	6.37	7.46	8.11	8.72	10.07
140.71	OCTAVIUS	5.42	5.88	6.82	7.33	7.88	9.25
	FLUKA	4.89	6.13	7.02	7.63	8.22	9.50
158.08	*OCTAVIUS*	*4.75*	*5.21*	*6.16*	*6.66*	*7.17*	*8.30*
	FLUKA	*4.37*	*5.46*	*6.38*	*6.92*	*7.41*	*8.62*
172.28	OCTAVIUS	6.79	6.70	7.02	7.35	7.72	8.64
	FLUKA	4.93	5.87	6.64	7.03	7.52	8.51
182.43	OCTAVIUS	6.64	6.50	6.75	7.01	7.35	8.20
	FLUKA	4.86	5.79	6.48	6.90	7.26	8.19
190.85	OCTAVIUS	6.65	6.41	6.63	6.84	7.16	7.94
	FLUKA	4.67	5.53	6.18	6.57	7.00	7.86
201.71	OCTAVIUS	6.86	6.55	6.67	6.88	7.13	7.83
	FLUKA	4.79	5.56	6.18	6.52	6.90	7.77
220.51	*OCTAVIUS*	*6.41*	*6.14*	*6.07*	*6.17*	*6.31*	*6.72*
	FLUKA	*4.69*	*5.35*	*5.95*	*6.26*	*6.60*	*7.33*

Scaling the measured profiles with the daily deviation factor to nominal settings resulted in an agreement within ±0.8 mm between simulation and measurement in air.

For positions close to the beamline, the deviation between measured and simulated profiles was the largest. Scaling the measured data with the nominal beam width at the isocenter, as described in **Section 2.4**, improved the match between simulation and measurement for all positions.

As a variation of the beamwidth at the isocentre between ±15% is occasionally observed in daily quality assurance measurements, the reproduction of nominal settings and measured beam widths by the simulation is very well achieved. Thus, the simulated profiles are validated to become a critical component of the base data for the clinical TPS.

The enlarged deviation close to the beamline could originate from secondaries produced by high Z components in the beamline, as interaction cross-sections for these might not be known accurately enough in FLUKA for these materials [17]. Another contribution could originate from beam optics that were not considered in the FLUKA simulation. Further investigations have been made regarding deviations in shape.

4.2 Beam Shape

A systematic deviation in the order of $10^{-3}D_{max}$ is well visible in the profiles obtained at position "-85 cm". The measured profiles seem to have a second Gaussian envelope, which the simulation does not fully reproduce. Two solutions would be possible: An improvement in the geometric representation of the high Z material in the beamline in FLUKA or the correction of the initial beam shape in vacuum. Introducing a double Gaussian (DG) beam shape in vacuum instead of the single Gaussian (SG) approach used for the database improved the match between simulated and measured lateral beam profiles. The estimated parameters for the double Gaussian were approximately equal to the weighted sum of the original single Gaussian with a 6.5-8.0% contribution of a second Gaussian. The second Gaussian had an FWHM between 2 and 4 times the FWHM of the first Gaussian. With the double Gaussian approach matched to isocentric measurement, the shape deviations at other measurement positions in air were reduced, as shown for the same three energies in **Figure 5**. For further investigation in water, we used a dedicated water tank provided by PTB (Physikalisch-Technische Bundesanstalt, Braunschweig, Germany). This water tank includes a

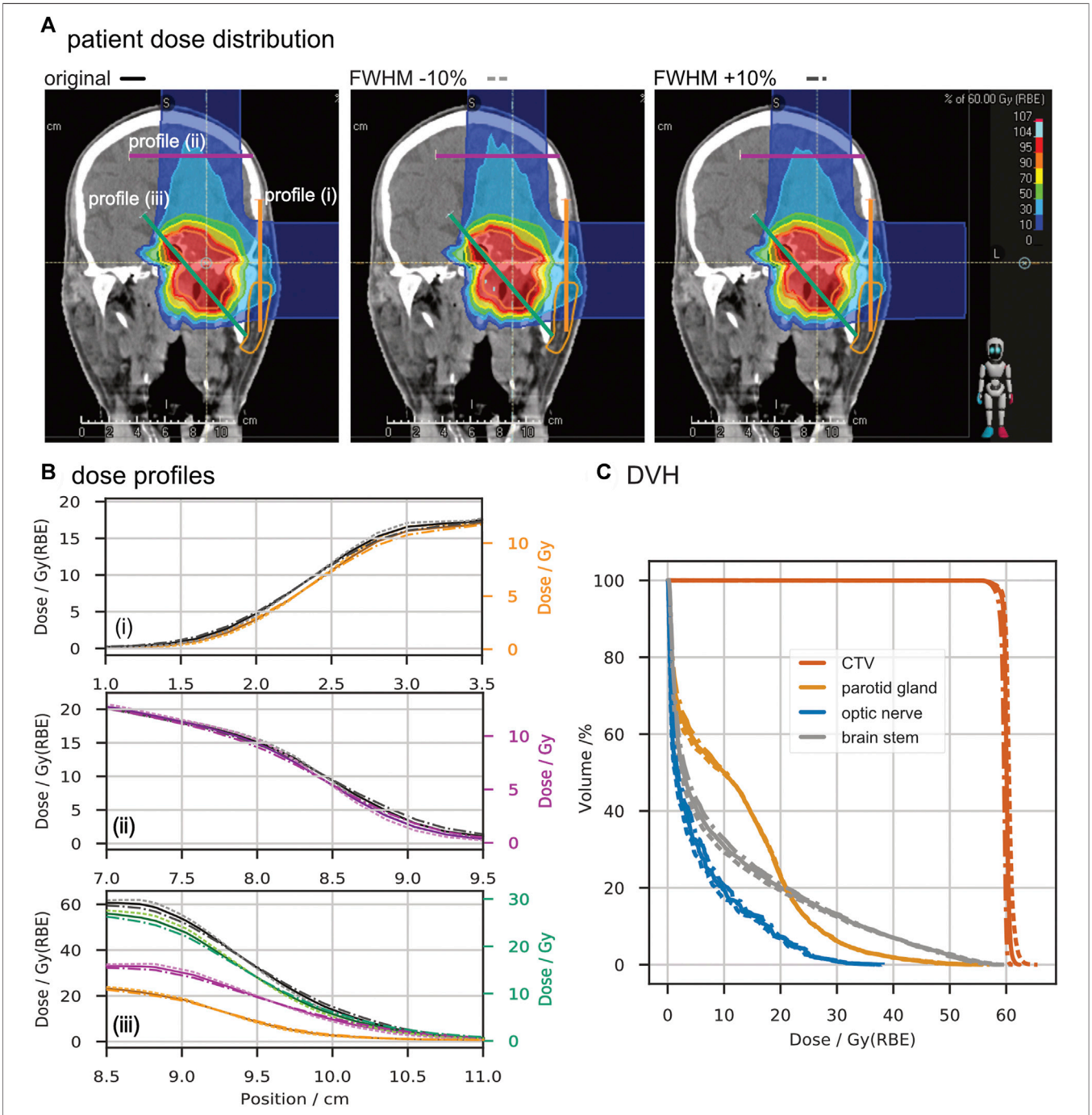

FIGURE 4 | Comparison of a patient treatment plan with a change of ∓10% in beamwidth. Panel **(A)** shows screenshots of the dose distribution in the TPS with lines marked for profile extraction. Panel **(B)** depicts the extracted profiles in units of biologically equivalent dose (Gy (RBE)) and absorbed dose (Gy). From top to bottom, the entrance profile of the superior treatment field (i), the entrance profile of the lateral treatment field (ii), and a profile through the target volume (iii) are drawn. Panel **(C)** shows the dose-volume histograms for the clinical target volume (CTV) and critical organs (parotid gland, optic nerve, and brain stem) obtained from the three scenarios. In panels **(B)** and **(C)**, solid lines represent data of the original plan, dotted lines depict the data with reduced beamwidth, and dash-dotted lines represent the increased beamwidth.

motorized PMMA-sleeve for detector accommodation. With the entrance window placed at the isocenter of the treatment room, profiles at about five positions around the maximum dose of each investigated energy were measured for each investigated beam. MC scoring of the lateral dose distribution in water was obtained in a water cylinder ($r = 14$ cm, $z = 32$ cm, $\Delta z = 0.1$ mm and $\Delta r = 0.5$ mm) behind the isocenter summing over the azimuthal angle. **Figure 6**

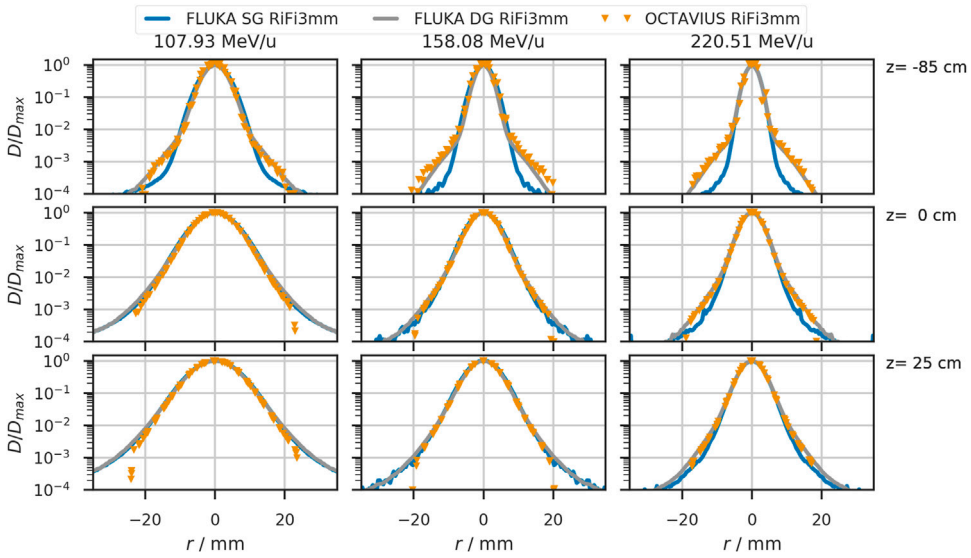

FIGURE 5 | Lateral beam profiles in air for helium beams with initial beam energies of 107.93 MeV/u, 158.08 MeV/u, and 220.51 MeV/u. The solid blue line shows the simulated profiles with a single Gaussian (SG) in vacuum. Orange triangles depict profiles obtained from the OCTAVIUS chamber array at indicated depth z. The grey line shows the profiles obtained from simulation with a double Gaussian (DG) beam profile in vacuum. Positions at which the detector was placed relative to the treatment room's isocenter are indicated on the right of each row.

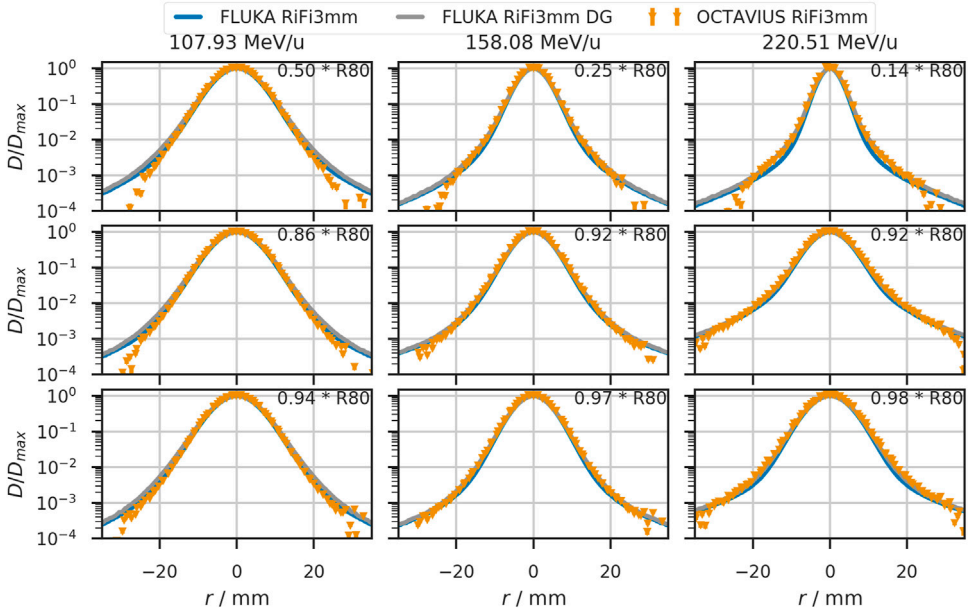

FIGURE 6 | Lateral beam profiles in water for helium beams with initial beam energies of 107.93 MeV/u, 158.08 MeV/u, and 220.51 MeV/u. The solid blue line shows the simulated profiles with a single Gaussian (SG) in vacuum. Orange triangles depict profiles obtained from the OCTAVIUS chamber array at indicated depth z. The grey line shows the profiles obtained from simulation with a double Gaussian (DG) beam profile in vacuum. Detector positions are given relative to the distal 80% range of the depicted beam.

shows that the double gaussian approach improves the agreement between simulations and measurements even in water.

4.3 Comparison to Other Ions

To compare the width evolution of the three available ions, the beamwidth is plotted against the detector positions for three beam energies of comparables ranges (approx. 8.8 cm in water) in **Figure 7**. The beam is simulated as a single Gaussian profile in vacuum, with the FWHM being 5.55 mm (6.17 mm, 4.95 mm) for helium (protons and carbon ions), corresponding to the smallest clinical beamwidth.

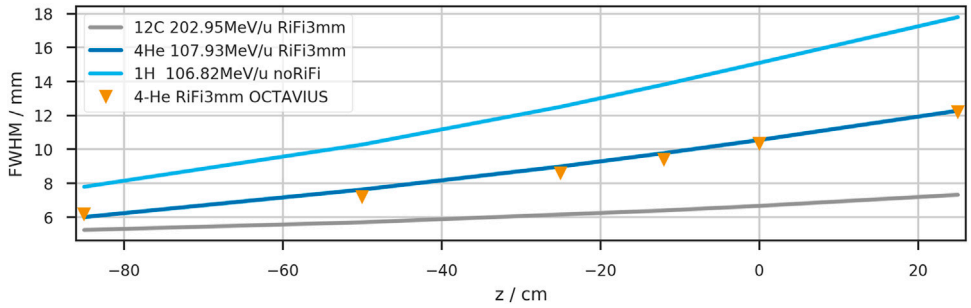

FIGURE 7 | Depth dependency of the beam width (FWHM) in air for three therapeutically available ions. The initial beamwidth in vacuum was chosen to reproduce the nominal accelerator settings at z = 0 cm when the RiFi is not inserted.

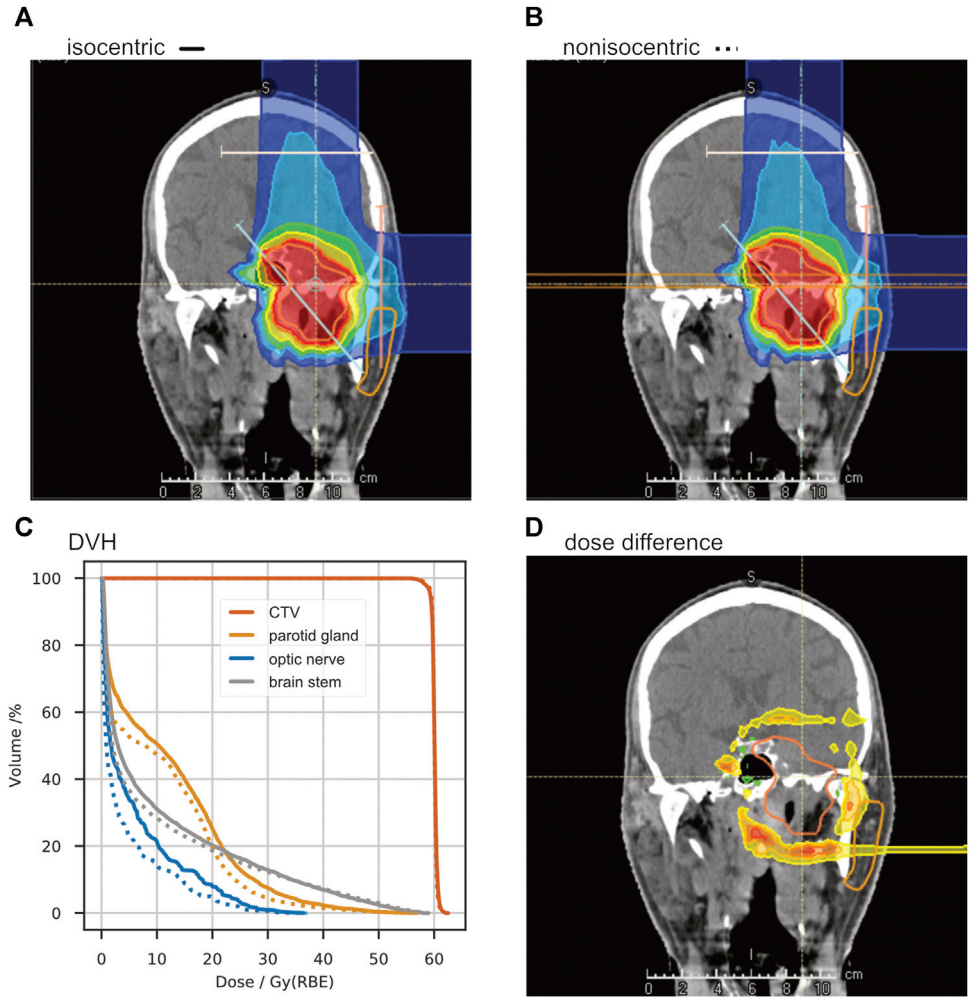

FIGURE 8 | A study of non-isocentric treatment planning. Panel **(A)** shows the dose distribution of a "standard" treatment plan with the room's isocenter in the target volume. With the same beam angles, another treatment plan was optimized with the patient placed as close as possible to the treatment nozzle, reducing the air gap to about 20 cm **(B)**. The dose-volume-histogram in panel **(C)** shows a significant dose reduction in the organs at risk (ipsilateral parotid gland, contralateral optic nerve, and brainstem). The absolute dose difference is shown in panel **(D)**.

While the carbon beam shows minor widening in the air gap (39% increase from −85 cm to +25 cm), the proton width increases by 228%. The helium beamwidth increases by 204% in the same air distance. Between vacuum and isocenter, the beamwidth increases by 29% for carbon ions, 90% for helium ions, and 144% for protons.

4.4 Patient Case

With the variation of the beamwidth by ∓10% FWHM, the differences in field profiles and DVH are minor, as depicted in **Figure 4**. This observation is in line with the clinical intervention limits of +25% and −15% deviation from tabulated widths. Thus, we have shown for this specific case that variations up to approximately 10% in the beamwidths do not critically impact dose conformity and lateral organs at risk.

To further exploit the fact that the beamwidth is much smaller with reduced air gap and the lateral profiles' implementation into the TPS, we performed a second patient plan investigation positioning the patient much closer to the beam exit and reducing the air gap. At MedAustron in Wiener Neustadt, Austria, a similar approach of non-isocentric treatment planning has already been commissioned for protons [36, 37].

This approach enables a dose reduction – in the organs at risk lateral to the treatment field – by decreasing the beamwidth at the patient entrance point. **Figure 8** shows the differences in dose distribution for the same slice as **Figure 4**. In the right (contralateral) optic nerve, a reduction of $D_{50\%}$ from 1.71 to 0.89 Gy (RBE) is achieved and the $D_{50\%}$ in the left (ipsilateral) parotid gland can be reduced from 10.34 to 7.71Gy (RBE). In the brain stem the $D_{50\%}$ could be reduced by 31% from 2.94 to 2.04 Gy (RBE), whereas the target coverage remains the same. The maximum dose received by the three OARs remains approximately unchanged. There is no visible change in the DVH for the CTV in panel (C), which is expected since the plan was reoptimized for the reduced air gap.

5 CONCLUSION AND OUTLOOK

In summary, our accurate simulation and measurement of beam profiles in air along the beam path led to a more precise TPS beam model which has been applied for the first patient irradiation with helium ions at HIT.

While other groups have investigated the effect of airgaps in a phantom [16], we can now provide a precise representation of the beam characteristics between beamline exit and entering any patient or phantom. The commercial TPS and any experimental investigations rely on energy and setting-specific MC beam model to calculate dose and particle distributions in phantoms placed downstream of the beamline exit.

In principle, the gained knowledge affords greater freedom in patient positioning along the beam axis. Since the helium beam broadens in air, not as much as protons but significantly more than the carbon beam, a reduced air gap would be favorable if critical organs are in lateral proximity to the beam axis. However, routine non-isocentric treatment planning would require a patient positioning and alignment system that is as precise close to the beam exit as it is in the treatment room's isocenter.

As expected, the broadening of the helium ion beam is intermediate between that of protons and carbon ions. With a complete representation of all available beam energies in the FLUKA simulation framework, we were able to quantify the broadening and directly compare available beamwidths for specific ranges and positions along the beam axis.

Regarding the good results while looking at the scenario of beamwidth variation in **Section 3.2**, the clinical approach to ensure a good field homogeneity with a spot spacing smaller than 1/3 width of the unmodified beam seems sufficient for helium ions and agrees with previous studies for protons and carbon ions [20].

For even better accuracy of the TPS, non-Gaussian beam shapes in vacuum could be investigated further. Then, the asymmetric shapes created by the particle extraction from the accelerator could be accounted for. With the observed agreements between measurement and simulation in the setup at HIT, airgaps smaller than about 50 cm would most likely benefit from such a further investigation.

The beamwidth of the helium ion beam would reduce further if the ripple filter had been removed from the beamline. This would, however, require the measurement and simulation of an entire additional database with depth dose curves, lateral profiles, absolute dosimetry, and secondary particle spectra. The treatment time for each patient field would also increase.

Together with measured depth dose curves, the lateral dose distributions reported in this paper add another milestone in the development of the physical beam model for raster-scanned helium ions. With the MC model verified against measurements and particle spectra for biological equivalent dose calculation [24] simulated, the first clinical TPS for helium ions is finished. So, after the first clinical trials with helium ion beams at the LBNL observed positive outcomes, especially for patients with small tumors, such as uveal melanoma [2], we now have the means to restart helium ion therapy with raster scanning beam technology.

DATA AVAILABILITY STATEMENT

The raw data supporting the conclusions of this article will be made available by the authors, without undue reservation.

AUTHOR CONTRIBUTIONS

TT gave substantial scientific advice and created the patient treatment plans. AM contributed to the conception and design of the study and pre-optimized the initial beamwidths for helium. SM pre-optimized the initial beamwidths for carbon. BK pre-optimized the lateral profiles for the proton beam. JB performed the analysis and most measurements, simulated the

last version of the helium base data, recalculated the proton and carbon profiles, and wrote the manuscript. All authors contributed to manuscript revision, read, and approved the submitted version.

FUNDING

JB's position is funded via grant NCT3.0-2015.22 BioDose.

ACKNOWLEDGMENTS

Thanks to Stephan Brons from the HIT medical physics team for performing additional measurements with all available beam foci of the helium beam; Amir Abdollahi for providing the research position in his group and Jürgen Debus for being the principal scientific advisor to the Ph.D. project of JB.

REFERENCES

1. Lyman JT, Howard J. Dosimetry and Instrumentation for Helium and Heavy Ions. *Int J Radiat Oncol Biol Phys* (1977) 3:81–5. doi:10.1016/0360-3016(77)90231-0
2. Castro JR, Char DH, Petti PL, Daftari IK, Quivey JM, Singh RP, et al. 15 Years Experience with Helium Ion Radiotherapy for Uveal Melanoma. *Int J Radiat Oncol Biol Phys* (1997) 39(5):989–96. doi:10.1016/s0360-3016(97)00494-x
3. Castro JR. Results of Heavy Ion Radiotherapy. *Radiat Environ Biophys* (1995) 34:45–8. doi:10.1007/BF01210545
4. Jermann M. Particle Therapy Statistics in 2014. *Int J Part Ther* (2015) 2(1):50–4. doi:10.14338/ijpt-15-00013
5. Saunders W, Castro JR, Chen GTY, Collier JM, Zink SR, Pitluck S, et al. Helium-Ion Radiation Therapy at the Lawrence Berkeley Laboratory: Recent Results of a Northern California Oncology Group Clinical Trial. *Radiat Res* (1985) 104:S227–34. doi:10.2307/3576652
6. Saunders WM, Char DH, Quivey JM, Castro JR, Chen GT, Collier JM, et al. Precision, High Dose Radiotherapy: Helium Ion Treatment of Uveal Melanoma. *Int J Radiat Oncol Biol Phys* (1985) 11(2):227–33. doi:10.1016/0360-3016(85)90143-9
7. Haberer T, Becher W, Schardt D, Kraft G. Magnetic Scanning System for Heavy Ion Therapy. *Nucl Instr Methods Phys Res Section A: Acc Spectrometers, Detectors Associated Equipment* (1993) 330(1-2):296–305. doi:10.1016/0168-9002(93)91335-k
8. Germany's Heidelberg University Hospital will become the world's first cancer center to use RayStation for helium ion therapy planning (2021). URL: https://www.raysearchlabs.com/media/press-releases/2020/germanys-heidelberg-university-hospital-will-become-the-worlds-first-cancer-center-to-use-raystation-for-helium-ion-therapy-planning/. (Accessed December 2, 2021).
9. Tessonnier T, Böhlen TT, Ceruti F, Ferrari A, Sala P, Brons S, et al. Dosimetric Verification in Water of a Monte Carlo Treatment Planning Tool for Proton, Helium, Carbon and Oxygen Ion Beams at the Heidelberg Ion Beam Therapy center. *Phys Med Biol* (2017) 62:6579–94. doi:10.1088/1361-6560/aa7be4
10. Tessonnier T, Mairani A, Brons S, Sala P, Cerutti F, Ferrari A, et al. Helium Ions at the Heidelberg Ion Beam Therapy center: Comparisons between FLUKA Monte Carlo Code Predictions and Dosimetric Measurements. *Phys Med Biol* (2017) 62:6784–803. doi:10.1088/1361-6560/aa7b12
11. Tessonnier T, Mairani A, Brons S, Haberer T, Debus J, Parodi K. Experimental Dosimetric Comparison of 1H, 4H, 12C and 16O Scanned Ion Beams. *Phys Med Biol* (2017) 62:3958–82. doi:10.1088/1361-6560/aa6516
12. Parodi K, Mairani A, Brons S, Hasch BG, Sommerer F, Naumann J, et al. Monte Carlo Simulations to Support Start-Up and Treatment Planning of Scanned Proton and Carbon Ion Therapy at a Synchrotron-Based Facility. *Phys Med Biol* (2012) 57:3759–84. doi:10.1088/0031-9155/57/12/3759
13. Böhlen TT, Cerutti F, Chin MPW, Fassò A, Ferrari A, Ortega PG, et al. The FLUKA Code: Developments and Challenges for High Energy and Medical Applications. *Nucl Data Sheets* (2014) 120:211–4. doi:10.1016/j.nds.2014.07.049
14. Ferrari A, Sala PR, Fassó A, Ranft J. FLUKA: a Multi-Particle Transport Code (2005). Available From: http://www.slac.stanford.edu/pubs/slacreports/reports16/slac-r-773.pdf. doi:10.2172/877507
15. Horst F, Aricò G, Brinkmann K-T, Brons S, Ferrari A, Haberer T, et al. Measurement of He4 Charge- and Mass-Changing Cross Sections on H, C, O, and Si Targets in the Energy Range 70-220 MeV/u for Radiation Transport Calculations in Ion-Beam Therapy. *Phys Rev C* (2019) 99:1. doi:10.1103/physrevc.99.014603
16. Gallas RR, Arico G, Burigo LN, Gehrke T, Jakůbek J, Granja C, et al. A Novel Method for Assessment of Fragmentation and Beam-Material Interactions in Helium Ion Radiotherapy with a Miniaturized Setup. *Physica Med* (2017) 42:116–26. doi:10.1016/j.ejmp.2017.09.126
17. Norbury JW, Battistoni G, Besuglow J, Bocchini L, Boscolo D, Botvina A, et al. Are Further Cross Section Measurements Necessary for Space Radiation Protection or Ion Therapy Applications? Helium Projectiles. *Front Phys* (2020) 8:409. doi:10.3389/fphy.2020.565954
18. Weber U, Kraft G. Comparison of Carbon Ions versus Protons. *Cancer J* (2009) 15(4):325–32. doi:10.1097/ppo.0b013e3181b01935
19. Uhl M, Herfarth K, Debus J. Comparing the Use of Protons and Carbon Ions for Treatment. *Cancer J* (2014) 20(6):433–9. doi:10.1097/ppo.0000000000000078
20. Parodi K, Mairani A, Brons S, Naumann J, Krämer M, Sommerer F, et al. The Influence of Lateral Beam Profile Modifications in Scanned Proton and Carbon Ion Therapy: a Monte Carlo Study. *Phys Med Biol* (2010) 55:5169–87. doi:10.1088/0031-9155/55/17/018
21. Parodi K, Mairani A, Sommerer F. Monte Carlo-Based Parametrization of the Lateral Dose Spread for Clinical Treatment Planning of Scanned Proton and Carbon Ion Beams. *J Radiat Res* (2013) 54(suppl_1):i91–i96. doi:10.1093/jrr/rrt051
22. Schwaab J, Brons S, Fieres J, Parodi K. Experimental Characterization of Lateral Profiles of Scanned Proton and Carbon Ion Pencil Beams for Improved Beam Models in Ion Therapy Treatment Planning. *Phys Med Biol* (2011) 56:7813–27. doi:10.1088/0031-9155/56/24/009
23. Krämer M, Jäkel O, Haberer T, Kraft G, Schardt D, Weber U. Treatment Planning for Heavy-Ion Radiotherapy: Physical Beam Model and Dose Optimization. *Phys Med Biol* (2000) 45:3299–317. doi:10.1088/0031-9155/45/11/313
24. Kopp B, Mein S, Tessonnier T, Besuglow J, Harrabi S, Heim E, et al. Rapid Effective Dose Calculation for Raster-Scanning 4He Ion Therapy with the Modified Microdosimetric Kinetic Model (mMKM). *Physica Med* (2021) 81:273–84. doi:10.1016/j.ejmp.2020.11.028
25. Schardt D, Elsässer T, Schulz-Ertner D. Heavy-ion Tumor Therapy: Physical and Radiobiological Benefits. *Rev Mod Phys* (2010) 82(1):383–425. doi:10.1103/revmodphys.82.383
26. Highland VL. Some Practical Remarks on Multiple Scattering. *Nucl Instr Methods* (1975) 129(2):497–9. doi:10.1016/0029-554x(75)90743-0
27. Highland VL. Erratum: Some Practical Remarks on Multiple Scattering. *Nucl Instr Methods* (1979) 161(1):171. doi:10.1016/0029-554x(79)90379-3
28. Scott WT. The Theory of Small-Angle Multiple Scattering of Fast Charged Particles. *Rev Mod Phys* (1963) 35(2):231–313. doi:10.1103/RevModPhys.35.231
29. Molière G. Theorie der Streuung schneller geladener Teilchen. III Die Vielfachstreuung von Bahnspuren unter Berücksichtigung der statistischen Kopplung. *Z für Naturforschung A* (1955) 10(3):177–211. doi:10.1515/zna-1955-0301
30. Hollmark M, Gudowska I, Belkić D, Brahme A, Sobolevsky N. An Analytical Model for Light Ion Pencil Beam Dose Distributions: Multiple Scattering of Primary and Secondary Ions. *Phys Med Biol* (2008) 53:3477–91. doi:10.1088/0031-9155/53/13/005
31. Würl M, Englbrecht F, Parodi K, Hillbrand M. Dosimetric Impact of the Low-Dose Envelope of Scanned Proton Beams at a ProBeam Facility: Comparison of Measurements with TPS and MC Calculations. *Phys Med Biol* (2016) 61:958–973. doi:10.1088/0031-9155/61/2/958

32. Ondreka D, Weinrich U. The Heidelberg Ion Therapy (HIT) Accelerator Coming into Operation. *Conf Proc C* (2008):0806233. Available from: https://accelconf.web.cern.ch/e08/papers/tuocg01.pdf (Accessed December 2, 2021).
33. Schoemers C, Feldmeier E, Naumann J, Panse R, Peters A, Haberer T. The Intensity Feedback System at Heidelberg Ion-Beam Therapy Centre. *Nucl Instr Methods Phys Res Section A: Acc Spectrometers, Detectors Associated Equipment* (2015) 795:92–9. doi:10.1016/j.nima.2015.05.054
34. Weber U, Kraft G. Design and Construction of a Ripple Filter for a Smoothed Depth Dose Distribution in Conformal Particle Therapy. *Phys Med Biol* (1999) 44 (11):2765–75. doi:10.1088/0031-9155/44/11/306
35. Krämer M, Scholz M. Treatment Planning for Heavy-Ion Radiotherapy: Calculation and Optimization of Biologically Effective Dose. *Phys Med Biol* (2000) 45 (11):3319–30. doi:10.1088/0031-9155/45/11/314
36. Elia A, Resch AF, Carlino A, Böhlen TT, Fuchs H, Palmans H, et al. A GATE/Geant4 Beam Model for the MedAustron Non-isocentric Proton Treatment Plans Quality Assurance. *Physica Med* (2020) 71:115–23. doi:10.1016/j.ejmp.2020.02.006
37. Carlino A, Böhlen T, Vatnitsky S, Grevillot L, Osorio J, Dreindl R, et al. Commissioning of Pencil Beam and Monte Carlo Dose Engines for Non-isocentric Treatments in Scanned Proton Beam Therapy. *Phys Med Biol* (2019) 64:17NT01. doi:10.1088/1361-6560/ab3557

Conflict of Interest: The authors declare that the research was conducted in the absence of any commercial or financial relationships that could be construed as a potential conflict of interest.

NOMENCLATURE

BAMS active beam monitoring system consisting of three transmission ionization chambers and two multi-wire proportional chambers in the beamline downstream of the vacuum pipe

CTV clinical target volume

contralateral on the opposite side of a person's body

$D_{xx\%}$ dose received by at least xx% of the volume

DVH dose volume histogram

FLUKA an MC code to simulate particle propagation through material

FWHM full width half maximum

iDDD laterally integrated depth dose distribution, typically integrated over radii matching the sensitive region of the used detector, or infinity.

ipsilateral on the same side of a person's body

irradiation or treatment plan a set of beam angles and energy-specific particle intensity maps necessary to achieve the desired dose distribution in a patient or phantom

LIBC accelerator library containing nominal beam energies, beamwidths and intensity settings

MC Monte Carlo

mMKM modified microdosimetric-kinetic model

noRiFi no ripple filter in the beamline

OAR organ at risk

patient entrance point the point of the patient that is closest to the beamline at a given patient position

penumbra lateral fall-off in the dose distribution accumulated by all irradiated spots of an irradiated field, typically defined as the distance between 80 and 20% isodose line perpendicular to the beam direction.

PMMA Polymethylmethacrylate

PTB Physikalisch Technische Bundesanstalt

range (R80) distal point along the depth dose curve at which 80% of the maximal dose is reached

RaShi range shifter

RiFi3mm ripple filter

spot one point in the plane perpendicular to the beam axis aimed at by a single pencil beam of the raster scanning system

slice a slice in a CT scan refers to a two-dimensional plane extracted from a three-dimensional image volume

TPS treatment planning system

width FHWM of the lateral beam profile at any given point along the beam

5 Second Publication: Commissioning of Helium Ion Therapy and the First Patient Treatment With Active Beam Delivery

Authors: Thomas Tessonnier, Swantje Ecker, **Judith Besuglow**, Jakob Naumann, Stewart Mein, Friderike K. Longarino, Malte Ellerbrock, Benjamin Ackermann, Marcus Winter, Stephan Brons, Abdalla Qubballah, Thomas Haberer, Jürgen Debus, Oliver Jäkel, Andrea Mairani
Publication status: Received 28 July 2022, Accepted 9 January 2023, Available online 19 January 2023, Version of Record 22 June 2023.
Journal reference: International Journal of Radiation Oncology • Biology • Physics, Volume 116, Issue 4, 15 July 2023, Pages 935-948
DOI: 10.1016/j.ijrobp.2023.01.015

Authors' contributions: **JB** is co-author of this publication. **JB** performed measurements and simulations for the input database, which was used to create the physical beam model in the analytical pencil beam (APB) dose engine for two room models, see Table 1 of this publication. Specifically these were:

- Measurement of integral depth dose distributions (IDDs) in water for 24 energies within the therapeutic range from a minimum of 50.57 MeV u^{-1} to a maximum of 220.51 MeV u^{-1} with the PEAKFINDER® water column (PTW, Freiburg)
- Measurement of lateral dose distributions in air at 6 different positions relative to the room isocentre with and without ripple filter in two rooms
- Measurement of the room specific monitor calibrations with square spot pattern
- FLUKA simulations of lateral profiles in air for 16 energies and comparing them to measurements acquired with a 2-dimensional IC array (OCTAVIUS® 1000 SRS P air filled prototype, PTW, Freiburg).

Towards the commissioning of the APB, **JB** performed the following tasks

- Creation of FLUKA-DB
- FLUKA simulations of IDDs for 2 rooms of all 255 energies

- An initial verification of spread-out Bragg peaks with FLUKA dose engine, before APB was validated
- Generation of mMKM z^*_{1D} tables for $(\alpha/\beta)_x = 2\,\mathrm{Gy}$ (AB2), for $\beta_x = 0.025\,\mathrm{Gy}^{-2}$
- Creation of FRoG mMKM database for RBE prediction verification

INTERNATIONAL JOURNAL OF
RADIATION ONCOLOGY • BIOLOGY • PHYSICS
www.redjournal.org

PHYSICS CONTRIBUTION

Commissioning of Helium Ion Therapy and the First Patient Treatment With Active Beam Delivery

Thomas Tessonnier, PhD,[*,†,‡] Swantje Ecker, MSc,[*] Judith Besuglow, MSc,[†,‡,§,‖] Jakob Naumann, PhD,[*] Stewart Mein, PhD,[†,‡,§,¶] Friderike K. Longarino, MSc,[†,‡,§,‖] Malte Ellerbrock, PhD,[*] Benjamin Ackermann, MSc,[*] Marcus Winter, PhD,[*] Stephan Brons, PhD,[*] Abdallah Qubala, MSc,[*,‡,#] Thomas Haberer, PhD,[*] Jürgen Debus, MD, PhD,[*,†,‡,§,¶] Oliver Jäkel, PhD,[*,‡,**] and Andrea Mairani,[*,†,‡,††]

[*]*Heidelberg Ion-Beam Therapy Center, Department of Radiation Oncology, Heidelberg University Hospital, Heidelberg, Germany;* [†]*Clinical Cooperation Unit Radiation Oncology, National Center for Tumor Diseases, Heidelberg University Hospital and German Cancer Research Center, Heidelberg, Germany;* [‡]*Heidelberg Institute of Radiation Oncology in the National Center for Radiation Oncology, Heidelberg, Germany;* [§]*Division of Molecular and Translational Radiation Oncology, Department of Radiation Oncology, Heidelberg Faculty of Medicine and Heidelberg University Hospital, Heidelberg Ion-Beam Therapy Center, Heidelberg, Germany;* [‖]*Department of Physics and Astronomy, Heidelberg University, Germany;* [¶]*German Cancer Consortium Core-Center Heidelberg, German Cancer Research Center, Heidelberg, Germany;* [#]*Faculty of Medicine, University of Heidelberg, Heidelberg, Germany;* [**]*German Cancer Research Center, Heidelberg, Germany; and* [††]*National Centre of Oncological Hadrontherapy, Medical Physics, Pavia, Italy*

Received Jul 28, 2022; Accepted for publication Jan 9, 2023

Purpose: Helium ions offer intermediate physical and biological properties to the clinically used protons and carbon ions. This work presents the commissioning of the first clinical treatment planning system (TPS) for helium ion therapy with active beam delivery to prepare the first patients' treatment at the Heidelberg Ion-Beam Therapy Center (HIT).

Methods and Materials: Through collaboration between RaySearch Laboratories and HIT, absorbed and relative biological effectiveness (RBE)-weighted calculation methods were integrated for helium ion beam therapy with raster-scanned delivery in the TPS RayStation. At HIT, a modified microdosimetric kinetic biological model was chosen as reference biological model. TPS absorbed dose predictions were compared against measurements with several devices, using phantoms of different complexities, from homogeneous to heterogeneous anthropomorphic phantoms. RBE and RBE-weighted dose predictions of the

Corresponding authors: Oliver Jäkel, PhD; and Andrea Mairani, PhD; E-mails: Oliver.Jaekel@med.uni-heidelberg.de, Andrea.Mairani@med.uni-heidelberg.de

Oliver Jäkel and Andrea Mairani made equal contributions to this study.

S. Ecker is currently at Städttisches Klinikum Karlsruhe, medical physics department, Karlsruhe, Germany.

This work was supported by the Dietmar-Hopp foundation and the Klaus-Tschira foundation as well as by intramural funds from National Center for Tumor diseases (NCT3.0_2015.21/22 NCT-PRO and Biodose programs). The funders had no role in study design, data collection and analysis, decision to publish or preparation of the manuscript.

Disclosures: J.D. reports grants from the following: the Clinical Research Institute, View Ray Inc., Accuray International, Accuray Incorporated, RaySearch Laboratories AB, Vision RT Limited, Merck Serono GmbH, Astellas Pharma GmbH, AstraZeneca GmbH, Siemens Healthcare GmbH, Solution Akademie GmbH, Eromed PLC Surrey Research Park, Quintiles GmbH, Pharmaceutical Research Associates GmbH, Boehringer Ingelheim Pharma GmbH Co, PTW-Freiburg Dr Pychlau GmbH, and Nanobiotix.

Research data are stored in an institutional repository and will be shared upon request to the corresponding author.

Ethical statement: The project was performed following institutional guidelines and the Declaration of Helsinki of 1975 in its most recent version (64th WMA General Assembly, Fortaleza, Brazil, October 2013). Patient confidentiality was maintained by anonymizing patient data to remove any identifying information. Written informed consent for the usage of patient data for research was handed to the patient. The patient was treated individually and was not part of a prospective trial requiring approval from the ethics committee of the University of Heidelberg.

Supplementary material associated with this article can be found in the online version at doi:10.1016/j.ijrobp.2023.01.015.

Acknowledgments—The authors acknowledge Dr Kopp and Dr Harrabi for the fruitful discussions and support along this work.

Int J Radiation Oncol Biol Phys, Vol. 116, No. 4, pp. 935–948, 2023
0360-3016/$ - see front matter
https://doi.org/10.1016/j.ijrobp.2023.01.015

TPS were verified against calculations with an independent RBE-weighted dose engine. The patient-specific quality assurance of the first treatment at HIT using helium ion beam with raster-scanned delivery is presented considering standard patient-specific measurements in a water phantom and 2 independent dose calculations with a Monte Carlo or an analytical-based engine.
Results: TPS predictions were consistent with dosimetric measurements and independent dose engines computations for absorbed and RBE-weighted doses. The mean difference between dose measurements to the TPS calculation was 0.2% for spread-out Bragg peaks in water. Verification of the first patient treatment TPS predictions against independent engines for both absorbed and RBE-weighted doses presents differences within 2% in the target and with a maximum deviation of 3.5% in the investigated critical regions of interest.
Conclusions: Helium ion beam therapy has been successfully commissioned and introduced into clinical use. Through comprehensive validation of the absorbed and RBE-weighted dose predictions of the RayStation TPS, the first clinical TPS for helium ion therapy using raster-scanned delivery was employed to plan the first helium patient treatment at HIT.

Introduction

Three decades after the end of the Lawrence Berkeley National Laboratory (LBNL) clinical program with helium ion beams[1,2] the first patient treatment with raster-scanned helium ions was performed in July 2021[3,4] at the Heidelberg Ion-Beam Therapy Center (HIT).[5] Over the last decade, several works have investigated helium ions in preparation for their possible return into clinical practice.[3,4,6-20]

Recent investigations have characterized the dosimetric properties of helium ion beams with respect to current particle therapy technologies with active beam delivery.[13-17,21] Compared to proton therapy, helium ions present advantageous physical properties because of their increased mass with reduced lateral scattering and sharper distal fall-off, promising enhanced target coverage and conformity with a reduction in dose to surrounding healthy tissues. Helium ions exhibit a relatively high linear energy transfer (LET) compared to the LET of protons. This suggests that during treatment planning, spatial variations in relative biological effectiveness (RBE) along the Bragg peak should be considered, in contrast to the clinical assumption of a constant RBE for protons. RBE dependencies of helium ions have been investigated in several works[16,22] under different set-ups (ie, various cell lines, doses, and LET levels). More recently, an in vivo study of the biological effect of helium ion beams in normal tissue (rat spinal cord) was performed with single- and split-dose irradiation.[18] Several biological models[23] have been reported in the literature to reproduce these data, with an additional focus on assessing model uncertainties on RBE predictions. Carbon ion beams, on the other hand, exhibit larger LET and RBE variations, with 20% to 30% uncertainty in clinical RBE prediction.[24] With a lower LET, uncertainty in RBE prediction for helium ion beams in clinical-like scenarios is expected to be smaller.[16,19]

Considering these enhanced physical properties compared to protons, as well as the reduced fragmentation tail, lower LET variations and reduced RBE uncertainty compared to carbon ions,[4,6,13,20] helium ion therapy should be considered as a promising therapeutic tool in the treatment of deep-seated solid tumors. Among the indications, helium ion therapy could be particularly useful for in treating pediatric patients and reirradiation cases.[4,7] For treating pediatric patients, application of carbon ion radiation therapy is clinically disputed because of the possible increased risk of late treatment-related secondary malignancies due to the fragmentation tail. Proton therapy could also lead to an increased risk of adverse events (eg, secondary malignancies, cognitive and endocrine dysfunctions) compared with helium ion therapy from higher doses in the surrounding healthy tissues.

A recent roadmap[4] presents the different research efforts in physics and biology to reintroduce helium ion therapy into the modern-day clinic. In-silico treatment planning studies have investigated the possible advantages of helium ion therapy compared to proton therapy[7-9] with Monte Carlo (MC) or analytical pencil beam dose engine (APB) platforms since no clinical treatment planning system (TPS) was yet available to perform preclinical patient planning. A collaboration between industry (RaySearch Laboratories) and HIT led to the development of a clinical TPS (RayStation, RaySearch Laboratories, Stockholm) for helium ion beam therapy, enabling RBE-weighted dose calculation and optimization using variable RBE models.

This work presents the commissioning of the clinical TPS at HIT for raster-scanned helium ion therapy. It describes databases for physical and radiobiological modeling followed by dosimetric validations in water and complex phantoms. Biological validations are performed against independent calculations toward the first patient treatment verification (measurements and in-silico). Here, we present the first validation of a clinical TPS for helium ion therapy from commissioning to the first patient treatment plan verification.

Methods and Materials

Treatment planning system and input databases

The TPS RayStation is in clinical use at HIT for treatment planning with protons and carbon ions for both horizontal beam lines and gantry treatment rooms. Development, validation, and implementation of an APB for helium ions by

RaySearch Laboratories, with the collaboration of HIT, enabled dose computation for helium ion beams in the clinical version of the RayStation TPS (version 9B and superiors). The TPS version 10A was used for all the validations presented in this work.

The APB absorbed dose engine for helium ion beams (Pencil beam v4.1) performs calculations with integral depth dose kernels combined with a lateral dose profile in medium. To generate the physical beam model required for computation, several key input parameters were needed and generated from specific measurements or through MC simulations: integral depth dose distributions (IDD) in water, lateral dose distributions in air at different positions relative to the room isocenter, and a room-specific monitor calibration. In a similar fashion to carbon ions at HIT, a ripple filter was introduced at the end of the beam nozzle to broaden the Bragg peak. The acquisition of these data, together with specific room characteristics (gantry/table rotation, virtual source axis distance, maximum field size, range shifter description) led to the creation of 2 room models, one for the horizontal rooms and one for the gantry. This work focuses on the results for the commissioning of the horizontal rooms.

The IDDs in water were acquired experimentally for 24 energies within the therapeutic range from a minimum of 50.57 to a maximum of 220.51 MeV/u with the PeakFinder water column (PTW, Freiburg), equipped with 2 large Bragg peak plane-parallel ionization chambers (IC) of 4.08cm radius.[13] A summary of the acquired energies is presented in Table 1. The step sizes of the measurements were ranging from 50.00 mm to 0.05 mm, as a function of the position of the IC within the dose distribution.

The lateral dose distributions in air were provided for 16 energies at 6 different positions from the isocenter, from +850 mm (closer to the beam nozzle), +500 mm, +250 mm, +120 mm, 0 mm (isocenter) to −250 mm (away from the beam nozzle) (Table 1). Dedicated MC simulations using a detailed model of the beamline were performed using the FLUKA (FLUktuierende KAskade) code[25,26] (version 2021.1) to generate the air dose profiles. The generated data set was also compared with measurements acquired with a 2-dimensional IC array (OCTAVIUS 1000SRS − air-filled prototype, PTW, Freiburg). A dedicated separate work[10] presents in detail the generation of the air profile database and the comparisons between FLUKA MC code and measurements.

The monitor calibration in terms of the dose per primary helium ion under reference conditions was performed for 10 energies over the therapeutic energy range, according to the specifications of the TPS manufacturer. To characterize this dose/ion relationship, a reference plan of 8 × 8 cm^2, with a 2 mm spot spacing, was measured with an IC at depth in water of 0.5 cm to 20 cm. Following clinical practice, a constant spot spacing value is chosen for plan generation and correspond to ∼1/3 of the minimum beam width at isocenter allowed in the beam model, being here 6 mm. Thus, depending on the spot pattern, either a spot spacing of 2 mm is chosen (square spot pattern) or 2.4 mm (hexagonal spot pattern). The in-depth position of the IC in water for calibration was defined as 75% of the peak position (except for the 2 lowest and the highest energies). The IC used for the measurement was a pinpoint chamber (TM31015, PTW, Freiburg), calibrated by an accredited secondary standard dosimetry calibration laboratory and following the procedures for carbon ions[27] and using the k_Q-factor given in TRS-398.[28] A k_Q-factor of 1.026 was used consistently to the values used for both protons and carbon ions at HIT, this value was further confirmed with independent measurement with an advanced Markus chamber (PTW, Freiburg) presenting a k_Q-factor close to 1.00. Additional information can be found in Table 1.

The modified Microdosimetric Kinetic Model (mMKM) was selected as the reference radiobiological model[16,19,29] for helium ion therapy at HIT. Compared to the Local Effect Model 1 (LEM1) used in European particle therapy center for carbon ion therapy, mMKM more accurately predicts RBE value for lower LET particles, while LEM1 systematically overestimates the RBE.[16,24] To perform RBE-weighted dose calculation, several parameters must be considered in each voxel, including the absorbed dose, particle/energy spectra (ie, ion energy and fluence for all ion types), and the tissue type (commonly defined as α_x and β_x from the linear quadratic model for photon irradiation). The underlying particle spectrum (protons and helium ions) for each primary helium ion has been generated with FLUKA for 27 energies, representative of the clinical energy range (Table 1). The spectra were scored in water with a 1 mm bin size and an energy binning of 0.1 MeV/u from 0 to 500 MeV/u for secondary protons and 0 to 300 MeV/u for helium ions. Then, depending on the tissue-type, tables of the saturation-corrected mean specific energy of the domain delivered in a single event as a function of the mixed radiation field (mMKM z^*_{1D} table), were generated to predict the RBE.[16,19] z^*_{1D} tables were created for α_x/β_x = 2Gy (AB2), for β_x = 0.025 Gy^{-2}.

Physical validations

Beam modeling

The computed physical beam model was compared against the measured input database following our standard protocol for commissioning.[30] RS-computed IDDs (1 mm dose grid), considering the finite size of the PeakFinder chambers, were compared with measurements in terms of range differences, mean dose-weighted and mean relative dose differences. Full-width half maximum (FWHM) differences between TPS predictions and input database were calculated and compared for the different lateral dose profiles in air. The verification of the absolute dosimetry for 9 energies (50.57, 56.44, 82.33, 107.93, 133.21, 158.08, 182.43, 201.71 and 220.51 MeV/u) was achieved through additional measurements with a Farmer chamber (PTW, Freiburg). The

Table 1 Description of the physical database inputs

		iE	1	6	11	13	21	22	28	31	33	41	46	51	56	61	67	71	80
		Energy (MeV/u)	**50.57**	**56.44**	**61.86**	**63.93**	**71.73**	**72.65**	**78.05**	**80.64**	**82.33**	**88.85**	**92.75**	**96.52**	**101.19**	**103.76**	**107.93**	**110.64**	**116.58**
Input	IDDs	PeakFinder (measurement)	X	X		X		X	X		X		X		X		X		X
	Lateral profiles in air	FLUKA (simulation)	X	X				X			X						X		
	Absolute dosimetry	PinPoint Chamber (measurement depth [cm])	X 0.5cm	X 0.5cm							X 3.7cm						X 6.3cm		
	Spectra	FLUKA (simulation)	X		X		X			X		X		X		X		X	
		iE	81	90	91	101	107	111	120	121	131	141	151	152	161	165	169	170	171
		Energy (MeV/u)	117.23	122.93	123.55	129.64	133.21	135.55	140.71	141.27	146.84	152.26	157.56	158.08	162.73	164.78	166.8	167.3	171.29
Input	IDDs	PeakFinder (measurement)		X			X		X			X		X		X			
	Lateral profiles in air	FLUKA (simulation)		X			X		X					X			X	X	
	Absolute dosimetry	PinPoint Chamber (measurement depth [cm])					X 9.3cm		X 10.3cm					X 12.7cm					
	Spectra	FLUKA (simulation)	X		X	X		X		X	X	X	X		X				X
		iE	180	181	191	198	200	201	210	211	221	226	231	235	240	241	251	255	
		Energy (MeV/u)	172.28	172.77	177.64	182.43	183.85	184.56	190.85	191.54	198.36	201.71	205.03	207.66	210.92	211.57	217.98	220.51	
Input	IDDs	PeakFinder (measurement)	X			X	X		X			X		X	X			X	
	Lateral profiles in air	FLUKA (simulation)	X			X			X			X						X	
	Absolute dosimetry	PinPoint Chamber (measurement depth [cm])				X 16.3cm						X 19.5cm						X 20cm	
	Spectra	FLUKA (simulation)		X	X			X		X	X		X			X	X	X	

The characteristics imported in the TPS are presented for each energy (iE): PeakFinder-measured IDDs, FLUKA-generated lateral profiles in air (position = +850 mm (closer to the beam nozzle), +500 mm, +250 mm, +120 mm, 0 mm (isocenter) to −250 mm (away from the beam nozzle)), Pinpoint chamber-measured absolute dosimetry calibration (and depth of calibration), FLUKA-generated mix-radiation field spectra.

Abbreviations: IDD, integral depth dose profile; iE, energy index; FLUKA, FLUktuierende KAskade Monte-Carlo engine; TPS, treatment planning system.

Farmer chamber was calibrated by an accredited dosimetry calibration laboratory and the same measurement procedure as for the pinpoint chamber was used. The measurements were performed at 0.5 cm depth equivalent in water for 10×10 cm^2 fields (2 mm spot spacing) and compared with the TPS predicted doses ($1 \times 1 \times 1$ mm^3 grid).

Spread-out Bragg peaks

Spread-out Bragg peaks (SOBP) in water were optimized in the TPS for small ($3 \times 3 \times 3$ cm^3), medium ($6 \times 6 \times 6$ cm^3), and large ($10 \times 10 \times 10$ cm^3) cube-shaped volumes, centered at different positions in water of 5, 12.5, 20, and 27 cm, respectively, for an absorbed dose of 1 Gy. A hexagonal spot pattern (2.4 mm spacing) and a 3.1 mm energy spacing were used. These parameters are set accordingly to the HIT clinical experience with protons and carbon ions using RayStation or SyngoPT (Siemens, Erlangen, Germany) were constant values for spot spacing and energy layer spacing (~2 or 3 mm depending the ions/target size and depth) are used. Furthermore, for the shallowest small and medium SOBPs, plans with a range shifter (RASHI) for airgaps of 5 or 20 cm were created. The final dose grid for all calculations was $1 \times 1 \times 1$ mm^3.

For each SOBP, measurements in a water phantom[31] (MP3, PTW, Freiburg) with a 24 pinpoint IC array were performed for several positions in depth, from phantom entrance to the tail. Lateral dose profiles were acquired at mid-SOBP. The step size for the measurements (in depth/lateral) depended on the position of the IC in the dose profile, with a step size down to 2 mm and 1 mm for the depth and lateral dose profiles, respectively. Measurements at different depths were used to assess dose accuracy of RS by comparing measured doses relative to the planned dose, taking only ICs in regions with a dose gradient <20 mGy/mm into account to avoid distortion of the results by setup uncertainties. Differences in the following geometric quantities of the SOBPs were reported: the proximal and distal in-depth positions of the 90% isodose of the planned dose; the lateral field size, defined as the 50% and 90% isodose; and the lateral and distal dose fall-off defined as the distance between the 80% and 20% isodoses.

Additional measurements were performed for the small- and medium-sized SOBPs with the 2-dimensional array for several positions in depth in water from 4.1 cm to 30.4 cm. Between 3 and 13 measurements were taken for each SOBP, with at least 2 measurements in the high dose region (mid and end of SOBP) and one measurement in the 50% distal fall-off region. Local γ-index analyses were performed using the VeriSoft software (v7.0, PTW, Freiburg) with 3%/1.5 mm (local dose difference and distance to agreement) criteria and a dose threshold of 5%. A stricter 1.5 mm distance to agreement was chosen in comparison with the commonly used 3 mm or 2 mm[32] because a larger value would overlook the possible differences in the sharp helium dose fall-off (lateral and distal).

Complex target volumes and beam modifiers

Complex shaped target volumes in water were optimized and measured with the water tank setup: cylindrical, spherical, U-shaped, and L-shaped targets. The targets were centered at 10 cm depth in water with an in-depth size of 6 cm for the cylindrical and spherical target or 3 cm for the U- and L-shaped ones. The lateral target size varied between 6 cm and 10 cm. For these more complex shaped targets, relative dose differences of measurements to TPS predictions were reported.

Double-wedge and anthropomorphic phantoms

A medium-sized SOBP centered at 5 cm in water was optimized behind a double-wedge PMMA phantom (30° and 60°) or an Alderson head phantom[33] (RANDO Alderson phantom, Radiology Support Devices, Long Beach, California). Measurements were performed in different depths and at lateral positions, as detailed for the SOBPs. Octavius measurements were performed as well in water. Analyses were done as performed for the SOBPs in water (MP3 and Octavius). Additional information can be found in Figure E1 and Table E1.

Additional Octavius measurements were performed with a body phantom (Model 186-801-*P*, CIRS, Norfolk, Virginia). Two targets were optimized for 1Gy absorbed dose: a $6 \times 6 \times 6$ cm^3 cubic-shaped SOBP and a prostate-like volume. Measurements were performed in the high-dose region for both targets directly at the center of the phantom, and in the dose fall-off region (at 95%, 81%, and 63% of the target dose level) for the prostate plan by adding RW3 slabs in front of the detector. Local γ-index analyses were performed with 3%/1.5 mm criteria.

RBE prediction verification

The verification of the mMKM implementation was performed against an independent dose engine using different databases and computing approaches.

The medium-size SOBPs were used for recalculation in an independent analytical dose engine for RBE calculations (FRoG (Fast Recalculation on GPU))[19]. A dedicated mMKM database for AB2 was created. In comparison to RS, the database of FRoG was derived directly from MC-FLUKA simulations giving an estimation of z^*_{1D} from the mixed radiation field for each energy in depth. The percentage difference of the RBE predictions at the center of the SOBP along the depth in water was analyzed.

Toward the 1st patient treatment with a scanned Helium ion beam

The first patient treatment with an intensity modulated, scanned helium ion beam therapy took place in Q2 2021 at one of the horizontal beamline treatment rooms. Written informed consent was obtained from the individual for the publication of any potential data included in this article.

The TPS plan involved 3 beams for a prescribed RBE-weighted dose of 60 Gy (RBE) (2 Gy (RBE)/fraction), impinging on a 6 cm^3 target. The couch rotation was 5° for the first beam, 305° for the second, and 175° for the third. The initial spot selection was achieved with a hexagonal pattern with a 2.4 mm spot spacing and 2.1 mm energy spacing. The tissue-specific parameter was set to AB2 and the dose grid to $2 \times 2 \times 2$ mm^3. Multifield optimization was performed, resulting in 20 energy layers for the first beam, and 18 and 20 for the second and third beams, respectively. Before treatment, the beams were verified against measurements in water following the HIT clinical protocol for patient-specific quality assurance in water with the 24-IC array. Measurements at 2 positions per beam were acquired, and dose differences relative to the maximum dose of each beam were reported for chambers with a dose gradient below a field specific value. The dose gradient was set as 5% of the maximum predicted dose per mm for each beam, following internal quality assurance procedure (5% D_{max} [mGy/mm]).

The maximum predicted doses of each beam were 42 cGy, 58 cGy, and 40 cGy, respectively. Additional verification measurements with a 2-dimensional array and information can be found in supplementary materials.

To verify the absorbed and RBE-weighted dose calculation, in-silico independent recalculations with FLUKA and FRoG were performed. FLUKA calculations were performed on the computed tomography (CT) grid and reported to a matching dose grid (voxels $0.6 \times 0.6 \times 1$ mm^3), with a number of primary ions sufficient to reach a dose uncertainty level of approximately 1%. FRoG performs dose calculation on the CT grid and reports the dose in the same grid as the TPS ($2 \times 2 \times 2$ mm^3). The resulting dose cubes were imported into RS, and the dose volume histograms (DVH) of some regions of interest, targets, and organs at risk were analyzed.

Results

Absorbed dose validation

The physical beam model predictions were compared against the database provided and additional measurements for the monitor calibration. A summary of the results is provided in Figure 1 and Figure E2. The range difference derived from the IDDs was found to be <0.2 mm for all investigated energies. The mean dose-weighted dose differences range from 1.9% for the lowest energy to 0.06% at the highest, while the maximum value of the mean relative differences was 0.6% with a statistical standard deviation (SD) of ± 0.9% for one of the lowest energy (56.44MeV/u). The FWHM differences of the lateral dose profiles in air at the different positions from the isocenter were <0.1 mm. The absolute local dose differences of TPS predictions to measurements with the Farmer chamber at 4.8 mm water equivalent depth were <1.3% in all cases.

TPS absorbed dose engine and planning capacities were investigated for different optimized SOBPs, with different levels of complexity measured with pinpoint ICs in water. Depth dose and lateral dose distributions are shown for both TPS predictions and measurements in the water phantom of the small and medium-sized SOBPs at the shallowest and deepest positions in Figure 2A. The overall relative dose difference for all measurements in the water phantom is also presented, demonstrating a good agreement between TPS predictions and the measurements with a mean relative dose difference of 0.19% (SD of ±0.75%). In the SOBP high- dose region alone, the relative dose difference was 0.26% (SD of ±0.62%) with a maximum/minimum difference (max/min) of 1.7%/−1.3%. In the entrance region of the SOBP, the relative dose difference was 0.16% (SD of ±0.89%, max/min = 3.2%/−2.7%) and at some larger depths, in the plateau region it was 0.09% (SD of ±0.68% max/min = 1.9%/−2.6%). The geometric differences were within our defined clinical tolerance of 1.5 mm. The mean 90% field size difference was −0.12 mm (SD of ±0.39 mm, max = −0.71 mm). The mean 50% field size difference was 0.01 mm (SD of ±0.12 mm, max = −0.19 mm). The mean lateral fall-off difference was 0.27 mm (SD of ±0.19 mm, max = 0.7 mm). The mean proximal 90% range difference was −0.19 mm (SD of ±0.38 mm, max = −0.75 mm). The mean distal 90% range difference was −0.35 mm (SD of ±0.20 mm, max = −0.66 mm). The mean distal fall-off difference was 0.26 mm (SD of ±0.24 mm, max = 0.71 mm).

For the more complex scenarios with either: beam modifier (RASHI), complex forms, or complex phantoms (double wedge and head phantom), an overview of the results is presented in Figure 2B. The overall mean relative dose difference for the RASHI measurements was −1.05% (SD of ±0.95%) and more specifically of −0.05% (SD of ±0.85%) and −1.33% (SD of ±0.77%) for the 5 cm and 20 cm airgap measurements, respectively. For the complex form, the relative dose difference was 0.56% (SD of ±0.71%). The double wedge relative dose difference was 1.21% (SD of ± 0.68%), while being −0.01% (SD of ±1.61%) for the head phantom. The geometric SOBP value differences between TPS and lateral dose measurements were below the tolerance value of 1.5 mm, with a maximum 50%− and 90%− field size difference of 0.13 mm and 0.12 mm, respectively. The maximal difference in lateral fall-off was 0.4 mm and corresponds to the medium size SOBP with a 20 cm air gap.

An overview of the γ-index passing rate between measurement and TPS, for each planning scenario is presented in Figure 3A. For all the SOBPs measurements in water without beam modifiers, the γ-index was >95% with a 3%/1.5 mm criterion. In the high dose region of the SOBPs, a γ-index >95% was achieved even with a stricter 2%/1 mm criterion. At each position in depth, the mean dose from the 4 central ICs from the Octavius was extracted and compared with TPS predictions, resulting in mean dose differences of 0.33% (SD of ±0.39%). The superficial SOBPs with range

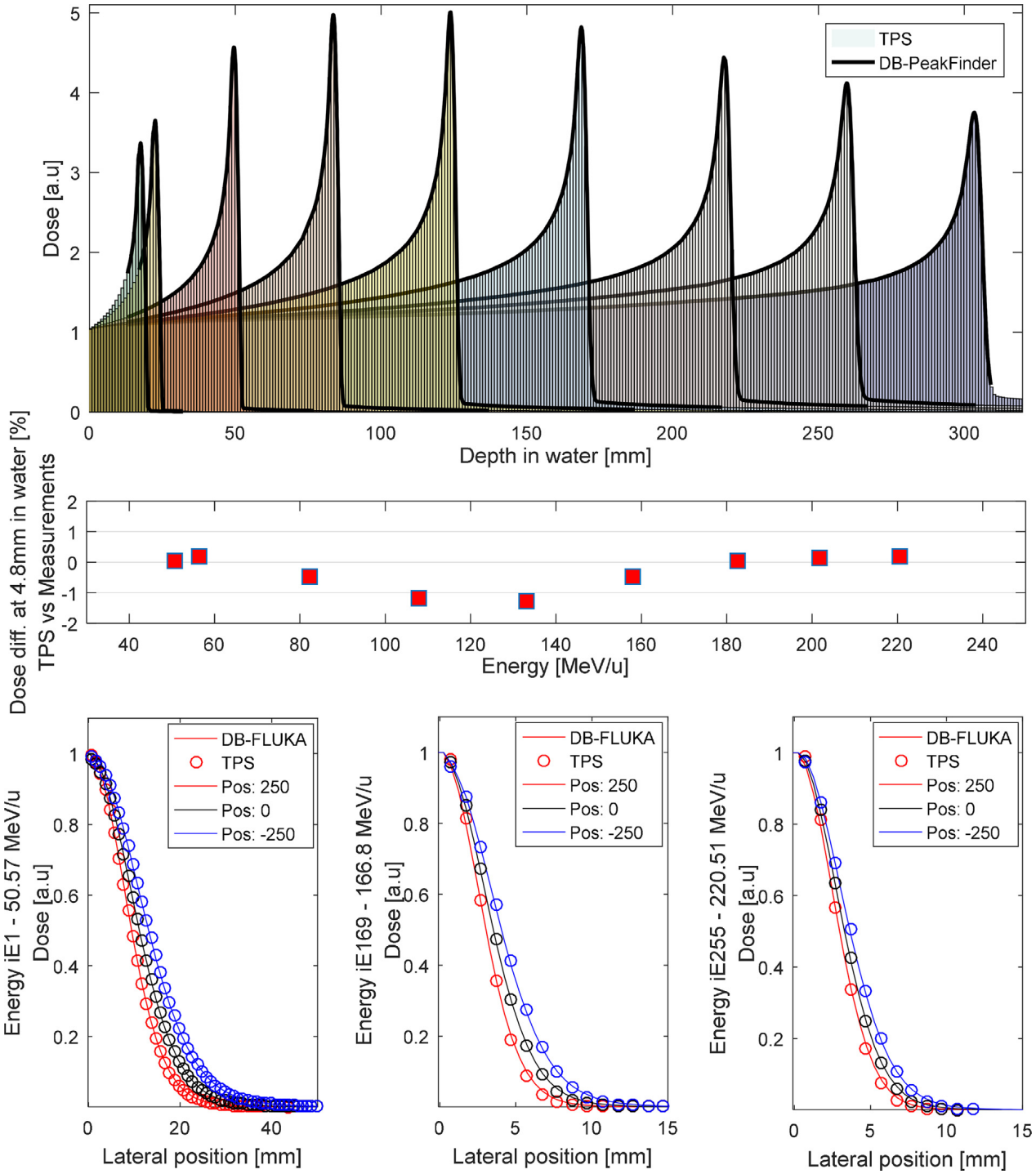

Fig. 1. Physical database treatment planning system (TPS) computations against database inputs: top figure shows the integral depth dose profiles for different energies (50.57, 56.44, 82.33, 107.93, 133.21, 158.08, 182.43, 201.71 and 220.51MeV/u) with the TPS (bars) and measurements (solid lines); middle figure displays the absolute dosimetry verification at 4.8 mm in water for the 8 energies; bottom 3 figures depicts the lateral dose profile from the database (solid line) and computed by the TPS (circles) for 3 energies and 3 positions in air (low-, mid- and high- energy from left to right).

shifter present a γ-index >95%. With complex phantoms (double-wedge, Alderson-head and CIRS-body phantom), except for some measurements within the dose fall-off, the majority of the measurements showed a γ-index >95%. For the double-wedge, 9 out of 10 measurements (excluding the one for dose fall-off) showed a γ-index >95% (min = 93.2%). For the head phantom, 7 out of 8 measurements presented a γ-index >95% (min = 94.6%, excluding the dose fall-off measurements). For the body phantom all measurements in the high dose region had a γ-index >95%. Qualitatively, even in the dose fall-off regions, the measurements were in good agreement with the TPS predictions, as seen for the Alderson-head phantom in Figure 3B.

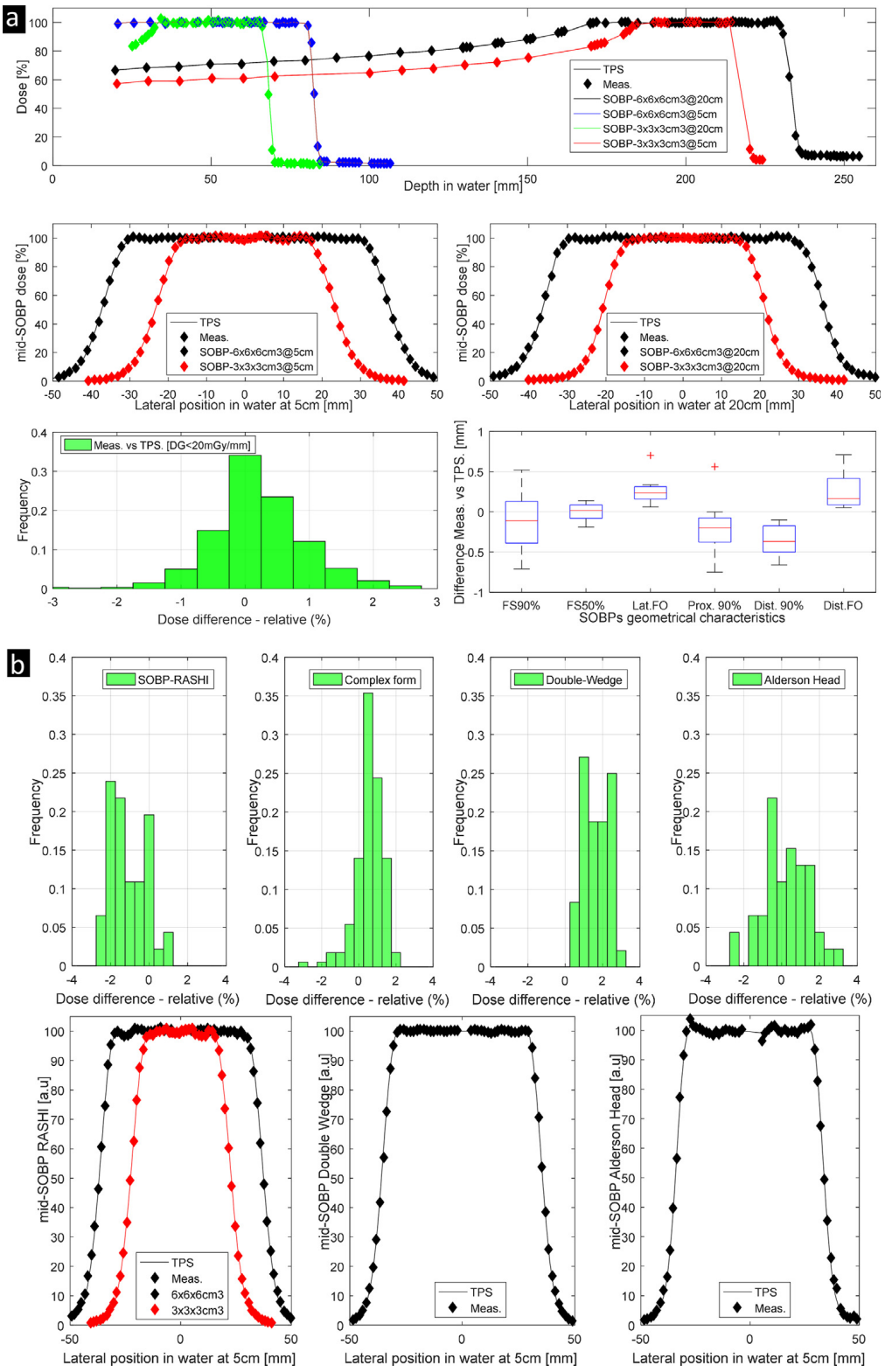

Fig. 2. Dosimetric measurements in water and difference to treatment planning system (TPS) predictions for: *(a)* simple spread-out Bragg peaks plans in water. In-depth (top figure) and lateral dose distributions (middle figures) of the measurements (diamonds) and the TPS (solid line) for the small-/middle spread-out Bragg peaks centered at 5 and 20cm are displayed. The distribution of the dose differences between measurements and TPS is shown (bottom figure left). Bottom figure right presents SOPBs-extracted geometric differences as boxplots: field size (FS) 90%, FS50%, lateral fall-off (Lat. FO) proximal range 90% (Prox. 90%), distal range 90% (Dist. 90%), distal fall-off (DFO); *(b)* Plans with complex forms, range shifter (RASHI), double-wedge and Alderson-head phantoms: the probability distributions of the dose differences between measurements and TPS are presented for each scenario (top figures). The lateral dose distributions at midtarget with RASHI or the complex phantoms for the measurements (diamonds) and TPS (solid line) are displayed in the bottom figure.

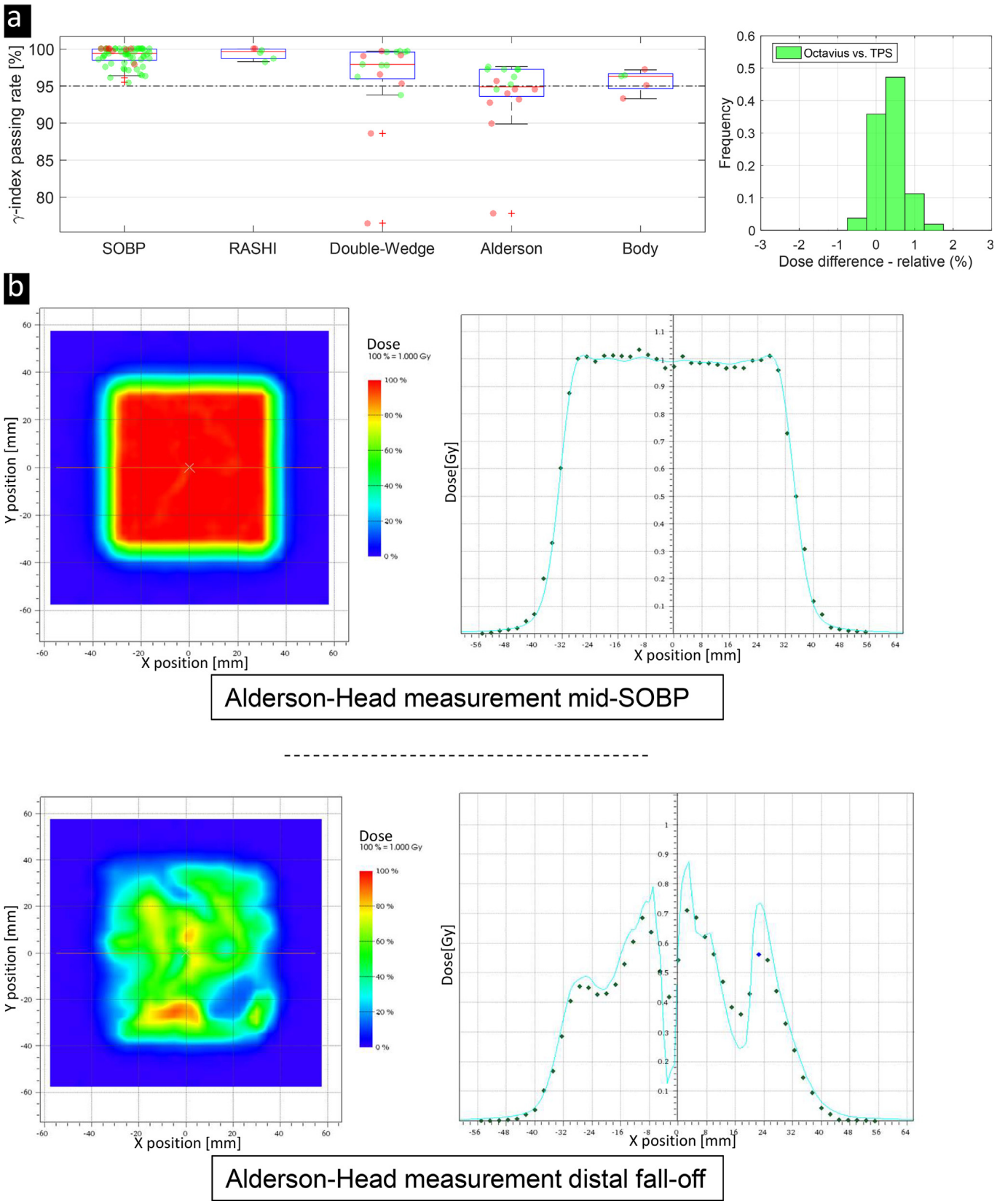

Fig. 3. (A) In the left figure, γ-index (3%/1.5 mm, local) analyses between Octavius measurements and treatment planning system (TPS), presented as boxplots, for the simple spread-out Bragg peak plans, plans with range shifter (RASHI, with 20cm airgap), the double-wedge, Alderson-head and CIRS-body phantom. Green and red dots represent individual measurements with the latter being in the dose fall-off regions. In the right figure, the probability distribution of the dose differences for the spread-out Bragg peaks between extracted central ICs from the Octavius compared with the TPS predictions are presented (B) Example of acquired 2D dose maps after the Alderson head and dose line profiles (TPS = solid line, measurements = diamonds), for a position in the high dose region and one in the distal fall-off. (For interpretation of the references to colour in this figure legend, the reader is referred to the web version of this article.)

RBE prediction verification

RBE predictions and differences between FRoG and the TPS are presented in Figure 4, alongside the absorbed dose distribution, for the 4 medium-sized SOBPs. The RBE difference curves allow observing the general agreement of the RBE predictions (within 4%). Two regions were defined for quantitative comparisons, the "entrance-region" from the entrance in water to the proximal 90% of the SOBP and the "SOBP-region" for a 5 cm region within the 6 cm SOBP in depth. For the SOBP centered at 5cm the difference in the entrance-region was 0.8% (SD of ±0.1%) and −0.3% (SD of ±0.4%) in the SOBP-region. For the SOBP centered at 12.5 cm the difference was 1.8% (SD of ±0.1%) and 0.3% (SD of ±0.2%) for the entrance- and SOBP-region, respectively. For the SOBP centered at 20 cm the difference was 2.3% (SD of ±0.2%) and 0.6% (SD of ±0.2%) for the entrance- and SOBP-region, respectively. For the SOBP centered at 27 cm the difference was 2.8% (SD of ±0.4%) and 1.0% (SD of ±0.1%) for the entrance- and SOBP-region, respectively.

Dosimetric verification of the 1st patient plan

The verification procedure of the 3 beams passed the clinical patient-specific quality assurance tolerances, for every position. Considering the pinpoint chambers within a dose gradient below the beam-specific threshold (<5% the beam maximum dose per mm), 112 measurements were kept from a total of 144, presenting an overall relative dose difference of 0.20% (SD of ±1.73%, max/min = 5.64%/−3.37%). While considering a threshold dose gradient <3% of the beam maximum dose per mm, 74 measurements were considered and was resulting in an overall relative dose difference of 0.18% (SD of ±1.34%, max/min = 3.59%/−2.58%). With respect to the small field size, the number of ICs located in a dose region >50% to its respective maximum beam dose was 43 (mean = 0.71%, SD = ±2.03%, max/min = 5.64%/−3.37%) and 28 (mean = 0.91%, SD = ±1.28%, max/min = 3.59%/−2.58%) for the 5% and 3% dose gradient threshold, respectively. An overview of the results, using the clinical dose gradient threshold, is presented in Figure 5A for both dose gradients limitations. Results with the stricter dose gradient threshold are reported in Figure E3.

The DVHs were qualitatively similar for the different dose engines, in particular for the absorbed dose DVHs, as seen in Figure 5B and in the Table E2 for the extracted DVHs metrics. In addition to the comparison in coronal plane of the absorbed dose and RBE-weighted dose distributions (Figure 5B), axial and sagittal views are presented in Figure E5. The differences, from the extracted DVH metrics between the FRoG and RS, were in average -0.1Gy(RBE) (SD of ±0.6 Gy (RBE), max/min = 1.2/−1.1 Gy (RBE)) for the RBE-weighted dose, and of -0.1Gy (SD of ±0.2Gy, max/min = 0.2/−0.5Gy) for the absorbed dose. The dose

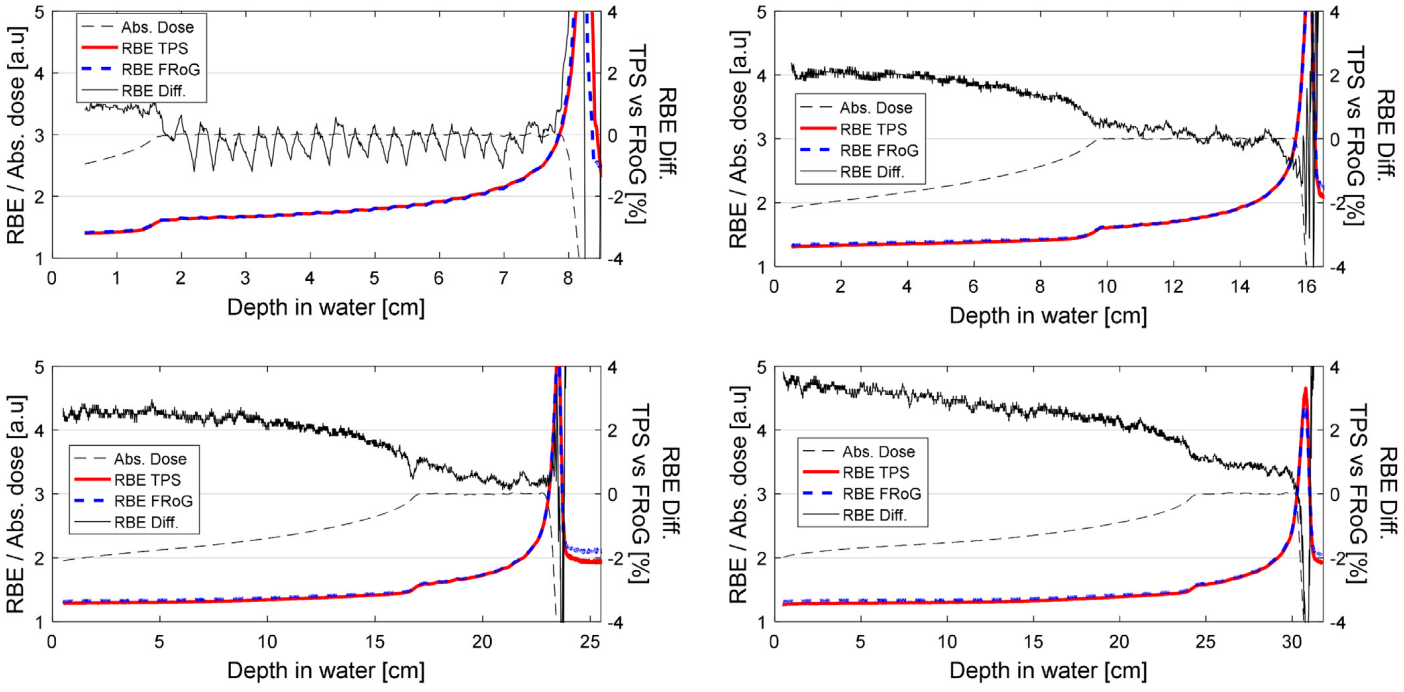

Fig. 4. Biological validation: The figure presents the relative biological effectiveness predictions for the 4 medium- spread-out Bragg peaks (centered at 5, 12.5, 20 and 27cm) from the treatment planning system (TPS; red) and FRoG (blue). For indication, the absorbed dose distribution is shown as well (black dashed line) for a high dose region of 1Gy. The local relative biological effectiveness differences between the engines over the depth are depicted in black. (For interpretation of the references to colour in this figure legend, the reader is referred to the web version of this article.)

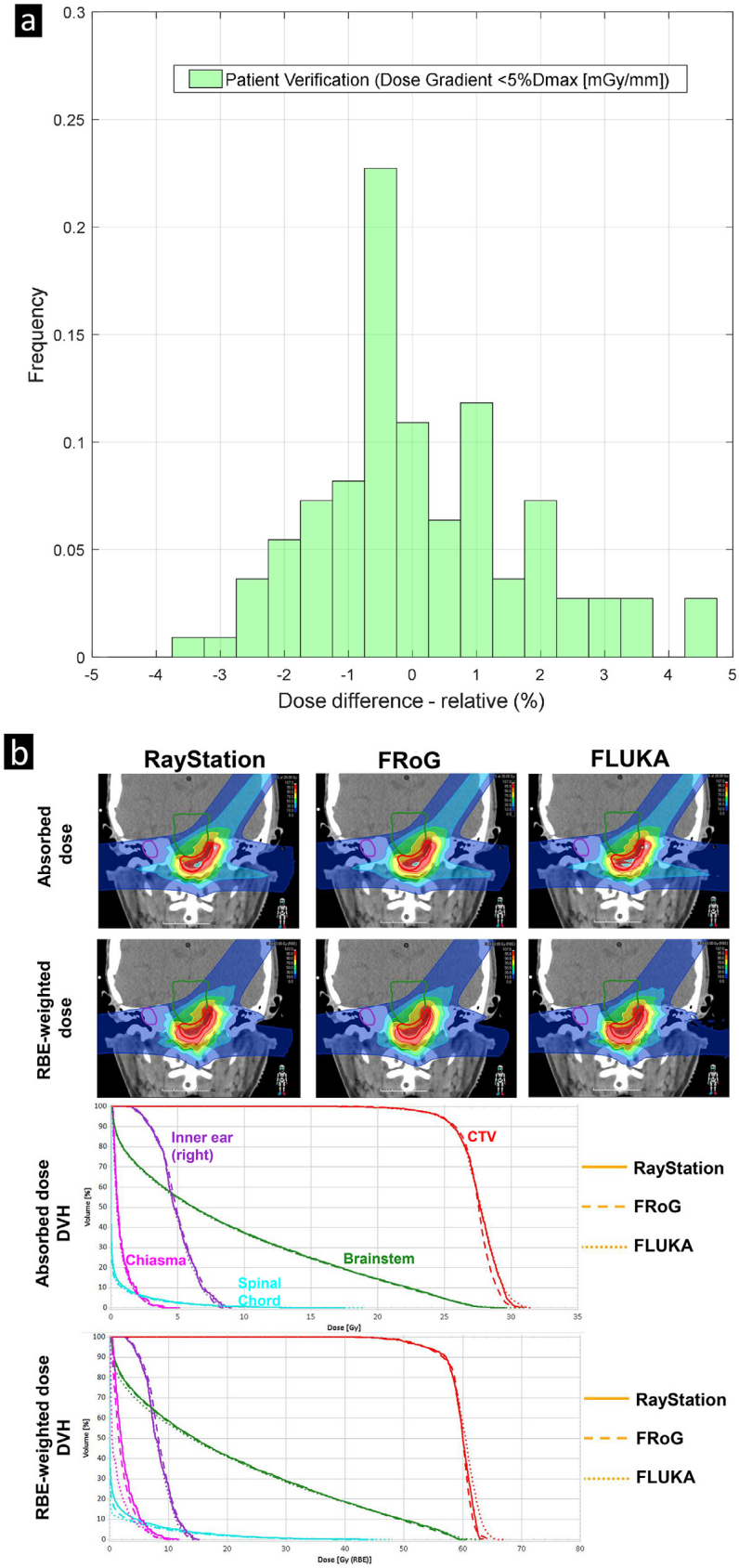

Fig. 5. 1st patient treatment with raster-scanned helium ion beam validation: (A) the figure presents the probability distribution of the relative dose difference between measurements in a water tank (ICs pinpoint) and the treatment planning system (TPS) using the clinical dose gradient threshold (<5% the beam maximum dose); (B) the figure displays in the patient coronal plane absorbed and relative biological effectiveness−weighted dose calculations for the TPS, FRoG and FLUKA. The DVHs for the clinical target volume (CTV), chiasma, brain stem, inner ear (right) and spinal cord are displayed for both absorbed and relative biological effectiveness−weighted dose calculations.

differences, from the extracted DVH metrics MC-FLUKA and RS, were on average 0.1 Gy (RBE) (SD of ±1.2Gy (RBE), max/min = 3.5/−1.5 Gy (RBE)) for the RBE-weighted dose, while for the absorbed dose these were about 0.0Gy (SD of ±0.2Gy, max/min = 0.5/−0.3Gy).

Discussion

This work demonstrates that RayStation TPS can accurately optimize and predict absorbed and RBE-weighted dose within the specified tolerances for intensity modulated, scanned helium ion beam therapy. The agreements of the implemented APB for dose calculation shown through this study were at the same level as other published work for both the clinical TPS calculations for protons and carbon ions, and as good as previous studies with helium ions based on APB or MC-dose engines.[34-41] Results of dose measurements in water were found to be within ∼3%.[35,37,39,41,42] Among the 537 measurements in SOBPs (dose gradient <20 mGy/mm), only one measurement was found at 3.2% in the entrance region of one of the deepest SOBPs. Within the high-dose region of the SOBPs, all measurements were within 2%, with 85% being found within 1%.

More specifically, the relatively poorer agreement in the IDDs results between the TPS and measurements at low energy can be explained by the 1 mm dose grid at low energy for the TPS compared with the sharpness of the Bragg peak at such energies as seen in Figure E6A. The largest deviation in the absolute dosimetry verification stems from the position of this measurement where the TPS can no longer use the measured IDDs but must interpolate the database with external sources (such as FLUKA simulations). Thus, some uncertainties may be introduced within this process. However, the absolute dosimetry made at a deeper position ensures a good compromise between entrance- and high-dose regions. This means that this difference of 1.3% at 4.8 mm, when considered relatively to the Bragg peak dose, is brought down to ≈0.3%. This also implies that if an adjustment of the monitor calibration to the dose at 4.8 mm was performed, the SOBP dose would be brought down by 1.3%, while correcting only for 0.3% relative to the SOBP dose in the entrance.

All geometric quantities were found close to predictions, for both pristine peaks (difference in range and FWHM <0.2 mm) and SOBPs (difference <0.7 mm) which was within the range of results from other commissioning works with ions.[34,36,39,41] The largest differences in proximal and distal range of SOBPs were related to: (a) position setup-uncertainties: as seen in Figure 2A, proximal and distal 90% position differences dose were negative (within the same direction), thus the largest deviations were brought back below 1 mm, and (b) the lack of sampling for some measurements and the interpolation process in these 90% regions as displayed in Figure E6B. The main differences in measured dose appeared for SOBPs with RASHI (≈-1.3%) as expected from literature with APB.[38,43] Future improvements of the APB and the development of a fast MC engine for helium ions are expected to reduce these discrepancies with a better description of interaction in air after the beam modifier.

The γ-index passing rates for the SOBPs in water were >95% with a 3%/1.5 mm local criterion, which are stricter values than employed in some other studies (3%/3 mm, 2%/2 mm, global).[32,35,37,44] With respect to the recommendation of the AAPM-TG185,[32] the SOBPs in water arrived all with a γ-index >98% with a 2%/2 mm (local) criterion. With a tighter criterion of 2%/1 mm (local), all measurements within the high dose region presented a γ-index >95%. Irradiation through heterogeneous phantoms showed γ-index passing rate >95% with the tight 3%1.5 mm (local) constraint, except for one measurement with the double-wedge. However, using a 3%/3 mm criterion, in all measurements the γ-index passed >99%. The measurements with the double-wedge phantom, emulating oblique beam incidences, and the heterogeneous anthropomorphic phantom geometries showed good agreement to the TPS predictions in the same range as MC-TPS for protons.[43,44] Despite the good agreement, the double-wedge phantom (oblique beam incidences) results presented dose differences slightly higher (1.2%) than the overall dose cubes (0.3%) with perpendicular beam entry. To resolve this limitation, refinement of the TPS APB engine or introduction of MC-based engine could be beneficial.

The SOBPs measurements in water showed agreement in the entrance region with the TPS compared with previous publications using MC-based or analytical-based dose engines.[12,45] Similarly, measurements of helium ion beams through an anthropomorphic head phantom with a 2-dimensional array detector compared with MC-FLUKA and FRoG exhibited γ-index passing rates about 96% and 92% respectively, with a 3%/3 mm global criterion,[11] thus with predictions less accurate than the TPS in this study. These effects are mainly linked to the TPS database of the Bragg peaks which is based on measurements compared with MC-FLUKA simulations or a FLUKA-generated database for FRoG. The MC-FLUKA code is not able to model perfectly the IDDs compared with measurements,[12] underscoring the difference in the entrance and plateau region of SOBPs, mainly for deep-seated targets. This may be linked to known weakness in the fragmentation models of MC-codes.[4]

Previous work[19] compared RBE predictions between mMKM-based calculations using a mix-radiation field spectra approach (łas performed in the TPS) to predictions with FLUKA-generated z^*_{1D} database in depth for every energy. Their results were within 2% to 3% for entrance regions of the deepest SOBP as found in this work. One could argue that the physical database of RS, with IDDs based on measurements to result in better absorbed dose, and the underlying physical spectra used for RBE-weighted dose calculation based on MC-FLUKA do not match. New versions of FLUKA (release version >2021.1) provide better IDDs compared with the previous versions, better describing the mixed radiation field spectra. Nevertheless, a study

investigating the effect of particle spectra from different MC-codes for carbon ion plans with the same physical database has found relatively low effect of the choice of the MC-codes on the RBE calculation[46] (1% in the target region). Although further sensitivity studies based on the spectra should be conducted, these differences are below the known uncertainty on the RBE predictions. The tissue-type attribution has a stronger effect on RBE predictions with variations of ≈5% for a fixed α_x/β_x (2 Gy) with changing the β_x value, and >20% when changing the α_x/β_x from a relatively low value (2 Gy) to a relatively high value (10 Gy).[19]

Before treatment of the first patient using helium ions, in-depth validation was successfully performed. The verification procedure in water passed the tolerance of a relative mean dose deviation of 3% for a min/max local relative difference of ±7%. Because of the small size of the target and corresponding relatively high dose gradients, the minimum and maximum differences are significantly improved when using a stricter dose gradient threshold. Furthermore, only a few chambers were located in the high-dose region. Thus, the patient beams specific measurements with the 2-dimensional array through the head phantom allowed to verify more accurately the patient plan. The absorbed and RBE-weighted dose estimations of the 3 engines were consistent, with differences further reduced when using a 1 mm^3 voxel grid in the TPS (as seen in Table E2). These overall agreements between the TPS and the 2 engines calculations are promising sound absorbed and RBE-weighted dose predictions in the patient (with respect to the implemented model and assume tissue-type) because these 3 engines do have different physical and biological approaches as well as a different interpretation of the CT (conversion from CT numbers to stopping power ratio, interaction at the CT grid or dose grid). The TPS rescales the CT grid to the dose grid for calculation while both FLUKA and the APB engine compute on the CT grid directly.

The larger differences arising between the TPS (and the APB engine) to FLUKA for RBE-weighted dose predictions may come from the fact that in FLUKA the lateral variation of the biological effect (z^*_{1D}) is considered while for the TPS and APB engine a unique value is considered along the lateral profile. Future implementation of a new analytical approach, such as the trichrome model[47] or fast MC-based calculation, could reduce these differences. All clinical goals were still met in all recalculations other than $D_{0.03cc}$ for the brain stem with a dose of 61 Gy (RBE) for FLUKA predictions as opposed to the planned dose of 60 Gy (RBE). However, statistical effects from MC-FLUKA calculations on small volumes can explain these variations on RBE-weighted and absorbed dose of 1.7% and 1.4%, respectively, with an averaged uncertainty level around 1 to 1.5%.

The clinical quality assurance program that already existed for protons and carbon ions at HIT was extended to helium ions. With respect to the consistent agreements between the TPS and measurements or independent predictions, the validation provided confidence in the robustness of the physical model and the consistency of the biological implementation to start patient treatments and clinical trials. With the growing interest of the particle therapy community in helium ions, this work could provide reference for other centers interested on helium ion beam therapy.[48,49]

Further works, comparing the potential advantages of helium ions against other particle species for different treatment sites are ongoing, including pediatric patients, with focus on robustness of the helium ion plans and benefits in terms of normal tissue complication probabilities compared with proton treatments.

Conclusion

A comprehensive commissioning of the clinical research TPS for helium ion beam therapy using active beam delivery was conducted and led to the first patient treatment using a scanned helium ion beam since the LBNL shutdown. Additionally, the overall excellent agreement of the TPS dose engine to the measurements and the similarity of TPS biological predictions to other references promise safe and as well as efficient future treatments during upcoming clinical trials.

References

1. Castro JR, Quivey JM. Clinical experience and expectations with helium and heavy ion irradiation. *Int J Radiat Oncol Biol Phys* 1977;3:127-131.
2. Saunders W, Castro JR, Chen GT, et al. Helium-ion radiation therapy at the Lawrence Berkeley Laboratory: Recent results of a Northern California Oncology Group Clinical Trial. *Radiat Res Suppl* 1985;8:S227-S234.
3. Heidelberg Ion Beam Therapy Center treats first patient using helium ion therapy with RayStation | RaySearch Laboratories. Available at: https://www.raysearchlabs.com/media/press-releases/2021/heidelberg-ion-beam-therapy-center-treats-first-patient-using-helium-ion-therapy-with-raystation/. Accessed February 10, 2023.
4. Mairani A, Mein S, Blakely E, et al. Roadmap: Helium ion therapy. *Phys Med Biol* 2022;67(15). https://doi.org/10.1088/1361-6560/ac65d3.
5. Haberer T, Debus J, Eickhoff H, Jäkel O, Schulz-Ertner D, Weber U. The Heidelberg ion therapy center. *Radiother Oncol* 2004;73:S186-S190.
6. Kantemiris I, Karaiskos P, Papagiannis P, Angelopoulos A. Dose and dose averaged LET comparison of 1H, 4He, 6Li, 8Be, 10B, 12C, 14N, and 16O ion beams forming a spread-out Bragg peak. *Med Phys* 2011;38:6585-6591.
7. Knäusl B, Fuchs H, Dieckmann K, Georg D. Can particle beam therapy be improved using helium ions? — A planning study focusing on pediatric patients. *Acta Oncol. (Madr).* 2016;55:751-759.
8. Fuchs H, Alber M, Schreiner T, Georg D. Implementation of spot scanning dose optimization and dose calculation for helium ions in Hyperion. *Med Phys* 2015;42:5157-5166.
9. Tessonnier T, Mairani A, Chen W, et al. Proton and helium ion radiotherapy for meningioma tumors: A Monte Carlo-based treatment planning comparison. *Radiat Oncol* 2018;13(1):2.
10. Besuglow J, Tessonnier T, Kopp B, Mein S, Mairani A. The evolution of lateral dose distributions of helium ion beams in air: From measurement and modeling to their impact on treatment planning. *Front. Phys* 2022;9. https://doi.org/10.3389/fphy.2021.797354.

11. Mein S, Kopp B, Tessonnier T, et al. Dosimetric validation of Monte Carlo and analytical dose engines with raster-scanning 1H, 4He, 12C, and 16O ion-beams using an anthropomorphic phantom. *Phys Medica* 2019;64:123-131.
12. Tessonnier T, Mairani A, Brons S, et al. Helium ions at the heidelberg ion beam therapy center: Comparisons between FLUKA Monte Carlo code predictions and dosimetric measurements. *Phys Med Biol* 2017;62:6784-6803.
13. Tessonnier T, Mairani A, Brons S, Haberer T, Debus J, Parodi K. Experimental dosimetric comparison of 1H, 4He, 12C and 16O scanned ion beams. *Phys. Med. Biol.* 2017;62:3958-3982.
14. Horst F, Schardt D, Iwase H, Schuy C, Durante M, Weber U. Physical characterization of 3He ion beams for radiotherapy and comparison with 4He. *Phys Med Biol* 2021;66 095009.
15. Krämer M, Schifoni E, Schuy C, et al. Helium ions for radiotherapy? Physical and biological verifications of a novel treatment modality. *Med Phys* 2016;43:1995-2004.
16. Mein S, Dokic I, Klein C, et al. Biophysical modeling and experimental validation of relative biological effectiveness (RBE) for 4He ion beam therapy. *Radiat Oncol* 2019;14:123.
17. Grün R, Friedrich T, Krämer M, et al. Assessment of potential advantages of relevant ions for particle therapy: A model based study. *Med Phys* 2015;42:1037-1047.
18. Hintz L, Glowa C, Saager M, et al. Relative biological effectiveness of single and split helium ion doses in the rat spinal cord increases strongly with linear energy transfer. *Radiother Oncol* 2022;170:224-230.
19. Kopp B, Mein S, Tessonnier T, et al. Rapid effective dose calculation for raster-scanning 4He ion therapy with the modified microdosimetric kinetic model (mMKM). *Phys Medica* 2021;81:273-284.
20. Ströbele J, Schreiner T, Fuchs H, Georg D. Comparison of basic features of proton and helium ion pencil beams in water using GATE. *Z Med Phys* 2012;22:170-178.
21. Tommasino F, Scifoni E, Durante M. New ions for therapy. *Int J Part Ther* 2015;2:428-438.
22. Kase Y, Kanai T, Matsumoto Y, et al. Microdosimetric measurements and estimation of human cell survival for heavy-ion beams. *Radiat Res* 2006;166:629-638.
23. Stewart RD, Carlson DJ, Butkus MP, Hawkins R, Friedrich T, Scholz M. A comparison of mechanism-inspired models for particle relative biological effectiveness (RBE). *Med Phys* 2018;45:e925-e952.
24. Mein S, Klein C, Kopp B, et al. Assessment of RBE-weighted dose models for carbon ion therapy toward modernization of clinical practice at HIT: In vitro, in vivo, and in patients. *Int J Radiat Oncol Biol Phys* 2020;108:779-791.
25. Böhlen TT, et al. The FLUKA code: Developments and challenges for high energy and medical applications. *Nucl Data Sheets* 2014;120:211-214.
26. Ferrari A, Sala PR, Fasso A, Ranft J, et al. *FLUKA: A multi-particle transport code (Program version2005)*. 2005. https://doi.org/10.5170/cern-2005-010.
27. Jäkel O, Hartmann GH, Karger CP, Heeg P, Vatnitsky S. A calibration procedure for beam monitors in a scanned beam of heavy charged particles. *Med. Phys.* 2004;31:1009-1013.
28. Karger CP, Jäkel O, Palmans H, Kanai T. Dosimetry for ion beam radiotherapy. *Phys. Med. Biol.* 2010;55. https://doi.org/10.1088/0031-9155/55/21/R01.
29. Inaniwa T, Furukawa T, Kase Y, et al. Treatment planning for a scanned carbon beam with a modified microdosimetric kinetic model. *Phys Med Biol* 2010;55:6721-6737.
30. Jäkel O, Hartmann GH, Karger CP, Heeg P, Rassow J. Quality assurance for a treatment planning system in scanned ion beam therapy. *Med. Phys.* 2000;27:1588-1600.
31. Karger CP, Jäkel O, Hartmann GH, Heeg P. A system for three-dimensional dosimetric verification of treatment plans in intensity-modulated radiotherapy with heavy ions. *Med. Phys.* 1999;26:2125-2132.
32. Farr JB, Moyers MF, Allgower CE, et al. Clinical commissioning of intensity-modulated proton therapy systems: Report of AAPM Task Group 185. *Med Phys* 2021;48:e1-e30.
33. Jäkel O, Ackermann B, Ecker S, et al. Methodology paper: A novel phantom setup for commissioning of scanned ion beam delivery and TPS. *Radiat Oncol* 2019;14(1):77.
34. Ruangchan S, PalmansH Knäusl B, Georg D, Clausen M. Dose calculation accuracy in particle therapy: Comparing carbon ions with protons. *Med Phys* 2021;48:7333-7345.
35. Vilches-Freixas G, Unipan M, Rinaldi I, et al. Beam commissioning of the first compact proton therapy system with spot scanning and dynamic field collimation. *Br J Radiol* 2020;93 20190598.
36. Lin L, Huang S, Kang M, et al. A benchmarking method to evaluate the accuracy of a commercial proton Monte Carlo pencil beam scanning treatment planning system. *J Appl Clin Med Phys* 2017;18:44-49.
37. Pidikiti R, Patel BC, Maynard MR, et al. Commissioning of the world's first compact pencil-beam scanning proton therapy system. *J Appl Clin Med Phys* 2018;19:94-105.
38. Saini J, Cao N, Bowen SR, et al. Clinical commissioning of a pencil beam scanning treatment planning system for proton therapy. *Int J Part Ther* 2016;3:51-60.
39. Yagi M, Tsubouchi T, Hamatani N, et al. Commissioning a newly developed treatment planning system, VQA Plan, for fast-raster scanning of carbon-ion beams. *PLoS One* 2022;17 e0268087.
40. Fujitaka S, Fujii Y, Nihongi H, et al. Physical and biological beam modeling for carbon beam scanning at Osaka Heavy Ion Therapy Center. *J Appl Clin Med Phys* 2021;22:77-92.
41. Zhu XR, Poenisch F, Lii M, et al. Commissioning dose computation models for spot scanning proton beams in water for a commercially available treatment planning system. *Med Phys* 2013;40 041723.
42. Carlino A, Böhlen T, Vatnitsky S, et al. Commissioning of pencil beam and Monte Carlo dose engines for non-isocentric treatments in scanned proton beam therapy. *Phys Med Biol* 2019;64: 17NT01.
43. Widesott L, Lorentini S, Fracchiolla F, Farace P, Schwarz M. Improvements in pencil beam scanning proton therapy dose calculation accuracy in brain tumor cases with a commercial Monte Carlo algorithm. *Phys Med Biol* 2018;63 145016.
44. Fracchiolla F, Lorentini S, Widesott L, Schwarz M. Characterization and validation of a Monte Carlo code for independent dose calculation in proton therapy treatments with pencil beam scanning. *Phys Med Biol* 2015;60:8601-8619.
45. Mein S, Choi K, Kopp B, et al. Fast robust dose calculation on GPU for high-precision 1H, 4He, 12C and 16O ion therapy: the FRoG platform. *Sci Rep* 2018;8(1):14829.
46. Resch AF, Schafasand M, Lackner N, et al. Technical note: Impact of beamline-specific particle energy spectra on clinical plans in carbon ion beam therapy. *Med Phys* 2022 Jun;49:4092-4098.
47. Inaniwa T, Kanematsu N. A trichrome beam model for biological dose calculation in scanned carbon-ion radiotherapy treatment planning. *Phys Med Biol* 2015;60:437-451.
48. Pompos A, Foote RL, Koong AC, et al. National effort to re-establish heavy ion cancer therapy in the United States. *Front Oncol* 2022;12:880712.
49. Gambino N, Kausel M, Guidoboni G, et al. First injector commissioning results with helium beam at MedAustron Ion Therapy Center. *J Phys Conf Ser* 2022;2244 012109.

6 Third Publication: Understanding RBE and clinical outcome of prostate cancer therapy using particle irradiation: analysis of tumor control probability with mMKM

Authors: **Judith Besuglow**, Thomas Tessonnier, Stewart Mein, Tanja Eichkorn, Thomas Haberer, Klaus Herfarth, Amir Abdollahi, Jürgen Debus and Andrea Mairani
Publication status: Received 27 July 2023, Accepted 10 February 2024, Available online 27 February 2024, Version of Record 22 July 2024.
Journal reference: International Journal of Radiation Oncology • Biology • Physics, Volume 119, Issue 5, 1 August 2024, Pages 1545-1556
DOI: 10.1016/j.ijrobp.2024.02.025

Authors' contributions: **JB** is the principal author of this publication. **JB**, AM and TT conceptualized the study. **JB** recalculated the RTPlans of all 91 IPI patients and performed all analysis. TT optimized the new patient plans in RayStation®. SM wrote the scripts for creation of FROG databases. TE accumulated survival data of IPI patients. KH oversaw the IPI trial. **JB**, with the assistance of AM, wrote the original draft and revision of the manuscript. **JB**, with the assistance of TT, created all figures. All authors contributed to the review, read and approved the final manuscript. TH, AA and JD provided clinical direction during project development, project administration and funding acquisition.

The supplementary to this publication is attached as appendix D.

INTERNATIONAL JOURNAL OF
RADIATION ONCOLOGY • BIOLOGY • PHYSICS
www.redjournal.org

PHYSICS CONTRIBUTION

Understanding Relative Biological Effectiveness and Clinical Outcome of Prostate Cancer Therapy Using Particle Irradiation: Analysis of Tumor Control Probability With the Modified Microdosimetric Kinetic Model

Judith Besuglow, MSc,[*,†,‡,§,‖] Thomas Tessonnier, PhD,[*,¶] Stewart Mein, PhD,[*,†,‡,§,#] Tanja Eichkorn, MD,[§,¶,**,††] Thomas Haberer, PhD,[§,¶] Klaus Herfarth, MD,[§,¶,**,††] Amir Abdollahi, MD,[*,†,‡,§] Jürgen Debus, MD, PhD,[‡,§,¶,**,††,‡‡] and Andrea Mairani, PhD[*,¶,§§]

[*]*Clinical Cooperation Unit Translational Radiation Oncology (E210), National Center for Tumor Diseases (NCT), Heidelberg University Hospital (UKHD) and German Cancer Research Center (DKFZ), Heidelberg, Germany;* [†]*Division of Molecular and Translational Radiation Oncology, Department of Radiation Oncology, Heidelberg Faculty of Medicine (MFHD) and Heidelberg University Hospital (UKHD), Heidelberg Ion-Beam Therapy Center (HIT), Heidelberg, Germany;* [‡]*German Cancer Consortium (DKTK) Core-Center Heidelberg, German Cancer Research Center (DKFZ), Heidelberg, Germany;* [§]*National Center for Radiation Oncology (NCRO), Heidelberg Institute of Radiation Oncology (HIRO), Heidelberg University and German Cancer Research Center (DKFZ), Heidelberg, Germany;* [‖]*Department of Physics and Astronomy, Heidelberg University, Heidelberg, Germany;* [¶]*Heidelberg Ion-Beam Therapy Center (HIT), Heidelberg, Germany;* [#]*Department of Radiation Oncology, Perelman School of Medicine, University of Pennsylvania, Philadelphia, Pennsylvania, USA;* [**]*Department of Radiation Oncology, Heidelberg University Hospital (UKHD), Heidelberg, Germany;* [††]*National Center for Tumor Diseases (NCT), Heidelberg, Germany;* [‡‡]*Clinical Cooperation Unit Radiation Oncology (E050), German Cancer Research Center (DKFZ), Heidelberg, Germany; and* [§§]*Medical Physics, National Centre of Oncological Hadrontherapy (CNAO), Pavia, Italy*

Received Jul 27, 2023; Accepted for publication Feb 10, 2024

Purpose: Recent experimental studies and clinical trial results might indicate that—at least for some indications—continued use of the mechanistic model for relative biological effectiveness (RBE) applied at carbon ion therapy facilities in Europe for several decades (LEM-I) may be unwarranted. We present a novel clinical framework for prostate cancer treatment planning and tumor control probability (TCP) prediction based on the modified microdosimetric kinetic model (mMKM) for particle therapy.

Methods and Materials: Treatment plans of 91 patients with prostate tumors (proton: 46, carbon ions: 45) applying 66 GyRBE [RBE = 1.1 for protons and LEM-I, $(\alpha/\beta)_x$ = 2.0 Gy, for carbon ions] in 20 fractions were recalculated using mMKM [$(\alpha/\beta)_x$ = 3.1 Gy]). Based solely on the response data of photon-irradiated patient groups stratified according to risk and usage

Corresponding author: Andrea Mairani, PhD; E-mail: Andrea.Mairani@med.uni-heidelberg.de

Disclosures: J.D. reports grants from CRI The Clinical Research Institute, ViewRay Incl., Accuray International, Accuray Incorporated, RaySearch Laboratories AB, Vision RT limited, Merck Serono GmbH, Astellas Pharma GmbH, AstraZeneca GmbH, Siemens Healthcare GmbH, Solution Akademie GmbH, Eromed PLC Surrey Research Park, Quintiles GmbH, Pharmaceutical Research Associates GmbH, Boehringer Ingelheim Pharma GmbH Co, PTW-Frieburg Dr Pychlau GmbH, and Nanobiotix A.a., outside the submitted work. A.A. reports grants and other from Merck and EMD, grants and other from Fibrogen, other from BMS, and other from Roche, outside the submitted work. This work was supported by intramural funds from the National Center for Tumor Diseases (NCT3.0_2015.21/22 NCT-PRO and Biodose programs). The funders had no role in the study design, data collection and analysis, decision to publish, or preparation of the manuscript.

Data Sharing Statement: Research data are stored in an institutional repository and will be shared upon request to the corresponding author.

Supplementary material associated with this article can be found in the online version at doi:10.1016/j.ijrobp.2024.02.025.

Int J Radiation Oncol Biol Phys, Vol. 119, No. 5, pp. 1545–1556, 2024
0360-3016/$ - see front matter
https://doi.org/10.1016/j.ijrobp.2024.02.025

of androgen deprivation therapy, we derived parameters for an mMKM-based Poisson-TCP model. Subsequently, new carbon and helium ion plans, adhering to prescribed biological dose criteria, were generated. These were systematically compared with the clinical experience of Japanese centers employing an analogous fractionation scheme and existing proton plans.

Results: mMKM predictions suggested significant biological dose deviation between the proton and carbon ion arms. Patients irradiated with protons received (3.25 ± 0.08) $GyRBE_{mMKM}/Fx$, whereas patients treated with carbon ions received (2.51 ± 0.05) $GyRBE_{mMKM}/Fx$. TCP predictions were $(86 \pm 3)\%$ for protons and $(52 \pm 4)\%$ for carbon ions, matching the clinical outcome of 85% and 50%. Newly optimized carbon ion plans, guided by the mMKM/TCP model, effectively replicated clinical data from Japanese centers. Using mMKM, helium ions exhibited similar target coverage as proton and carbon ions and improved rectum and bladder sparing compared with proton.

Conclusions: Our mMKM-based model for prostate cancer treatment planning and TCP prediction was validated against clinical data for proton and carbon ion therapy, and its application was extended to helium ion therapy. Based on the data presented in this work, mMKM seems to be a good candidate for clinical biological calculations in carbon ion therapy for prostate cancer.

Introduction

Apart from radical prostatectomy, irradiation with adjuvant androgen deprivation therapy (ADT) often provides excellent curative treatment even for advanced prostate cancer.[1] Of all available modalities for radiation therapy, heavy ion beams promise a better dose conformality, thus improving tumor coverage while sparing organs at risk such as bladder and rectum.[2]

In the 1990s carbon ion therapy was introduced in Europe[3] and Japan[4] independently, following the initial experience with heavy ions at Berkeley.[5,6] Coincidently, 2 distinct approaches to model variable relative biological effectiveness (RBE), and hence biological dose prediction, were devised for carbon ion therapy, thereby leading to differing prescription doses between European and Japanese facilities. Hence, 2 patients treated with carbon ions for given disease may receive significantly different physical doses, despite the reported biological prescription dose levels being the same. Methods for prescription conversion from European to Japanese, although approximate, are published.[7-9] However, the differences in prescription practice complicate not just inter-institutional comparison for carbon ion therapy, but also interparticle comparison, such as efficacy between protons and carbon ion therapy for a particular disease site.

Several clinical trials with protons and carbon ions employed differing fractionation schemes and total doses in various facilities.[10-16] At the Heidelberg University Hospital, a randomized clinical trial for prostate cancer called Ion Prostate Irradiation (IPI) trial (NCT01641185)[17] was carried out to compare efficacy and toxicity between proton and carbon ion therapy directly. This published prospective study[17-19] intended to employ the same fractionation scheme of 66 GyRBE in 20 fractions in both treatment arms. Consequently, its results allow a direct comparison of the biological models assumed in the clinical treatment planning system (TPS). IPI[17-19] is thus well-suited to test radiobiological hypothesis for prostate cancer. According to the study protocol,[17] IPI initially aimed to investigate the safety and feasibility of mildly hypo-fractionated ion therapy by recording adverse effects such as rectal or bladder toxicity. The secondary endpoints, long-term prostate-specific antigen progression-free survival (85% and 50%) and overall survival (98% and 91%), were reported with a median follow-up of 8.6 years for proton and carbon ions.[19] The drastic difference in progression-free survival between protons and carbon ions raised concern over the biological approach employed. In other words, considering these results, should we change the biological dose prescription approach for prostate treatment planning? The lack of iso-effectiveness in IPI's two cohorts indicates uncertainty in the radiobiological framework used for planning: RBE of 1.1 ($RBE_{1.1}$) for protons and LEM-I (Local Effect Model, version I[20])-based RBE with $(\alpha/\beta)_x = 2\,Gy$ for carbon ions. A previous analysis[19] suggests that an overestimation in the prediction of RBE in LEM-I when using $(\alpha/\beta)_x = 2\,Gy$ ($RBE_{LEM\text{-}I}$) resulted in the observed lower local control for carbon ions.

Overestimation of RBE by LEM-I in the low/midrange linear energy transfer (LET) is also shown in a previous publication[21] that compared LEM-I, LEM-IV, and the modified microdosimetric kinetic model (mMKM) to in vitro data over a large range of dose, LET, and tissue parameters. That study found that the mMKM best described the collected experimental data in vitro and in vivo. Originally developed by Hawkins[22] and then modified by Inaniwa et al,[23] (m)MKM considers the specific energy of a mixed radiation field to predict the radiobiological effects of ion beam radiation. Specifically, mMKM derives RBE from the linear-quadratic parameters of cell survival measured in low-LET radiation together with the saturation-corrected dose-weighted average of the specific energy $z^*_{1_d}$ deposited by single events in one area (domain) of a cell's nucleus.[23-25] Adaptations of this mMKM for treatment planning with protons, helium, and carbon ions are published.[26-28] Adaptations of clinical RBE models for treatment planning in Japanese treatment facilities are described by Inaniwa et al[25] and Ishikawa et al.[29]

Apart from radiobiological modeling uncertainties, the radiosensitivity of prostate tissue and corresponding linear-quadratic parameters remain a continuously discussed

subject, with expected values of $(\alpha/\beta)_x$ mostly ranging between from 1.5 and 4.98 Gy.[30]

To tackle the uncertainty in radiobiological modeling in the clinical setting, we developed a treatment planning and tumor control probability (TCP) framework based on RBE-weighted dose. This work applied the mMKM, which has been benchmarked[21,27] in vivo and in vitro to predict the RBE-weighted dose of proton, helium, and carbon ions. The treatment plans of the IPI trial were analyzed with mMKM and LEM-I. TCP depends on a patient's risk category[31] (low, intermediate, or high according to National Comprehensive Cancer Network[47]/D'Amico criteria[46]) and usage of ADT.[32-34] Therefore, TCP was derived from parameters fitted to stratified photon reference clinical data.[35] Our novel mMKM/TCP predictions were compared against previous clinical experience with protons and carbon ions and the Japanese clinical experience[11,36] with carbon ions. In preparation for clinical trials for prostate treatments with helium beams, the treatment planning and TCP prediction framework based on mMKM was applied to evaluate the potential clinical benefit of this new treatment modality.

Methods and Materials

Choosing RBE model and tissue parameters

In the IPI trial, LEM-I was chosen for carbon ion treatment planning with $(\alpha/\beta)_x$ = 2 Gy, α_x = 0.1 Gy^{-1}, and β_x = `0.05 Gy^{-2}, and a threshold dose D_t=30 Gy ($RBE_{LEM-I,2}$). Clinical practice at the treatment facility HIT (Heidelberg Ion-Beam Therapy Center) applied the same tissue parameters for both prostate tumor and normal tissue. A fixed RBE of 1.1 was assumed to predict the effective dose for protons ($RBE_{1.1}$). However, based on the publication of Wang et al,[37] we chose the following settings as the linear quadratic model parameters for prostate cancer tissue: $(\alpha/\beta)_x$= 3.1 Gy, with $\alpha_x = 0.15\,Gy^{-1}$ and $\beta_x = 0.0484\,Gy^{-2}$. For this analysis, the mMKM was investigated. The mMKM derives RBE from the saturation-corrected dose-weighted average specific energy z^*_{1d} of the mixed radiation field, which depends on the photon reference $(\alpha/\beta)_x$ and β_x, as well as the parameters for radii of domain R_d and nucleus R_n. As previously benchmarked for proton, helium, and carbon ions, the mMKM-specific parameters R_d and R_n were set to the best fit,[21,27] 0.3 μm and 3.6 μm, respectively. In the following, $mMKM_{3.1}$ refers to this parameter set. Additionally, LEM-I was investigated with Wang et al's[37] prostate tissue parameters ($LEM\text{-}I_{3.1}$).

To recalculate RBE-weighted dose distributions, a database, consisting of the linear (α_{mix}) and quadratic term (β_{mix}) of the mixed radiation field as a function of depth in water, was created with FLUKA[38,39] for each proton and carbon ion beam energy employed in the cohort. Then, this database was imported into the dose engine FRoG (Fast Recalculation on GPU[21,40-42]), which has been extensively benchmarked in previous publications.

Inaniwa et al[23,25] published a mMKM-derived approach for carbon ion planning which matches previous clinical experience in Japan.[43,44] The Japanese approach to carbon ion treatment planning uses the survival data of human salivary gland (HSG) cells to derive the tissue parameters for all treatment indications. HSG cells were selected as the biological reference system and are considered representative of early responding tissues and tumors.[44] The optimal biological dose per indication was then found through dose escalation studies. Because IPI's design had been based on results of Tsuji et al,[45] we applied Inaniwa's implementation (RBE_{JP}) for individual patient plans to cross-validate our $mMKM_{3.1}$-based predictions for effective dose.

Patient cohort of IPI trial

The retrospectively investigated patient cohort consisted of 91 patients with histologically proven localized prostate cancer, 45 of whom had received ^{12}C ion irradiation. The remaining 46 patients were irradiated with protons at the same facility under the same institutional conditions. All patients were stratified into 3 risk categories[18] using the D'Amico[46] criteria, which are comparable to the criteria of the National Comprehensive Cancer Center,[47] and 22% of all patients received ADT.[18]

The treatment facility HIT provided active pencil-beam scanning[48] in a horizontal beam line for both protons and carbon ions. Delivered treatment plans were optimized in the former clinical TPS (syngo RT), aiming at 66 GyRBE ($RBE_{1.1}$ for protons; RBE_{LEM-I} for carbon ions) to at least 95% of the PTV in 20 fractions. Clinical target volumes (CTVs) included prostate and the inferior two-thirds of seminal vesicles plus a margin of 2 mm. The definition of PTV included a 7 mm margin lateral to the beam direction and 5 mm AP and IS. Exact volume definitions and planning constraints were reported in the protocol.[17] In this cohort, the CTVs ranged from 50.88 to 273.12 cm^3. The irradiation was administered at 5 to 6 fractions per week over 3.5 weeks in the years 2012 and 2013.

The project was performed in accordance with institutional guidelines and the Declaration of Helsinki of 1975 in its most recent version. Ethics approval and a waiver of written informed consent for the IPI trial (registered as NCT01641185) that contributed data to this project was granted by the Heidelberg University ethics committee in 2015 (Ethics Approval Number #S-298/2011). Patient confidentiality was maintained by anonymizing patient data to remove any identifying information.

Recalculating dose, dose-averaged LET, and biological dose distribution for the patient cohort

To compute the RBE-weighted dose distribution with our framework, we received anonymized DICOM-RT data of the delivered treatment plans for the entire patient cohort from

the clinicians.[17-19] For each patient, our validated dose engine FRoG[40-42] recalculated voxel-based absorbed dose and dose-averaged LET (LET_d) distribution of the delivered treatment plan, as well as effective dose distribution, using $mMKM_{3.1}$[21] with $(\alpha/\beta)_x = 3.1$ Gy ($\alpha_x = 0.15\,Gy^{-1}$ and $\beta_x = 0.0484\,Gy^{-2}$). Additionally, the LEM-I–based effective dose was recalculated with these parameters for the carbon ion arm ($LEM\text{-}I_{3.1}$). Finally, LET_d- and RBE-weighted dose-volume histograms (LET_dVH and $D_{RBE}VH$) of the CTV were extracted for each patient, and the distribution of LET_dVH and $D_{RBE}VH$ statistics among the patient cohorts was analyzed.

Developing a TCP model derived from clinical photon data

Biological relapse-free survival (bRFS) at 5 years according to the Phoenix definition[49] is an indicator of tumor control. A large collection of survival data for photon cohorts, with various fractionation schemes and risk stratification similar to the cohort of the IPI trial and differentiated for the usage of ADT, was published by Miralbell et al.[35] Other publications[32-34] show significant increase of bRFS with ADT for high-risk patients, whereas Royce et al[50] report no significant difference of TCP between low and intermediate risk groups.

Therefore, TCP parameters were derived for patient groups stratified according to risk (low-intermediate vs high risk) and use of ADT. With the assumed $(\alpha/\beta)_x$ of 3.1 Gy, the biological effective dose (BED) for all fractionation schemes within the Miralbell data[35] was calculated according to $\mathrm{BED} = nd\left[1 + \frac{d}{(\alpha/\beta)_x}\right]$, where d is the fraction dose and n the number of fractions. For each stratified group, a Poisson-TCP curve[51,52] was fitted to the data points of bRFS at 5 years against BED using the Trust Region Reflective Least Square algorithm in *curve_fit* from Python's *SciPy.Optimize* package:

$$\mathrm{TCP(BED)} = (1/2)^{exp(e\gamma[1-(\mathrm{BED}/TBED_{50})])}$$

with γ as the maximum slope of the TCP curve and $TBED_{50}$ as the BED at which TCP = 50%.

Validating the TCP model against clinical data for protons and carbon ions

To predict TCP for the IPI trial, we first derived the mean BED for each treatment arm with d representing the RBE-weighted $D_{95\%}$ per fraction to the CTV. The relative number of IPI's patients in each stratified cohort (risk and ADT) was used for a weighted sum of the photon derived TCPs. This weighted sum was then compared with the clinical results of IPI.

Comparing treatment planning approaches for carbon ions against clinical experience in Japan

Additionally, we created new treatment plans for 5 patients of the cohort with the clinical TPS RayStation 11B (RaySearch Laboratories). The patients were chosen to represent large, medium, and small CTVs. With these treatment plans, we evaluated the Japanese biological planning approach (JP) against our new mMKM/TCP framework ($mMKM_{3.1}$) and the clinical approach for prostate cancer LEM-I (LEM-I). The first approach followed the Japanese biological planning, where 2 opposing fields are independently optimized and then irradiated on alternating days.[4,29,44,53] The optimization strategy involved a single beam optimization approach with a biologically weighted fraction dose of 3.3 $GyRBE_{JP}$ in the PTV calculated with the Japanese biological model, which relies on Inaniwa's adaptation of the mMKM. Second, we forward calculated these treatment plans with LEM-I, assuming $(\alpha/\beta)_x = 2$ Gy ($RBE_{LEM\text{-}I}$), as applied by the delivered treatment plans of the IPI trial. Lastly, we forward calculated the Japanese-like treatment plans with our proposed mMKM model of $(\alpha/\beta)_x = 3.1$ Gy ($RBE_{mMKM3.1}$). Thus, 3 biologically weighted dose distributions were calculated for each of the 5 patients, which have the same physical absorbed dose as the optimized Japanese-like treatment plan.

mMKM-based treatment planning with proton, helium, and carbon ions

Toward updating and extending the clinical trial for treating prostate adenocarcinoma at our facility,[54] treatment plans for protons, helium, and carbon ion beams were optimized with the clinical TPS RayStation 11B (RaySearch Laboratories). For the biologically weighted dose of protons, an RBE of 1.1 was assumed. Helium and carbon ion plans were optimized with mMKM, considering $(\alpha/\beta)_x = 3.1$ Gy for both tumor and normal tissue. The primary objectives for optimization were target coverage ($D_{95\%} > 95\%\ D_{presc}$ in PTV, $D_{99.5\%} > 95\%\ D_{presc}$ of CTV) and homogeneity ($D_{95\%}/D_{5\%} > 0.95$ in CTV). Dose to bladder and rectum was reduced as much as was possible without jeopardizing the primary objectives. Thereby, we explored the impact of beam modality on achieving a reduced dose to the organs at risk.

Results

Dose and LET_d distributions in the patient cohort with different RBE parameterizations

Recalculation of the original treatment plan for each patient in the proton and carbon ion arms of the cohort showed a large deviation in biological dose between the arms. Figure 1 depicts dose and LET_d profiles for one representative patient per treatment arm. Here, the deviation between LEM-I and $mMKM_{3.1}$-based effective dose was roughly 20% for carbon ions in the target, and a fixed $RBE_{1.1}$ for protons matched the $mMKM_{3.1}$ prediction within 3%.

The mMKM weighted dose-volume histograms ($D_{RBE}VH$) and LET_d-volume histograms (LET_dVH) for all 91 patients are depicted in Figure 2. The figure provides

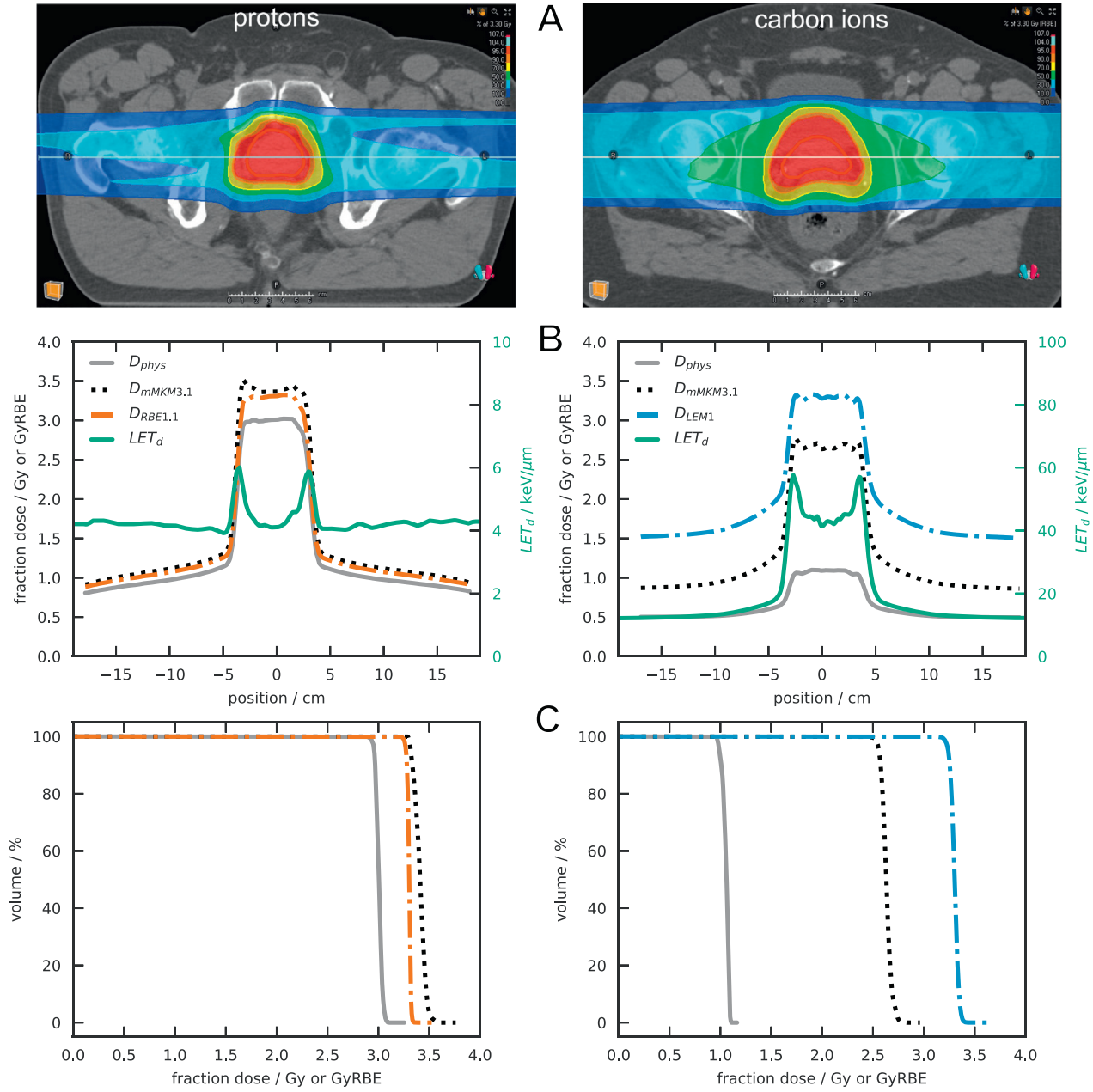

Fig. 1. The top panels (A) show a slice of the biological dose distribution of a showcase proton (left) and carbon ion (right) patient. The middle panels (B) show dose, biological dose, and LET_d profiles extracted at the position marked with a gray line in (A). The bottom panels (C) show the dose-volume histograms of the clinical target volumes delineated in the treatment planning system screenshots. Absorbed physical dose is shown in gray solid line. Orange dash-dotted lines represent the originally assumed effective dose with a fixed RBE of 1.1 for protons. Blue dash-dotted lines depict the LEM-I, $(\alpha/\beta)_x = 2$ Gy–based effective dose for carbon ions. Green solid lines represent LET_d, and black dotted lines indicate mMKM, $(\alpha/\beta)_x = 3.1$ Gy–based effective dose. *Abbreviations:* LEM-I = *Local Effect Model, version 1*[20]; LET_d = *dose-averaged linear energy transfer;* mMKM = *modified microdosimetric kinetic model*; *RBE = relative biological effectiveness;* RBE1.1 = *fixed RBE of 1.1.*

boxplots of both treatment arms' LET_dVH and D_{RBE}VH statistics. According to our calculations with mMKM and $(\alpha/\beta)_x = 3.1$ Gy, the patients irradiated with protons received a biological dose of 3.25 ± 0.08 $GyRBE_{mMKM}$/Fx (min: 3.00 $GyRBE_{mMKM}$/Fx; max: 3.34 $GyRBE_{mMKM}$/Fx) to 95% of the CTV. In contrast, the carbon ion irradiated patients received (2.61 ± 0.05) $GyRBE_{mMKM}$/Fx (min: 2.47 $GyRBE_{mMKM}$/Fx; max: 2.68 $GyRBE_{mMKM}$/Fx). Regarding LET_d, 95% of the CTV received more than (4.05 ± 0.15) keV/µm (min: 3.84 keV/µm; max: 4.21 keV/µm) for protons and (37.7 ± 3.8) keV/µm (min: 24.0 keV/µm; max: 43.7 keV/µm) for carbon ions. Recalculation results of the carbon patients with LEM-I and $(\alpha/\beta)_x = 3.1$ Gy yielded a $D_{95\%}$ to the CTV of (2.91 ± 0.04) $GyRBE_{LEM\text{-}I3.1}$/Fx (min: 2.80 $GyRBE_{LEM\text{-}I3.1}$/Fx; max: 2.97 $GyRBE_{LEM\text{-}I3.1}$/Fx). D_{RBE}VH and corresponding statistics for $LEM\text{-}I_{3.1}$ are reported in Figure E1.

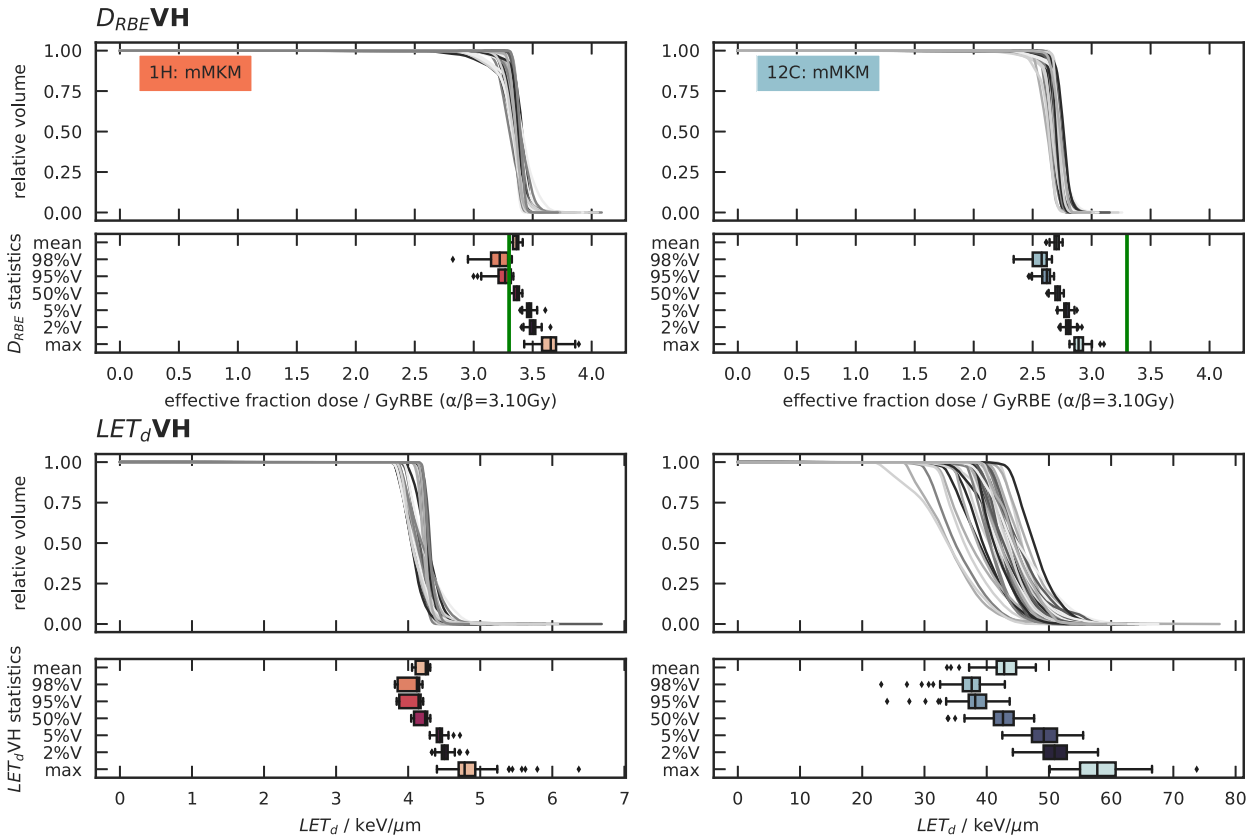

Fig. 2. The subpanels show $D_{RBE}VH$ and LET_dVH with corresponding statistics as boxplots. Effective biological dose follows mMKM with $(\alpha/\beta)_x = 3.1$ Gy. The left column (^{1}H) depicts the proton cases (n = 46), and the right column (^{12}C) represents the carbon cases (n = 45) of the IPI trial. The boxplot for each statistical parameter indicates the inner quartiles and 1.5 times the interquartile range. The green vertical line in the statistics of the effective fraction dose indicates the prescribed fraction dose of 3.3 GyRBE of the trial. *Abbreviations*: $D_{RBE}VH$ = *RBE-weighted dose-volume histogram*; LET_dVH = *dose-averaged linear energy transfer–weighted dose-volume histogram*; mMKM = *modified microdosimetric kinetic model*; RBE = *relative biological effectiveness.*

Determination of the TCP-photon parameters and prediction for the proton and carbon ion cohorts

Poisson-TCP curves were fitted individually for each combination of risk stratification and usage of ADT to data of biological recurrence-free survival (5-year bRFS) after photon irradiation, as shown in Figure 3. Without ADT, the free parameters of TCP are $\gamma = 1.40 \pm 0.43$ and $TBED_{50} = (93.1 \pm 4.7)$ Gy for the low-to-intermediate risk cohorts. The high-risk cohorts in photon data[22] have a TCP with $\gamma = 1.28 \pm 0.71$ and $TBED_{50} = (108.7 \pm 6.2)$ Gy. If ADT is given, the TCP fit yields $\gamma = 1.82 \pm 0.51$ and $TBED_{50} = (93.3 \pm 4.6)$ Gy for low-intermediate and $\gamma = 1.04 \pm 0.41$ and $TBED_{50} = (97.1 \pm 7.8)$ Gy for high-risk patients, respectively.

The $mMKM_{3.1}$-based $BED_{3.1Gy}$ was (96.1 ± 2.9) Gy (min: 88.6 Gy; max: 100.0 Gy) for the carbon arm of the IPI trial. Its proton arm received a mean $BED_{3.1Gy}$ of (132.9 ± 5.1) Gy (min: 118.0 Gy, max: 138.5 Gy) based on the mMKM-calculated fraction doses. The recalculation with LEM-$I_{3.1}$ yielded a mean $BED_{3.1Gy}$ of (113.1 ± 2.3) Gy (min: 106.7 Gy, max: 116.2 Gy).

With 22% ADT usage equally distributed over all risk groups of the IPI trial, our mMKM/TCP framework predicts an average 5-year bRFS of (85.8 ± 2.6)% (min: 76.0%, max: 88.4%) for the proton arm and (51.5 ± 4.0)% (min: 40.6%, max: 56.8%) for the carbon ion arm, matching the clinical observation of 85% (^{1}H) and 50% (^{12}C) PSA progression-free survival as reported in the right panel of Figure 3. When repeating the same formalism with LEM-$I_{3.1}$, our TCP framework predicted a 5-year bRFS of (71.6 ± 2.2)% (min: 65.0%, max: 74.5%) for the carbon ion arm of IPI's cohort.

Results of various treatment planning approaches for carbon ions

A planning study following the Japanese biological model and beam delivery approach was performed for 5 patients, assigning a total target dose of 66 $GyRBE_{JP}$ in 20 fractions. Figure 4 presents screenshots of this new Japanese-like treatment plan for the patient with the largest CTV (for the additional patients, see Figs. E2-E5). Forward-calculated biological doses with $mMKM_{3.1}$ and LEM-I for the same treatment plans are also included in the corresponding figures. Japanese-like

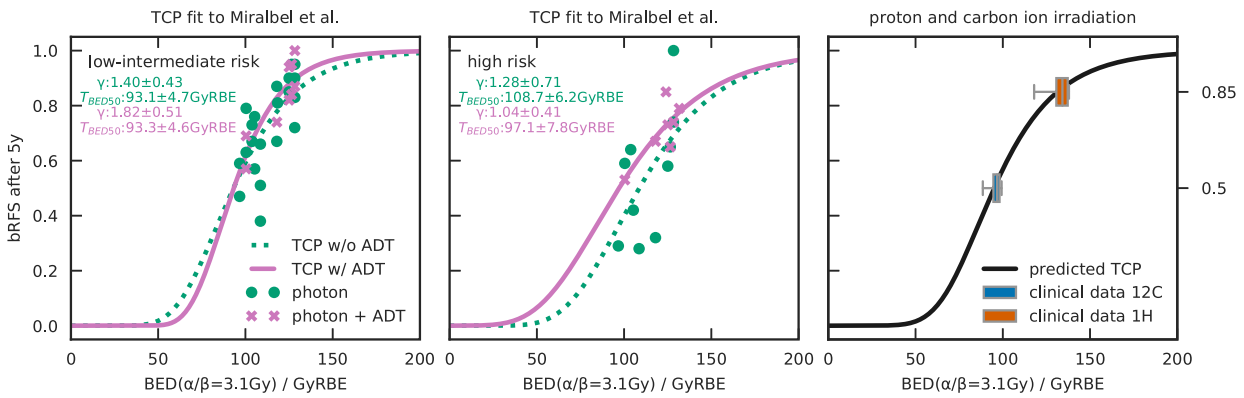

Fig. 3. Biochemical relapse-free survival rates after 5 years collected by Miralbell et al[35] are separated into 4 groups: low-intermediate risk (left panel) versus high risk (center panel) and therapy solely with photon irradiation (green dots) versus addition of ADT (pink crosses), plotted against the BED of each treatment regimen. Poisson TCP curves are fitted to each group. The fitted parameters γ and $TBED_{50}$ are provided in each panel, with the colors corresponding to the fitted curve. The TCP prediction for the IPI trial is weighted according to the IPI cohorts' risk stratification and plotted in the right panel. Boxplots in the right panel indicate the mMKM-based BED applied during the IPI trial and observed biochemical relapse-free survival after 5 years. *Abbreviations:* ADT = *androgen deprivation therapy*; BED = *biological effective dose*; mMKM = *modified microdosimetric kinetic model*; RBE = *relative biological effectiveness*; TCP = *tumor control probability; bRFs = biochemical relapse-free survival.*

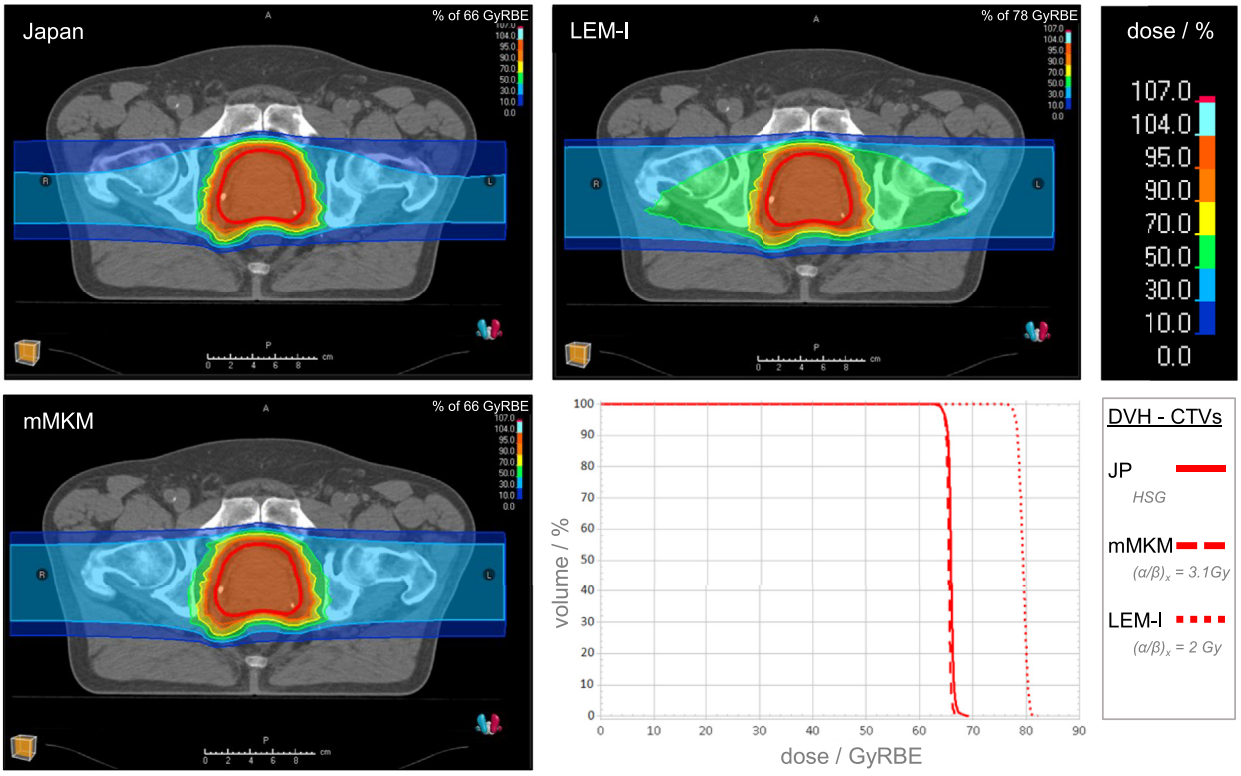

Fig. 4. Top left panel: Japanese-like optimization of the prostate treatment for Patient A using 2 opposing fields irradiated on alternating days. Bottom left panel: recalculation of the Japanese plan applying mMKM with $(\alpha/\beta)_x$ = 3.1 Gy. Top right panel: recalculation of the Japanese plan using LEM-I with $(\alpha/\beta)_x$ = 2 Gy. Note the scale change in the applied color bar. Bottom right panel: $D_{RBE}VH$ comparison of the 3 optimization approaches. With the same physical dose, as expected, LEM-I yields a much higher biological dose than the JP and mMKM approaches. *Abbreviations*: $D_{RBE}VH$ = *RBE-weighted dose-volume histogram*; JP = *Japanese-like*; LEM-I = *Local Effect Model, version 1*[20]; mMKM = *modified microdosimetric kinetic model*; RBE = *relative biological effectiveness.*

Table 1 Dose-volume histogram statistics of carbon ion planning approaches

Patient (clinical target volume)	Plan and RBE model	Dose/GyRBE						
		$D_{99\%}$	$D_{98\%}$	$D_{95\%}$	Average	$D_{50\%}$	$D_{2\%}$	$D_{1\%}$
Patient A (273.12 cm^3) largest	JP	64.08	64.47	65.03	65.97	66.00	67.18	67.49
	JP → LEM-I $(\alpha/\beta)_x$ = 2 Gy	77.32	77.66	78.10	79.42	79.48	80.84	81.01
	JP → mMKM $(\alpha/\beta)_x$ = 3.1 Gy	64.20	64.48	64.87	65.56	65.58	66.40	66.62
Patient B (114.19 cm^3)	JP	65.27	65.35	65.50	65.97	65.96	66.73	66.98
	JP → LEM-I $(\alpha/\beta)_x$ = 2 Gy	75.13	75.41	75.95	77.92	78.11	79.18	79.28
	JP → mMKM $(\alpha/\beta)_x$ = 3.1 Gy	65.08	65.15	65.25	65.60	65.60	66.12	66.29
Patient C (104.17 cm^3) median	JP	65.13	65.28	65.47	66.01	66.00	66.80	66.95
	JP → LEM-I $(\alpha/\beta)_x$ = 2 Gy	76.16	76.58	77.13	78.35	78.44	79.44	79.54
	JP → mMKM $(\alpha/\beta)_x$ = 3.1 Gy	64.99	65.09	65.22	65.62	65.62	66.19	66.30
Patient D (101.62 cm^3)	JP	63.61	64.11	64.75	65.93	66.01	67.09	67.34
	JP → LEM-I $(\alpha/\beta)_x$ = 2 Gy	75.56	75.94	76.34	77.88	77.97	79.43	79.63
	JP → mMKM $(\alpha/\beta)_x$ = 3.1 Gy	63.90	64.27	64.72	65.58	65.64	66.40	66.57
Patient E (52.83 cm^3) smallest	JP	65.27	65.35	65.50	65.97	65.96	66.73	66.98
	JP → LEM-I $(\alpha/\beta)_x$ = 2 Gy	75.13	75.41	75.95	77.92	78.11	79.18	79.28
	JP → mMKM $(\alpha/\beta)_x$=3.1 Gy	65.08	65.15	65.25	65.60	65.60	66.12	66.29

D_{RBE}VH characteristics for comparison of 3 biological planning approaches: (a) Japanese-like 2 opposing beams irradiated on alternating days; (b) recalculation of the Japanese-likeplan applying the clinical standard LEM-I with $(\alpha/\beta)_x$ = 2 Gy; and (c) recalculation of the Japanese-like plan applying the proposed mMKM with $(\alpha/\beta)_x$ = 3.1 Gy. Evaluated patients are ordered according to clinical target volume.

Abbreviations: D_{RBE}VH = *RBE-weighted dose-volume histogram*; JP = *Japanese-like;* LEM-I = *Local Effect Model, version 1*[20]; mMKM = *modified microdosimetric kinetic model*; RBE = *relative biological effectiveness*.

effective $D_{95\%}$ of the CTV is 65.03 $GyRBE_{JP}$, whereas LEM-I yields 78.10 $GyRBE_{LEM\text{-}I}$ and mMKM 64.87 $GyRBE_{mMKM3.1}$. For the $D_{50\%}$, the Japanese-like plan yields 66.00 $GyRBE_{JP}$, whereas the LEM-I and mMKM plan have a $D_{50\%}$ of 79.48 $GyRBE_{LEM\text{-}I}$ and 65.58 $GyRBE_{mMKM3.1}$, respectively. Further DVH statistics are provided in Table 1, together with the results for 4 additional patients.

Comparison of mMKM-optimized treatment plans with proton, helium, and carbon ions

The mMKM-based optimization of each ion for the largest tumor volume resulted in the biological dose distributions depicted in Figure 5 (results for median and smallest CTV are shown in Figs. E6 and E7). The attempted target coverage of at least 95% biological dose at 99.5% of the CTV was met for all 3 treatment plans with 63.51 $GyRBE_{1.1}$, 63.22 $GyRBE_{mMKM3.1}$, and 63.35 $GyRBE_{mMKM3.1}$ for protons, carbon, and helium ions, respectively. The homogeneity index ($D_{95\%}/D_{5\%}$) was at 0.97 for protons and carbon ions. In the helium treatment plan, the homogeneity index was slightly higher at 0.98.

Average biological dose to the rectum $D_{50\%}$ (an independent risk factor for late rectal morbidity)[55] was noticeably reduced from 21.66 $GyRBE_{1.1}$ for protons to 14.65 $GyRBE_{mMKM}$ and 15.38 $GyRBE_{mMKM}$ for carbon and helium ions, respectively. The rectum biological dose $D_{2\,cc}$ (ie, the

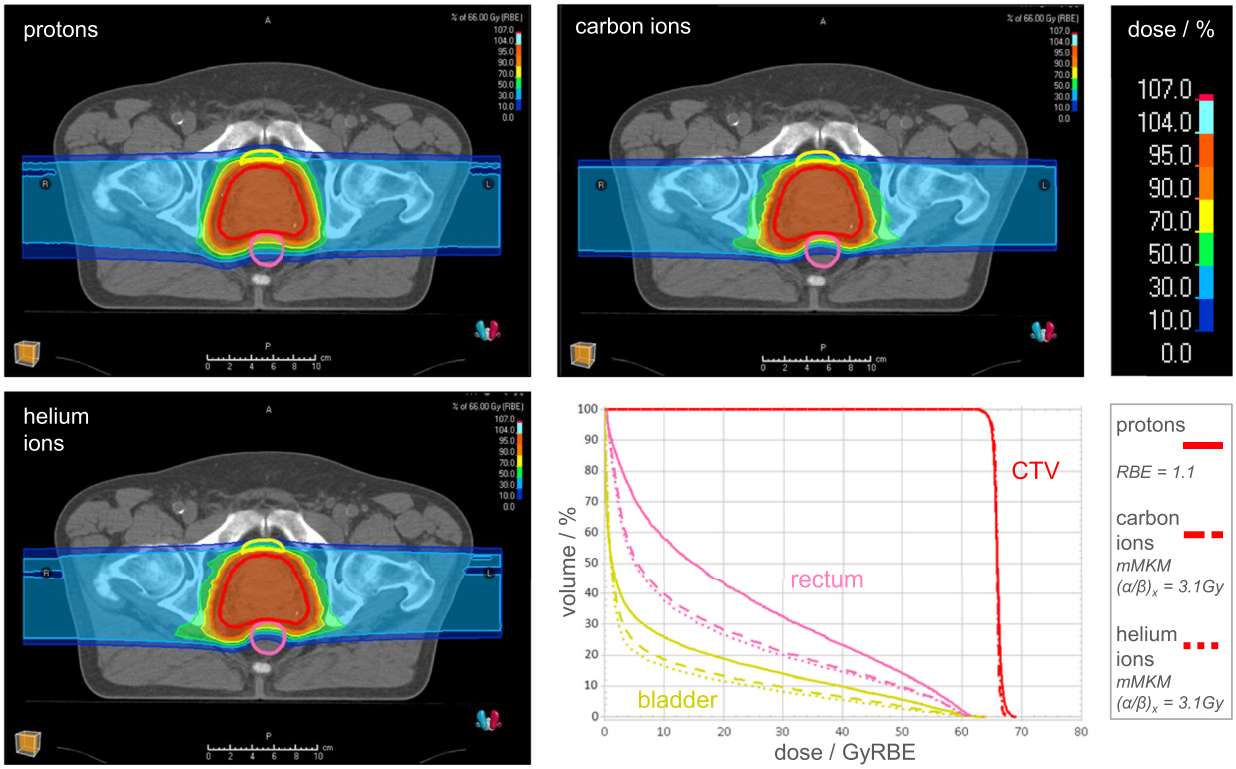

Fig. 5. Comparing protons (upper-left panel), carbon ions (upper-right panel), and helium ions (lower-left panel) treatment plans optimized using mMKM with $(\alpha/\beta)_x = 3.1$ Gy. The $D_{RBE}VH$ comparison in the bottom right panel indicates a considerable dose reduction in rectum (pink) and bladder (yellow) for carbon (dotted) and helium ions (dashed) compared with protons (solid). The CTV (red) coverage remains approximately the same for all ions. *Abbreviations:* CTV = *clinical target volume;* $D_{RBE}VH$ = *RBE-weighted dose-volume histogram*; mMKM = *modified microdosimetric kinetic model*; *RBE = relative biological effectiveness*.

biological dose received by 2.00 cm^3) was 59.47 $GyRBE_{1.1}$, 58.36 $GyRBE_{mMKM}$, and 58.33 $GyRBE_{mMKM}$ for protons, carbon, and helium ions, respectively.

The biological dose to the bladder could be reduced from $D_{5\ cc} = 56.36\ GyRBE_{1.1}$ for protons to 50.25 $GyRBE_{mMKM}$ and 52.57 $GyRBE_{mMKM}$ for carbon and helium ions, respectively. This patient had a contoured bladder volume of 202.26 cm^3, so 5 cm^3 corresponded to 2.5% of the bladder volume. Further analysis is reported in Table E8, together with the DVH statistics of the 2 additional cases.

Discussion

The IPI trial[17,18] employing 66 GyRBE protons or ^{12}C ions in 20 fractions found that protons were extensively more effective than carbon ions in terms of 5-year progression-free survival: 85% ^{1}H versus 50% ^{12}C ions.[19] Based on this inconsistency, we decided to evaluate the 2 patient groups using a modern validated biological model such as mMKM.[21,27] The aim of the investigation was to find radiobiological tissue parameters and a TCP model that is capable of explaining the deviations between proton and carbon ion arms of the IPI trial. The created TCP/mMKM framework should function consistently for photons, protons, and heavier ions. For tumor tissue parameters, we chose those suggested by Wang et al[37]: $(\alpha/\beta)_x = 3.1$ Gy, with $\alpha_x = 0.15\ Gy^{-1}$ and $\beta_x = 0.0484\ Gy^{-2}$.

Evaluation of dose and LET_d in clinical patient cohort of IPI trial

As shown in Figures 1 and 2, variable RBE predictions for protons in the CTV, 1.125 ± 0.007, calculated using $D_{50\%}$ of the CTV, matched with the clinically assumed RBE of 1.1. However, regions of higher RBE in the CTV are expected in the distal parts and at the borders of the fields where the highest LET_d regions are located (Figs. 1 and 2). In general, the biological recalculations for the proton arm support the clinical findings in terms of 5-year bRFS based on literature expectation.[19] Biological recalculations with mMKM demonstrated severe under dosage of about 20% for carbon ions, as displayed in Figures 1 and 2, pointing to a less effective treatment in terms of tumor control as noted clinically. Recalculations with LEM-I and the LQ parameters of Wang et al[37] predicted an underdosage for the carbon ion arm of about 10% compared with the proton arm. Additionally, an enhanced patient-to-patient variation of the biological dose was observed for the recalculations with mMKM (Fig. 2). This effect might result from

differences in RBE-LET prediction between LEM-I and mMKM.[21] The observed variation of LET_d in the proton cohort was lower than in IPI's carbon ion cohort.

TCP prediction and validation against different planning approaches

To quantitatively predict the clinical 5-year progression-free survival starting from the mMKM-based patient specific calculations, we developed a Poisson TCP model starting from the photon data available in literature converted in BED using an $(\alpha/\beta)_x = 3.1$ Gy and stratified in terms of low-intermediate risk (left panel of Fig. 3) versus high risk (center panel of Fig. 3) and with or without the usage of ADT. Applying the mMKM/TCP model, we could predict within 2% the IPI clinical data for both proton and carbon ions, as shown in the right panel of Figure 3. It is thus possible that the reduced TCP in the carbon ion arm originates from a drastic overestimation of effective dose by the LEM-I biomodel employing $(\alpha/\beta)_x = 2$ Gy. In fact, using $(\alpha/\beta)_x = 3.1$ Gy with LEM-I, we obtained a TCP of 72%. As such, the inconsistency in the clinical results can only partially be explained by the choice of radiosensitivity parameters for prostate. The choice of an appropriate radiobiological model plays an important part. In addition to mMKM, newer versions of the local effect model, such as LEM-IV, might also provide more appropriate predictions of biological dose.

The IPI trial was designed in terms of 66 $GyRBE_{LEM-I}$ in 20 fractions and relied on the Japanese clinical experience with carbon ions,[45] which used the same fractionation scheme but applied the Japanese biological model. As described by Fossati et al[7] and Molinelli et al,[8] $GyRBE_{JP}$ for tumor targets needs to be accurately translated to $GyRBE_{LEM-I}$, and the conversion is dose and tumor volume dependent. As shown in Figure 4, clinical LEM-I based effective $D_{50\%}$ to the CTV is 20.4% higher than the Japanese-like effective dose, whereas $mMKM_{3.1}$ yields a $D_{50\%}$ that is 0.6% lower. Other DVH parameters show about the same 20% overestimation of effective dose for LEM-I compared with Japanese and $mMKM_{3.1}$-based dose (see Table 1). The conversion factor calculated by Fossati et al[7] would be about 18% for the prescribed doses of the IPI trial, which matches our results well, as Figures 4 and E2 to E5 indicate. Hence, we believe that mMKM-based clinical trials could be more effective for prostate patient treatment for carbon ions without requiring tedious patient to patient conversion between different biological approaches (LEM-I vs JP).

We additionally investigated the prediction power of our treatment planning and TCP model for other published prostate cancer TCP data of carbon ion treatments with similar fractionation schemes. Ishikawa et al published survival data of 66 $GyRBE_{JP}$ in 20 fractions,[11,36] which corresponds to a $BED_{3.1Gy}$ of about 136 Gy using our formalism. They reported bRFS after 4 years for risk-stratified cohorts. For true high-risk patients receiving ADT, they reported a 4-year bRFS of 85% with a 95% CI between 78% and 92%, which includes our predicted value of 80%. Their low-risk group had a 4-year bRFS of 87% (95% CI, 77%-98%; without ADT), and the rate for intermediate-risk patients was 97% (95% CI, 92%-100%; with ADT). Without ADT, our model predicts 88.8% tumor control, which is in good agreement with their reported data.

Based on the data presented in this work, mMKM seems to be a good candidate for clinical biological calculations in carbon ion therapy for prostate cancer.

Expansion of RBE/TCP framework to helium ions

The potential advantage of the reduced lateral scattering of helium compared with protons,[54,56,57] resulting in lower dose in bladder and rectum, has been explored in this paper. As shown for patients with low and high CTV in Figures E2 and E5, respectively, we were able to reduce the relevant DVH parameters for toxicity D_{5cc} in bladder and D_{2cc} in rectum[58] while keeping the same level of coverage. Helium ions could become an interesting modality for the treatment of prostate cancer.

Limitations of the framework

The mMKM/TCP framework reproduces well our clinical experience and the Japanese data using the same fractionation scheme. However, our approach may still have limitations that require future studies with ad hoc clinical trials. For example, we assigned the same $(\alpha/\beta)_x$ of 3.1 Gy for both low-intermediate and high-risk tumors, and a differentiation of the radiosensitivity could not be excluded. Additionally, we included the ADT effect in a binary fashion (ie, with or without), neglecting for example the time span of the adjuvant therapy. For optimal decision on prescription doses, further adjustment of RBE and TCP models to individualized tumor properties, such as genome-adjusted radiation doses (GARD),[59] might become necessary. However, incorporating particle and LET dependency into the GARD framework will require extensive research.

Thus far, our framework has been developed and validated only for prostate cancer. However, extension to other treatment sites is foreseen by further investigating appropriate tissue and model parameters.

Conclusion

In this work, a particle therapy treatment planning and TCP prediction framework was developed for prostate cancer. The framework was successfully validated against our clinical data for proton and carbon ion therapy and extended to helium ion beams. It employs the mMKM as the radio-biological model and accounts for patient risk classification and usage of ADT. Helium ions could be more advantageous than protons for prostate treatment due to the superior sparing of the rectum and bladder.

References

1. Mohler JL, Antonarakis ES, Armstrong AJ, et al. Prostate cancer, version 2.2019, NCCN clinical practice guidelines in oncology. *J Natl Compr Canc Netw* 2019;17:479-505.
2. Schwarz M, Molinelli S. What can particle therapy add to the treatment of prostate cancer? *Phys Med* 2016;32:485-491.
3. Jäkel O, Kraft G, Karger CP. The history of ion beam therapy in Germany. *Z Für Med Phys* 2022;32:6-22.
4. Okada T, Kamada T, Tsuji H, et al. Carbon ion radiotherapy: Clinical experiences at National Institute of Radiological Science (NIRS). *J Radiat Res (Tokyo)* 2010;51:355-364.
5. Degiovanni A, Amaldi U. History of hadron therapy accelerators. *Phys Med* 2015;31:322-332.
6. Slater JM, Archambeau JO, Miller DW, Notarus MI, Preston W, Slater JD. The proton treatment center at Loma Linda University Medical Center: Rationale for and description of its development. *Int J Radiat Oncol* 1992;22:383-389.
7. Fossati P, Molinelli S, Matsufuji N, et al. Dose prescription in carbon ion radiotherapy: A planning study to compare NIRS and LEM approaches with a clinically-oriented strategy. *Phys Med Biol* 2012;57:7543-7554.
8. Molinelli S, Magro G, Mairani A, et al. Dose prescription in carbon ion radiotherapy: How to compare two different RBE-weighted dose calculation systems. *Radiother Oncol* 2016;120:307-312.
9. Choi K, Molinelli S, Russo S, et al. Rectum dose constraints for carbon ion therapy: Relative biological effectiveness model dependence in relation to clinical outcomes. *Cancers* 2019;12:46.
10. Slater JD, Rossi CJ, Yonemoto LT, et al. Proton therapy for prostate cancer: The initial Loma Linda University experience. *Int J Radiat Oncol* 2004;59:348-352.
11. Ishikawa H, Tsuji H, Kamada T, et al. Carbon ion radiation therapy for prostate cancer: Results of a prospective phase II study. *Radiother Oncol* 2006;81:57-64.
12. Walsh S, Roelofs E, Kuess P, et al. A validated tumor control probability model based on a meta-analysis of low, intermediate, and high-risk prostate cancer patients treated by photon, proton, or carbon-ion radiotherapy: TCP of prostate cancer treated EBRT. *Med Phys* 2016;43:734-747.
13. Rørvik E, Fjæra LF, Dahle TJ, et al. Exploration and application of phenomenological RBE models for proton therapy. *Phys Med Biol* 2018;63185013.
14. Marteinsdottir M, Paganetti H. Applying a variable relative biological effectiveness (RBE) might affect the analysis of clinical trials comparing photon and proton therapy for prostate cancer. *Phys Med Biol* 2019;64115027.
15. Kawamura H, Kubo N, Sato H, et al. Moderately hypofractionated carbon ion radiotherapy for prostate cancer: A prospective observational study "GUNMA0702". *BMC Cancer* 2020;20:75.
16. Bao A, Barsky AR, Both S, et al. Case-matched outcomes of proton beam and intensity-modulated radiation therapy for localized prostate cancer. *Int J Part Ther* 2023;10:1-12.
17. Habl G, Hatiboglu G, Edler L, et al. Ion Prostate Irradiation (IPI) - a pilot study to establish the safety and feasibility of primary hypofractionated irradiation of the prostate with protons and carbon ions in a raster scan technique. *BMC Cancer* 2014;14:202.
18. Habl G, Uhl M, Katayama S, et al. Acute toxicity and quality of life in patients with prostate cancer treated with protons or carbon ions in a prospective randomized Phase II study–The IPI trial. *Int J Radiat Oncol Biol Phys* 2016;95:435-443.
19. Eichkorn T, Karger CP, Brons S, et al. Results of a prospective randomized trial on long-term effectiveness of protons and carbon ions in prostate cancer: LEM I and α/β = 2 Gy overestimates the RBE. *Radiother Oncol* 2022;173:223-230.
20. Scholz M, Kellerer AM, Kraft-Weyrather W, Kraft G. Computation of cell survival in heavy ion beams for therapy. *Radiat Environ Biophys* 1997;36:59-66.
21. Mein S, Klein C, Kopp B, et al. Assessment of RBE-weighted dose models for carbon ion therapy toward modernization of clinical practice at HIT: In vitro, in Vivo, and in patients. *Int J Radiat Oncol Biol Phys* 2020;108:779-791.
22. Hawkins RB. A statistical theory of cell killing by radiation of varying linear energy transfer. *Radiat Res* 1994;140:366.
23. Inaniwa T, Furukawa T, Kase Y, et al. Treatment planning for a scanned carbon beam with a modified microdosimetric kinetic model. *Phys Med Biol* 2010;55:6721-6737.
24. Hawkins RB. A microdosimetric-kinetic model for the effect of non-Poisson distribution of lethal lesions on the variation of RBE with LET. *Radiat Res* 2003;160:61-69.
25. Inaniwa T, Kanematsu N, Matsufuji N, et al. Reformulation of a clinical-dose system for carbon-ion radiotherapy treatment planning at the National Institute of Radiological Sciences, Japan. *Phys Med Biol* 2015;60:3271-3286.
26. Mein S, Dokic I, Klein C, et al. Biophysical modeling and experimental validation of relative biological effectiveness (RBE) for 4He ion beam therapy. *Radiat Oncol* 2019;14 123.
27. Mairani A, Magro G, Tessonnier T, et al. Optimizing the modified microdosimetric kinetic model input parameters for proton and ^{4}He ion beam therapy application. *Phys Med Biol* 2017;62:N244-N256.
28. Magro G, Dahle TJ, Molinelli S, et al. The FLUKA Monte Carlo code coupled with the NIRS approach for clinical dose calculations in carbon ion therapy. *Phys Med Biol* 2017;62:3814-3827.
29. Ishikawa H, Hiroshima Y, Kanematsu N, et al. Carbon-ion radiotherapy for urological cancers. *Int J Urol* 2022;29:1109-1119.
30. Van Leeuwen CM, Oei AL, Crezee J, et al. The alfa and beta of tumours: A review of parameters of the linear-quadratic model, derived from clinical radiotherapy studies. *Radiat Oncol* 2018;13:96.
31. Levegrün S, Jackson A, Zelefsky MJ, et al. Risk group dependence of dose–response for biopsy outcome after three-dimensional conformal radiation therapy of prostate cancer. *Radiother Oncol* 2002;63:11-26.
32. Jones CU, Hunt D, McGowan DG, et al. Radiotherapy and short-term androgen deprivation for localized prostate cancer. *N Engl J Med* 2011;365:107-118.
33. Jones CU, Pugh SL, Sandler HM, et al. Adding short-term androgen deprivation therapy to radiation therapy in men with localized prostate cancer: Long-term update of the NRG/RTOG 9408 randomized clinical trial. *Int J Radiat Oncol* 2022;112:294-303.
34. Bolla M, Maingon P, Carrie C, et al. Short androgen suppression and radiation dose escalation for intermediate- and high-risk localized prostate cancer: Results of EORTC trial 22991. *J Clin Oncol* 2016;34:1748-1756.
35. Miralbell R, Roberts SA, Zubizarreta E, Hendry JH. Dose-fractionation sensitivity of prostate cancer deduced from radiotherapy outcomes of 5,969 patients in seven international institutional datasets: α/β = 1.4 (0.9–2.2) Gy. *Int J Radiat Oncol* 2012;82:e17-e24.
36. Kang Y, Ishikawa H, Inaniwa T, et al. The clinical relative biological effectiveness and prostate-specific antigen kinetics of carbon-ion radiotherapy in low-risk prostate cancer. *Cancer Med* 2023;12:1540-1551.
37. Wang JZ, Guerrero M, Li XA. How low is the α/β ratio for prostate cancer? *Int J Radiat Oncol* 2003;55:194-203.
38. A Ferrari, PR Sala, A Fassó, J Ranft, FLUKA: A multi-particle transport code. CERN-2005-10 (2005), INFN/TC_05/11, SLAC-R-773. Available at: http://www.slac.stanford.edu/pubs/slacreports/reports16/slac-r-773.pdf. Accessed March 20, 2024.
39. Böhlen TT, Cerutti F, Chin MPW, et al. The FLUKA code: Developments and challenges for high energy and medical applications. *Nucl Data Sheets* 2014;120:211-214.
40. Kopp B, Mein S, Tessonnier T, et al. Rapid effective dose calculation for raster-scanning 4He ion therapy with the modified microdosimetric kinetic model (mMKM). *Phys Med* 2021;81:273-284.
41. Kopp B, Fuglsang Jensen M, Mein S, Hoffmann L, Nyström H, Falk M, Haberer T, Abdollahi A, Debus J, Mairani A. FRoG: An independent dose and LET_d prediction tool for proton therapy at ProBeam® facilities. *Med. Phys* 2020;47:5274-5286.

42. Mein S, Choi K, Kopp B, et al. Fast robust dose calculation on GPU for high-precision 1H, 4He, 12C and 16O ion therapy: the FRoG platform. *Sci Rep* 2018;8:14829.
43. Suzuki M, Kase Y, Yamaguchi H, Kanai T, Ando K. Relative biological effectiveness for cell-killing effect on various human cell lines irradiated with heavy-ion medical accelerator in Chiba (HIMAC) carbon-ion beams. *Int J Radiat Oncol* 2000;48:241-250.
44. Kanai T, Endo M, Minohara S, et al. Biophysical characteristics of HIMAC clinical irradiation system for heavy-ion radiation therapy. *Int J Radiat Oncol* 1999;44:201-210.
45. Tsuji H, Yanagi T, Ishikawa H, et al. Hypofractionated radiotherapy with carbon ion beams for prostate cancer. *Int J Radiat Oncol* 2005;63:1153-1160.
46. D'Amico AV. Biochemical outcome after radical prostatectomy, external beam radiation therapy, or interstitial radiation therapy for clinically localized prostate cancer. *JAMA* 1998;280:969-974.
47. Schaeffer E, Srinivas S, Antonarakis ES, et al. NCCN Guidelines insights: Prostate cancer, version 1.2021: Featured updates to the NCCN guidelines. *J Natl Compr Canc Netw* 2021;19:134-143.
48. Haberer T, Becher W, Schardt D, Kraft G. Magnetic scanning system for heavy ion therapy. *Nucl Instrum Methods Phys Res Sect Accel Spectrometers Detect Assoc Equip* 1993;330:296-305.
49. Roach M, Hanks G, Thames H, et al. Defining biochemical failure following radiotherapy with or without hormonal therapy in men with clinically localized prostate cancer: Recommendations of the RTOG-ASTRO Phoenix Consensus Conference. *Int J Radiat Oncol* 2006;65:965-974.
50. Royce TJ, Mavroidis P, Wang K, et al. Tumor control probability modeling and systematic review of the literature of stereotactic body radiation therapy for prostate cancer. *Int J Radiat Oncol* 2021;110:227-236.
51. Warkentin B, Stavrev P, Stavreva N, Field C, Fallone BG. A TCP-NTCP estimation module using DVHs and known radiobiological models and parameter sets. *J Appl Clin Med Phys* 2004;5:50-63.
52. Källman P, Ågren A, Brahme A. Tumour and normal tissue responses to fractionated non-uniform dose delivery. *Int J Radiat Biol* 1992;62:249-262.
53. Kamada T, Tsujii H, Blakely EA, et al. Carbon ion radiotherapy in Japan: An assessment of 20 years of clinical experience. *Lancet Oncol* 2015;16:e93-e100.
54. Tessonnier T, Ecker S, Besuglow J, et al. Commissioning of helium ion therapy and the first patient treatment with active beam delivery. *Int J Radiat Oncol* 2023;116:935-948.
55. Ishikawa H, Tsuji H, Kamada T, et al. Risk factors of late rectal bleeding after carbon ion therapy for prostate cancer. *Int J Radiat Oncol* 2006;66:1084-1091.
56. Mairani A, Mein S, Blakely E, et al. Roadmap: Helium ion therapy. *Phys Med Biol* 2022;67:15TR02.
57. Besuglow J, Tessonnier T, Kopp B, Mein S, Mairani A. The evolution of lateral dose distributions of helium Ion beams in air: From measurement and modeling to their impact on treatment planning. *Front Phys* 2022;9:797354.
58. Okonogi N, Fukahori M, Wakatsuki M, et al. Dose constraints in the rectum and bladder following carbon-ion radiotherapy for uterus carcinoma: A retrospective pooled analysis. *Radiat Oncol* 2018;13:119.
59. Nolan B, O'Sullivan B, Golden A. Exploring breast and prostate cancer RNA-seq derived radiosensitivity with the Genomic Adjusted Radiation Dose (GARD) model. *Clin Transl Radiat Oncol* 2022;36:127-131.

Part III

Discussion and Outlook

7 Reflection

Since the installation of the helium ion source at Heidelberg Ion Beam Therapy Center (HIT) in 2012 [6], much progress was made towards their clinical application. In 2021, a first patient could be treated with active raster-scanned helium ions [13, 215, 216]. This chapter reflects on the necessary steps and challenges taken by its author to facilitate the commissioning of a commercial clinical treatment planning system (TPS) (RayStation®, RaySearch Laboratories, Stockholm, Sweden) for helium ions and its regular clinical application.

7.1 Dosimetry and Simulation of Base Data for a Treatment Planning System

The first step towards a TPS was collecting base data of the physical beam properties. The methodology of which is extensively described in sections 3.1 to 3.3.

Laterally integrated depth dose distributions (IDDs) of individual Bragg peaks (BPs) in water build the backbone for any beam model as they provide information on the dose and the position of the peak for each initial beam energy. The water-equivalent depth of a tumor determines which beam energies are best used for treatment. For 28 initial beam energies, these distributions were measured with the PEAKFINDER® (section 3.2.1 and Table A.1). The measurements were compared to simulations of the Monte Carlo (MC) code Fluktuierende Kaskade (FLUKA) [169–171, 174]. Within the MC simulation, the momentum distribution of each quasi-mono-energetic beam was determined to match the measured depth dose distributions. At the depth, where impacting ions have an energy around 100 MeV, a 'bump' appeared in the simulated IDDs. This energy coincides with the transition between two models of interactions, the relativistic quantum molecular dynamics model (RQMD) and the Boltzmann Master equation (BME). This 'bump' was resolved by smoothing the transition energy range, gradually weighting the two models. When adjusting the momentum distribution, the curves were scaled by the area under the curve, which resulted in a mean square deviation of less than 1 %. However, scaling to absolute dosimetry at a fixed position was necessary. Scaling in the entrance channel at 2 cm depth resulted in a substantial deviation of peak height of 4 %. The deviation of peak heights differed among the tested versions of FLUKA.

Lateral dose profiles were extracted from the simulation, once the simulation parameters adequately reproduced measured IDDs. Measurements with the OCTAVIUS® 1000 SRS P phantom (sections 3.2.2 and 3.2.3) were compared to the simulated beam width. Where necessary, the initial beam width (Gaussian full width at half maximum (FWHM)) at the virtual source axis distance (VSAD) in vacuum of the simulation was refined. This process has been described in depth in the first publication (Chapter 4, [14]). Single, double and triple Gaussian functions were fitted to the lateral profiles along the beam path in air and water. These envelope functions are used for the analytical beam model of the independent fast calculation machine Fast Recalculation on GPU (FRoG) [185, 186]. This quantification of lateral scattering was repeated for the already established proton and carbon ion beams at HIT. For the clinical TPS, RaySearch Laboratories performed their own modeling from the simulated lateral beam profiles. Since the gantry's isocentre is closer to the beam line exit and beam application and monitoring system (BAMS) chambers than in the horizontal treatment rooms, the process of finding reasonable initial beam widths at the VSAD was repeated for the gantry.

In the low dose region of the lateral profiles below 0.1 % of the local maximum, the simulation underestimated the dose. Adding a double Gaussian beam profile at the VSAD, with the second Gaussian weighted to about 1 % to 7.5 % amplitude, improved the match of lateral profiles. Simulating the IDDs with this initial double Gaussian lateral beam profile improved the match of entrance-to-peak ratio (EPR) with measured depth dose profiles. Figure 7.1 shows the impact of the double Gaussian initial fluence profile on lateral dose distribution in air and along the IDD for one investigated initial beam energy. Deviations of about ±10 % in lateral FWHM of the beam at the isocentre, were shown to have little effect on the dose distribution of a patient treatment plan in Chapter 4.

Cubic treatment volumes, so called spread-out Bragg peaks (SOBPs), were recalculated with FLUKA versions fluka2019.2.dev and fluka2020.3.dev. The same SOBP plans were measured in a water tank (section 3.2.5). Especially for higher energies where the EPR of individual BPs had already deviated between simulation and measurement, the comparison showed some discrepancies. As the irradiation plans for these SOBPs were optimized with an older beam data set, the recalculated dose in the plateau was not flat. Together with the positioning uncertainty of the measurements, the comparison of doses was even harder. With implementation of the double Gaussian lateral beam profile, the deviations could nonetheless be reduced to about ±4 % of the mean dose. This remaining deviation is within the acceptance limit of verification measurements.

Ultimately, RaySearch Laboratories used the measured IDDs as base data for their helium ion beam model. So the slightly larger discrepancies in EPR should not have any significant effect on dose calculation within RayStation®. Measurements of the high dose region in RayStation® optimized SOBPs were within

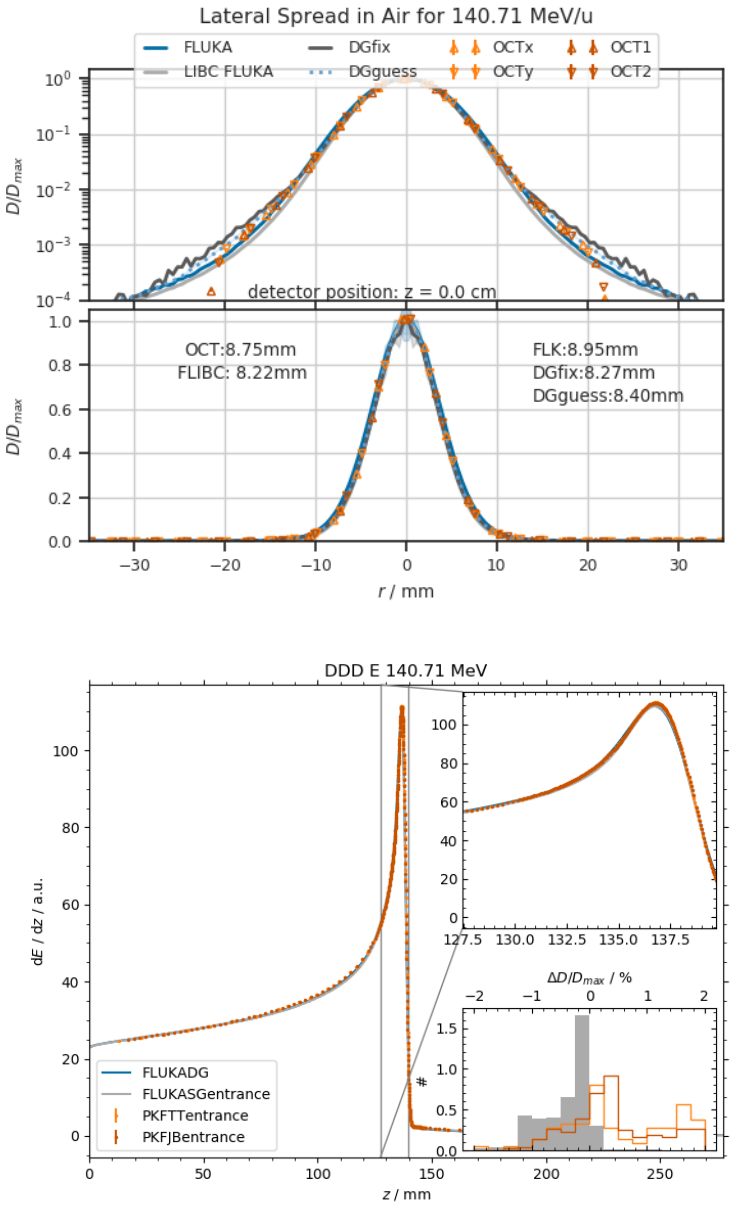

Figure 7.1: The initial beam profile in vacuum influences the low dose penumbra of (a) the lateral dose distribution in air and (b) the depth dose distribution in water. FLUKA simulation with a single Gaussian (SG) in gray is compared to initial double Gaussian (DG) beam shape in blue. Measured dose is depicted by orange markers.

2 % of the predicted local dose, with 85 % of the measured point doses matching within 1 % (compare Chapter 5, [13]).

A collection of secondary particle fluences, their energies and dose-averaged linear energy transfer (LET_d) was simulated. These so called *secondary particle spectra* are used for the biological dose calculation in the analytical dose model of the commercial TPS, see Chapter 5 [13]. The spectra are also required for calculation of biologically weighted dose in FRoG [97]. The review of Norbury et al. [39] requested more precise measurements of the nuclear interaction cross-sections and double differential yields. Once the FLUKA code will be validated against such new measurements, the MC-simulated secondary particle spectra and dose distributions might reproduce measured clinical dose distributions even more closely.

7.2 Commissioning of the Commercial Treatment Planning System

With all the base data gathered, RaySearch Laboratories developed its own analytical pencil beam algorithm for helium ions and released it in the end of 2020 [194]. RayStation® thus became the first commercial TPS for helium ions. It was then the responsibility of the clinical staff at HIT to commission this new TPS. Details of the commissioning process are published in the second publication (Chapter 5, [13]). It validated the dose predictions and thus base data of RayStation® against measurements in simple and more complex scenarios. Commissioning was successful, showing very good agreement between measurements and TPS predictions even in an anthropomorphic phantom. The availability of a commercial CE-labeled TPS, licensed under the "Medizinproduktegesetz", is an important prerequisite to begin clinical trials with active-scanning helium ions. Even before actual treatment of any patients, direct comparison of all clinically available ions (protons, helium and carbon ions) within one calculation and treatment platform allows for planning studies. Thus, advantages and disadvantages of each ion can be balanced against each other coherently. To facilitate the reasonable application of helium ions, planning studies can now predict treatment sites and tumor types, which will especially benefit from helium ion irradiation.

7.3 Treatment Planning on Patient Data

Because treatment outcome doesn't simply depend on the absorbed dose distribution in a patient, relative biological effectiveness (RBE) models for protons and carbon ions were investigated with regard to their applicability in helium ion treatment. For these means, the author investigated a past trial with protons and carbon ions in the third publication (Chapter 6, [15]). Published results of the Ion Prostate Irradiation (IPI) trial [200, 214, 217] promised a good starting

point to determine, which $(\alpha/\beta)_x$ combination as input for the modified Microdosimetric Kinetic Model (mMKM) best describes treatment outcome for proton and/or carbon ions. Once a parameter set of prostate tissue's radio-sensitivity to protons and carbon ions was found, the same model and parameter set was used to create helium ion treatment plans, that would potentially yield a comparable outcome. The applied RBE model and its calculation algorithm had previously been published by Mein et al. [82]. In the course of this RBE investigation for prostate cancer, biological databases for five parameter sets and two models were created as described in section 3.5. Ninety-one patients' treatment plans were recalculated with these parameters using the in house recalculation tool FRoG [185, 186]. In mMKM and Wang et al.'s [218] parameters ($(\alpha/\beta)_x = 3.1\,\mathrm{Gy}$), an RBE calculation model was found that adequately predicts tumor control probability (TCP) for protons and carbon ions. Its prediction capability for helium ions may only be assumed probable until clinical results for helium ion irradiation of prostate cancer become available. Ongoing work analyzes the normal tissue complication probability for organs at risk (OARs) in close proximity to the prostate [219].

7.4 Further Achievements

Towards the clinical application of helium ions, several side projects also yielded result useful for this and other projects.

The FRoG bio databases for proton, helium and carbon ions were updated for six combinations of radio-sensitivity parameters. In addition, the output of FRoG was altered to save dose-volume-histogram (DVH) curves and dose metrics. Thus, FRoG became capable to perform recalculations for large cohorts of patients, such as the treatment plans of the 91 IPI patients.

For RayStation®, the energy fluence spectra and bio databases were created for β_x in increments of $0.1\,\mathrm{Gy}^{-2}$ to facilitate multiple RBE estimates in the research version.

A framework for database creation was set up for the FLUKA code. Lateral base data for carbon ions with the clinical energy and focus settings FWHM6mm and FWHM10mm (compare to section 2.6) has already been created with this framework. It was implemented into RayStation®in summer 2021. In case additional clinical energy and focus combinations will be requested for clinical use, this framework allows the quick and systematic simulation of a new dose distribution database. The same applies for fluence spectra and z^*_{1d} databases of other ions or radiobiological parameters. Currently, the framework is currently used to create base data for an oxygen beam model.

8 Current and Future Clinical Context

As other centers are preparing for the application of helium ions [220–223], the implications of this work for current and future clinical research will be discussed in this chapter. The first section recapitulates historical helium ion therapy and presents current applications of the new clinical TPS. A second section focuses on the implications of this work on the treatment of prostate cancer. And lastly, open questions raised by this research are discussed.

8.1 Helium Treatments in History and Now

Previously, passively scattered helium ions were applied to a multitude of tumors. Over ten years of experience with helium ions at the Lawrence Berkeley National Laboratory [4] were followed by a more versatile new beam line at the Bevalac [5] after the shutdown of the 184"-synchrocyclotron in 1988. The BP of helium ions seemed a good alternative to conventional photon therapy for tumors in the eye [1, 224]. In 1984, Grizzard et al. reported the successful treatment of choroidal melanoma with helium ions preserving useful vision [225]. For uveal melanoma, helium ion therapy seemed to be even more effective than localized brachytherapy with I-125 plaques [2]. Without the availability of helium ions, other treatment methods for ocular melanoma became more prevalent, often balancing visual impairment against tumor control[226]. Blakely et al. [227] studied the late effects of helium ion irradiation, such as the cataract formation. Pancreatic carcinoma [3] were also treated with helium ions, yielding similar survival rates as other treatments available at the time. Arteriovenous malformations and angiographically occult vascular malformations were treated successfully as well [228].

For the past decade, active pencil beam scanning of helium ions was available for experimental research at HIT. In the meantime, pre-clinical studies in vivo [229] and in vitro [78, 82, 93, 230–233] have been evaluated and are still taking place to estimate the biological effectiveness of helium ions.

Since 2020, a clinically commissioned TPS became available due to the efforts of this works' author and many others [13, 94, 194]. This enabled the very first patient treatment with helium ions at HIT in summer of 2021, details of which were discussed in Chapter 5 [13]. To find tumor sites, which could benefit from helium ion treatment over protons or carbon ions, many *planning studies* have been performed in the mean time. An earlier TPS Hyperion tested helium ion

plans for pediatric tumors [234]. Specifically, irradiation of pediatric ependymoma [235] and juvenile nasopharyngeal angiofibroma [236] was investigated focussing on helium ions as treatment modality. Bonaccorsi et al. showed the benefit of helium ions as post-mastectomy irradiation for left-sided breast cancer [98]. And Tessonnier et al. compared meningioma treatments with protons and helium ions [237]. In Chapter 6 [15], we showed that helium ions might spare bladder and rectum to the same extend as carbon ions, without compromising the target coverage.

As of August 2024, a handful of patients were treated with helium ions. Each was provided with a choice between an established proton plan and a helium ion plan, carefully calculated with mMKM and $(\alpha/\beta)_x = 2\,\mathrm{Gy}$ for RBE estimation. A total of twenty-nine successful treatments are required by the "Bundesamt für Strahlenschutz" before Heidelberg's helium ion beam is approved for general clinical use[1]. A clinical trial is currently in preparation.

Future clinical application of helium ions might revolve around the application of multiple ions together [196, 238–240] to create smoother RBE or LET_d distributions. Another idea that is currently under investigation in pre-clinical and planning studies is spot-scanning hadron arc therapy [241–244].

8.2 Implications of Presented Research for the Treatment of Prostate Cancer

Since results of the IPI trial became eminent [214], carbon ion irradiation of prostate cancers at HIT was planned with Local Effect Model, version 1 (LEM-I) and $(\alpha/\beta)_x = 4\,\mathrm{Gy}$ to compensate the previous underdosage[2]. Dose to OARs is typically calculated with $(\alpha/\beta)_x = 10\,\mathrm{Gy}$ unless their radio-sensitivity is more precisely known. Most often proton irradiation would have been chosen, however.

With the results of the third publication in this thesis, the former approach for carbon ions does not seem justified anymore. Suggesting mild or ultra hypofraction is based on the presumption that the tumor's radio-sensitivity is lower than surrounding tissues. Bladder and rectum are commonly estimated to exhibit $(\alpha/\beta)_x$ between 3 Gy and 5 Gy. Although this is questioned by [245, 246], suggesting the $(\alpha/\beta)_x$ of the genitourinary system to be lower.

Recent publications on photon therapy tend to favor mild or even ultra-hypofractionated irradiation. The PACE A, B and C trials [247, 248] are testing the non-inferiority of normofractionated (78 Gy/ 39 irradiation fraction (Fx) over 7.8 weeks), mildy hypofractionated (62 Gy/ 20 Fx over 4 weeks) and ultra-hypofractionated photon irradiation (36.25 Gy/ 5 Fx over 1 to 2 weeks). The

[1] T. Tessonnier, personal communication, August 2024
[2] A. Mairani, personal communication

mildly hypofractionated FLAME trial [249–252] assumed a much lower $(\alpha/\beta)_x$ than our re-analysis of IPI suggested, but was unable to find risk factors corresponding to the higher survival with focal boosts [249]. The Radiation Therapy Oncology Group, USA (RTOG) 0938 trial [122] compared 5 and 12 fractions of hypofractionated photon therapy that resulted in a 5-year disease free survival of 89.6 % (95% CI: 84.0 % to 95.2 %) and 92.3 % (95% CI: 87.4 % to 97.1 %) at a biologically effective dose (BED) of 123.85 (36.25 Gy/ 5 Fx) and 125.56 (51.6 Gy/12 Fx). Lilleby et al. [121] warn that genitourinary and gastro-intestinal toxicity might increase with ultra-hypofractionated photon therapy because the radiobiology of these OARs is insufficiently reflected in planning. They suggest to infer patient reported outcome measures (PROMs) to improve the measurability of adverse effects, as the RTOG 0938 trial did. Very recent results of ultra-hypofractionated photon therapy are presented for the SPARC trial [253].

Corrao et al. showed in their meta-analysis [254], that proton therapy improved gastro-intestinal outcome and the 5y-survival for high risk/advanced prostate cancer patients. Results of the local PAROS trial[3] are still awaited. The Japanese experience with carbon ions has been gathered by Ishikawa et al. [255] and updated by Takakusagi et al. [256]. Their 12 fraction treatment with a total dose of 51.6 Gy_{NIRS} resulted in a 5-year biological relapse-free survival (bRFS) of 87.5 %, 93.7 % and 93.4 % depending on the risk group. The TCP model proposed in Chapter 6 would predict 73 % and 60 % for the equivalent biologically-weighted dose of 47.5 $Gy_{mMKM3.1}$ and corresponding BED of 108.34. Their four fraction trial[4] applies the equivalent of 26.8 $Gy_{mMKM3.1}$ to 30.7 $Gy_{mMKM3.1}$ corresponding to a BED of 85 to 106 and predicted TCP of 22 % to 47 % when $(\alpha/\beta)_x = 3.1$ Gy. In this ultra-hypofractionated region, mMKM like most other current RBE-models reaches its prediction limits. So either the switch to the stochastic microdosimetric kinetic model [116] or an inclusion of ultra-hypofractionated photon data in the fit of our TCP-model would be necessary to justify the assumption of $(\alpha/\beta)_x = 3.1$ Gy. Figure 8.1 indicates how the newer data relates to the TCP functions presented in Chapter 6.

For preparation of a future prostate trial with carbon or helium ions, the advancements of treatment planning and trials would certainly have to be taken into account. This includes following updated delineation guidelines [258–262]; eliminating certain treatment angles when prosthesis are present [263]; and considering heterogeneous prescription doses for dose escalation [264]. Combining treatments for high risk patients [265] is another option to reach about 95 % tumor control without suffering normal tissue complications. Choosing treatments based on predicted normal tissue complication probability (NTCP) like Chen et al. [266] might be an option, when several modalities promise similar tumor control. Considering the results and approaches presented in this thesis, the author certainly advises on the forward calculation of new treatment protocols with sev-

[3] https://www.clinicaltrials.gov/ct2/show/NCT04083937
[4] protocol 1891, UMIN000032340

eral RBE models[5] and to check the dose constraints for the full range of estimated $(\alpha/\beta)_x$. Constraints and dose prescriptions derived from the experience at other treatment centers require adequate conversion [267–273]. Dose predictions with mMKM seem to be consistent among protons, carbon and helium ions. Thus mMKM should at least be considered in the future. In cases, where the radiosensitivity is too uncertain, pushing the high linear energy transfer (LET) of the irradiation field inside the target promises a lower failure rate [240, 274].

[5] In cases other than prostate cancer, dose distributions have recently been optimized in both mMKM and LEM-I for some patients treated with carbon ions at HIT.

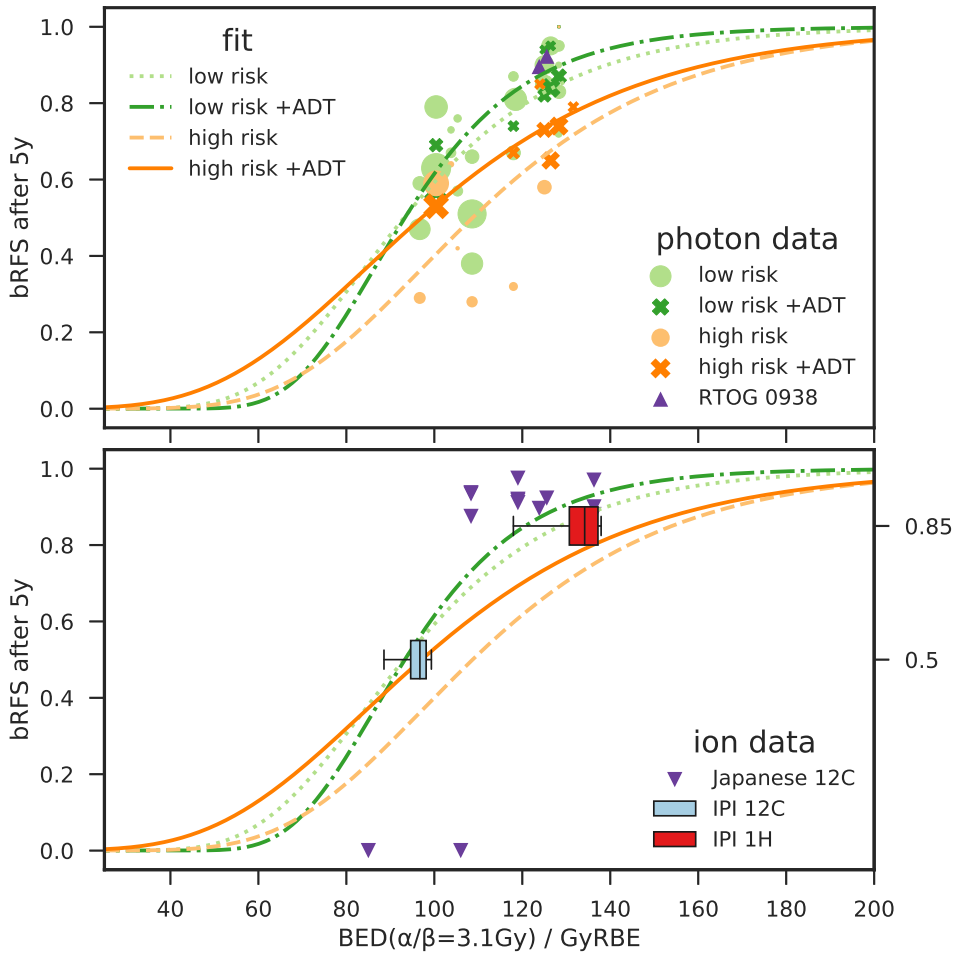

Figure 8.1: *Tumor control of prostate cancer patients against the BED of their treatment plan.* Photon data was stratified for usage of androgen deprivation therapy (ADT) and risk categories, with marker size denoting relative number of patients. IPI data shows forward calculated BED of RBE-weighted dose with Wang's parameters [218] for mMKM against bRFS prediction according to weighted TCP. Triangles mark additional data from more recent prostate trials [122, 255–257]. The fitted curves are the same as depicted in figure 3 of Chapter 6.

9 Outlook and Summary

After reflecting on the achievements of this project and putting them into the clinical context, this Chapter provides an outlook on future possibilities for their application.

Regarding the treatment of prostate cancer with carbon ions, two questions remain. The final decision on a mild or ultra hypo-fractionated treatment schedule, RBE model and thus treatment plan has to be taken by physicians. A possibility to optimize treatment plans with multiple RBE-models in future versions of RayStation® enables physicists to aid in that decision. Additionally aforementioned NTCP-based decision systems [266] might provide assistance. This leads to the second question, which regards the prediction of adverse effects and accounting for NTCP in a treatment plan. Chapter 6 showed the advantages of carbon and helium ions in sparing bladder and rectum. However, their radiosensitivity was considered to be the same as that of the prostate, which is a conservative assumption. Preliminary evaluation of a NTCP prediction based on the Lyman-Kutcher-Burman (LKB) model parameters published by Gulliford et al. [208] correctly predicted the rectal toxicity observed in the IPI trial [275]. More elaborate adaptation of NTCP models based on local patient data with more recent treatments is planned. These will hopefully yield comprehensible dose constraints for planning prostate treatment with carbon and helium ions. Some recently published approaches seem promising: surface dose models for the bladder or rectum [276], the constraints on urethra dose suggested by [277] and the considerations of hematological toxicity of [209, 278].

Regarding future ideas for helium ion therapy, the experimental approaches of ultra-high dose rates (FLASH) [179, 231, 232, 279–281] and arc therapy (SHArc) [241, 242, 274] are starting to be technically possible. For patient treatment, especially the ultra-high dose rate approach still requires a lot of development, such as providing a stable dose rate, increasing the achievable treatment field and a validated biological model to calculate safe treatment doses. A recent report [282] highlights the shortcoming of current radiobiological models in FLASH ion therapy. Multi-ion therapy [196, 221], the combination of several ions to create a homogeneous dose and LET_d distribution is another experimental approach that could now benefit from the availability of a commercial TPS for helium ions.

The radiotherapy department in Hyogo, Japan, is preparing a biologically optimized SOBP for their helium ion beam [220] and RayStation®'s helium dose algorithm will be commissioned at CNAO, Pavia, Italy. Meanwhile in Heidel-

berg, 29 voluntary patients with a variety of tumors are treated with helium ions as requirement for the final governmental approval for clinical application. Awaiting the success of their treatment, more clinical trials are under preparation.

A trial idea for helium irradiation of the prostate is under discussion with the clinicians responsible for prostate treatment. Currently this idea is aiming for a dose regimen, that predicts at least 95 % progression free survival to compete with the FLAME trial [249–252]. In accordance to our TCP model, a BED about 140 to 150 would have to be reached with $(\alpha/\beta)_x$=3.1 Gy which requires either an LET or dose boost in the central area of the tumor to avoid high toxicity in surrounding OARs. Competing with established treatment schemes, new approaches would have to promise considerable improvement in OAR sparing, as hardly any adverse effects of Grade 3 or more are seen in anymore with conventional treatment.

To sum-up all these efforts and answer the research questions stated in Chapter 1:

This thesis provided the database of absorbed and RBE-weighted dose distributions that was required for a commercial TPS for helium ions, which ultimately led to the very first treatment of a patient with raster-scanned helium ions. The commissioning of this TPS now allows the routine use of helium ions, adding an additional technique to the fight against cancer.

Over the course of this research, this author showed that the lateral scattering of the helium ion beam in the air gap between BAMS and the treatment rooms' iso-center increases by 90 % in contrast to about 30 % and 144 % for carbon ions and protons. By introducing a double Gaussian lateral beam profile in vacuum into the MC beam model, the deviation between measured and simulated SOBPs was reduced to 4 %. For the treatment plan of a meningioma patient, we showed that a fluctuation of the lateral beam width in the order of 10 % has a visible but insignificant influence on the delivered dose distribution. The commercial TPS RayStation® was proven to adequately predict the absorbed dose distribution of even complex intensity-modulated helium ion treatments. Thus, RayStation® was successfully validated and commissioned as a clinical TPS for helium ions at HIT. With the retrospective investigation into ion therapy of prostate cancer, this author dug up some pitfalls in ion therapy. However, she was able to find an RBE-model and corresponding set of radiosensitivity parameters that explain the tumor control of both the proton and carbon ion cohort of the IPI trial. So it is likely, that this model also predicts the radiobiological effectiveness of helium ion treatment for prostate cancer. Only treatment of actual patients, will bring certainty on the clinical RBE of helium ions.

This clinical application of helium ions for the treatment of patients is now possible, thanks to the efforts presented in this thesis and other works preceding its research.

10 Scientific Contributions

Peer Reviewed Articles included in Thesis

[13]T. Tessonnier, S. Ecker, J. Besuglow, J. Naumann, et al., "Commissioning of Helium Ion Therapy and the First Patient Treatment With Active Beam Delivery", en, Int J Radiat Oncol Biol Phys **116**, 935–948 (2023).

[14]J. Besuglow, T. Tessonnier, B. Kopp, S. Mein, and A. Mairani, "The Evolution of Lateral Dose Distributions of Helium Ion Beams in Air: From Measurement and Modeling to Their Impact on Treatment Planning", Front Phys **9**, 797354 (2022).

[15]J. Besuglow, T. Tessonnier, S. Mein, T. Eichkorn, et al., "Understanding Relative Biological Effectiveness and Clinical Outcome of Prostate Cancer Therapy Using Particle Irradiation: Analysis of Tumor Control Probability With the Modified Microdosimetric Kinetic Model", Int J Radiat Oncol Biol Phys **119**, 1545–1556 (2024).

Peer Reviewed Articles not included in Thesis

[39]J. W. Norbury, G. Battistoni, J. Besuglow, L. Bocchini, et al., "Are Further Cross Section Measurements Necessary for Space Radiation Protection or Ion Therapy Applications? Helium Projectiles", Front Phys **8**, 565954 (2020).

[97]B. Kopp, S. Mein, T. Tessonnier, J. Besuglow, et al., "Rapid effective dose calculation for raster-scanning 4He ion therapy with the modified microdosimetric kinetic model (mMKM)", en, Phys Med **81**, 273–284 (2021).

[180]P. Lysakovski, A. Ferrari, T. Tessonnier, J. Besuglow, et al., "Development and Benchmarking of a Monte Carlo Dose Engine for Proton Radiation Therapy", Front Phys **9**, 741453 (2021).

[181]P. Lysakovski, J. Besuglow, B. Kopp, S. Mein, et al., "Development and benchmarking of the first fast Monte Carlo engine for helium ion beam dose calculation: MonteRay", en, Med Phys **50**, 2510–2524 (2023).

Selected Conference Contributions

[216]T. Tessonnier, R. Wickert, J. Besuglow, S. Mein, et al., "PO-1976 Commissioning of helium ion therapy: physics, radiobiology and clinical directions at HIT", en, in Radiotherapy and Oncology, Vol. 182, ESTRO 2023, 13 - 16 May 2023, Vienna, Austria (May 2023), S1744–S1745.

[219]J. Besuglow, T. Tessonnier, S. Mein, T. Eichkorn, et al., "3187: The applied radiobiological effectiveness model influences tumor control when treating with ions", en, in Radiotherapy and Oncology, Vol. 194, ESTRO 2024, Physics - Optimisation, algorithms and applications for ion beam treatment planning (May 2024), S4726–S4727.

[275]J. Besuglow, T. Tessonnier, S. Mein, T. Eichkorn, et al., "SC17.06 RBE's role in ion therapy of prostate cancer", en, in Physica Medica, Vol. 125, Abstracts of the 5th European Congress of Medical Physics (Sept. 2024), p. 103492.

[283]J. Besuglow, S. Mein, B. Kopp, S. Brons, et al., "Towards a Helium Ion-Beam Therapy Program in 2020: Physical, Biological and Clinical Considerations", in Joint AAPM|COMP Meeting, Issue: WE-B-Track 3-1 (July 2020).

[284]A. Mairani, S. Mein, B. Kopp, J. Besuglow, et al., "Back to the Future: Helium Ion Therapy 2020", en, in International Journal of Radiation Oncology*Biology*Physics, Vol. 108, Proceedings of the American SocieTy for Radiation Oncology (Nov. 2020), S67–S68.

[285]T. Tessonnier, S. Mein, J. Besuglow, B. Kopp, et al., "Next Evolutions in Particle Therapy: Helium Ion Treatment Planning, Delivery and Clinical Implications of Biological Modeling", in International Journal of Radiation Oncology*Biology*Physics, Vol. 111, 2021 Proceedings of the ASTRO 63rd Annual Meeting, Issue: 3 (Nov. 2021), e516–e517.

References

[1]J. R. Castro, D. H. Char, P. L. Petti, I. K. Daftari, et al., "15 years experience with helium ion radiotherapy for uveal melanoma", Int J Radiat Oncol Biol Phys **39**, Publisher: Elsevier BV, 989–996 (1997).

[2]D. H. Char, S. Kroll, T. L. Phillips, and J. M. Quivey, "Late radiation failures after iodine 125 brachytherapy for uveal melanoma compared with charged-particle (proton or helium ion) therapy", eng, Ophthalmology **109**, 1850–1854 (2002).

[3]K. H. Woodruff, J. R. Castro, J. M. Quivey, W. M. Saunders, et al., "Postmortem examination of 22 pancreatic carcinoma patients treated with helium ion irradiation", eng, Cancer **53**, 420–425 (1984).

[4]W. Saunders, J. R. Castro, G. T. Y. Chen, J. M. Collier, et al., "Helium-Ion Radiation Therapy at the Lawrence Berkeley Laboratory: Recent Results of a Northern California Oncology Group Clinical Trial", Radiat Res **104**, Publisher: Radiation Research Society, S227–S234 (1985).

[5]B. A. Ludewigt, W. T. Chu, M. H. Phillips, and T. R. Renner, "Accelerated helium-ion beams for radiotherapy and stereotactic radiosurgery", en, Med Phys **18**, 36–42 (1991).

[6]T. Winkelmann, R. Cee, T. Haberer, B. Naas, and A. Peters, "Test bench to commission a third ion source beam line and a newly designed extraction system", en, Rev Sci Instrum **83**, 02B904 (2012).

[7]T. Haberer, W. Becher, D. Schardt, and G. Kraft, "Magnetic scanning system for heavy ion therapy", Nucl Instrum Methods Phys Res A **330**, Publisher: Elsevier BV, 296–305 (1993).

[8]J. T. Lyman and J. Howard, "Dosimetry and instrumentation for helium and heavy ions", Int J Radiat Oncol Biol Phys **3**, Publisher: Elsevier BV, 81–85 (1977).

[9]J. Schwaab, S. Brons, J. Fieres, and K. Parodi, "Experimental characterization of lateral profiles of scanned proton and carbon ion pencil beams for improved beam models in ion therapy treatment planning", Phys Med Biol **56**, Publisher: IOP Publishing, 7813–7827 (2011).

[10]K. Parodi, "Monte Carlo Methods for Dose Calculations", in , edited by U. Linz, Biological and Medical Physics, Biomedical Engineering, Section: 5 (Springer Verlag, 2012), pp. 97–116.

[11]T. Tessonnier, A. Mairani, S. Brons, T. Haberer, J. Debus, and K. Parodi, "Experimental dosimetric comparison of1H,4He,12C and16O scanned ion beams", Phys Med Biol **62**, Publisher: IOP Publishing, 3958–3982 (2017).

[12]T. Tessonnier, A. Mairani, S. Brons, P. Sala, et al., "Helium ions at the heidelberg ion beam therapy center: comparisons between FLUKA Monte Carlo code predictions and dosimetric measurements", Phys Med Biol **62**, 6784 (2017).

[16]W. Bragg and R. Kleeman, "On the Ionization Curves of Radium", Philos Mag **8**, Publisher: Taylor & Francis, 726–738 (1904).

[17]R. R. Wilson, "Radiological Use of Fast Protons", Radiology **47**, Publisher: Radiological Society of North America, 487–491 (1946).

[18]G. Molière, "Theorie der Streuung schneller geladener Teilchen I. Einzelstreuung am abgeschirmten Coulomb-Feld", Z Naturforsch A **2**, 133–145 (1947).

[19]H. A. Bethe, "Molière's Theory of Multiple Scattering", Phys Rev **89**, Publisher: American Physical Society, 1256–1266 (1953).

[20]W. T. Scott, "The Theory of Small-Angle Multiple Scattering of Fast Charged Particles", Rev Mod Phys **35**, Publisher: American Physical Society, 231–313 (1963).

[21]V. L. Highland, "Some practical remarks on multiple scattering", Nucl Instrum Methods **129**, Publisher: Elsevier BV, 497–499 (1975).

[22]G. R. Lynch and O. I. Dahl, "Approximations to multiple Coulomb scattering", Nucl Instrum Methods Phys Res B **58**, 6–10 (1991).

[23]"4. Charged-Particle Stopping Powers and Related Quantities", en, in *Journal of the International Commission on Radiation Units and Measurements*, Vol. 14, edited by ICRU, ICRU Report 93, Publisher: SAGE Publications Inc (Apr. 2014), pp. 21–30.

[24]W. Schlegel, C. P. Karger, O. Jäkel, and P. Bachert, *Medizinische Physik Grundlagen - Bildgebung - Therapie - Technik*, ger, edited by W. Schlegel, C. P. Karger, and O. Jäkel, Springer eBook Collection (Springer Spektrum, Berlin ; [Heidelberg], 2018).

[25]J. F. Ziegler, *Helium: Stopping powers and ranges in all elemental matter*, Vol. 4 (Pergamon, 1977).

[26]J. F. Ziegler, M. D. Ziegler, and J. P. Biersack, "SRIM – The stopping and range of ions in matter", Nucl Instrum Methods Phys Res B **268**, 1818–1823 (2010).

[27]*Key Data for Ionizing-Radiation Dosimetry: Measurement Standards and Applications*, en, Vol. 14, ICRU Report 90 (SAGE Publications Inc, Apr. 2014).

[28]M. J. Berger and S. M. Seltzer, *Stopping powers and ranges of electrons and positrons (2nd Ed.)* en, tech. rep. NBS IR 82-2550A, Edition: 0 (National Bureau of Standards, Gaithersburg, MD, 1983), NBS IR 82–2550A.

[29]H. Paganetti, "Range uncertainties in proton therapy and the role of Monte Carlo simulations", Phys Med Biol **57**, R99 (2012).

[30]B. Tatischeff and I. Brissaud, "166 MeV Elastic and Inelastic Alpha-Particle Scattering; Macroscopic and Microscopic Analysis", Nucl Phys A **155**, 89 (1970).

[31]I. Brissaud, M. Brussel, M. Sowinski, and B. Tatischeff, "Elastic scattering of 166 MeV alpha particles on D, C, Si, Sn and Pb", Phys Lett B **30**, 324–326 (1969).

[32]M. Marafini, R. Paramatti, D. Pinci, G. Battistoni, et al., "Secondary radiation measurements for particle therapy applications: nuclear fragmentation produced by 4He ion beams in a PMMA target", en, Phys. Med. Biol. **62**, Publisher: IOP Publishing, 1291 (2017).

[33]T. Kurosawa, T. Nakamura, N. Nakao, T. Shibata, Y. Uwamino, and A. Fukumura, "Spectral Measurements of Neutrons, Protons, Deuterons and Tritons Produced by 100 MeV/nucleon He Bombardment", Nucl Instrum Methods Phys Res A **430**, 400–422 (1999).

[34]H. Sato, T. Kurosawa, H. Iwase, T. Nakamura, Y. Uwamino, and N. Nakao, "Measurement of Double Differential Neutron Production Cross Sections by 135 MeV/nucleon He, C, Ne and 95 MeV/nucleon Ar Ions", Phys Rev C **64**, 034607 (2001).

[35]D. Satoh, T. Kurosawa, T. Sato, A. Endo, et al., "Reevaluation of secondary neutron spectra from thick targets upon heavy-ion bombardment", Nucl Instrum Methods Phys Res A **583**, 507 (2007).

[36]M. Rovituso, C. Schuy, U. Weber, S. Brons, et al., "Fragmentation of 120 and 200 MeV u-14He ions in water and PMMA targets", Phys Med Biol **62**, Publisher: IOP Publishing, 1310–1326 (2017).

[37]N. Otuka, E. Dupont, V. Semkova, B. Pritychenko, et al., "Towards a More Complete and Accurate Experimental Nuclear Reaction Data Library (EXFOR): International Collaboration Between Nuclear Reaction Data Centres (NRDC)", Nuclear Data Sheets **120**, 272–276 (2014).

[38]V. Zerkin and B. Pritychenko, "The experimental nuclear reaction data (EXFOR): Extended computer database and Web retrieval system", Nucl Instrum Methods Phys Res A **888**, 31–43 (2018).

[39]J. W. Norbury, G. Battistoni, J. Besuglow, L. Bocchini, et al., "Are Further Cross Section Measurements Necessary for Space Radiation Protection or Ion Therapy Applications? Helium Projectiles", Front Phys **8**, 565954 (2020).

[40]F. Luoni, F. Horst, C.-A. Reidel, A. Quarz, et al., "Total nuclear reaction cross-section database for radiation protection in space and heavy-ion therapy applications", New J. Phys. **23**, Publisher: IOP Publishing, 101201 (2021).

[41]H. Sorge, H. Stöcker, and W. Greiner, "Relativistic quantum molecular dynamics approach to nuclear collisions at ultrarelativistic energies", Nucl Phys A **498**, Publisher: Elsevier BV, 567–576 (1989).

[42]M. Cavinato, E. Fabrici, E. Gadioli, E. G. Erba, and E. Galbiati, "Monte Carlo calculations using the Boltzmann Master Equation theory of nuclear reactions", Phys Lett B **382**, 1–5 (1996).

[43]M. Cavinato, E. Fabrici, E. Gadioli, E. G. Erba, and G. Riva, "Monte Carlo calculations of heavy ion cross-sections based on the Boltzmann Master equation theory", Nucl Phys A **679**, 753–764 (2001).

[44]E. B. Podgorsak, *Radiation Physics for Medical Physicists*, eng, 3rd ed. 2016, Graduate Texts in Physics (Springer, 2016).

[45]IAEA, ed., *Absorbed Dose Determination in External Beam Radiotherapy*, Technical Reports Series 398 (IAEA, Vienna, 2000).

[46]IAEA, ed., *Dosimetry of Small Static Fields Used in External Beam Radiotherapy*, Technical Reports Series 483 (INTERNATIONAL ATOMIC ENERGY AGENCY, Vienna, 2017).

[47]*DIN 6800-1:2016-08, Dosismessverfahren nach der Sondenmethode für Photonen- und Elektronenstrahlung_- Teil_1: Allgemeines*, Aug. 2016.

[48]*DIN 6800-2:2020-08, Dosismessverfahren nach der Sondenmethode für Photonen- und Elektronenstrahlung_- Teil_2: Dosimetrie hochenergetischer Photonen- und Elektronenstrahlung mit Ionisationskammern*, Aug. 2020.

[49]*DIN 6800-4:2000-12, Dosismessverfahren nach der Sondenmethode für Photonen- und Elektronenstrahlung_- Teil_4: Filmdosimetrie*, DIN, Dec. 2000.

[50]C. P. Karger, O. Jäkel, H. Palmans, and T. Kanai, "Dosimetry for ion beam radiotherapy", Phys Med Biol **55**, R193 (2010).

[51]D. Schardt, T. Elsässer, and D. Schulz-Ertner, "Heavy-ion tumor therapy: Physical and radiobiological benefits", Rev Mod Phys **82**, Publisher: American Physical Society, 383–425 (2010).

[52]*DIN 6801-1:2019-09, Dosismessverfahren nach der Sondenmethode für Protonen- und Ionenstrahlung_- Teil_1: Ionisationskammern*, DIN, Sept. 2019.

[53]O. Jäkel, G. H. Hartmann, P. Heeg, and D. Schardt, "Effective point of measurement of cylindrical ionization chambers for heavy charged particles", Phys Med Biol **45**, 599 (2000).

[54]H. Palmans and F. Verhaegen, "On the effective point of measurement of cylindrical ionization chambers for proton beams and other heavy charged particle beams", Phys Med Biol **45**, L20 (2000).

[55]H. Palmans, "Perturbation factors for cylindrical ionization chambers in proton beams. Part I: corrections for gradients", Phys Med Biol **51**, 3483 (2006).

[56]H. Palmans, "Comments on 'The effective depth of cylindrical ionization chambers in water for clinical proton beams'", Phys Med Biol **57**, 7219 (2012).

[57]J. Osorio, R. Dreindl, L. Grevillot, V. Letellier, et al., "Beam monitor calibration of a synchrotron-based scanned light-ion beam delivery system", Z Med Phys **31**, 154–165 (2020).

[58]S. Mein, B. Kopp, T. Tessonnier, B. Ackermann, et al., "Dosimetric Validation of Monte Carlo and Analytical Dose Engine with Raster-Scanning 1H, 4He, 12C, and 16O ion-beams using an Anthropomorphic Phantom", Phys Med **64**, 123–131 (2019).

[59]C. P. Karger, O. Jäkel, G. H. Hartmann, and P. Heeg, "A system for three-dimensional dosimetric verification of treatment plans in intensity-modulated radiotherapy with heavy ions", en, Med Phys **26**, 2125–2132 (1999).

[60]T. V. M. Lima, M. Dosanjh, A. Ferrari, S. Molineli, M. Ciocca, and A. Mairani, "Monte Carlo Calculations Supporting Patient Plan Verification in Proton Therapy", English, Front. Oncol. **6**, Publisher: Frontiers, 10.3389/fonc.2016.00062 (2016).

[61]A. Niroomand-Rad, C. R. Blackwell, B. M. Coursey, K. P. Gall, et al., "Radiochromic film dosimetry: Recommendations of AAPM Radiation Therapy Committee Task Group 55", Med Phys **25**, Publisher: American Association of Physicists in Medicine, 2093–2115 (1998).

[62]B. Spielberger, M. Scholz, M. Krämer, and G. Kraft, "Experimental investigations of the response of films to heavy-ion irradiation", Phys Med Biol **46**, 2889 (2001).

[63]B. D. Lynch, J. Kozelka, M. K. Ranade, J. G. Li, W. E. Simon, and J. F. Dempsey, "Important considerations for radiochromic film dosimetry with flatbed CCD scanners and EBT GAFCHROMIC® film", Med Phys **33**, Publisher: American Association of Physicists in Medicine, 4551–4556 (2006).

[64]M. Martišíková and O. Jäkel, "Dosimetric properties of Gafchromic® EBT films in monoenergetic medical ion beams", Phys Med Biol **55**, 3741 (2010).

[65]D. Kirby, S. Green, H. Palmans, R. Hugtenburg, C. Wojnecki, and D. Parker, "LET dependence of GafChromic films and an ion chamber in low-energy proton dosimetry", Phys Med Biol **55**, 417 (2010).

[66]D. Lewis, A. Micke, X. Yu, and M. F. Chan, "An efficient protocol for radiochromic film dosimetry combining calibration and measurement in a single scan", Med Phys **39**, Publisher: American Association of Physicists in Medicine, 6339–6350 (2012).

[67]S. Reinhardt, M. Hillbrand, J. J. Wilkens, and W. Assmann, "Comparison of Gafchromic EBT2 and EBT3 films for clinical photon and proton beams", Med Phys **39**, Publisher: American Association of Physicists in Medicine, 5257–5262 (2012).

[68]S. Stefanowicz, H. Latzel, L. R. Lindvold, C. E. Andersen, O. Jäkel, and S. Greilich, "Dosimetry in clinical static magnetic fields using plastic scintillation detectors", Radiation Measurements, Proceedings of the 8th International Conference on Luminescent Detectors and Transformers of Ionizing Radiation (LUMDETR 2012) **56**, 357–360 (2013).

[69]S. Russo, A. Mirandola, S. Molinelli, E. Mastella, et al., "Characterization of a commercial scintillation detector for 2-D dosimetry in scanned proton and carbon ion beams", Phys Med **34**, 48–54 (2017).

[70]H. Latzel, *Usage of Scintillation Screens at the Medical Facility HIT*, en, Apr. 2019.

[71]P. v. Luijk, A. A. van't Veld, H. D. Zelle, and J. M. Schippers, "Collimator scatter and 2D dosimetry in small proton beams", Phys Med Biol **46**, 653 (2001).

[72]T. Tessonnier, G. Verona-Rinati, L. Rank, R. Kranzer, A. Mairani, and M. Marinelli, "Diamond detectors for dose and instantaneous dose-rate measurements for ultra-high dose-rate scanned helium ion beams", eng, Med Phys **51**, 1450–1459 (2024).

[73]I. Martínez-Rovira, W. González, S. Brons, and Y. Prezado, "Carbon and oxygen minibeam radiation therapy: An experimental dosimetric evaluation", Med Phys **44**, 4223–4229 (2017).

[74]C. Gomà, M. Marinelli, S. Safai, G. Verona-Rinati, and J. Würfel, "The role of a microDiamond detector in the dosimetry of proton pencil beams", Z Med Phys **26**, 88–94 (2016).

[75]M. Marinelli, G. Prestopino, C. Verona, G. Verona-Rinati, et al., "Dosimetric characterization of a microDiamond detector in clinical scanned carbon ion beams", Med Phys **42**, Publisher: American Association of Physicists in Medicine, 2085–2093 (2015).

[76]J. Vedelago, C. P. Karger, and O. Jäkel, "A review on reference dosimetry in radiation therapy with proton and light ion beams: status and impact of new developments", en, Radiat Meas **157**, 106844 (2022).

[77]H. Liew, S. Meister, S. Mein, B. Kopp, et al., "Combined DNA Damage Repair Inhibition and Ion Beam Therapy: Development, Benchmark and Clinical Implications of a Mechanistic Biological Model", Int J Radiat Oncol Biol Phys **111**, Publisher: Elsevier BV, e247–e248 (2021).

[78]L. Bronk, F. Guan, D. Patel, D. Ma, et al., "Mapping the Relative Biological Effectiveness of Proton, Helium and Carbon Ions with High-Throughput Techniques", en, Cancers **12**, 3658 (2020).

[79]E. Rørvik, L. F. Fjæra, T. J. Dahle, J. E. Dale, et al., "Exploration and application of phenomenological RBE models for proton therapy", en, Phys. Med. Biol. **63**, Publisher: IOP Publishing, 185013 (2018).

[80]A. Mairani, G. Magro, I. Dokic, S. M. Valle, et al., "Data-driven RBE parameterization for helium ion beams", en, Phys. Med. Biol. **61**, Publisher: IOP Publishing, 888 (2016).

[81]A. Mairani, I. Dokic, G. Magro, T. Tessonnier, et al., "A phenomenological relative biological effectiveness approach for proton therapy based on an improved description of the mixed radiation field", Phys. Med. Biol. **62**, 1378–1395 (2017).

[82]S. Mein, I. Dokic, C. Klein, T. Tessonnier, et al., "Biophysical modeling and experimental validation of relative biological effectiveness (RBE) for 4He ion beam therapy", en, Radiat Oncol **14**, 123 (2019).

[83]A. L. McNamara, J. Schuemann, and H. Paganetti, "A phenomenological relative biological effectiveness (RBE) model for proton therapy based on all published *in vitro* cell survival data", Phys. Med. Biol. **60**, 8399–8416 (2015).

[84]M. C. Frese, V. K. Yu, R. D. Stewart, and D. J. Carlson, "A Mechanism-Based Approach to Predict the Relative Biological Effectiveness of Protons and Carbon Ions in Radiation Therapy", en, Int J Radiat Oncol Biol Phys **83**, 442–450 (2012).

[85]R. D. Stewart, S. W. Streitmatter, D. C. Argento, C. Kirkby, et al., "Rapid MCNP simulation of DNA double strand break (DSB) relative biological effectiveness (RBE) for photons, neutrons, and light ions", Phys. Med. Biol. **60**, 8249–8274 (2015).

[86]D. J. Carlson, R. D. Stewart, V. A. Semenenko, and G. A. Sandison, "Combined Use of Monte Carlo DNA Damage Simulations and Deterministic Repair Models to Examine Putative Mechanisms of Cell Killing", en, Radiat Res **169**, 447–459 (2008).

[87]A. M. Kellerer and H. H. Rossi, "The theory of dual radiation action", Curr Top Radiat Res **8**, 85–158 (1974).

[88]A. M. Kellerer and H. H. Rossi, "A Generalized Formulation of Dual Radiation Action", Radiat Res **75**, 471 (1978).

[89]R. D. Stewart, D. J. Carlson, M. P. Butkus, R. Hawkins, T. Friedrich, and M. Scholz, "A comparison of mechanism-inspired models for particle relative biological effectiveness (RBE)", en, Med Phys **45**, `10.1002/mp.13207` (2018).

[90]V. E. Bellinzona, F. Cordoni, M. Missiaggia, F. Tommasino, et al., "Linking Microdosimetric Measurements to Biological Effectiveness in Ion Beam Therapy: A Review of Theoretical Aspects of MKM and Other Models", English, Front Phys **8**, Publisher: Frontiers, `10.3389/fphy.2020.578492` (2021).

[91]T. Elsässer, W. K. Weyrather, T. Friedrich, M. Durante, et al., "Quantification of the Relative Biological Effectiveness for Ion Beam Radiotherapy: Direct Experimental Comparison of Proton and Carbon Ion Beams and a Novel Approach for Treatment Planning", Int J Radiat Oncol Biol Phys **78**, 1177–1183 (2010).

[92]M. Krämer, E. Scifoni, C. Schuy, M. Rovituso, et al., "Helium ions for radiotherapy? Physical and biological verifications of a novel treatment modality", Med Phys **43**, 1995–2004 (2016).

[93]A. Mairani, I. Dokic, G. Magro, T. Tessonnier, et al., "Biologically optimized helium ion plans: calculation approach and its in vitro validation", en, Phys. Med. Biol. **61**, Publisher: IOP Publishing, 4283 (2016).

[94]A. Mairani, S. Mein, E. Blakely, J. Debus, et al., "Roadmap: helium ion therapy", Phys. Med. Biol. **67**, 15TR02 (2022).

[95]H. Fuchs, M. Alber, T. Schreiner, and D. Georg, "Implementation of spot scanning dose optimization and dose calculation for helium ions in Hyperion", Med Phys **42**, 5157–5166 (2015).

[96]A. Mairani, G. Magro, T. Tessonnier, T. T. Böhlen, et al., "Optimizing the modified microdosimetric kinetic model input parameters for proton and ^{4} He ion beam therapy application", Phys. Med. Biol. **62**, N244–N256 (2017).

[97]B. Kopp, S. Mein, T. Tessonnier, J. Besuglow, et al., “Rapid effective dose calculation for raster-scanning 4He ion therapy with the modified microdosimetric kinetic model (mMKM)”, en, Phys Med **81**, 273–284 (2021).

[98]S. G. Bonaccorsi, T. Tessonnier, L. Hoeltgen, E. Meixner, et al., “Exploring Helium Ions’ Potential for Post-Mastectomy Left-Sided Breast Cancer Radiotherapy”, en, Cancers **16**, 410 (2024).

[99]M. Scholz and G. Kraft, “Calculation of Heavy Ion Inactivation Probabilities Based on Track Structure, X Ray Sensitivity and Target Size”, Radiat Prot Dosim **52**, 29–33 (1994).

[100]M. Scholz, A. M. Kellerer, W. Kraft-Weyrather, and G. Kraft, “Computation of cell survival in heavy ion beams for therapy”, Radiat Environ Biophys **36**, 59–66 (1997).

[101]M. Krämer, O. Jäkel, T. Haberer, G. Kraft, D. Schardt, and U. Weber, “Treatment planning for heavy-ion radiotherapy: physical beam model and dose optimization”, Phys Med Biol **45**, 3299 (2000).

[102]C. P. Karger and P. Peschke, “RBE and related modeling in carbon-ion therapy”, en, Phys. Med. Biol. **63**, Publisher: IOP Publishing, 01TR02 (2017).

[103]T. Elsässer and M. Scholz, “Cluster Effects within the Local Effect Model”, Radiat Res **167**, 319–329 (2007).

[104]T. Elsässer, R. Cunrath, M. Krämer, and M. Scholz, “Impact of track structure calculations on biological treatment planning in ion radiotherapy”, en, New J. Phys. **10**, 075005 (2008).

[105]T. Pfuhl, “Influence of secondary electron spectra on the enhanced effectiveness of ion beams”, en, Ph.D. Thesis (Technische Universität Darmstadt, Darmstadt, 2021).

[106]S. Mein, C. Klein, B. Kopp, G. Magro, et al., “Assessment of RBE-Weighted Dose Models for Carbon Ion Therapy Toward Modernization of Clinical Practice at HIT: In Vitro, in Vivo, and in Patients”, en, Int J Radiat Oncol Biol Phys **108**, 779–791 (2020).

[107]T. J. Dahle, G. Magro, K. S. Ytre-Hauge, C. H. Stokkevåg, K. Choi, and A. Mairani, “Sensitivity study of the microdosimetric kinetic model parameters for carbon ion radiotherapy”, en, Phys. Med. Biol. **63**, Publisher: IOP Publishing, 225016 (2018).

[108]R. B. Hawkins, “A Statistical Theory of Cell Killing by Radiation of Varying Linear Energy Transfer”, Radiat Res **140**, 366 (1994).

[109]R. B. Hawkins, “A microdosimetric-kinetic model of cell death from exposure to ionizing radiation of any LET, with experimental and clinical applications”, en, Int J Radiat Biol **69**, 739–755 (1996).

[110]R. B. Hawkins, “A Microdosimetric-Kinetic Model for the Effect of Non-Poisson Distribution of Lethal Lesions on the Variation of RBE with LET”, en, Radiat Res **160**, 61–69 (2003).

[111]A. Parisi, C. J. Beltran, and K. M. Furutani, “The Mayo Clinic Florida microdosimetric kinetic model of clonogenic survival: formalism and first benchmark against in vitro and in silico data”, en, Phys. Med. Biol. **67**, Publisher: IOP Publishing, 185013 (2022).

[112]Y. Kase, T. Kanai, Y. Matsumoto, Y. Furusawa, et al., “Microdosimetric Measurements and Estimation of Human Cell Survival for Heavy-Ion Beams”, Radiat Res **166**, 629 – 638 –10 (2006).

[113]T. Inaniwa, T. Furukawa, Y. Kase, N. Matsufuji, et al., "Treatment planning for a scanned carbon beam with a modified microdosimetric kinetic model", Phys. Med. Biol. **55**, 6721–6737 (2010).

[114]Y. Kase, T. Kanai, N. Matsufuji, Y. Furusawa, T. Elsässer, and M. Scholz, "Biophysical calculation of cell survival probabilities using amorphous track structure models for heavy-ion irradiation", en, Phys. Med. Biol. **53**, Epub 2007-12-13, 37 (2008).

[115]T. Sato and Y. Furusawa, "Cell Survival Fraction Estimation Based on the Probability Densities of Domain and Cell Nucleus Specific Energies Using Improved Microdosimetric Kinetic Models", en, Radiat Res **178**, 341–356 (2012).

[116]T. Inaniwa and N. Kanematsu, "Adaptation of stochastic microdosimetric kinetic model for charged-particle therapy treatment planning", en, Phys. Med. Biol. **63**, Publisher: IOP Publishing, 095011 (2018).

[117]A. Niemierko, "Reporting and analyzing dose distributions: A concept of equivalent uniform dose", en, Med Phys **24**, 103–110 (1997).

[118]M. Roach, G. Hanks, H. Thames, P. Schellhammer, et al., "Defining biochemical failure following radiotherapy with or without hormonal therapy in men with clinically localized prostate cancer: Recommendations of the RTOG-ASTRO Phoenix Consensus Conference", en, Int J Radiat Oncol Biol Phys **65**, 965–974 (2006).

[119]E. L. Kaplan and P. Meier, "Nonparametric Estimation from Incomplete Observations", J Am Stat Assoc **53**, 457–481 (1958).

[120]B. E. Wilson, M. B. Nadler, A. Desnoyers, and E. Amir, "Quantifying Withdrawal of Consent, Loss to Follow-Up, Early Drug Discontinuation, and Censoring in Oncology Trials", J Natl Compr Canc Netw **19**, 1433–1440 (2021).

[121]W. Lilleby, A. Kishan, and H. Geinitz, "Acute and long-term toxicity in primary hypofractionated external photon radiation therapy in patients with localized prostate cancer", en, World J Urol **42**, 41 (2024).

[122]H. R. Lukka, S. Deshmukh, D. W. Bruner, J.-P. Bahary, et al., "Five-Year Patient-Reported Outcomes in NRG Oncology RTOG 0938, Evaluating Two Ultrahypofractionated Regimens for Prostate Cancer", Int J Radiat Oncol Biol Phys **116**, 770–778 (2023).

[123]S. Malone, D. E. Spratt, S. C. Morgan, S. Grimes, et al., "Association of Short-Term Patient-Reported Outcomes With Long-Term Oncologic Outcomes in Localized Prostate Cancer Treated With Radiotherapy and ADT in a Phase III Randomized Controlled Trial", Int J Radiat Oncol Biol Phys **111**, Publisher: Elsevier BV, S75 (2021).

[124]F. Yang, S. Ghosh, D. Yee, S. I. Patel, et al., "Conventional vs. Hypofractionation Radiation for High-Risk Prostate Cancer Patients (CHIRP): 24 Months Patient-Reported Quality of Life Outcomes of the Randomized Phase II CHIRP Trial", Int J Radiat Oncol Biol Phys **111**, Publisher: Elsevier BV, S79 (2021).

[125]K. E. Hoffman, H. Skinner, T. J. Pugh, K. R. Voong, et al., "Patient-reported Urinary, Bowel, and Sexual Function After Hypofractionated Intensity-modulated Radiation Therapy for Prostate Cancer: Results From a Randomized Trial", en, Am J Clin Oncol **41**, 558–567 (2018).

[126]T. Shaikh, T. Li, E. A. Handorf, M. E. Johnson, et al., "Long-Term Patient-Reported Outcomes From a Phase 3 Randomized Prospective Trial of Conventional Versus Hypofractionated Radiation Therapy for Localized Prostate Cancer", en, Int J Radiat Oncol Biol Phys **97**, 722–731 (2017).

[127]P. Chang, K. M. Szymanski, R. L. Dunn, J. J. Chipman, et al., "Expanded Prostate Cancer Index Composite for Clinical Practice: Development and Validation of a Practical Health Related Quality of Life Instrument for Use in the Routine Clinical Care of Patients With Prostate Cancer", EN, J Urol, Publisher: Wolters KluwerPhiladelphia, PA, 10.1016/j.juro.2011.04.085 (2011).

[128]A.-M. Talvitie, M. Helminen, H. Ojala, T. Tammela, A. Auvinen, and I. Pietilä, "Missingness in the expanded prostate cancer index short form (EPIC-26) – prevalence, patterns, and explanatory factors", Health Qual Life Outcomes **21**, 89 (2023).

[129]M. Marteinsdottir and H. Paganetti, "Applying a variable relative biological effectiveness (RBE) might affect the analysis of clinical trials comparing photon and proton therapy for prostate cancer", Phys. Med. Biol. **64**, 115027 (2019).

[130]P. Källman, A. Ågren, and A. Brahme, "Tumour and Normal Tissue Responses to Fractionated Non-uniform Dose Delivery", en, Int J Radiat Biol **62**, 249–262 (1992).

[131]B. Warkentin, P. Stavrev, N. Stavreva, C. Field, and B. G. Fallone, "A TCP-NTCP estimation module using DVHs and known radiobiological models and parameter sets", en, J Applied Clin Med Phys **5**, 50–63 (2004).

[132]*Common Terminology Criteria for Adverse Events (CTCAE) Version 5.0*, eng, Nov. 2017.

[133]J. D. Cox, J. Stetz, and T. F. Pajak, "Toxicity criteria of the Radiation Therapy Oncology Group (RTOG) and the European organization for research and treatment of cancer (EORTC)", en, Int J Radiat Oncol Biol Phys **31**, 1341–1346 (1995).

[134]L. R. Coia, R. J. Myerson, and J. E. Tepper, "Late effects of radiation therapy on the gastrointestinal tract", Int J Radiat Oncol Biol Phys, Late Effects of Normal Tissues (LENT) Consensus Conference **31**, 1213–1236 (1995).

[135]C. Burman, G. J. Kutcher, B. Emami, and M. Goitein, "Fitting of normal tissue tolerance data to an analytic function", Int J Radiat Oncol Biol Phys **21**, 123–135 (1991).

[136]J. T. Lyman, "Complication Probability as Assessed from Dose-Volume Histograms", Radiat Res **104**, 13–19 (1985).

[137]J. T. Lyman and A. B. Wolbarst, "Optimization of radiation therapy,III: A method of assessing complication probabilities from dose-volume histograms", Int J Radiat Oncol Biol Phys **13**, 103–109 (1987).

[138]J. T. Lyman and A. B. Wolbarst, "Optimization of radiation therapy, IV: A dose-volume histogram reduction algorithm", Int J Radiat Oncol Biol Phys **17**, 433–436 (1989).

[139]B. Emami, J. Lyman, A. Brown, L. Cola, et al., "Tolerance of normal tissue to therapeutic irradiation", Int J Radiat Oncol Biol Phys **21**, 109–122 (1991).

[140]L. B. Marks, R. K. Ten Haken, and M. K. Martel, "Guest Editor's Introduction to QUANTEC: A Users Guide", Int J Radiat Oncol Biol Phys **76**, S1–S2 (2010).

[141]S. M. Bentzen, L. S. Constine, J. O. Deasy, A. Eisbruch, et al., "Quantitative Analyses of Normal Tissue Effects in the Clinic (QUANTEC): An Introduction to the Scientific Issues", Int J Radiat Oncol Biol Phys **76**, Publisher: Elsevier BV, S3–S9 (2010).

[142]J. M. Michalski, H. Gay, A. Jackson, S. L. Tucker, and J. O. Deasy, "Radiation Dose-Volume Effects in Radiation-Induced Rectal Injury", en, Int J Radiat Oncol Biol Phys **76**, S123–S129 (2010).

[143]A. Jackson, L. B. Marks, S. M. Bentzen, A. Eisbruch, et al., "The Lessons of QUANTEC: Recommendations for RepReport and Gathering Data on Dose-Volume Dependencies of Treatment Outcome", Int J Radiat Oncol Biol Phys **76**, S155–S160 (2010).

[144]I. Roach Mack, G. Gagliardi, I. El Naqa, J. O. Deasy, and L. B. Marks, "Radiation Dose-Volume Effects and the Penile Bulb", Int J Radiat Oncol Biol Phys **76**, S130–S134 (2010).

[145]A. N. Viswanathan, E. D. Yorke, L. B. Marks, P. J. Eifel, and W. U. Shipley, "Radiation Dose-Volume Effects of the Urinary Bladder", Int J Radiat Oncol Biol Phys **76**, S116–S122 (2010).

[146]B. D. Kavanagh, C. C. Pan, L. A. Dawson, S. K. Das, et al., "Radiation Dose–Volume Effects in the Stomach and Small Bowel", en, Int J Radiat Oncol Biol Phys **76**, S101–S107 (2010).

[147]J. O. Deasy, S. M. Bentzen, A. Jackson, R. K. Ten Haken, et al., "Improving Normal Tissue Complication Probability Models: The Need to Adopt a "Data-Pooling" Culture", Int J Radiat Oncol Biol Phys **76**, S151–S154 (2010).

[148]S. M. Bentzen, M. Parliament, J. O. Deasy, A. Dicker, et al., "Biomarkers and Surrogate Endpoints for Normal-Tissue Effects of Radiation Therapy: The Importance of Dose–Volume Effects", Int J Radiat Oncol Biol Phys **76**, Publisher: Elsevier BV, S145–S150 (2010).

[149]M. T. Milano, L. B. Marks, A. J. Olch, E. D. Yorke, et al., "Comparison of Risks of Late Effects From Radiation Therapy in Children Versus Adults: Insights From the QUANTEC, HyTEC, and PENTEC Efforts", Int J Radiat Oncol Biol Phys, PEdiatric Normal Tissue Effects in the Clinic (PENTEC) **119**, 387–400 (2024).

[150]*DICOM®*, ISO.

[151]U. Schneider, E. Pedroni, and A. Lomax, "The calibration of CT Hounsfield units for radiotherapy Treatment planning", Phys Med Biol **41**, 111 (1996).

[152]O. Jäkel, C. Jacob, D. Schardt, C. P. Karger, and G. H. Hartmann, "Relation between carbon ion ranges and x-ray CT numbers", Med Phys **28**, 701–703 (2001).

[153]F. K. Faller, S. Mein, B. Ackermann, J. Debus, W. Stiller, and A. Mairani, "Preclinical evaluation of dual-layer spectral computed tomography-based stopping power prediction for particle therapy planning at the Heidelberg Ion Beam Therapy Center", en, Phys. Med. Biol. **65**, Publisher: IOP Publishing, 095007 (2020).

[154]F. K. Longarino, T. Tessonnier, S. Mein, S. B. Harrabi, et al., "Dual-layer spectral CT for proton, helium, and carbon ion beam therapy planning of brain tumors", en, J Applied Clin Med Phys **23**, e13465 (2022).

[155]J. Grimm, L. B. Marks, A. Jackson, B. D. Kavanagh, J. Xue, and E. Yorke, "High Dose per Fraction, Hypofractionated Treatment Effects in the Clinic (HyTEC): An Overview", Int J Radiat Oncol Biol Phys, A Red Journal Special Issue: HyTEC **110**, 1–10 (2021).

[156]L. S. Constine, A. J. Olch, A. Jackson, C.-H. Hua, et al., "Pediatric Normal Tissue Effects in the Clinic (PENTEC): An International Collaboration to Assess Normal Tissue Radiation Dose-Volume-Response Relationships for Children With Cancer", en, Int J Radiat Oncol Biol Phys **119**, 316–320 (2024).

[157]ICRU, ed., *Prescribing, Recording, and Reporting Light Ion Beam Therapy*, Vol. 16, ICRU Report 93 (Sage, Dec. 2016).

[158]O. Jäkel, G. Kraft, and C. P. Karger, "The history of ion beam therapy in Germany", en, Z Med Phys **32**, 6–22 (2022).

[159]D. A. Tuffs, J. Bird, and D. K. Henke-Wendt, eds., *Heidelberger Ion Beam Therapy Center*, en, Oct. 2012.

[160]T. Haberer, J. Debus, H. Eickhoff, O. Jäkel, D. Schulz-Ertner, and U. Weber, "The heidelberg ion therapy center", Radiotherapy and Oncology, Carbon-Ion Theraphy **73**, S186–S190 (2004).

[161]T. Winkelmann, R. Cee, T. Haberer, B. Naas, et al., "Electron cyclotron resonance ion source experience at the Heidelberg Ion Beam Therapy Center", en, Rev Sci Instrum **79**, 02A331 (2008).

[162]T. Winkelmann, R. Cee, T. Haberer, B. Naas, and A. Peters, "Progress in ion source injector development at the ion beam therapy center (Heidelberg Ion Beam Therapy Center)", en, Rev Sci Instrum **81**, 02A311 (2010).

[163]T. Winkelmann, R. Cee, T. Haberer, B. Naas, A. Peters, and J. Schreiner, "Improvements for extending the time between maintenance periods for the Heidelberg ion beam therapy center (HIT) ion sources", en, Rev Sci Instrum **85**, 02A951 (2014).

[164]D. Ondreka and U. Weinrich, "The Heidelberg Ion Therapy (HIT) Accelerator Coming into Operation", in Conf. Proc. C, Vol. 0806233, edited by I. Andrian and C. Petit-Jean-Genaz (2008), TUOCG01.

[165]C. Schoemers, E. Feldmeier, J. Naumann, R. Panse, A. Peters, and T. Haberer, "The intensity feedback system at Heidelberg Ion-Beam Therapy Centre", Nucl Instrum Methods Phys Res A **795**, 92–99 (2015).

[166]T. Tessonnier, T. T. Boehlen, F. Cerutti, A. Ferrari, et al., "Dosimetric verification in water of a Monte Carlo treatment planning tool for proton, helium, carbon and oxygen ion beams at the Heidelberg ion beam therapy center", Phys Med Biol **62**, 6579 (2017).

[167]U. Weber and G. Kraft, "Design and construction of a ripple filter for a smoothed depth dose distribution in conformal particle therapy", Phys Med Biol **44**, 2765–2775 (1999).

[168]K. Parodi, A. Mairani, S. Brons, J. Naumann, et al., "The influence of lateral beam profile modifications in scanned proton and carbon ion therapy: a Monte Carlo study", Phys Med Biol **55**, 5169 (2010).

[169]A. Ferrari, P. R. Sala, A. Fassó, and J. Ranft, *FLUKA: a multi-particle transport code*, tech. rep. (CERN-2005-10, 2005).

[170]T. Böhlen, F. Cerutti, M. Chin, A. Fassò, et al., "The FLUKA Code: Developments and Challenges for High Energy and Medical Applications", en, Nuclear Data Sheets **120**, 211–214 (2014).

[171]T. T. Böhlen, J. Bauer, M. Dosanjh, A. Ferrari, et al., "A Monte Carlo-based treatment-planning tool for ion beam therapy", J Radiat Res (Tokyo) **54**, 77–81 (2013).

[172]A. Mairani, T. T. Böhlen, A. Schiavi, T. Tessonnier, et al., "A Monte Carlo-based treatment planning tool for proton therapy", Phys Med Biol **58**, 2471 (2013).

[173]J. Bauer, F. Sommerer, A. Mairani, D. Unholtz, et al., "Integration and evaluation of automated Monte Carlo simulations in the clinical practice of scanned proton and carbon ion beam therapy", Phys Med Biol **59**, 4635 (2014).

[174]G. Battistoni, J. Bauer, T. T. Boehlen, F. Cerutti, et al., "The FLUKA Code: An Accurate Simulation Tool for Particle Therapy", Front Oncol **6**, Publisher: Frontiers Media SA, 116 (2016).

[175]G. Magro, T. J. Dahle, S. Molinelli, M. Ciocca, et al., "The FLUKA Monte Carlo code coupled with the NIRS approach for clinical dose calculations in carbon ion therapy", Phys. Med. Biol. **62**, 3814–3827 (2017).

[176]K. Parodi, A. Mairani, and F. Sommerer, "Monte Carlo-based parametrization of the lateral dose spread for clinical treatment planning of scanned proton and carbon ion beams", J Radiat Res (Tokyo) **54**, i91–i96 (2013).

[177]T. Tessonnier, A. Mairani, F. Cappucci, A. Mirandola, et al., "Development and application of tools for Monte Carlo based simulations in a particle beam radiotherapy facility", Appl Radiat Isot **83**, 155–158 (2014).

[178]P. Lysakovski, "MonteRay: A Fast Monte Carlo Dose Engine for Protons, Helium Ions and Carbon Ions", Publisher: Heidelberg University Library, Dissertation (Heidelberg University, Heidelberg, Germany, 2024).

[179]L. Rank, O. Dogan, B. Kopp, S. Mein, et al., "Development and benchmarking of a dose rate engine for raster-scanned FLASH helium ions", en, Med Phys **51**, 2251–2262 (2024).

[180]P. Lysakovski, A. Ferrari, T. Tessonnier, J. Besuglow, et al., "Development and Benchmarking of a Monte Carlo Dose Engine for Proton Radiation Therapy", Front Phys **9**, 741453 (2021).

[181]P. Lysakovski, J. Besuglow, B. Kopp, S. Mein, et al., "Development and benchmarking of the first fast Monte Carlo engine for helium ion beam dose calculation: MonteRay", en, Med Phys **50**, 2510–2524 (2023).

[182]P. Lysakovski, B. Kopp, T. Tessonnier, S. Mein, et al., "Development and validation of MonteRay, a fast Monte Carlo dose engine for carbon ion beam radiotherapy", en, Med Phys **51**, 1433–1449 (2024).

[183]M. Janson, L. Glimelius, A. Fredriksson, E. Traneus, and E. Engwall, "Treatment planning of scanned proton beams in RayStation", Medical Dosimetry, Treatment Planning in Proton Therapy **49**, 2–12 (2024).

[184]S. Mein, "FRoG: a fast robust analytical dose engine on GPU for p, 4He, 12C and 16O particle therapy", Publisher: Heidelberg University Library, PhD thesis (2020).

[185]S. Mein, K. Choi, B. Kopp, T. Tessonnier, et al., "Fast robust dose calculation on GPU for high-precision 1H, 4He, 12 C and 16O ion therapy: the FRoG platform", Sci Rep **8**, 14829 (2018).

[186]B. Kopp, M. Fuglsang Jensen, S. Mein, L. Hoffmann, H. Nyström, and M. Falk M. AND, "FRoG: An independent dose and LETd prediction tool for proton therapy at ProBeam® facilities", Med Phys (2020).

[187]L. Hong, M. Goitein, M. Bucciolini, R. Comiskey, et al., "A pencil beam algorithm for proton dose calculations", Phys. Med. Biol. **41**, 1305–1330 (1996).

[188]T. Inaniwa, T. Furukawa, A. Nagano, S. Sato, et al., "Field-size effect of physical doses in carbon-ion scanning using range shifter plates", en, Med Phys **36**, 2889–2897 (2009).

[189]T. Inaniwa, N. Kanematsu, Y. Hara, T. Furukawa, et al., "Implementation of a triple Gaussian beam model with subdivision and redefinition against density heterogeneities in treatment planning for scanned carbon-ion radiotherapy", Phys. Med. Biol. **59**, 5361–5386 (2014).

[190]T. Inaniwa, N. Kanematsu, Y. Hara, T. Furukawa, et al., "Erratum: Implementation of a triple Gaussian beam model with subdivision and redefinition against density heterogeneities in treatment planning for scanned carbon-ion radiotherapy (*Phys. Med. Biol.* 59 5361)", Phys. Med. Biol. **59**, 6305–6305 (2014).

[191]R. L. Siddon, "Prism representation: a 3D ray-tracing algorithm for radiotherapy applications", Phys. Med. Biol. **30**, 817–824 (1985).

[192]J. Löf, *RayStation order from Heidelberg University Hospital in Germany strenghtens the existing partnership*, en, July 2018.

[193]J. Löf and P. Thysell, *Heidelberg University Hospital treats first patient using carbon ion therapy with RayStation*, en, Aug. 2019.

[194]J. Löf and P. Thysell, "Germany's Heidelberg University Hospital will become the world's first cancer center to use RayStation for helium ion therapy planning", (2020).

[195]G. H. Hartmann, O. Jäkel, P. Heeg, C. P. Karger, and A. Krießbach, "Determination of water absorbed dose in a carbon ion beam using thimble ionization chambers", Phys. Med. Biol. **44**, 1193–1206 (1999).

[196]B. Kopp, S. Mein, I. Dokic, S. Harrabi, et al., "Development and Validation of Single Field Multi-Ion Particle Therapy Treatments", Int J Radiat Oncol Biol Phys **106**, 194–205 (2020).

[197]F. Horst, C. Schuy, U. Weber, K.-T. Brinkmann, and K. Zink, "Measurement of charge- and mass-changing cross sections for He 4 + C 12 collisions in the energy range 80–220 MeV/u for applications in ion beam therapy", en, Phys. Rev. C **96**, 024624 (2017).

[198]F. Horst, G. Aricò, K.-T. Brinkmann, S. Brons, et al., "Measurement of He 4 charge- and mass-changing cross sections on H, C, O, and Si targets in the energy range 70–220 MeV/u for radiation transport calculations in ion-beam therapy", en, Phys. Rev. C **99**, 014603 (2019).

[199]IAEA, *Absorbed Dose Determination in External Beam Radiotherapy*, edited by M. Carrara and K. Christaki, Technical Reports Series 398 (Rev. 1) (INTERNATIONAL ATOMIC ENERGY AGENCY, Vienna, 2024).

[200]T. Eichkorn, C. P. Karger, S. Brons, S. A. Koerber, et al., "Results of a prospective randomized trial on long-term effectiveness of protons and carbon ions in prostate cancer: LEM I and $\alpha/\beta = 2$ Gy overestimates the RBE", en, Radiother Oncol **173**, 223–230 (2022).

[201]R. Miralbell, S. A. Roberts, E. Zubizarreta, and J. H. Hendry, "Dose-Fractionation Sensitivity of Prostate Cancer Deduced From Radiotherapy Outcomes of 5,969 Patients in Seven International Institutional Datasets: $\alpha/\beta = 1.4$ (0.9–2.2) Gy", en, Int J Radiat Oncol Biol Phys **82**, e17–e24 (2012).

[202]G. Arcangeli, B. Saracino, S. Arcangeli, S. Gomellini, et al., "Moderate Hypofractionation in High-Risk, Organ-Confined Prostate Cancer: Final Results of a Phase III Randomized Trial", en, J Clin Oncol **35**, 1891–1897 (2017).

[203]G. Arcangeli, B. Saracino, S. Gomellini, M. G. Petrongari, et al., "A Prospective Phase III Randomized Trial of Hypofractionation Versus Conventional Fractionation in Patients With High-Risk Prostate Cancer", en, Int J Radiat Oncol Biol Phys **78**, 11–18 (2010).

[204]P. A. Kupelian, L. Potters, D. Khuntia, J. P. Ciezki, et al., "Radical prostatectomy, external beam radiotherapy <72 Gy, external beam radiotherapy ≥72 Gy, permanent seed implantation, or combined seeds/external beam radiotherapy for stage T1–T2 prostate cancer", en, Int J Radiat Oncol Biol Phys **58**, 25–33 (2004).

[205]H. Lukka, C. Hayter, J. A. Julian, P. Warde, et al., "Randomized Trial Comparing Two Fractionation Schedules for Patients With Localized Prostate Cancer", en, J Clin Oncol **23**, 6132–6138 (2005).

[206]E. E. Yeoh, R. H. Holloway, R. J. Fraser, R. J. Botten, et al., "Hypofractionated versus conventionally fractionated radiation therapy for prostate carcinoma: Updated results of a phase III randomized trial", en, Int J Radiat Oncol Biol Phys **66**, 1072–1083 (2006).

[207]T. J. Royce, P. Mavroidis, K. Wang, A. D. Falchook, et al., "Tumor Control Probability Modeling and Systematic Review of the Literature of Stereotactic Body Radiation Therapy for Prostate Cancer", en, Int J Radiat Oncol Biol Phys, A Red Journal Special Issue: HyTEC **110**, 227–236 (2021).

[208]S. L. Gulliford, M. Partridge, M. R. Sydes, S. Webb, P. M. Evans, and D. P. Dearnaley, "Parameters for the Lyman Kutcher Burman (LKB) model of Normal Tissue Complication Probability (NTCP) for specific rectal complications observed in clinical practise", en, Radiother Oncol **102**, 347–351 (2012).

[209]D. Wang, Y. Yin, Q. Zhou, Z. Li, et al., "Dosimetric predictors and Lyman normal tissue complication probability model of hematological toxicity in cervical cancer patients with treated with pelvic irradiation", en, Med Phys **49**, 756–767 (2022).

[210]S. L. Tucker, L. Dong, W. R. Bosch, J. Michalski, et al., "Late Rectal Toxicity on RTOG 94-06: Analysis Using a Mixture Lyman Model", en, Int J Radiat Oncol Biol Phys **78**, 1253–1260 (2010).

[211]T. Rancati, C. Fiorino, G. Gagliardi, G. Cattaneo, et al., "Fitting late rectal bleeding data using different NTCP models: results from an Italian multi-centric study (AIROPROS0101)", en, Radiother Oncol **73**, 21–32 (2004).

[212]G. Luxton, P. J. Keall, and C. R. King, "A new formula for normal tissue complication probability (NTCP) as a function of equivalent uniform dose (EUD)", Phys. Med. Biol. **53**, 23–36 (2008).

[213]W. Schaake, A. Van Der Schaaf, L. V. Van Dijk, A. H. Bongaerts, A. C. Van Den Bergh, and J. A. Langendijk, "Normal tissue complication probability (NTCP) models for late rectal bleeding, stool frequency and fecal incontinence after radiotherapy in prostate cancer patients", en, Radiother Oncol **119**, 381–387 (2016).

[214]G. Habl, M. Uhl, S. Katayama, K. A. Kessel, et al., "Acute Toxicity and Quality of Life in Patients With Prostate Cancer Treated With Protons or Carbon Ions in a Prospective Randomized Phase II Study—The IPI Trial", en, Int J Radiat Oncol Biol Phys **95**, 435–443 (2016).

[215]J. Löf and P. Thysell, "Heidelberg Ion Beam Therapy Center treats first patient using helium ion therapy with RayStation", (2021).

[216]T. Tessonnier, R. Wickert, J. Besuglow, S. Mein, et al., "PO-1976 Commissioning of helium ion therapy: physics, radiobiology and clinical directions at HIT", en, in Radiotherapy and Oncology, Vol. 182, ESTRO 2023, 13 - 16 May 2023, Vienna, Austria (May 2023), S1744–S1745.

[217]G. Habl, G. Hatiboglu, L. Edler, M. Uhl, et al., "Ion Prostate Irradiation (IPI) – a pilot study to establish the safety and feasibility of primary hypofractionated irradiation of the prostate with protons and carbon ions in a raster scan technique", en, BMC Cancer **14**, 202 (2014).

[218]J. Z. Wang, M. Guerrero, and X. Li, "How low is the α/β ratio for prostate cancer?", en, Int J Radiat Oncol Biol Phys **55**, 194–203 (2003).

[219]J. Besuglow, T. Tessonnier, S. Mein, T. Eichkorn, et al., "3187: The applied radiobiological effectiveness model influences tumor control when treating with ions", en, in Radiotherapy and Oncology, Vol. 194, ESTRO 2024, Physics - Optimisation, algorithms and applications for ion beam treatment planning (May 2024), S4726–S4727.

[220]T. Akagi, T. Maeda, M. Suga, and T. Yamashita, "Formation of spread-out Bragg peak for helium-ion beam using microdosimetric kinetic model", en, Phys Med **109**, 102587 (2023).

[221]T. Masuda and T. Inaniwa, "Effects of cellular radioresponse on therapeutic helium-, carbon-, oxygen-, and neon-ion beams: a simulation study", Phys. Med. Biol. **69**, 045003 (2024).

[222]N. Gambino, G. Guidoboni, M. Kausel, P. Mauro, et al., "Status of helium ion beams commissioning at MedAustron ion therapy center", en, in 15th International Particle Accelerator Conference (July 2024), pp. 1637–1640.

[223]A. M. R. Fira, O. D. Keta, V. D. Petković, M. Đorđević, et al., "In vitro validation of helium ion irradiations as a function of linear energy transfer in radioresistant human malignant cells", Int J Radiat Biol **0**, 1–12 (2024).

[224]W. M. Saunders, D. H. Char, J. M. Quivey, J. R. Castro, et al., "Precision, high dose radiotherapy: Helium ion treatment of uveal melanoma", Int J Radiat Oncol Biol Phys **11**, Publisher: Elsevier BV, 227–233 (1985).

[225]W. S. Grizzard, "Helium Ion Charged-Particle Therapy for Choroidal Melanoma: Histopathologic Findings in a Successfully Treated Case", en, Arch Ophthalmol **102**, 576 (1984).

[226]S. Kaliki and C. L. Shields, "Uveal melanoma: relatively rare but deadly cancer", eng, Eye (Lond) **31**, 241–257 (2017).

[227]E. Blakely, I. Daftari, W. Meecham, L. Alonso, et al., "Helium-ion-induced human cataractogenesis", en, Adv Space Res **14**, 501–505 (1994).

[228]S. D. Chang, R. P. Levy, J. R. Adler, D. P. Martin, P. R. Krakovitz, and G. K. Steinberg, "Stereotactic radiosurgery of angiographically occult vascular malformations: 14-year experience", en, Neurosurgery **43**, 213–220, discussion 220–221 (1998).

[229]C. P. Karger, C. Glowa, P. Peschke, and W. Kraft-Weyrather, "The RBE in ion beam radiotherapy: In vivo studies and clinical application", Z Med Phys, 10.1016/j.zemedi.2020.12.001 (2021).

[230]M. P. Carante, A. Embriaco, G. Arico, A. Ferrari, et al., "Biological effectiveness of He-3 and He-4 ion beams for cancer hadrontherapy: a study based on the BIANCA biophysical model", Phys Med Biol, Publisher: IOP Publishing, 10.1088/1361-6560/ac25d4 (2021).

[231]T. Tessonnier, S. Mein, D. W. Walsh, N. Schuhmacher, et al., "FLASH dose rate helium ion beams: first in vitro investigations", Int J Radiat Oncol Biol Phys **111**, Publisher: Elsevier BV, 1011–1022 (2021).

[232]I. Dokic, T. Tessonnier, S. Mein, D. Walsh, et al., "FLASH DOSE-RATE HELIUM ION BEAMS: FIRST IN VITRO INVESTIGATIONS", en, in Physica Medica, Vol. 94 (Feb. 2022), S92.

[233]B. Cepni, T. Tessonnier, I. Dokic, S. Brons, et al., "Evaluation of Helium Ion Radiotherapy in Combination with Gemcitabine in Pancreatic Cancer In Vitro", Cancers (Basel) **16**, Publisher: MDPI, 1497 (2024).

[234]B. Knäusl, H. Fuchs, K. Dieckmann, and D. Georg, "Can particle beam therapy be improved using helium ions? – a planning study focusing on pediatric patients", en, Acta Oncol **55**, 751–759 (2016).

[235]R. Wickert, T. Tessonnier, M. Deng, S. Adeberg, et al., "Radiotherapy with Helium Ions Has the Potential to Improve Both Endocrine and Neurocognitive Outcome in Pediatric Patients with Ependymoma", en, Cancers **14**, 5865 (2022).

[236]L. Hoeltgen, E. Meixner, P. Hoegen-Saßmannshausen, J.-Y. Kim, et al., "Helium Ion Therapy for Advanced Juvenile Nasopharyngeal Angiofibroma", en, Cancers **16**, 1993 (2024).

[237]T. Tessonnier, A. Mairani, W. Chen, P. Sala, et al., "Proton and helium ion radiotherapy for meningioma tumors: a Monte Carlo-based treatment planning comparison", Radiat Oncol **13**, Publisher: Springer Science and Business Media LLC, 2 (2018).

[238]D. K. Ebner, S. J. Frank, T. Inaniwa, S. Yamada, and T. Shirai, "The Emerging Potential of Multi-Ion Radiotherapy", Front Oncol **11**, 624786 (2021).

[239]T. Inaniwa, M. Kramer, A. Mairani, E. Scifoni, and O. Sokol, "Towards multiple ion applications in particle therapy", in *Monte Carlo in Heavy Charged Particle Therapy*, Num Pages: 13 (CRC Press, 2024).

[240]A. Mairani, "Innovative approaches to enhance high-LETd tumor targeting in carbon ion radiotherapy", en, Health Technol, 10.1007/s12553-024-00842-x (2024).

[241]S. Mein, T. Tessonnier, B. Kopp, S. Harrabi, et al., "Spot-Scanning Hadron Arc (SHArc) Therapy: A Study With Light and Heavy Ions", Adv Radiat Oncol **6**, 100661 (2021).

[242]S. Mein, T. Tessonnier, B. Kopp, J. Debus, et al., "Next Evolutions in Particle Therapy: Spot-Scanning Hadron Arc (SHArc) Therapy", Int J Radiat Oncol Biol Phys **111**, Publisher: Elsevier BV, S139–S140 (2021).

[243]L. Volz, Y. Sheng, L. Kong, M. Durante, and C. Graeff, "Exploring energy selection methods for robust biologically optimized carbon ion arc for head&neck cancer patients", en, Health Technol, 10.1007/s12553-024-00877-0 (2024).

[244]S. Mein, S. Wuyckens, X. Li, S. Both, et al., “Particle arc therapy: Status and potential”, Radiother Oncol **199**, 110434 (2024).

[245]D. H. Brand, S. C. Brüningk, A. Wilkins, O. Naismith, et al., “The Fraction Size Sensitivity of Late Genitourinary Toxicity: Analysis of Alpha/Beta (α/β) Ratios in the CHHiP Trial”, Int J Radiat Oncol Biol Phys **115**, 327–336 (2023).

[246]D. H. Brand, S. C. Brüningk, A. Wilkins, K. Fernandez, et al., “Estimates of Alpha/-Beta (α/β) Ratios for Individual Late Rectal Toxicity Endpoints: An Analysis of the CHHiP Trial”, Int J Radiat Oncol Biol Phys **110**, 596–608 (2021).

[247]D. H. Brand, A. C. Tree, P. Ostler, H. van der Voet, et al., “Intensity-modulated fractionated radiotherapy versus stereotactic body radiotherapy for prostate cancer (PACE-B): acute toxicity findings from an international, randomised, open-label, phase 3, non-inferiority trial”, Lancet Oncol **20**, 1531–1543 (2019).

[248]A. C. Tree, P. Ostler, H. van der Voet, W. Chu, et al., “Intensity-modulated radiotherapy versus stereotactic body radiotherapy for prostate cancer (PACE-B): 2-year toxicity results from an open-label, randomised, phase 3, non-inferiority trial”, Lancet Oncol **23**, 1308–1320 (2022).

[249]K. Menne Guricová, V. Groen, F. Pos, E. Monninkhof, et al., “Risk Modeling for Individualization of the FLAME Focal Boost Approach in External Beam Radiation Therapy for Patients With Localized Prostate Cancer”, en, Int J Radiat Oncol Biol Phys **118**, 66–73 (2024).

[250]A. M. Dornisch, A. Y. Zhong, D. M. C. Poon, A. C. Tree, and T. M. Seibert, “Focal radiotherapy boost to MR-visible tumor for prostate cancer: a systematic review”, en, World J Urol **42**, 56 (2024).

[251]L. G. W. Kerkmeijer, V. H. Groen, F. J. Pos, K. Haustermans, et al., “Focal Boost to the Intraprostatic Tumor in External Beam Radiotherapy for Patients With Localized Prostate Cancer: Results From the FLAME Randomized Phase III Trial”, J Clin Oncol **39**, Publisher: Wolters Kluwer, 787–796 (2021).

[252]C. Draulans, U. A. van der Heide, K. Haustermans, F. J. Pos, et al., “Primary endpoint analysis of the multicentre phase II hypo-FLAME trial for intermediate and high risk prostate cancer”, Radiother Oncol **147**, 92–98 (2020).

[253]B. Yasar, Y.-E. Suh, E. Chapman, L. Nicholls, et al., “Simultaneous Focal Boost With Stereotactic Radiation Therapy for Localized Intermediate- to High-Risk Prostate Cancer: Primary Outcomes of the SPARC Phase 2 Trial”, Int J Radiat Oncol Biol Phys **120**, 49–58 (2024).

[254]G. Corrao, G. Marvaso, F. Mastroleo, A. Biffi, et al., “Photon vs proton hypofractionation in prostate cancer: A systematic review and meta-analysis”, en, Radiother Oncol **195**, 110264 (2024).

[255]H. Ishikawa, Y. Hiroshima, N. Kanematsu, T. Inaniwa, et al., “Carbon-ion radiotherapy for urological cancers”, en, Int J Urol **29**, 1109–1119 (2022).

[256]Y. Takakusagi, H. Koge, K. Kano, S. Shima, et al., “Five-year clinical outcomes of scanning carbon-ion radiotherapy for prostate cancer”, en, PLoS ONE **19**, edited by C. Casà, e0290617 (2024).

[257]Y.-M. Kang, H. Ishikawa, T. Inaniwa, Y. Iwai, et al., “The clinical relative biological effectiveness and prostate-specific antigen kinetics of carbon-ion radiotherapy in low-risk prostate cancer”, en, Cancer Med **12**, 1540–1551 (2023).

[258]K. Sritharan, H. Akhiat, D. Cahill, S. Choi, et al., "Development of Prostate Bed Delineation Consensus Guidelines for Magnetic Resonance Image-Guided Radiotherapy and Assessment of Its Effect on Interobserver Variability", en, Int J Radiat Oncol Biol Phys **118**, 378–389 (2024).

[259]A. Dal Pra, P. Dirix, V. Khoo, C. Carrie, et al., "ESTRO ACROP guideline on prostate bed delineation for postoperative radiotherapy in prostate cancer", Clinical and Translational Radiation Oncology **41**, 100638 (2023).

[260]J. R. Murray, A. C. Tree, E. J. Alexander, A. Sohaib, et al., "Standard and Hypofractionated Dose Escalation to Intraprostatic Tumor Nodules in Localized Prostate Cancer: Efficacy and Toxicity in the DELINEATE Trial", en, Int J Radiat Oncol Biol Phys **106**, 715–724 (2020).

[261]O. D. Hertogh, G. L. Bihan, T. Zilli, S. Palumbo, et al., "Consensus Delineation Guidelines for Pelvic Lymph Node Radiation Therapy of Prostate Cancer: On Behalf of the Francophone Group of Urological Radiation Therapy (GFRU)", English, Int J Radiat Oncol Biol Phys **118**, 29–40 (2024).

[262]C. Salembier, G. Villeirs, B. De Bari, P. Hoskin, et al., "ESTRO ACROP consensus guideline on CT- and MRI-based target volume delineation for primary radiation therapy of localized prostate cancer", Radiotherapy and Oncology **127**, 49–61 (2018).

[263]M. Moteabbed, M. Bobić, H. Paganetti, and J. A. Efstathiou, "The Role of Proton Therapy for Prostate Cancer in the Setting of Hip Prosthesis", en, Cancers **16**, Number: 2 Publisher: Multidisciplinary Digital Publishing Institute, 330 (2024).

[264]Y. Zhao, A. Haworth, H. M. Reynolds, S. G. Williams, et al., "Towards optimal heterogeneous prostate radiotherapy dose prescriptions based on patient-specific or population-based biological features", en, Med Phys **51**, 3766–3781 (2024).

[265]A. Yorozu, M. Namiki, S. Saito, S. Egawa, et al., "Trimodality Therapy With Iodine-125 Brachytherapy, External Beam Radiation Therapy, and Short- or Long-Term Androgen Deprivation Therapy for High-Risk Localized Prostate Cancer: Results of a Multicenter, Randomized Phase 3 Trial (TRIP/TRIGU0907)", en, Int J Radiat Oncol Biol Phys **118**, 390–401 (2024).

[266]M. Chen, B. Pang, Y. Zeng, C. Xu, et al., "Evaluation of an automated clinical decision system with deep learning dose prediction and NTCP model for prostate cancer proton therapy", en, Phys Med Biol **69**, 115056 (2024).

[267]S. Molinelli, G. Magro, A. Mairani, A. Allajbej, et al., "How LEM-based RBE and dose-averaged LET affected clinical outcomes of sacral chordoma patients treated with carbon ion radiotherapy", Radiother Oncol **163**, 209–214 (2021).

[268]S. Grosshagauer, P. Fossati, M. Schafasand, A. Carlino, et al., "Organs at risk dose constraints in carbon ion radiotherapy at MedAustron: Translations between LEM and MKM RBE models and preliminary clinical results", en, Radiother Oncol **175**, 73–78 (2022).

[269]J. Góra, S. Grosshagauer, P. Fossati, M. Mumot, et al., "The sensitivity of radiobiological models in carbon ion radiotherapy (CIRT) and its consequences on the clinical treatment plan: Differences between LEM and MKM models", en, J Applied Clin Med Phys **25**, e14321 (2024).

[270]P. Fossati, A. Perpar, M. Stock, P. Georg, et al., "Carbon Ion Dose Constraints in the Head and Neck and Skull Base: Review of MedAustron Institutional Protocols", Int J Part Ther **8**, 25–35 (2021).

[271]S. Mein, B. Kopp, A. Vela, P. Dutheil, et al., "How can we consider variable RBE and LETd prediction during clinical practice? A pediatric case report at the Normandy Proton Therapy Centre using an independent dose engine", en, Radiat Oncol **17**, 23 (2022).

[272]K. Choi, S. Molinelli, S. Russo, A. Mirandola, et al., "Rectum Dose Constraints for Carbon Ion Therapy: Relative Biological Effectiveness Model Dependence in Relation to Clinical Outcomes", en, Cancers **12**, 46 (2019).

[273]W. Wang, Z. Huang, Y. Sheng, J. Zhao, et al., "RBE-weighted dose conversions for carbon ionradiotherapy between microdosimetric kinetic model and local effect model for the targets and organs at risk in prostate carcinoma", en, Radiother Oncol **144**, 30–36 (2020).

[274]F. Baltazar, T. Tessonnier, T. Haberer, J. Debus, et al., "Carbon-ion radiotherapy (CIRT) as treatment of pancreatic cancer at HIT: initial radiation plan analysis of the prospective phase II PACK-study", en, Radiother Oncol **188**, 109872 (2023).

[275]J. Besuglow, T. Tessonnier, S. Mein, T. Eichkorn, et al., "SC17.06 RBE's role in ion therapy of prostate cancer", en, in Physica Medica, Vol. 125, Abstracts of the 5th European Congress of Medical Physics (Sept. 2024), p. 103492.

[276]Y. Lao, M. Cao, Y. Yang, A. U. Kishan, et al., "Bladder surface dose modeling in prostate cancer radiotherapy: An analysis of motion-induced variations and the cumulative dose across the treatment", en, Med Phys **48**, 8024–8036 (2021).

[277]V. H. Groen, M. Van Schie, N. P. Zuithoff, E. M. Monninkhof, et al., "Urethral and bladder dose–effect relations for late genitourinary toxicity following external beam radiotherapy for prostate cancer in the FLAME trial", en, Radiother Oncol **167**, 127–132 (2022).

[278]P. Papanikolaou, G. Swanson, S. Stathakis, and P. Mavroidis, "NTCP Modeling and Dose-Volume Correlations of Significant Hematocrit Drop 3 Months After Prostate Radiation Therapy", en, Adv Radiat Oncol **9**, 101393 (2024).

[279]C. Karle, H. Liew, T. Tessonnier, N. Schuhmacher, et al., "EXPLORING ULTRA-HIGH DOSE RATE SPARING FOR HEAVY ION IRRADIATION", en, Int J Part Ther, Proceedings to the 62nd Annual Conference of the Particle Therapy Cooperative Group (PTCOG) **12**, 100184 (2024).

[280]I. Dokic, T. Tessonnier, S. Meister, M. Moustafa, et al., *Ultra-High Dose Rate Helium Ion Beams: First In Vivo Evidence for Neuroprotective FLASH Effect*, New Results, June 2024.

[281]A. Mairani, T. Tessonnier, S. Mein, D. Walsh, et al., "FLASH Dose-Rate Helium Ion Beams: First In Vitro Investigations", Int J Radiat Oncol Biol Phys **111**, Publisher: Elsevier BV, S20–S21 (2021).

[282]R. Ahmad, A. Barcellini, K. Baumann, M. Benje, et al., "Particle Beam Radiobiology Status and Challenges: A PTCOG Radiobiology Subcommittee Report", Int J Part Ther **13**, 100626 (2024).

[283]J. Besuglow, S. Mein, B. Kopp, S. Brons, et al., "Towards a Helium Ion-Beam Therapy Program in 2020: Physical, Biological and Clinical Considerations", in Joint AAPM|COMP Meeting, Issue: WE-B-Track 3-1 (July 2020).

[284]A. Mairani, S. Mein, B. Kopp, J. Besuglow, et al., "Back to the Future: Helium Ion Therapy 2020", en, in International Journal of Radiation Oncology*Biology*Physics, Vol. 108, Proceedings of the American SocieTy for Radiation Oncology (Nov. 2020), S67–S68.

[285]T. Tessonnier, S. Mein, J. Besuglow, B. Kopp, et al., "Next Evolutions in Particle Therapy: Helium Ion Treatment Planning, Delivery and Clinical Implications of Biological Modeling", in International Journal of Radiation Oncology*Biology*Physics, Vol. 111, 2021 Proceedings of the ASTRO 63rd Annual Meeting, Issue: 3 (Nov. 2021), e516–e517.

[286]T. Kurosawa, N. Nakao, T. Nakamura, Y. Uwamino, et al., "Measurements of Secondary Neutrons Produced from Thick Targets Bombarded by High-Energy Helium and Carbon Ions", Nucl Sci Eng **132**, 30–57 (1999).

[287]C. M. Van Leeuwen, A. L. Oei, J. Crezee, A. Bel, et al., "The alfa and beta of tumours: a review of parameters of the linear-quadratic model, derived from clinical radiotherapy studies", en, Radiat Oncol **13**, 96 (2018).

[288]C. R. King and C. S. Mayo, "Is the prostate α/β ratio of 1.5 from Brenner & Hall a modeling artifact?", en, Int J Radiat Oncol Biol Phys **47**, 536–538 (2000).

Part IV

Appendices

A Unpublished Results of Database Creation

A.1 Integrated Depth Dose Distribution of Pristine Bragg Peaks

As described in sections 3.2.1 and 3.3, IDDs are measured for several energies with 3mm thick ripple filter (RiFi3mm) and no ripple filter in the beamline (noRiFi) positioned in the beam. Table A.1 contains all measured energies and the corresponding RiFi and focus configuration.

The characteristics of measured and simulated IDDs were extracted and compared in Figure A.1.

A.2 Lateral Dose Distributions

Table A.2 contains an overview of all measured configurations for the lateral dose profiles in air and water.

The datasets 1 and 4 pf Table A.2 were measured by Stephan Brons. In contrast to the horizontal rooms, the detector positions had to be adjusted for the gantry room. For comparison, the reader is referred to Figure A.2.

Lateral Dose in Water

The lateral spread of the beam along the depth in material is particularly relevant for the new TPS. Once evaluated, this data can assist in adjusting the 'halo'-model of the RayStation®dose calculation engine. It also gives a hint, whether the interaction cross sections implemented in FLUKA are sufficiently correct.

For 50 % to 1 % of the maximum dose levels, the FLUKA simulation underestimates the lateral width of the beam. The width at 0.1 % level is overestimated by FLUKA in comparison to the measured width. In the later case, measurements for 0.1 % of the maximum sometimes yield in dose levels below the detector sensitivity, making the evaluation of the width unreliable.

The introduction of a double Gaussian (DG) beam shape in vacuum instead of the single Gaussian (SG) approach used for the database improved the match between simulated and measured lateral beam profiles. The estimated parameters for the double Gaussian are approximately equal to the weighted sum of the original single Gaussian with a 6.50 % to 8.00 % contribution of a second Gaussian. The second Gaussian has a FWHM between 2.00 to 4.00 times the FWHM of the first Gaussian. With the double Gaussian approach matched to isocentric measurement, the shape deviations at other measurement positions in air and

Table A.1: IDDs for TPS base data. Investigated energies with their corresponding width (FWHM) at isocenter and momentum spread (dp/p). The listed FWHM is extracted from the accelerator library containing nominal beam energies, beamwidths and intensity settings (LIBC). The indicators '+' and 'o' declare whether the simulations and measurements have been taken with RiFi3mm or noRiFi. *Set A*: measured by Thomas Tessonnier[11]. *Set B* measured by Judith Besuglow in October 2019. *Set C*: control data measured by Jakob Naumann and Benjamin Ackermann in January 2020.

Energy		FWHM	**dp/p**	**PEAKFINDER®**			**field size**
E#	MeV u^{-1}	mm	%	set B	set C	set A	
1	50.57	18.6	0.3710	+	+		+
6	56.44	16.7	0.3150	+		+ o	
13	63.93	14.6	0.2575		+		
22	72.65	12.8	0.2110	+			+
28	78.05	11.9	0.1904		+		
30	79.78	11.6	0.1850			+ o	
33	82.33	11.3	0.1780	+			+
37	85.64	10.9	0.1700		+		
46	92.75	10.1	0.1569		+		
56	100.91	9.4	0.1478		+		
60	103.05	9.2	0.1450			+ o	
67	107.93	8.9	0.1410	+			+
80	116.58	8.3	0.1340	+			
90	122.93	7.9	0.1300	+		+ o	
107	133.80	7.4	0.1260	+	+		+
120	140.71	7.1	0.1250	+		+ o	+
141	152.80	6.5	0.1008		+		
150	157.56	6.3	0.0900			+ o	
152	158.60	6.3	0.0880	+			+
165	164.78	6.0	0.0750	+			
180	172.28	5.8	0.0630	+		+ o	
198	182.43	5.7	0.0500	+			+
198	182.43	6.6	0.0500	+			
200	183.85	5.4	0.0485		+		
210	190.85	5.3	0.0410	+	+	+ o	
226	201.71	5.1	0.0320	+			+
226	201.71	6.3	0.0320	+			
235	207.66	5.0	0.0280		+		
240	210.92	5.0	0.0260			+ o	
255	220.51	4.9	0.0210		+	+ o	+

water were reduced as well. For one sampled beam energy the lateral dose profile is shown in Figure 6 of 4.

Table A.2: Measurements of lateral beam profiles for base data. This table contains the investigated energies with their LIBC width (FWHM) at isocenter and momentum spread (dp/p) used for simulation. The indicators '+' and 'o' declare whether the simulations and measurements have been taken with RiFi3mm or noRiFi. At isocenter, the profiles were always measured for both RiFi settings. Four data sets exits: *set 1* from March 2019; RAM settings of Oct 2019 in *set 2*; gantry Aug 2020 *set 3*; settings of gantry (G) and horizontal rooms (H) of Feb 2021 in *set 4*. F1-4 correspond to the focus steps.

	Energy	**F1 (FWHM)**	**dp/p**	air				water
#	MeV u^{-1}	mm	%	set 1	set 2	set 3	set 4	
1	50.57	18.6	0.3710	H, F1, +o	H, F1, +	G, F1, +	HG, F1-4, +	
6	56.44	16.7	0.3150	H, F1, +o	H, F1, +	G, F1, +	HG, F1-4, +	
22	72.65	12.8	0.2110	H, F1, +o	H, F1, +	G, F1, +	HG, F1-4, +	H, F1, +
33	82.33	11.3	0.1780	H, F1, +o	H, F1, +	G, F1, +	HG, F1-4, +	H, F1, +
67	107.93	8.9	0.1410	H, F1, +o	H, F1, +	G, F1, +	HG, F1-4, +	H, F1, +
90	122.93	7.9	0.1300	H, F1, +o	H, F1, +	G, F1, +	HG, F1-4, +	H, F1, +
107	133.80	7.4	0.1260	H, F1, +o	H, F1, +	G, F1, +	HG, F1-4, +	H, F1, +
120	140.71	7.1	0.1250	H, F1, +o	H, F1, +	G, F1, +	HG, F1-4, +	H, F1, +
152	158.60	6.3	0.0880	H, F1, +o	H, F1, +	G, F1, +	HG, F1-4, +	H, F1, +
180	172.28	5.8	0.0630	H, F1, +o	H, F1, +	G, F1, +	HG, F1-4, +	H, F1, +
198	182.43	5.7	0.0500	H, F1, +o	H, F1, +	G, F1, +	HG, F1-4, +	H, F1, +
210	190.85	5.3	0.0410	H, F1, +o	H, F1, +	G, F1, +	HG, F1-4, +	H, F1, +
226	201.71	5.1	0.0320	H, F1, +o	H, F1, +	G, F1, +	HG, F1-4, +	H, F1, +
255	220.51	4.9	0.0210	H, F1, +o	H, F1, +	G, F1, +	HG, F1-4, +	H, F1, +

A separation of the dose contribution by $Z = 1$ and $Z = 2$ particles in the simulation gave evidence, that the second Gaussian in the tail of the Bragg Peak is mostly produced by protons. Whether the proton contribution is underestimated due to misrepresentation of the BAMS geometry in the simulation or to fluctuating beam shape could not be determined yet. With a double Gaussian (DG) initial beam profile, the FLUKA simulation and measurements match adequately, see Figure A.3

A.3 Spread-out Bragg Peaks

SOBPs are used to evaluate the MC beam model. Therefor SOBP plans were optimized with PRECISE and then simulated with FLUKA, compare section 3.2.5. Table A.3 provides a list of all investigated SOBPs. The first simulation with version fluka2019.dev did not yield a satisfying match to measurements of these SOBPs. Updated nuclear interaction models and a double Gaussian initial beam profile in the developer's version 2020.3.dev of FLUKA reduced the local devi-

ation to about 4 % of the mean dose in the center of the high dose region. In the example of the $(3 \times 3 \times 3)\,\mathrm{cm}^3$ SOBP in Figure A.4, the limitation of these SOBP's become visible. The high dose region is not sufficiently homogeneous to account for positioning uncertainties. Therefor, newly optimized SOBPs were used to commission RayStation®as a clinical TPS (Chapter 5).

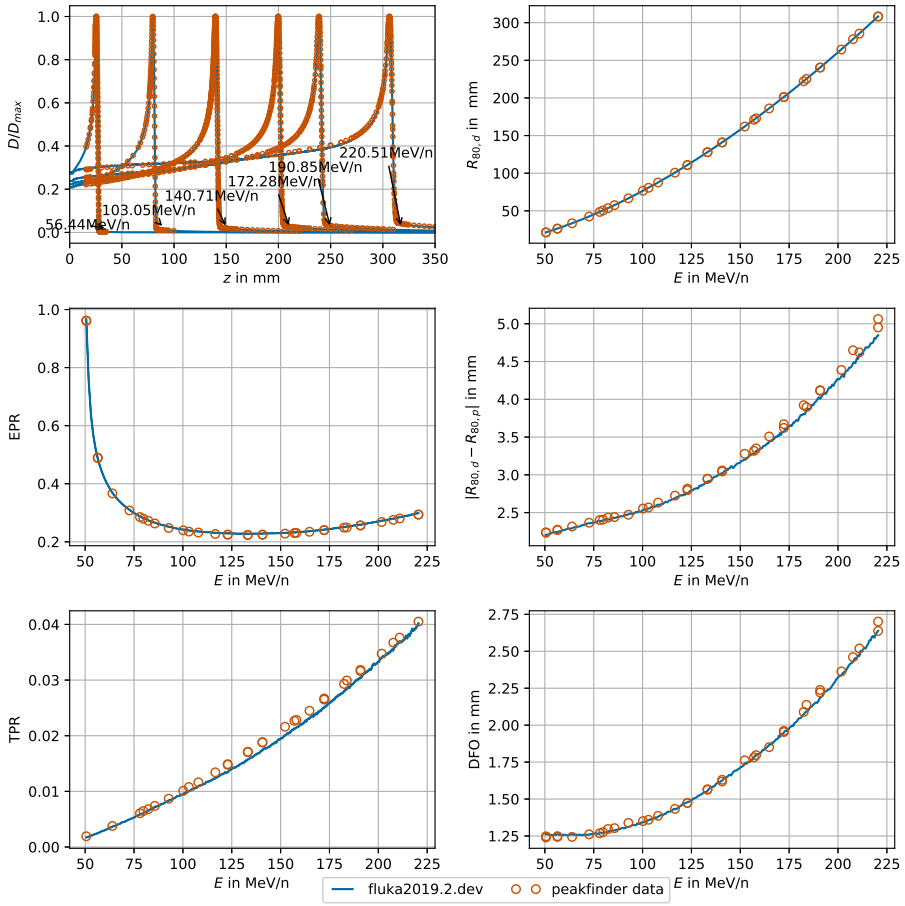

Figure A.1: *IDD Characteristics*: IDDs of Pristine Bragg peaks (a) and the energy dependence of their properties (b)-(f) show good agreement between measurements (orange) and simulation of the PEAKFINDER® setup (blue). The properties are extracted from the relative depth dose distributions in (a). The entrance-to-peak ratio (EPR) and tail-to-peak ratio (TPR) are provided in subplots (b) and (c), where the entrance dose was defined at a water-equivalent-depths of 20 mm and the tail dose defined at a position R_{tail} 10 mm behind the distal 90% dose level $R_{90,d}$. Subplot (d) shows the distal range $R_{80,d}$ at 80% of the maximal dose D_{max}. Subplot (e) shows the w_{peak} from proximal to distal 80% dose level and subplot (f) the DFO as the difference between distal 80% and 20% dose level.

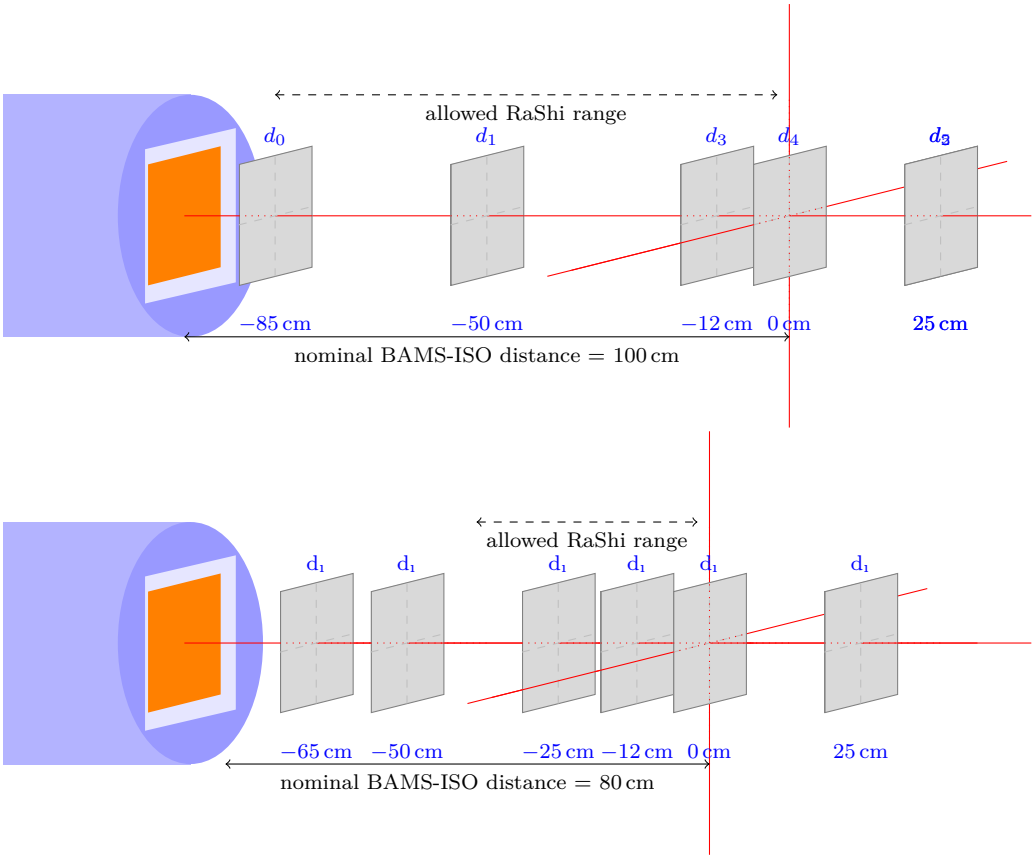

Figure A.2: *Measurement positions for the lateral dose profiles in air.* The gray rectangles indicate the positions of OCTAVIUS® 1000 SRS P . These measurement positions are named d_{0-6} and their distance relative to the isocentre in the horizontal (top) and gantry treatment room (bottom) provided in cm. Red lines indicate the lasers of the positioning system. The blue cylinder on the left represent the nozzle and RiFi3mm. The gray rectangles indicate the detector positions.

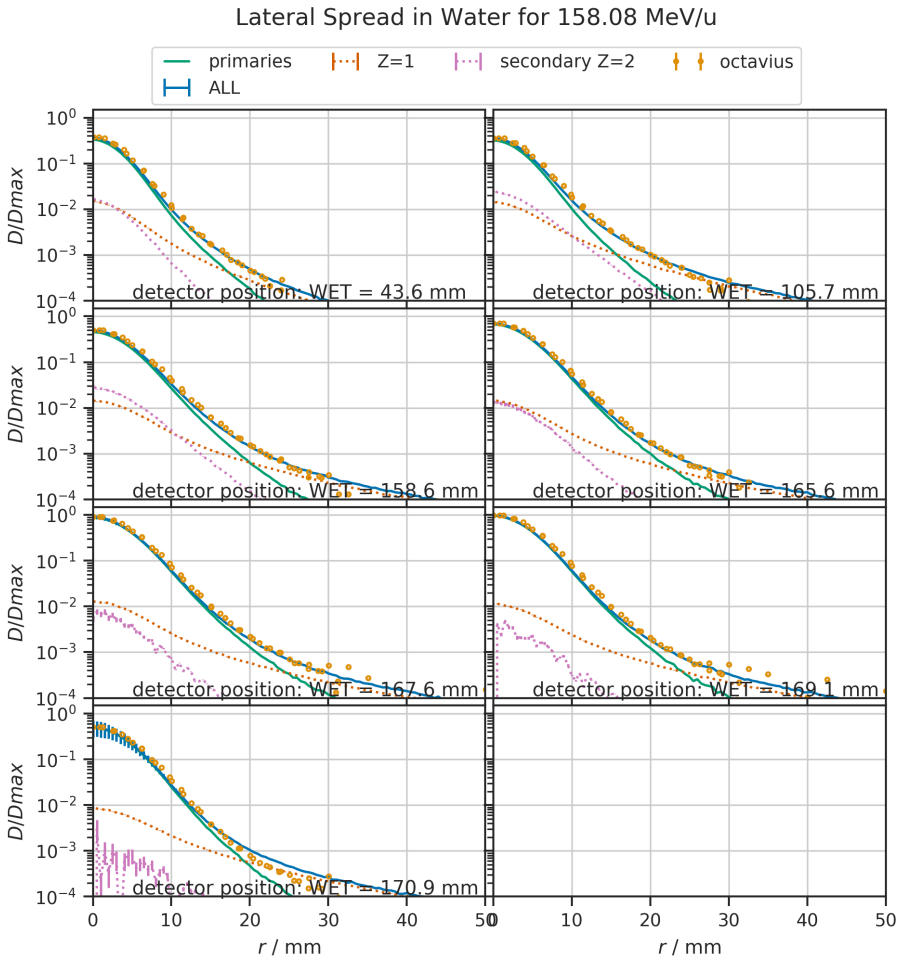

Figure A.3: Contribution of various primary and secondary beam particles discriminated by their charge number Z to the lateral dose distribution in water.

Table A.3: List of measured SOBP configurations

Name	**centered at**	**field size**	**lengths of field**	**RaShi**
	cm	cm	cm	
111	5.0	3x3	3	y/n
112	12.5	3x3	3	n
113	20.0	3x3	3	n
114	27.0	3x3	3	n
123	20.0	3x3	6	n
221	5.0	6x6	6	y/n
222	12.5	6x6	6	y/n
223	20.0	6x6	6	n
224	27.0	6x6	6	n
311	3.6	10x10	3	y
411	3.6	20x20	3	n
412	13.5	20x20	3	n
415	29.0	20x20	3	n

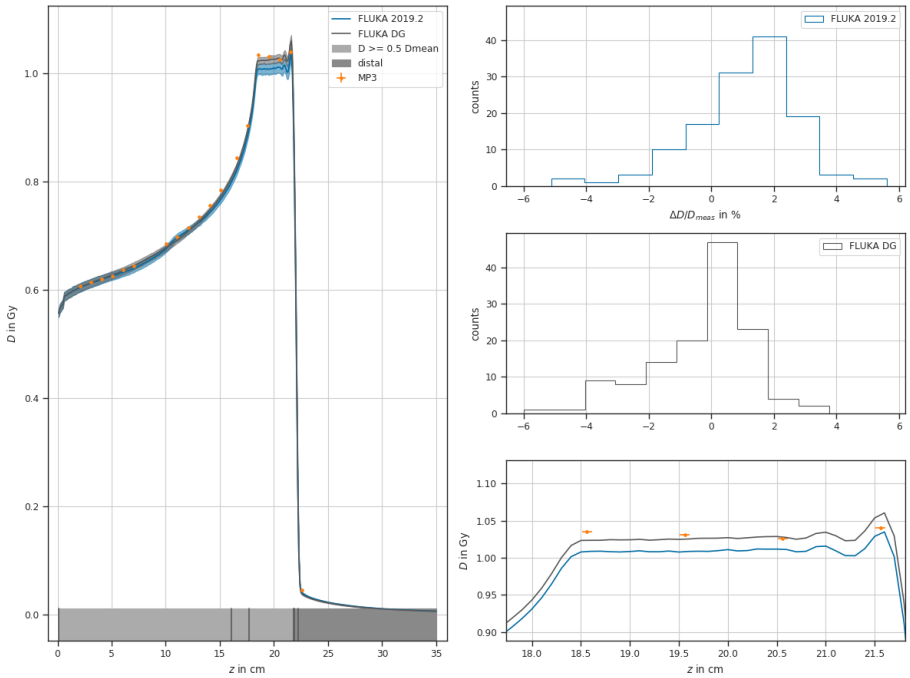

(a) $(3 \times 3 \times 3)\,\mathrm{cm}^3$ SOBP centered at a depth of 20 cm in water.

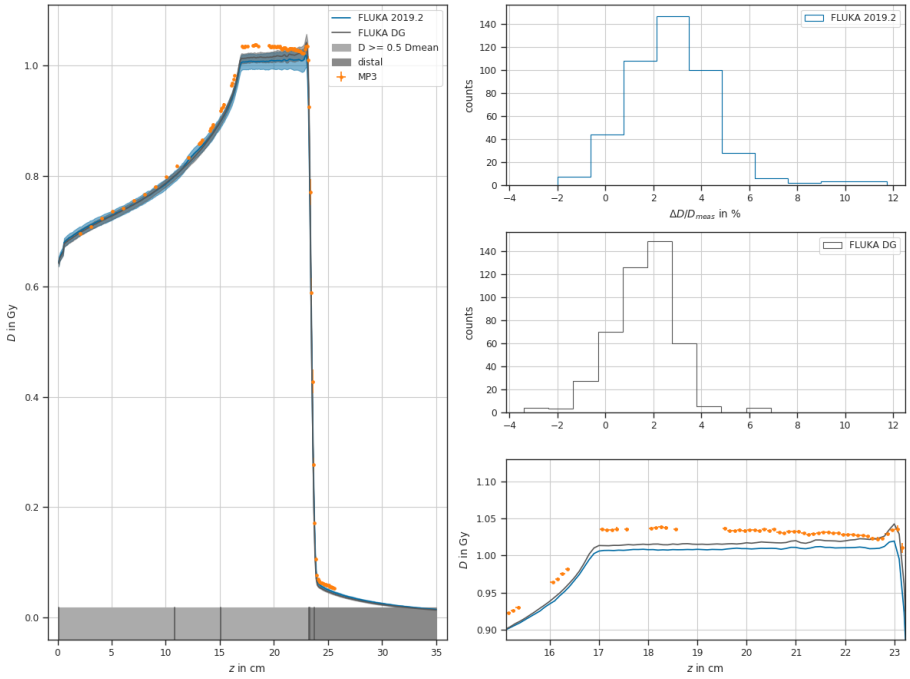

(b) $(6 \times 6 \times 6)\,\mathrm{cm}^3$ SOBP centered at a depth of 20 cm in water.

Figure A.4: *Measurement and FLUKA prediction for two SOBPs.* The left panel depicts the simulated depth dose profiles in blue (fluka2019.2) and grey (fluka2020.3 + double Gaussian). Doses measured with the MP3 waterphantom are depicted in orange. The to upper panels on the right show histograms of the relative deviation between measured and simulated doses. The lower right panel provides a closer look to the high dose region of the SOBP.

B Nuclear Reaction Models in FLUKA

For the therapeutically used energy range, FLUKA calculates nuclear interaction following two different physical approximations: Below 125 MeV/n the BME dominates and the modified RQMD model is applied for energies between 125 MeV/n to 5000 MeV/n. The transition between BME and RQMD can be smoothed out by weighting the two models around the transition energy. Since only very limited cross-section data for Helium is available at this energy range, the implementation of these to nuclear reaction models could possibly be improved. So we searched the EXFOR [37, 38] database for relevant cross-section data. Reasonable double differential yield or cross-section data can be found in two studies [33–35].

We modeled a geometrically equivalent setup of the thick target yield measured by Kurosawa et al. [33, 35, 286] in FLUKA. Then we separated the yields from different interaction channels. The same was repeated for the thin target double differential cross-section reported by Sato et al. [34]. While neutron and proton production seem symmetric in the thick target simulations, the measurements are not. Sato et al. [34] unfortunately only reported the neutron production cross-section which agrees nicely with the simulation. Extrapolation of the Sato set-up to 50 MeV/n revealed a spike in the double-differential cross-section, that cannot be explained by a known resonance, see figure B.1.

Since, no exact physical model exists to describe the nuclear interaction at these energies, changing the implementation in FLUKA will be digging in the dark. Although we can see from the plots, that the three- body interactions are the most promising to be tuned.

Updating the Nuclear Reaction Cross-sections

Before manipulating the nuclear reaction models in FLUKA a full database of double differential yield for all secondaries was simulated with the current FLUKA version. For the twelve most relevant target isotopes in the human body, the double differential production yield of protons, neutrons, deuterons, tritons, helions, alphas and photons and recoil energy by a proton and helium beam of 10 MeV u^{-1} to 300 MeV u^{-1} was extracted. While Alfredo Ferrari adjusted some of the nuclear reaction cross-sections on the RQMD side of the energy spectrum, I was unable to decipher the FLUKA source code far enough to make any sensible adjustments on the BME side. These improvements in FLUKA were left for another project to finish.

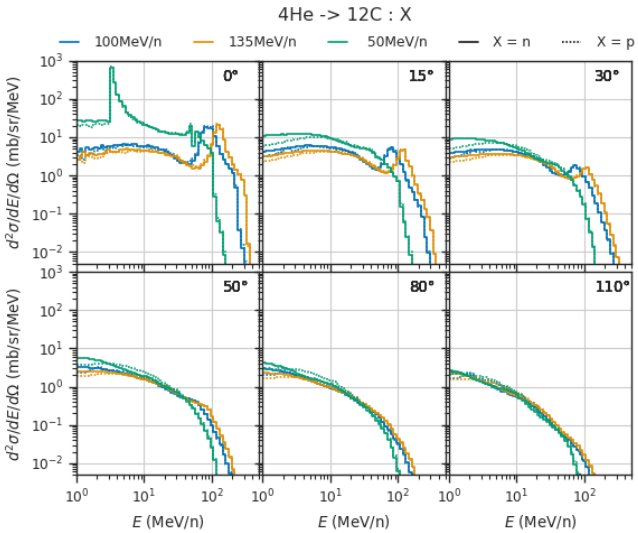

Figure B.1: Double differential cross-section for secondary production for three initial beam energies of 4-He on a thin 12-C target.

C Unpublished Results from Analysis of Prostate Patients

Based on the publications of [129, 287], we chose four combinations of tissue parameters spanning the clinically observed parameter range from $(\alpha/\beta)_x = 1.5\,\mathrm{Gy}$ to $5\,\mathrm{Gy}$. The mMKM-specific parameters R_d and R_n were chosen as proposed by [96]. Table C.1 gives an overview of all used parameters.

Table C.1: *Tissue parameters used for RBE calculation with mMKM.* Linear-quadratic (LQ)-parameters for prostate tissue according to literature and mMKM specific parameters R_d and R_n as fitted by Mairani et al. [96].

$(\alpha/\beta)_x$/Gy	α_x/Gy^{-1}	β_x/Gy^{-2}	R_d/µm	R_n/µm	Reference
1.5	0.036	0.024	0.3	3.6	[129]
2.0	0.05	0.025	0.3	3.6	HIT standard
3.1	0.15	0.0484	0.3	3.6	[129, 218]
4.96	0.346	0.0698	0.3	3.6	[129, 288]

For each tissue parameters, we scored the dose-weighted average z^*_{1d} profiles as a function of depth for all available beam energies and beam particles.

Resulting DVHs and TCP functions are reported in publication 6. Investigation and results of the other parameters are reported in the following sections.

Dose Estimation of IPI patients for other

Before a decision on a TCP function was taken, the RBE-weighted DVHs of all IPI patients were recalculated for all parameter sets in Table C.1. A collection of these DVHs is provided in Figure C.1.

NTCP of organs relevant in prostate irradiation

Similarly to the investigated target volume, effective DVHs for the most relevant OARs are presented in Figure C.2.

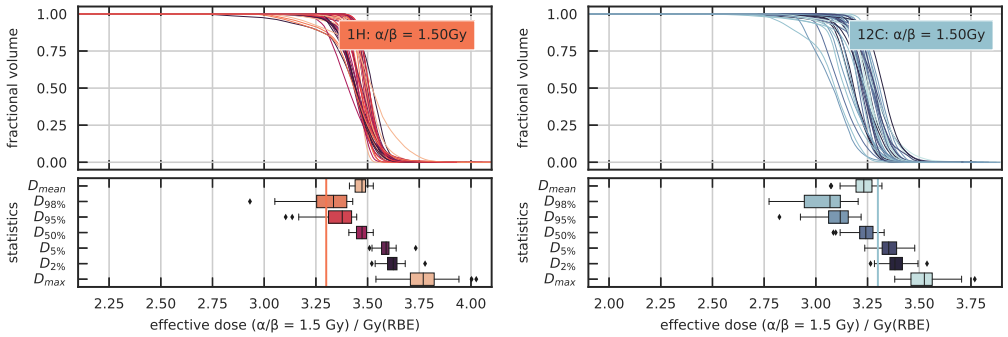

(a) $(\alpha/\beta)_x = 1.5\,\mathrm{Gy}$

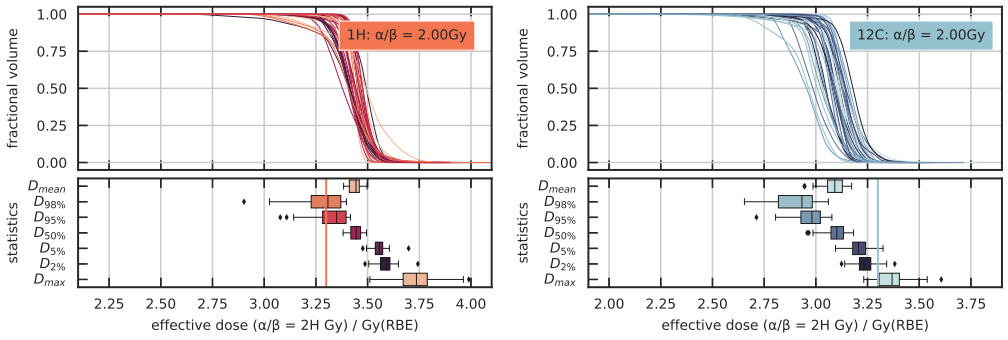

(b) $(\alpha/\beta)_x = 2\,\mathrm{Gy}$

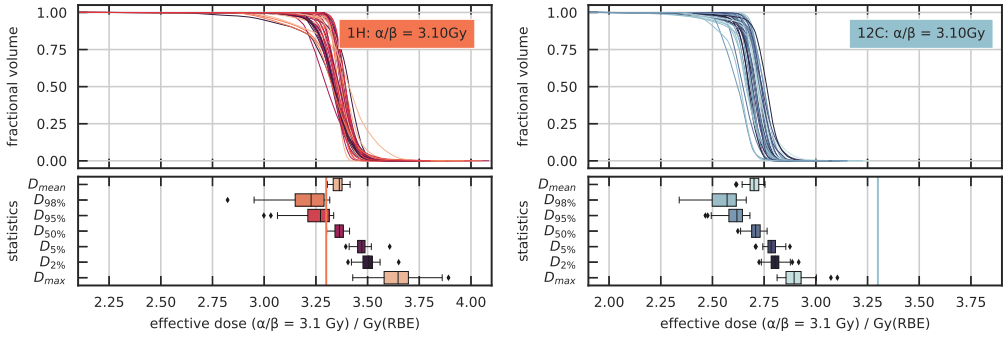

(c) $(\alpha/\beta)_x = 3.1\,\mathrm{Gy}$

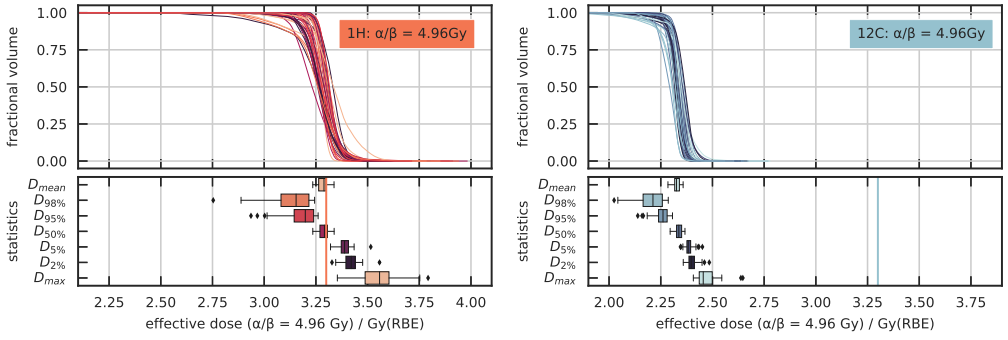

(d) $(\alpha/\beta)_x = 4.96\,\mathrm{Gy}$

Figure C.1: Effective Dose-Volume Histograms for the clinical target volume (CTV) of treatment plans in the IPI trial for additional radiobiological parameter sets. The data of Figure C.1c was presented in Besuglow et al. [15].

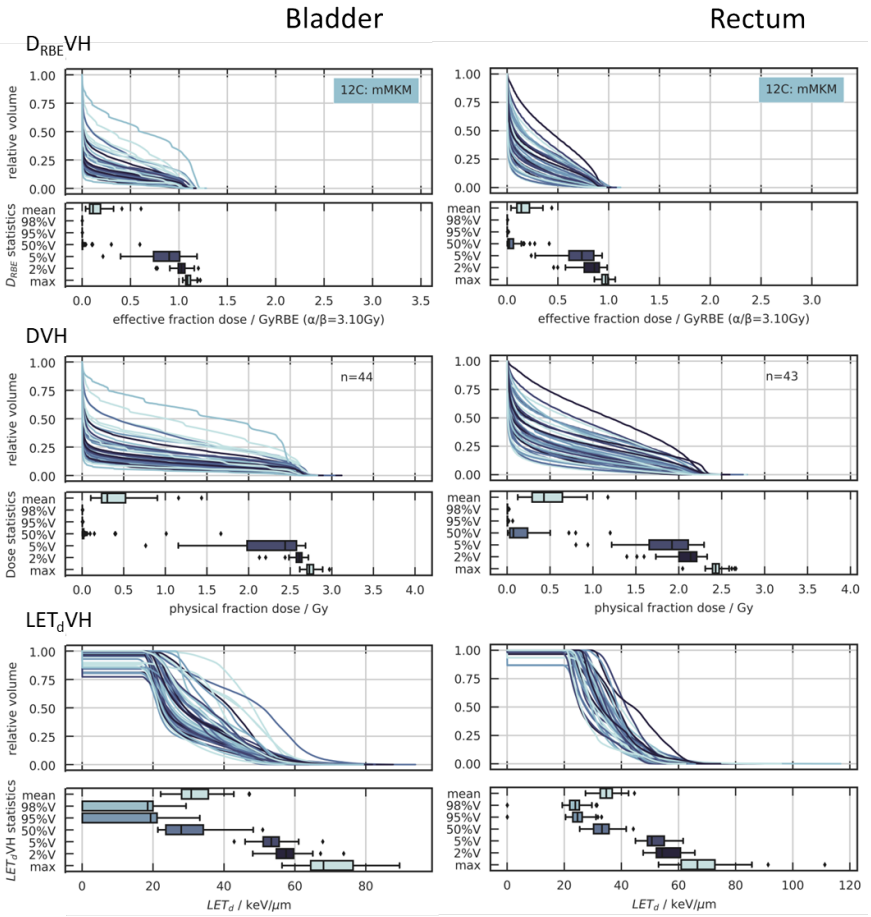

Figure C.2: DVHs of D, LET_d and RBE-weighted doses for bladder and rectum of the IPI carbon ion cohort. RBE is based on mMKM and $(\alpha/\beta)_x$=3.1 Gy.

D Supplementary to Third Publication

This supplementary is also available with the original publication as mmc1.pdf under the DOI: 10.1016/j.ijrobp.2024.02.025.

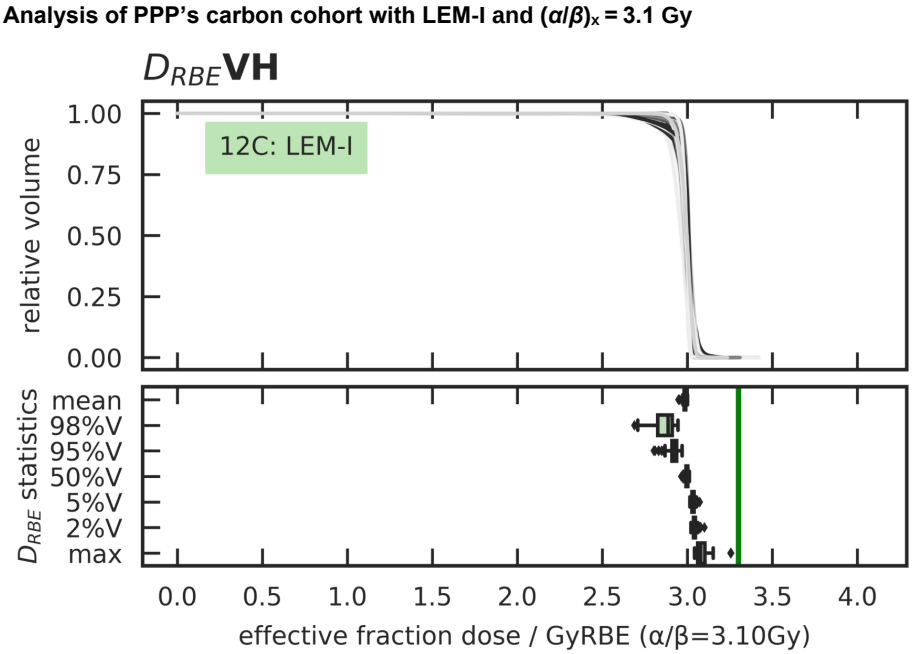

Figure E1 *D_{RBE}VH of effective biological dose applying LEM-I with $(\alpha/\beta)_x$ = 3.1 Gy.*

The boxplot for each statistical parameter indicates the inner quartiles and 1.5 times the interquartile range. The green vertical line in the statistics of the effective fraction dose indicates the prescribed fraction dose of 3.3 GyRBE of the trial.

Comparison of planning approaches for carbon ions – four additional patients

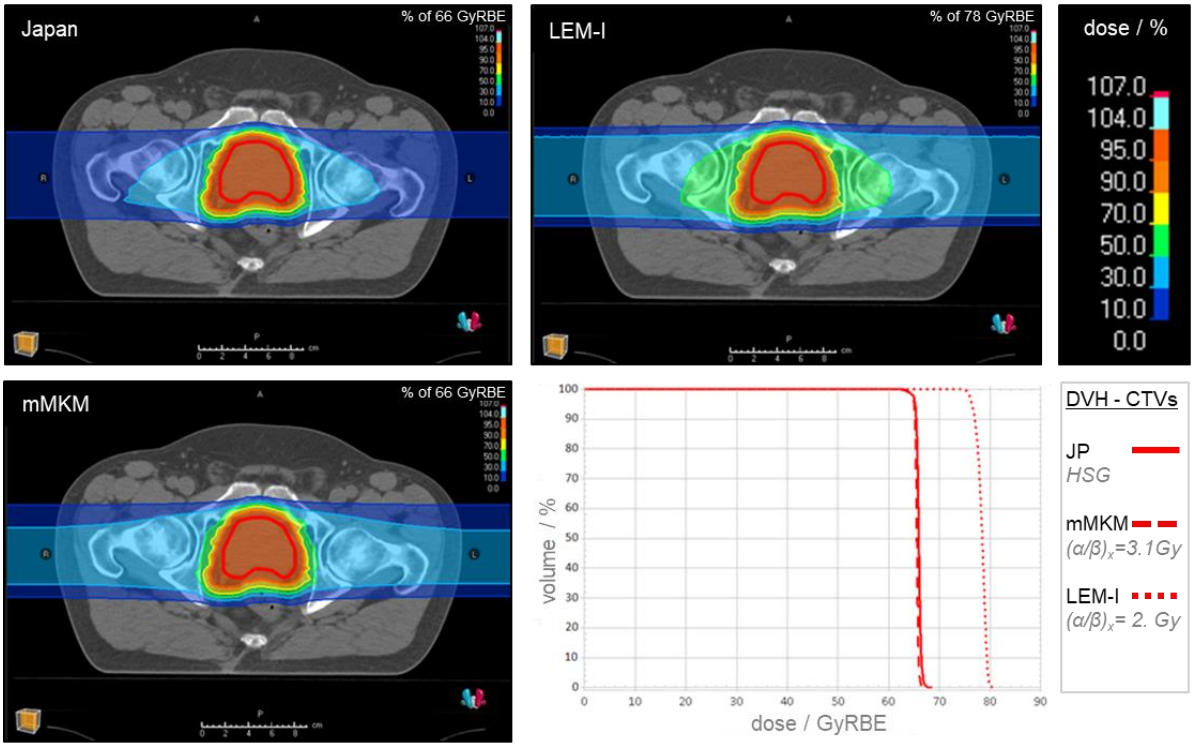

Figure E2 *Carbon ion planning approaches for patient B*

Top left panel: Japanese-like optimization (JP) of a carbon ion plan for a patient with medium CTV of the carbon arm using two opposing fields irradiated on alternating days. Bottom left panel: forward calculation of the JP-plan using $mMKM_{3.1}$. Top right panel: forward calculation of the JP-plan using LEM-I ($(\alpha/\beta)_x$ = 2 Gy). Be aware of the scale change in the applied color bar. Bottom right panel: $D_{RBE}VH$ comparison of the three optimization approaches. With the same physical dose, as expected LEM-I yields a much higher biological dose than the Japanese or mMKM approaches. *Abbreviations:* $D_{RBE}VH$ = *RBE-weighted dose-volume histogram*; JP = *Japanese-like*; LEM-I = *Local Effect Model, version 1*; mMKM = *modified microdosimetric kinetic model*; RBE = *relative biological effectiveness*.

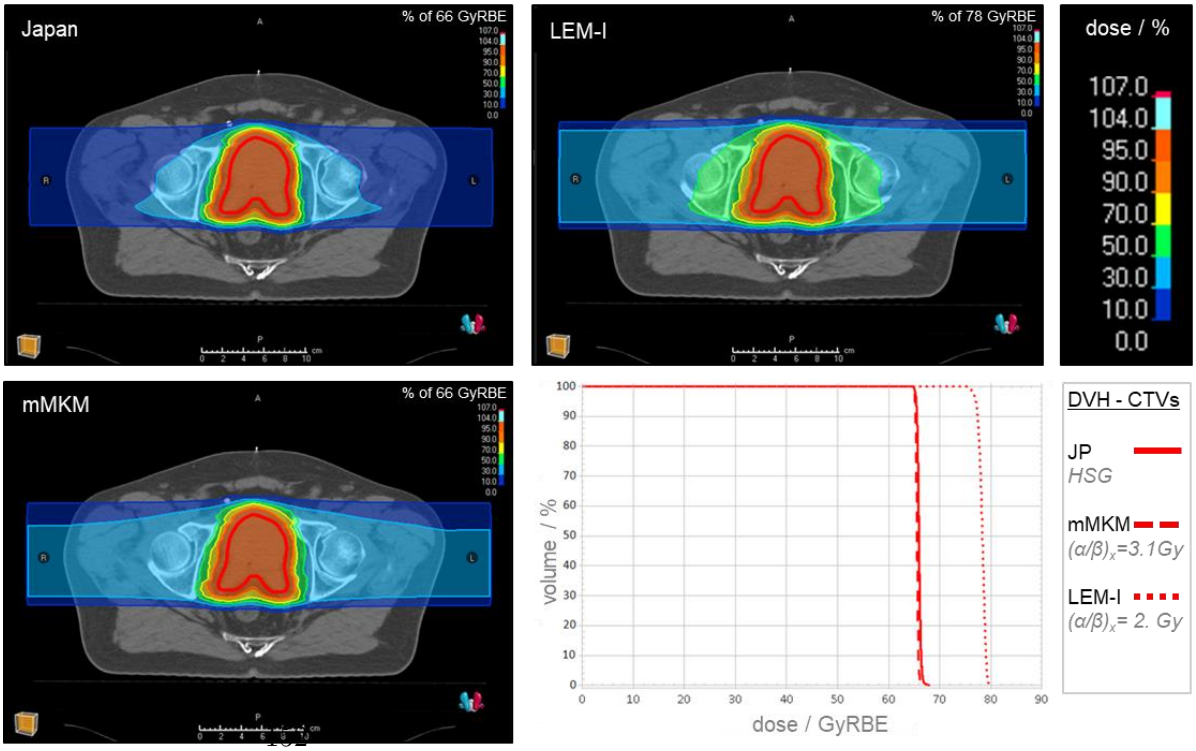

Figure E3 *Carbon ion planning approaches for patient C.*

Top left panel: Japanese-like optimization (JP) of a carbon ion plan for the patient with the median CTV of the carbon arm using two opposing fields irradiated on alternating days. Bottom left panel: forward calculation of the JP-plan using $mMKM_{3.1}$. Top right panel: forward calculation of the JP-plan using LEM-I ($(\alpha/\beta)_x$ = 2 Gy). Be aware of the scale change in the applied color bar. Bottom right panel: $D_{RBE}VH$ comparison of the three optimization approaches. With the same physical dose, as expected LEM-I yields a much higher biological dose than the Japanese or mMKM approaches. *Abbreviations*: $D_{RBE}VH$ = *RBE-weighted dose-volume histogram*; JP = *Japanese-like*; LEM-I = *Local Effect Model, version 1*; mMKM = *modified microdosimetric kinetic model*; RBE = *relative biological effectiveness*.

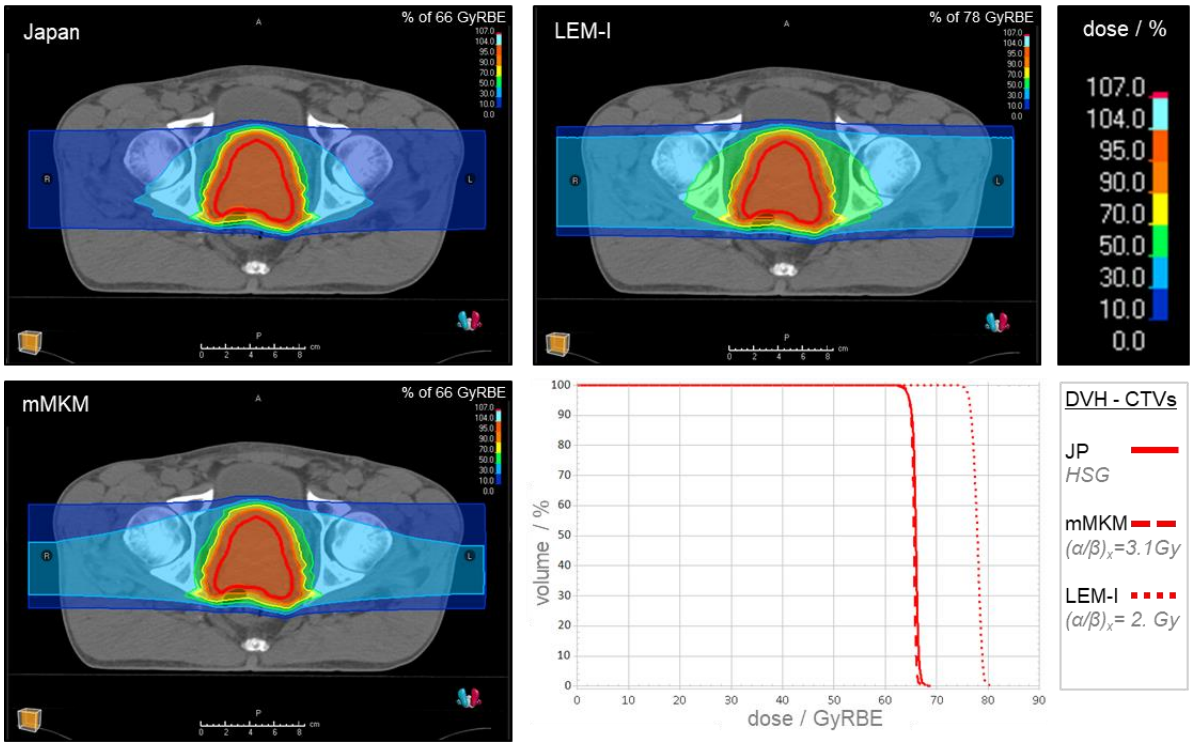

Figure E4 *Carbon ion planning approaches for patient D*

Top left panel: Japanese-like optimization (JP) of a carbon ion plan for a patient with medium CTV of the carbon arm using two opposing fields irradiated on alternating days. Bottom left panel: forward calculation of the JP-plan using mMKM ($(\alpha/\beta)_x$=3.1 Gy). Top right panel: forward calculation of the JP-plan using LEM-I ($(\alpha/\beta)_x$ = 2 Gy). Be aware of the scale change in the applied color bar. Bottom right panel: D_{RBE}VH comparison of the three optimization approaches. With the same physical dose, as expected LEM-I yields a much higher biological dose than the Japanese or mMKM approaches. *Abbreviations*: D_{RBE}VH = *RBE-weighted dose-volume histogram*; JP = *Japanese-like*; LEM-I = *Local Effect Model, version 1*; mMKM = *modified microdosimetric kinetic model*; RBE = *relative biological effectiveness*.

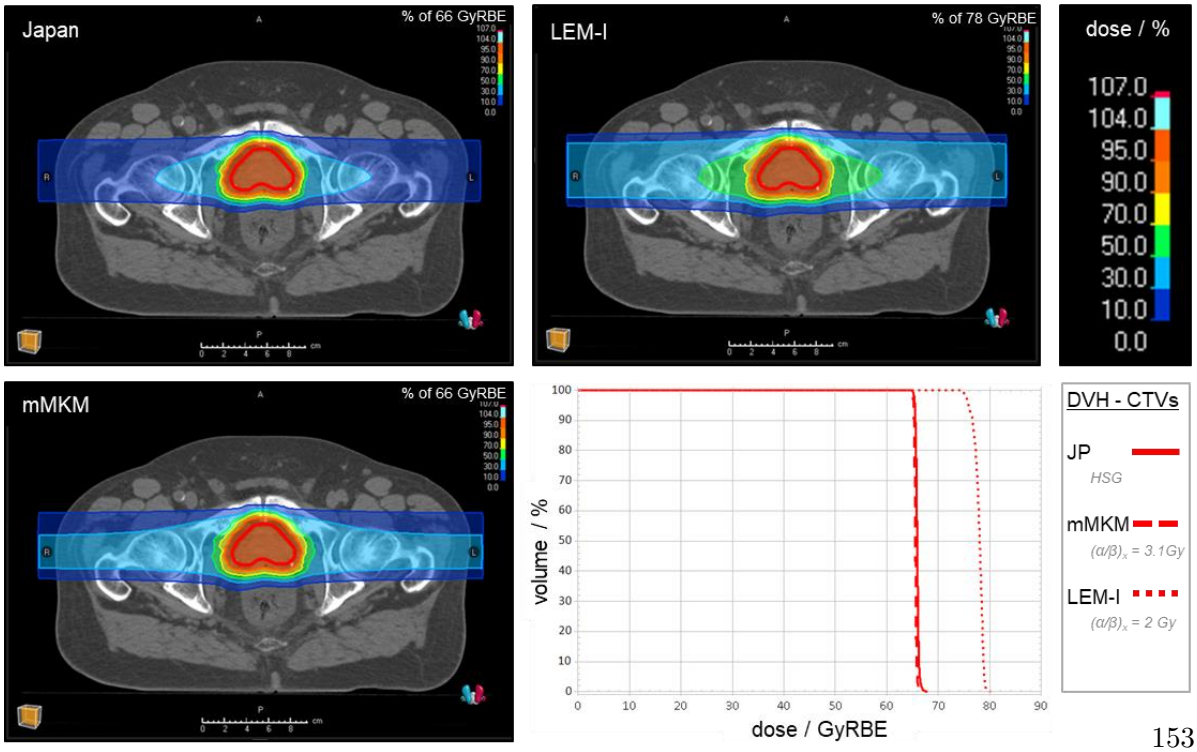

Figure E5 *Carbon ion planning approaches for patient E.*

Top left panel: Japanese-like optimization (JP) of a carbon ion plan for the patient with the smallest CTV of the carbon arm using two opposing fields irradiated on alternating days. Bottom left panel: forward calculation of the JP-plan using mMKM ($(\alpha/\beta)_x$ = 3.1 Gy). Top right panel: forward calculation of the JP-plan using LEM-I ($(\alpha/\beta)_x$ = 2 Gy). Be aware of the scale change in the applied color bar. Bottom right panel: D_{RBE}VH comparison of the three optimization approaches. With the same physical dose, as expected LEM-I yields a much higher biological dose than the Japanese or mMKM approaches. *Abbreviations*: D_{RBE}VH = *RBE-weighted dose-volume histogram*; JP = *Japanese-like*; LEM-I = *Local Effect Model, version 1*; mMKM = *modified microdosimetric kinetic model*; RBE = *relative biological effectiveness*.

Additional Patients with mMKM-optimized treatment plans for protons, carbon and helium ions

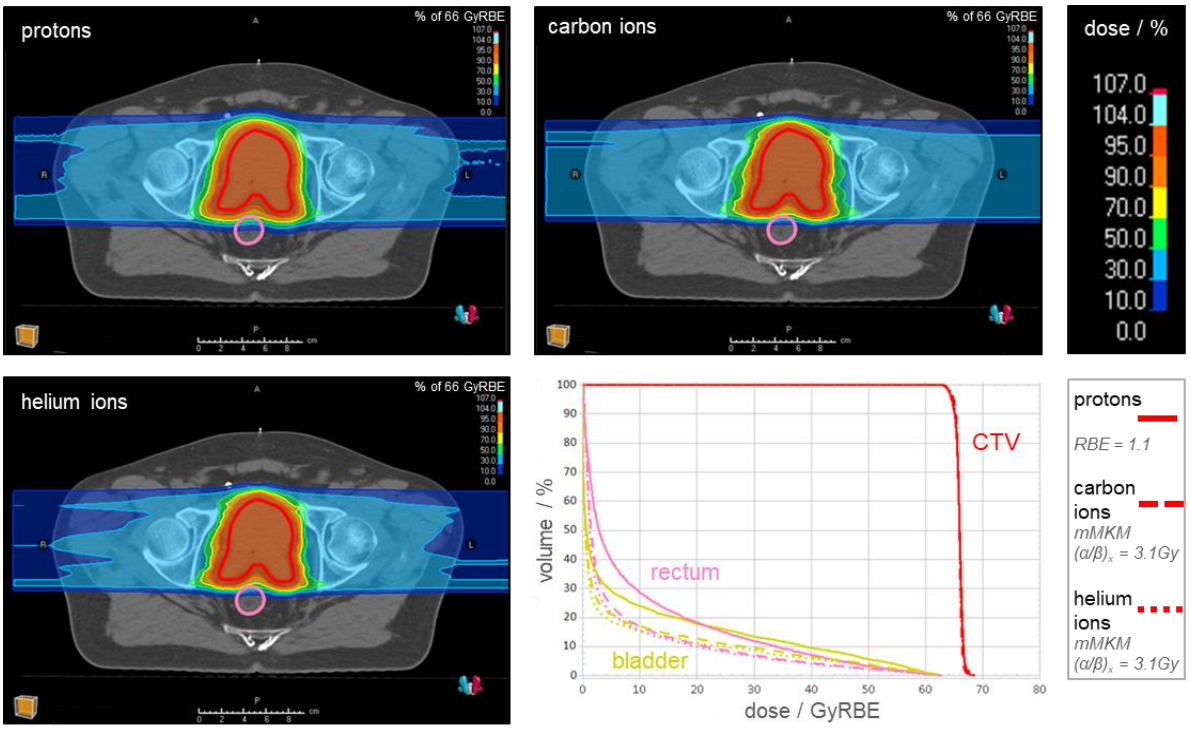

Figure E6 *mMKM optimized treatment plans for Patient C with protons, carbon and helium ions.*

Comparing protons (upper-left panel), carbon ions (upper-right panel) and helium ions (lower-left panel) treatment plans optimized using mMKM for the median CTV of the trial (Patient C). The $D_{RBE}VH$ comparison in the bottom right panel indicates a considerable dose reduction in rectum (pink) and bladder (yellow) for carbon (dotted) and helium ions (dashed) compared to protons (solid). The CTV (red) coverage remains approximately the same for all ions. *Abbreviations:* CTV = *clinical target volume;* $D_{RBE}VH$ = *RBE-weighted dose-volume histogram;* mMKM = *modified microdosimetric kinetic model*; RBE = *relative biological effectiveness.*

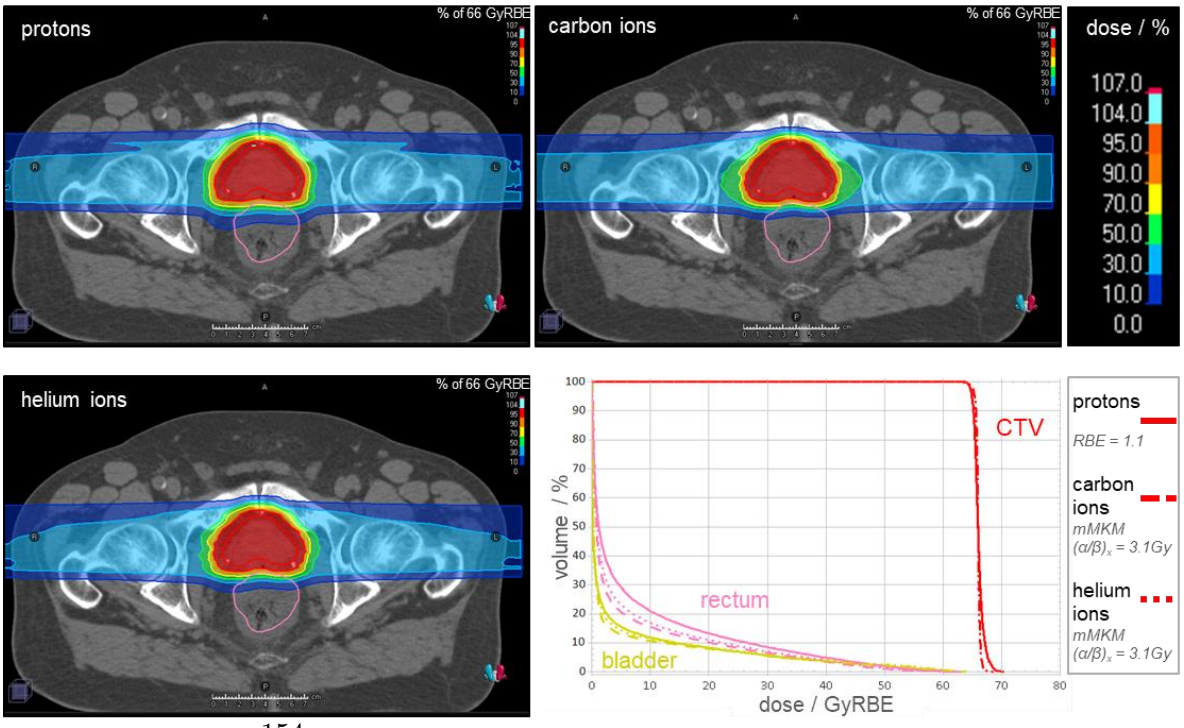

Figure E7 *mMKM optimized treatment plans for Patient C with protons, carbon and helium ions.*

Comparing protons (upper-left panel), carbon ions (upper-right panel) and helium ions (lower-left panel) treatment plans optimized using mMKM for the smallest CTV of the trial (Patient E). The $D_{RBE}VH$ comparison in the bottom right panel indicates a considerable dose reduction in rectum (pink) and bladder (yellow) for carbon (dotted) and helium ions (dashed) compared to protons (solid). The CTV (red) coverage remains approximately the same for all ions. *Abbreviations:* CTV = *clinical target volume;* $D_{RBE}VH$ = *RBE-weighted dose-volume histogram;* mMKM = *modified microdosimetric kinetic model*; RBE = *relative biological effectiveness.*

Table E8 *$D_{RBE}VH$ statistics of treatment plans with different particle beams for three patients.*

Treatment plans for protons (1H), helium ions (4He) or carbon ions (12C) were optimized with mMKM, applying $(\alpha/\beta)_x = 3.1$ Gy to target and normal tissues. Additional $D_{RBE}VH$ parameters were extracted for delineated rectum and the bladder without PTV.

Plan	ROI	ROI volume / cm³	Dose / GyRBE. (mMKM, $(\alpha/\beta)_x$ = 3.1 Gy)											Homogeneity Index $D_{95\%}/D_{5\%}$
			$D_{99\%}$	$D_{98\%}$	$D_{95\%}$	D_{mean}	$D_{50\%}$	$D_{2\%}$	$D_{1\%}$	$D_{0.3cc}$	D_{2cc}	D_{5cc}	D_{10cc}	
Patient A														
1H	Bladder-PTV	202.26	0.02	0.03	0.05	9.81	1.30	57.37	59.49	62.50	59.78	56.36	-	-
12C	Bladder-PTV	202.26	0.12	0.14	0.18	6.44	1.15	52.11	56.16	62.60	56.20	50.25	-	-
4He	Bladder-PTV	202.26	0.13	0.15	0.19	7.30	1.16	54.29	57.65	62.53	57.67	52.57	-	-
1H	CTV	237.12	63.92	64.38	64.90	66.00	65.99	67.66	67.99	-	-	-	-	0.97
12C	CTV	237.12	63.71	64.22	64.95	65.93	65.99	67.05	67.28	-	-	-	-	0.97
4He	CTV	237.12	63.58	64.39	65.10	65.90	65.95	66.84	67.03	-	-	-	-	0.98
1H	Rectum	68.87	68.87	0.26	0.36	0.64	21.66	14.87	60.11	62.28	59.47	56.15	49.61	-
12C	Rectum	68.87	68.87	0.41	0.49	0.65	14.65	5.14	59.07	62.41	58.36	53.08	41.57	-
4He	Rectum	68.87	68.87	0.44	0.52	0.69	15.38	5.56	59.01	62.17	58.33	53.61	39.96	-
Patient E														
1H	Bladder-PTV	523.26	0.00	0.00	0.00	4.36	0.18	49.39	55.12	62.95	59.14	55.39	-	-
12C	Bladder-PTV	523.26	0.00	0.00	0.00	4.17	0.36	51.12	57.01	62.59	60.61	57.29	-	-
4He	Bladder-PTV	523.26	0.00	0.00	0.02	4.51	0.37	53.06	58.02	62.59	60.91	58.30	-	-
1H	CTV	52.83	64.43	64.63	64.95	66.11	66.00	68.35	68.78	-	-	-	-	0.96
12C	CTV	52.83	64.59	65.01	65.42	66.01	66.02	66.83	66.99	-	-	-	-	0.98
4He	CTV	52.83	64.61	64.98	65.40	66.00	66.01	66.85	67.08	-	-	-	-	0.98
1H	Rectum	141.46	0.00	0.02	0.08	7.24	1.25	49.41	53.11	61.44	51.78	44.08	33.63	-
12C	Rectum	141.46	0.12	0.16	0.23	5.51	0.85	44.95	49.64	61.07	47.41	39.33	27.94	-
4He	Rectum	141.46	0.12	0.15	0.21	6.02	0.95	46.64	51.13	60.90	49.19	40.96	29.57	-
Patient C														
1H	Bladder-PTV	364.09	0.00	0.00	0.01	9.20	0.71	58.16	60.20	62.56	61.25	59.58	-	-
12C	Bladder-PTV	364.09	0.00	0.00	0.00	5.94	0.50	54.57	58.68	62.57	60.76	57.11	-	-
4He	Bladder-PTV	364.09	0.04	0.05	0.06	6.66	0.55	56.20	59.92	62.52	61.55	58.81	-	-
1H	CTV	104.17	63.72	64.02	64.59	64.94	66.00	67.20	67.53	-	-	-	-	0.97
12C	CTV	104.17	63.91	64.31	64.86	65.95	66.00	67.39	67.86	-	-	-	-	0.97
4He	CTV	104.17	63.83	64.35	64.95	65.90	65.95	66.90	67.15	-	-	-	-	0.97
1H	Rectum	84.85	0.13	0.15	0.21	10.01	2.91	54.04	57.77	62.34	52.86	42.77	30.00	-
12C	Rectum	84.85	0.26	0.28	0.34	6.01	1.30	50.54	57.00	62.52	48.38	31.94	16.13	-
4He	Rectum	84.85	0.27	0.29	0.33	6.50	1.53	51.85	57.63	62.49	49.53	33.20	17.57	-

Acknowledgements

There are many people, that have enabled me to put this thesis forward by encouraging me, providing comic relief, cheering me on or just enduring the times, when research seemed to have a higher priority than time with friend or tidying up. Even when I cannot mention all of you, be assured, I am no less grateful for your contribution.

First, I would like to thank *Prof. Dr. Dr. Jürgen Debus* for accepting me as his doctoral student and providing the awesome work environment between HIT, DKFZ, NCT and UKHD. I also thank *Prof. Dr. Amir Abdollahi* for providing the funds and research vision inside his clinical cooperation unit 'Translational Radiooncology'. *Prof. Dr. Hans-Christian Schultz-Coulon* kindly agreed to be my second referee and ensure that I would remain a physicist, albeit diving deep into the medical application. All three added valuable advice and direction to my research.

Most of all though, I am grateful to *Prof. Dr. Andrea Mairani* for being my supervisor and mentor. You entrusted me with this responsible topic and patiently believed in the scientist in me. You provided me with inspiration, encouragement and gentle guidance whenever necessary. I am very thankful for your commitment to this amazing BioPT research group, which has almost become family over the past years.

Out of this group, I am especially grateful to *Dr. Thomas Tessonnier* whose dissertation laid the foundation for my research and who upon his return back to Heidelberg became my accomplice in bringing helium ion therapy back to the future.

A big thank you also goes out to all the other members of the BioPT family. I am especially indebted to *Dr. Stewart 'Mac' Mein* and *Dr. Benedikt Kopp* who created FRoG and inspired my research with several inherited code snippets. A heartfelt thank you also goes to *Dr. Friderike Longarino* for surviving a pandemic together, always lending an open ear when life hit hard and becoming a really good friend. To those that joined later: *Nish, Peter, Luisa, Selver, Celine, Filipa, Yasmin, Hailey, Nico, Maria, Aaron, Ozan, Antonia and Una* thank you for the company in countless lunches, coffee brakes, hiking adventures and for all your commitment to the advancement of Biophysics in Particle Therapy. *Friderike*, *Yasmin* and *Filipa*, it was a delight to travel with you.

I would further like to thank *Dr. Alfredo Ferrari* for his help and guidance in the FLUKA jungle of reaction cross-sections. Without your input, the Monte Carlo beam model would only be half as accurate.

To all the HIT-team, I am also thankful. During all the early morning and late night shifts, you taught me so much about dosimetry and the finesse of

clinical day-to-day routine. I would like to especially thank the medical physicists *Dr. Stephan Brons, Dr. Jakob Naumann, Benjamin Ackermann, Swantje Ecker, Dr. Malte Ellerbrock and Dr. Harald Latzel* for assisting in and taking over parts of the night shifts of measuring dose distributions. I would also like to thank *Claudia Rittmüller* and *Rosi Vay-Mayer* who tamed the bureaucracy of working in the junction of four organizational entities. To *Dr. Tanja Eichkorn* and *Andreas Kudak*, I am thankful for collecting and retrieving all the patient data of the IPI trial from the HIRO Database.

Dr. Ronja Hetzel, Dr. Karim Laihem, Dr. Aleksandra Wrońska and Prof. Dr. Achim Stahl, you sparked and nourished my interest in medical physics, Monte Carlo and particle therapy over ten years ago. Working alongside *PD Dr. Julia Bauer* and *Prof. Dr. Markus Alber* during my Master's thesis inspired me to continue in this field. I will be eternally grateful for you feeding my curiosity.

Finally, I am deeply grateful for the love and encouragement, I received from *my family* and so many dear *friends*. Your support and prayers carried me through some very tough times. I can only hope to someday return the favor. And last but not least, I have to thank *my parents*, *my sister* and *my partner* from the bottom of my heart. Without your love, I would not have the confidence to pick a fight with tumors. I am fortunate to have you in my life.